Chemosensors for Selective Detection of Some Metal Ions, Cysteine and ATP

A Dissertation Submitted to the
Indian Institute of Technology Guwahati as
Partial Fulfillment for the Degree of Doctor of Philosophy
in Chemistry

by

Anisha Mondal
Roll No. 196122004

Department of Chemistry
Indian Institute of Technology Guwahati
Guwahati – 781039

AUGUST 2025

DEDICATED

TO

MY PARENTS AND FAMILY

DEPARTMENT OF CHEMISTRY

INDIAN INSTITUTE OF TECHNOLOGY GUWAHATI

GUWAHATI–781039

DECLARATION

I do hereby declare that the research work embodied in this thesis entitled "**Chemosensors for Selective Detection of Some Metal Ions, Cysteine and ATP**" is the outcome of research work carried out by me under the supervision of Prof. V. Manivannan, at the Department of Chemistry, Indian Institute of Technology Guwahati, Assam, India.

In keeping with the general practice of reporting scientific observations, due acknowledgments have been made wherever the work described is based on the findings of other investigators.

Anisha Mondal

IIT Guwahati — Anisha Mondal

August, 2025 — (Roll.No.-196122004)

Dr. V. Manivannan
Professor
Department of Chemistry
Indian Institute of Technology
Guwahati-781039
Assam, INDIA

Ph: +91 361 258 2306 (O)
E-mail: mani@iitg.ac.in

CERTIFICATE

This is to certify that the research work presented in this thesis entitled "**Chemosensors for Selective Detection of Some Metal Ions, Cysteine and ATP**" is an authentic record of the results obtained from the research work carried out by **Anisha Mondal** under my supervision in the Department of Chemistry, Indian Institute of Technology Guwahati, India. This work is original and has not been submitted elsewhere for a degree.

IIT Guwahati
March, 2025

Prof. V. Manivannan
(Thesis Supervisor)

ACKNOWLEDGMENTS

At the end of my PhD tenure, I would like to express my profound gratitude to everyone who has supported me in any way over this time.

I want to sincerely thank Prof. V. Manivannan, my PhD supervisor for his constant guidance and encouragement throughout my PhD. During this time, his valuable ideas, suggestions and patience helped me a lot to carry out the research work for successful completion. He allowed me to use my ideas freely and made corrections where necessary, which allowed me to gain a lot of knowledge. I consider myself fortunate to have worked under his guidance.

I am grateful to the doctoral committee members Prof. Anil Kumar Saikia, Prof. Seenipandian Ravi and Prof. Lal Mohan Kundu for their valuable suggestions. I am also thankful to the entire faculty and staff in the Department of Chemistry, Indian Institute of Technology Guwahati for providing the working environment throughout this period.

A special thanks to the Central Instruments Facility, North East Centre for Biological Science and Healthcare engineering and Department of Chemistry, Indian Institute of Technology Guwahati, for providing various instrumental facilities.

I am deeply grateful to my dear friends Anita, Anjela, Suravi, Santunu, Sanchari, Abhishek, Ahmad, Tammana, Poulami, who stood by me throughout my PhD journey, shared words of motivation during difficult times, and reminded me to celebrate small victories along the way. Special thanks to Ms. Mongoli Brahma for being a source of strength, positivity, and encouragement during the last phase of my doctoral research work. I would also like to express my heartfelt gratitude to some of my senior of IIT Guwahati Dr. Mihir Manna, Dr. Manideepa Paul, Dr. Sayanta Roy, Dr. Moumita Chandra, Mr. Arup Das for their valuable suggestions and constructive feedback throughout my research work.

My sincere gratitude is extended to my senior lab mates, Dr. Sandeep Kumar and Dr. Araghni Bhattacharya, for sharing their expertise in data analysis, instrument handling, and experimentation. I also like to thank my current lab partners Alok Kumar, Rituraj Hazra, and Amlan Ranjan Rayasingh for their cooperation throughout this time. I am also thankful to the project students Swati, Muskan, Krishan, Pooja, Nirupama who have worked with me.

The financial support from Indian Institute of Technology Guwahati is duly acknowledged.

Finally, I would like to thank my parents and family for their blessings, patience, faith and encouragement during this long period which helped me to stay positive in every circumstance.

Anisha Mondal

Preface

This Thesis contains five chapters. Chapter 1 is about Introduction, Materials and Methods. In this chapter introduction about chemosensors and various sensing mechanisms are explained. Some recent literature reports based on metal ion, biothiols and phosphate sensing have been discussed. Along with this, materials, methods and instrumentation related to this thesis are described in detail. In Chapter 2, a chemosensor 3-hydroxy-N'-(11H-indeno[1,2-b]quinoxalin-11-ylidene)-2-naphthohydrazide (**LH**) was synthesized for selective colorimetric recognition of Cu^{2+} ion in MeOH/HEPES buffer system (1:1, *v*/*v*, pH = 7.4). Upon adding Cu^{2+} ion to the probe solution, a characteristic chromogenic change from colorless to yellow was observed. The *in situ* generated [Cu(**L**)Cl(H_2O)$_2$] (complex **1**) was found to exhibit a discoloration, upon gradual addition of cysteine as well as ATP having 1:2 and 1:1 stoichiometry respectively. The binding ability of **LH** with BSA and HSA was examined by spectral and *in silico* docking analysis. Chapter 3 deals with the synthesis and characterization of a probe N-(naphthalen-1-yl)-2-(pyren-1-ylmethylene)hydrazine-1-carbothioamide (**L_1**) and exhibited a significant aggregation induced emission (AIE) property in 7:3 water-EtOH mixture. The nano-structure aggregates formation exhibited a yellowish-green fluorescence upon excitation with 380 nm light. A colorimetric and a fluorescence turn-off response was observed with the gradual addition of Pd^{2+} ion in a colorless EtOH/aqueous HEPES buffer (3:7, *v*/*v*) solution of **L_1**. The recognition of Pd^{2+} in real water and pharmaceutical drug samples also performed. In Chapter 4, a quinoline-linked benzimidazole scaffold AIE active probe 6-(quinolin-2-yl)-5,6-dihydrobenzo[4,5]imidazo[1,2-*c*]quinazoline (**L2H**) is utilized as a fluorescent turn-on sensor for the selective detection of Al^{3+} ion and cysteine in surfactant medium. Cyclic bidentate probe (**L2H**) upon binding with Al^{3+}, converted to tridentate **L2′**, having an open structure and cysteine converted **L2H** to a fluorescent dimer (**L2–L2**). Various practical applications such as food and real water samples were also performed for rapid on-site detection of both analytes. In Chapter 5, the probe (**L3H**) having quinazolinone and 4-diethylaminophenyl moieties has exhibited selective recognition of As^{3+} ion in aqueous HEPES medium. The rapid on-site detection of As^{3+} ion was achieved using a smartphone-based portable sensing device.

Abbreviations

a	Unit cell dimension *a*
b	Unit cell dimension *b*
c	Unit cell dimension *c*
α	Interfacial angle along *b, c* axes
β	Interfacial angle along *a, c* axes
γ	Interfacial angle along *a, b* axes
Z	Unit cell formula unit
δ	Chemical shift in NMR
ppm	Parts per million
NMR	Nuclear magnetic resonance
ESI	Electro spray ionisation
FT-IR	Fourier transformed-infra red
HOMO	Highest occupied molecular orbital
LUMO	Lowest unoccupied molecular orbital
ORTEP	Oak ridge thermal ellipsoid plot
US EPA	United States Environmental Protection Agency
HSAB	Hard soft acid base
ADP	Adenosine 5′-diphosphate
AMP	Adenosine 5′-monophosphate
HEPES	4-(2-hydroxyethyl)-1-piperazineethanesulfonic acid
EDTA	Ethylenediaminetetraacetic acid
THF	Tetrahydrofuran
DMSO	Dimethyl sulfoxide
DMF	N,N-Dimethylformamide

Table of Contents

Chapter 1

Chapter 2

Chapter 3

Chapter 4

Chapter 5

Chapter 1

Introduction, Materials and Methods

Abstract:

In this chapter, a concise overview has been explored on chemosensors and their underlying sensing mechanisms. Two primary categories of optical sensors *viz*., colorimetric and fluorescent were described. Diverse sensing pathways, including photoinduced electron transfer (PET), intramolecular charge transfer (ICT), excited state intramolecular proton transfer (ESIPT), chelation enhanced fluorescence (CHEF), aggregation induced emission (AIE), fluorescence resonance energy transfer (FRET) and C=N bond isomerization have been widely discussed for designing of various unique probe molecules. Along with this, based on selected literature reports, recent developments in metal ions, biothiols and phosphate sensing using different chromogenic and fluorogenic probes have been highlighted. At the end of this Chapter, materials and methods used in this study, sample preparation, spectral analysis methods, specifications and model of instrument used in experiments, theoretical calculations are also briefed.

1.1 Introduction:

The development of chemosensors for the specific detection of biologically active ionic species is significantly important. Chemosensors used for the selective detection of metal ions, biothiols and biomolecules are in high demand.[1,2] They offer excellent selectivity and sensitivity for low-cost and accurate detection of target analytes. Numerous chemosensors are designed for the selective qualitative analysis of various analytes through specific host-guest interactions like metal-ligand coordination, hydrogen bonding, and van der Waals interaction.[3,4] Owing to their affordability, simplicity and ease of use, most of these chemosensors are employed in solution using various spectroscopic techniques. Metal ion chemosensors specifically detect selective metal ions due to their high binding affinity with specific donor sites. Over the years, chemosensors have found valuable applications in environmental monitoring, biomedical science, food technology, and bioimaging.[5,6]

In biological systems, *s*-block metal ions Na^+, K^+, Ca^{2+}, and Mg^{2+} play crucial roles in metabolism, osmotic regulation, and hormonal signaling.[7] Several micronutrients, such as Fe, Zn, Cu, Mo, Co, Cr, V, Ni and W in their appropriate oxidation states, are vital for maintaining life processes.[8] Iron is the an important essential transition metal, functioning as a catalytic component in proteins and enzymes involved in oxygen transport and cellular metabolism.[9,10] However, excessive iron intake suppresses adsorption rates and leads to cancers and organ dysfunctions, including liver, heart and pancreatic issues.[11] Iron deficiency also causes anaemia, diabetes and Parkinson's disease. Zinc is the next most abundant transition metal, plays key roles in enzymatic regulation, neurotransmission, and DNA recognition.[12] Its excessive accumulation is associated with Alzheimer's disease, diabetes, apoptosis, and ischemia. Silver is well known for its antimicrobial activity and use in digital imaging.[13–15] However, due to its toxicity and bioaccumulation, prolonged Ag exposure negatively impacts human health, causing symptoms such as fatigue, headaches and skin irritation.[16] The most widely used trivalent metal ions Al^{3+}, Cr^{3+}, Fe^{3+} are very closely related to human health.[17,18] Since aluminium (Al) is one of the most abundant element on earth crust, it is widely used in battery manufacturing, automobile industries, water purification and various other fields.[19,20] Among the several metal ions, Bi^{3+} is one of the non-toxic and rare earth elements which obtained as a by-product of tin and copper refining.[21] The major health issues, such as bone and kidney related problems in human body, occur due to Bi^{3+} toxicity.[22,23] Heavy metal ions like Pd^{2+}, Cd^{2+}, Hg^{2+}, Pb^{2+} are not beneficial and cause severe health problems, including

kidney failure, neurological and digestive disorders when ingested through contaminated food or water.[24–26] Palladium (Pd) is one of the significant heavy transition metals and a precious heavy element, finding potential applications in various fields including electric devices, electronic equipment, automobile, fuel and jewellery industries.[27,28] However, the excessive accumulation of residual Pd causes water and land pollution, and creates a higher risk for human health by inhalation.[29,30] Likewise, Pd, gold (Au) is also an important precious metal that serves several major applications. It acts as a potential drug element for curing various diseases like asthma, cancer, HIV, and rhematic arthritis.[30,31] Excessive intake of Au causes several detrimental effects for both animal and human beings, causing damage to kidney, liver and nervous system.[32,33] The toxic metalloid arsenic (As) is present in natural water sources and it can causes serious health problem in human bodies related to neurodegenerative disorder, dermal toxicity and skin cancer like diseases.[34,35] Among the two common oxidation states of arsenic, As^{3+} and As^{5+}, As^{3+} is considerably more toxic due to its higher binding affinity for thiol groups present in protein and other biomolecule.[36,37] Therefore, the development of efficient and selective methods for metal ion recognition in biological and environmental samples is highly desirable.

The development of various chemosensors that allow rapid and easy detection of biothiols is essential for regulating human health metabolism.[38] Biothiols are often called mercaptans as they contain sulfhydryl groups.[39,40] Cysteine (Cys), glutathione (GSH) and homocysteine (Hcy) are the most relevant biological thiols. Cysteine is one of the most vital non-essential amino acid that help in the synthesis of glutathione.[41] To date, numerous studies have established a strong connection between cysteine and a variety of diseases, including liver damage, hair depigmentation, skin lesions, edema and loss of fat.[28] Therefore, cysteine detection is deemed essential for diagnosing the early onset of these disorders. Dysregulation of Hcy levels results in cardiovascular disorders, lung cancer, occlusive vascular disorders and neural tube abnormalities.[44,45] The most important intracellular biothiol GSH, acts as the cellular redox centre.[46] Furthermore, it also function as an intrinsic antioxidant, which helps in the preservation of intracellular redox metabolism.[47] Excessive intake of GSH is associated with various diseases such as cardiovascular, neurological disorders, cancer and so on.[48–50] Therefore, the development of selective colorimetric and fluorometric probes for their recognition became highly essential.[51,52] So, considerable efforts were made to design such probes using diverse analytical approaches.

Several phosphate containing compounds, namely PPi, ATP, ADP and AMP play important role in several biological processes for the living organism.[53,54] Such phosphate acts as an important nutrient in living beings and participates in several metabolic function, including protein activation, energy transfer and amino acid metabolism.[55,56] For example, adenosine phosphates (ATP, AMP, ADP) play a major role in metabolic reactions, such as phosphate donor group acting as a signalling molecule and pyrophosphate is necessary for both DNA replication and sequencing.[57,58] By considering the important physiological aspect of PO_4^{3-} ion, the quick and simple detection of phosphate is very significant.[59] Previously, many analytical methods such as ion chromatography, spectrophotometry and volumetric analysis were used for the detection of PO_4^{3-} ion.[60] Due to the high instrumentation cost, detection limit, and large time consumption the methods are limited for widespread applications. So it is very crucial to design a suitable chemosensor for the selective recognition of phosphate compounds.

A chemosensor consists of two main components *viz*., a receptor unit for analyte binding and a signalling unit for transducing the interaction into detectable changes in optical or electronic properties. The chemical sensors consist of signaling units that convert chemical information into optical signals, such as changes in colour or fluorescence.[61] Interaction between the analyte and the receptor triggered electronic changes in the signalling unit, leading to variations in emission and absorption spectra.[62] Chemosensors utilized a specific signaling pathway, where analyte-receptor interactions within the π-system of the receptor group translated recognition *via* colorimetric and fluorescence response.[63] The receptor and signalling units are linked with a spacer group, as illustrated in Figure 1.

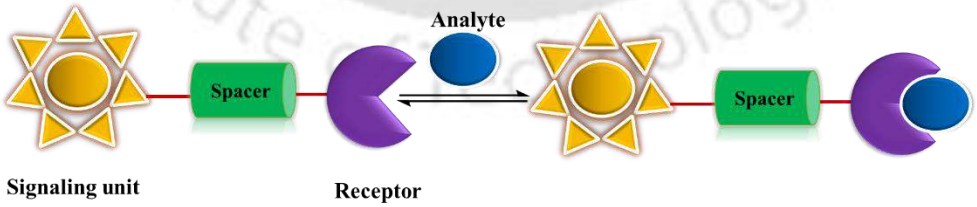

Figure 1. Schematic representation of chemosensor.

1.2 Optical Sensors

Among various types of chemosensors, optical sensors are utilized to transform the changes of various optical signals, which are again subdivided based on different photophysical properties

like absorbance, refractive index, luminescence, fluorescence and optothermal effect. It consists of a molecular binding site, a chromophore or fluorophore unit, upon interaction with analyte, it alters the optical properties like light absorption or emission. Compared to conventional sensors, optical sensors offer higher sensitivity and accuracy, acting as an ultrafast sensor that is useful in trace-level analysis. These sensors are further classified into two main categories *viz.,* colorimetric and fluorescent chemosensors.

1.2.1 Colorimetric Chemosensor

The design of colorimetric chemosensors for biologically relevant targets, including metal ions biothiols and biomolecules remained an active area of research. Such chemosensors consist of various coordination sites and upon analyte interaction they induce a visible colour change through the signaling unit. The signaling unit is composed of chromophore (Figure 2). Colorimetry served as the signaling mechanism due to its several advantages, including high selectivity, sensitivity, low cost and the ability to visually detect changes without using sophisticated instruments.[64] Colorimetric chemosensors are currently utilized in various sectors such as in medical diagnostics, environmental monitoring, food quality assessment and industrial pest control.[65] These sensors typically operated in the visible region of the electromagnetic spectrum, where analyte recognition was achieved using various photoactive moieties, including pyrene, anthracene, BODIPY, fluorescein, rhodamine, nitrophenyls, 1,8-naphthalimide and coumarin.[66] In conjugated systems, the absorption spectra of organic compounds depend on the presence of electron-donating (-NH_2, -NHR, -NR_2, -OMe, -OH) and electron-withdrawing groups (-NO_2, -COOH, -CN, -SO_3H). The introduction of both types of groups into the molecular framework leads to the appearance of charge transfer bands.

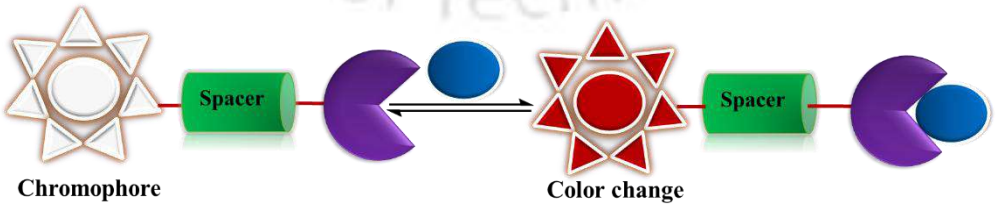

Figure 2. Schematic representation of colorimetric chemosensor.

1.2.2 Fluorescent Chemosensor

Fluorescent chemosensors are molecules whose fluorescence properties change in response to specific molecular recognition events.[67] These sensors generally measure variations in photophysical parameters such as emission wavelength shift, fluorescence intensity and fluorescence lifetime upon interaction with analytes like cations, anions. The fluorescence technique offers high sensitivity, selectivity, cost-effectiveness and enables detection at sub-micromolar levels. As a result, fluorescent chemosensors found widespread applications in environmental monitoring, food analysis and biomedical science.[68–70] For effective application in various fields, fluorescent chemosensors are required to meet several criteria: (i) high selectivity toward the target analyte even in the presence of other interfering analytes, (ii) strong and specific binding affinity to desired analytes, (iii) a clear and measurable fluorescence response upon binding, (iv) low toxicity and (v) good solubility in the sensing medium. Factors such as solvent polarity, protic or aprotic nature, hydrogen bonding ability, ionic strength and pH significantly influenced the binding efficiency, selectivity and the photophysical properties of the fluorophore.

In fluorescent chemosensors, analyte binding to the receptor induced notable changes in the photophysical properties of the fluorophore, which are converted into optical signals. These sensors operated primarily through two mechanisms: fluorescence "OFF" and fluorescence "ON" (Figure 3). The resulting signal involved either fluorescence enhancement or quenching effect.[71,72]

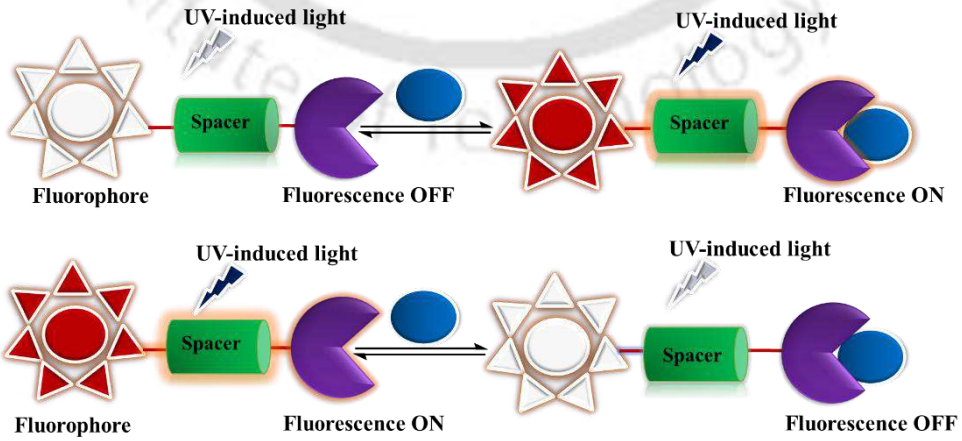

Figure 3. Schematic representation of fluorescent chemosensor.

1.3 Signalling Mechanism for Chemosensor

The main goals of chemosensor design is to investigate sensing mechanism based on interactions between receptors and signaling units. Various photophysical properties led to the development of several conventional signaling mechanisms, including photoinduced electron transfer (PET), intramolecular charge transfer (ICT), excited-state intramolecular proton transfer (ESIPT), chelation-enhanced fluorescence (CHEF), aggregation-induced emission (AIE), fluorescence resonance energy transfer (FRET) and C=N isomerization. These mechanisms are discussed below.

1.3.1 Photoinduced Electron Transfer

PET process involved the sensors, which typically consisted of a fluorophore linked to a receptor unit containing a non-bonding electron pair. Upon excitation, the fluorophore transferred an electron from HOMO to LUMO, followed by charge transfer and fluorescence emission. However, if the receptor's HOMO lay between the energy levels of the fluorophore, an electron could transfer from the receptor to the partially filled HOMO of the excited fluorophore, leading to non-radiative decay and fluorescence quenching (Figure 4A). In contrast, upon analyte binding, the receptor's HOMO energy decreased due to increased redox potential, suppressing electron transfer and allowing fluorescence emission (Figure 4B).

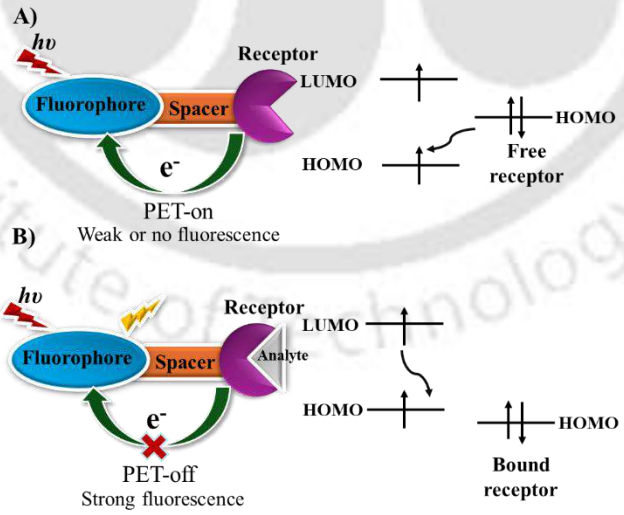

Figure 4. Schematic representation of PET mechanism.

1.3.2 Intramolecular Charge Transfer

The ICT process involved the sensors, in which the fluorophore and receptor were directly linked, forming a single molecule where each unit functioned as either an electron donor or

acceptor. In this mechanism, HOMO of the chemosensor was localized near the electron donating group, while the LUMO was closer to the electron acceptor group, enabling intramolecular charge transfer upon excitation. Analyte (guest) binding to either the donor or acceptor altered the dipole strength, leading to change in the photophysical properties.[73] When the fluorophore interacts with the donor group reduced its electron-donating ability, causing a blue shift in emission (Figure 5A), whereas binding to the acceptor enhanced its electron-withdrawing nature, resulting in a red shift (Figure 5B).

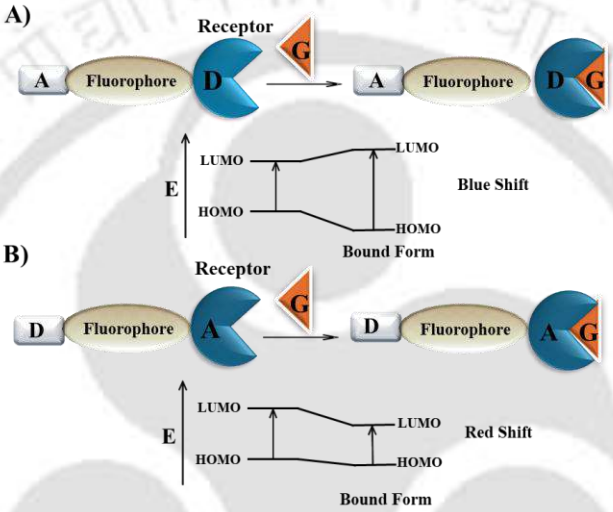

Figure 5. Schematic representation of ICT mechanism.

1.3.3 Excited-State Intramolecular Proton Transfer

Organic compounds undergoing the ESIPT process depend on the surrounding medium and reveal a large Stokes shift of emission. These probes contain a proton donor groups (amino or hydroxyl proton) and acceptor (imine nitrogen or carbonyl oxygen), facilitating intramolecular hydrogen bonding within a proximity of ~2 Å. Upon excitation, a proton shifted from the donor (E*) to the acceptor (K*) through a preorganized six-membered H-bond ring, termed as ESIPT mechanism.[74] After emission, the keto form returned to the enol state *via* the reverse proton transfer (RPT) process. So, ESIPT involves four-step photochemical process (Figure 6). ESIPT-based fluorophores were influenced by parameters such as pH, solvent polarity and hydrogen bonding, which could limit their application in bioimaging.

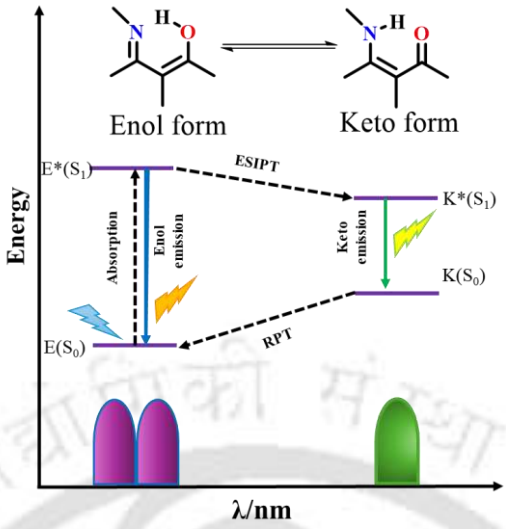

Figure 6. Schematic representation of ESIPT mechanism.

1.3.4 Chelation Enhanced Fluorescence

Most detection mechanisms involve small molecular probes based on changes in the fluorescence behaviour of the sensor upon interaction with specific metal ions. After the coordination of a metal ion to the sensor enhanced the intrinsic emission of the unbound probe. These effects are termed as chelation-enhanced fluorescence (CHEF) effect. By altering the emission intensity at different wavelengths, the maximum fluorescence intensity increased upon coordination with the metal ions (Figure 7).[75]

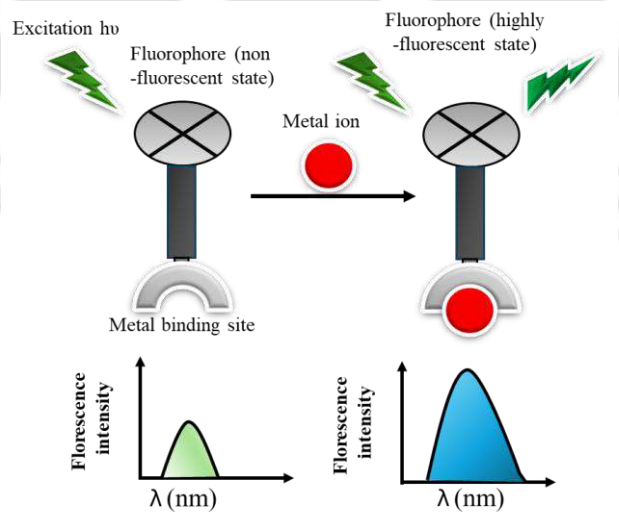

Figure 7. Schematic representation of CHEF mechanism.

1.3.5 Aggregation-Induced Emission

The photophysical behaviour arising from the aggregation of organic luminophores was termed Aggregation-Induced Emission (AIE). AIE-based probes remained non-emissive in solution but exhibited intense fluorescence upon aggregation. This distinct characteristic found widespread application in fields namely organic light-emitting diodes (OLEDs), organic field-effect transistors (OFETs), solar cells and laser dyes.[76,77] Most AIE-active molecules showed high solubility in organic solvents, resulting in weak emission bands. However, in aqueous medium (water or buffer), these luminogens aggregated and showed a strong emission band.[78] In the aggregated state, restriction of intramolecular rotation (RIR), vibration (RIV), and/or motion (RIM) leads to the emergence of AIE behaviour within the molecule.[17,79]

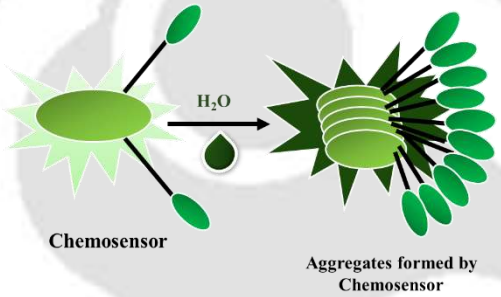

Figure 8. Schematic representation of AIE.

1.3.6 Fluorescence Resonance Energy Transfer

FRET is a non-radiative mechanism wherein an excited donor fluorophore transferred energy to an acceptor fluorophore in its ground state *via* dipole–dipole coupling.[80] FRET occurred effectively when the donor and acceptor groups are situated approximately within a distance of 10–100 Å, facilitating significant spectral overlap between donor's emission and acceptor's absorption (Figure 9). More overlap will result in a more efficient FRET. In fluorescence-based sensing schemes, the coordination of metal ion typically reduces the spatial separation between donor and acceptor, thereby enhancing FRET efficiency. FRET caused a reduction in both donor fluorescence intensity and excited-state lifetime, which could be monitored solely by observing the donor emission wavelength.[81] The FRET ratio was calculated by dividing the sensitized acceptor emission by the donor emission. The sensing function is achieved by modulating FRET, either enhancing or disrupting energy transfer through metal-induced structural changes that altered donor–acceptor distance, orientation, or both.

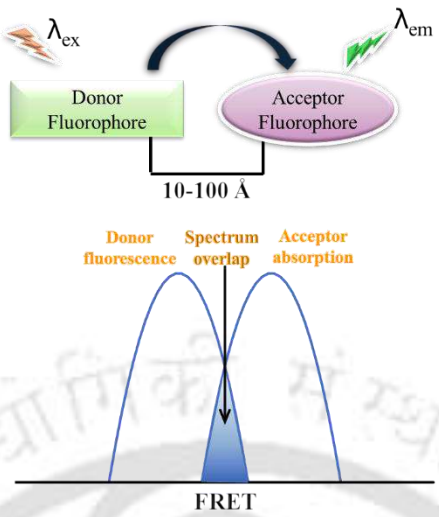

Figure 9. Schematic representation of FRET mechanism.

1.3.7 The C=N Isomerization

In this sensing mechanism, fast isomerization of C=N bond occurs, which facilitates non-radiative decay pathway for the formation of non-fluorescent and weakly fluorescent molecule.[80–82] The receptor upon binding with an analyte, this isomerization is suppressed through complexation, leading to fluorescence enhancement and offering a straightforward strategy for designing of fluorescent probes that act as chemosensors (Figure 10).

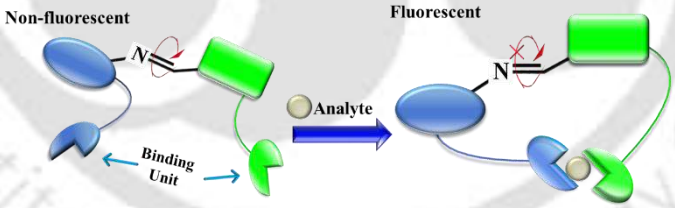

Figure 10. Schematic representation of C=N isomerization.

1.4 Recent Development of Chemosensors for Metal Ions and Amino Acids Detection

In this section, some selected reported sensing mechanism for metal ions, biothiols, and biomolecules in recent years are discussed. A chemosensor **1** bearing naphthalimide and picolinohydrazide moieties was reported for selective Al^{3+} ion detection through fluorescence turn-on response.[83] Free probe **1** showed a weak fluorescence emission peak. Upon complexation with Al^{3+}, the PET process was prohibited which resulting in a noticeable fluorescence enhancement.

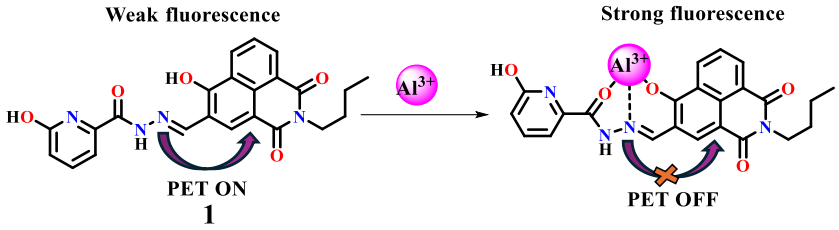

Scheme 1. Al^{3+} ion detection using PET based probe **1**.

For selective recognition of Cu^{2+} ion in aqueous medium, a oligothiophene scaffold based colorimetric and fluorescent probe **2** was designed and synthesized.[84] Upon addition of $CuCl_2$ solution, **3** showed a visible colour change from colorless to yellow and the fluorescence turn-off response was observed due to the paramagnetic quenching effect of Cu^{2+} ion. Moreover, the decrease of emission intensity of **2** towards Cu^{2+} was induced by ligand-to-metal charge transfer (LMCT) and intraligand charge transfer (ILCT) mechanism.

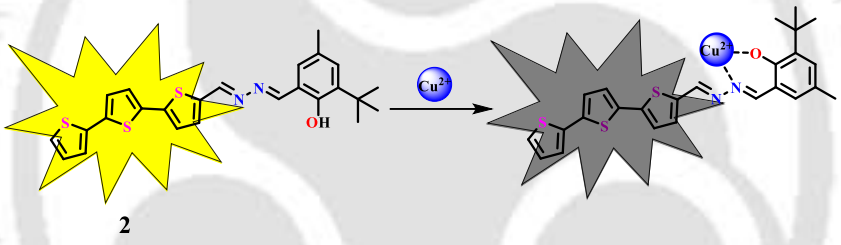

Scheme 2. Plausible binding mode of Cu^{2+} ion with probe **2**.

A coumarin-based multifunctional probe **3** was developed for colorimetric and fluorogenic sensing of biothiols, Cu^{2+} and Al^{3+} ions.[85] The presence of N, O chelating sites of **3** helped in the rapid complexation with Cu^{2+} and Al^{3+} ions. Such transfer of electrons from the nitrogen lone pair to the coumarin moiety was blocked due to the complexation. So, ICT pathway and the C=N isomerization were suppressed and fluorescence intensity got enhanced.

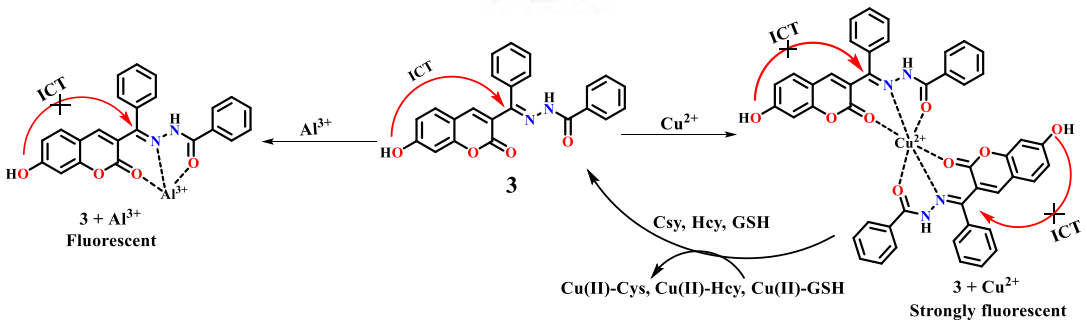

Scheme 3. Fluorescence sensing mechanism of biothiols and Cu^{2+}, Al^{3+} ions using probe **3**.

A dual colorimetric and fluorescent turn-on chemosensor **4** contains thiazole and thiosemicarbazide units used for the selective detection of toxic As^{3+} ion.[86] Probe **4** operates *via* CHEF mechanism upon interaction with As^{3+} ion.

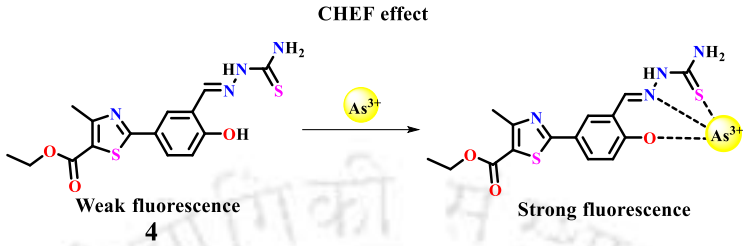

Scheme 4. Detection of As^{3+} ion through CHEF mechanism.

A chromone-based fluorescent probe **5** was introduced for the selective detection of Pd^{2+} ion.[87] Upon complexation with Pd^{2+} ion, **5** underwent deprotonation of hydroxyl proton, thus the ESIPT and ICT pathways were inhibited. The ratiometric enhancement of fluorescence intensity was also attributed to CHEF effect.

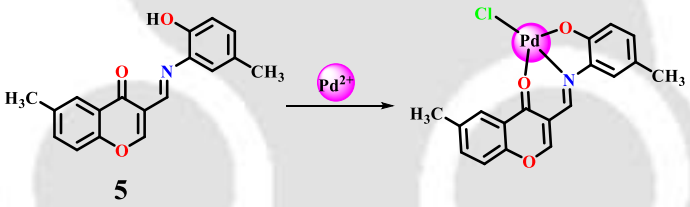

Scheme 5. Plausible recognition pathway of probe **5** with Pd^{2+} ion.

Based on AIE and ESIPT properties, a novel chromogenic and fluorescent turn-on probe **6** was used for the detection of cysteine (Cys) and homocysteine (Hcy).[88] Upon recognition of Cys/Hcy an isomerization of **6a** molecule was observed *via* ESIPT pathway, resulting in a large Stokes shift value.

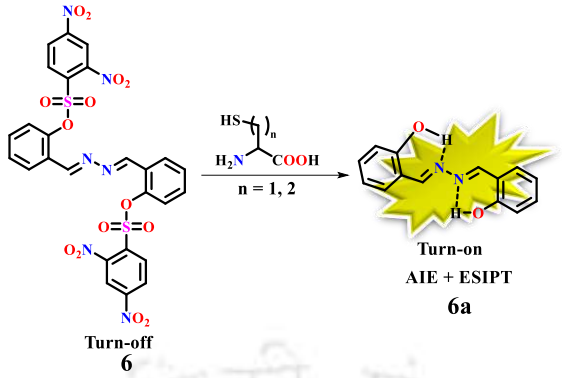

Scheme 6. Response mechanism of probe **6** towards cysteine and homocysteine.

A 2-hydroxynapthalene appended AIE active probe **7** was utilized as a highly effective chemosensor for selective recognition of Zn^{2+} ion.[89] The turn-on emissive behaviour observed upon complexation of Zn^{2+} with **7**, based on CHEF phenomenon. In DMSO-Water medium, introduction of Zn^{2+} also triggers the AIE property of **7**.

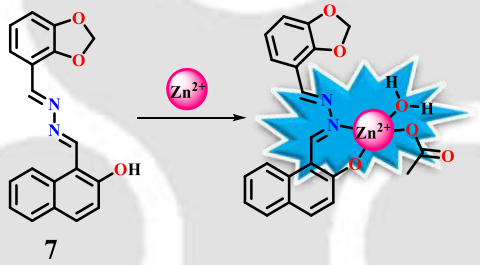

Scheme 7. Proposed sensing mode of probe **7** with Zn^{2+} ion.

For the distinct recognition of Cd^{2+} ion in presence of eleven transition metal ions, a highly fluorescent phenothiazine Schiff base probe **8** was synthesized.[90] Probe **8** showed a bright green fluorescence through aggregation-induced emission enhancement (AIEE) in THF-water medium. The active participation of -C=N group of **8** was responsible for the effective complexation process. Apart from the solution phase, sensor **8** also utilized on paper strips to generate a paper-based fluorescent sensor for on-spot Cd^{2+} detection.

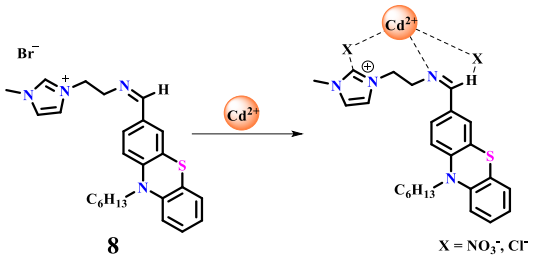

Scheme 8. Favourable binding mode of Cd^{2+} ion with **8**.

A Copper(II) quinoline based receptor **9** was synthesized for selective detection of methionine in purely aqueous medium through fluorescent on-off-on type pathways.[91] Probe **9a** initially exhibited strong fluorescence, but upon the addition of $CuCl_2$ solution, it resulted in quenching of fluorescence intensity.

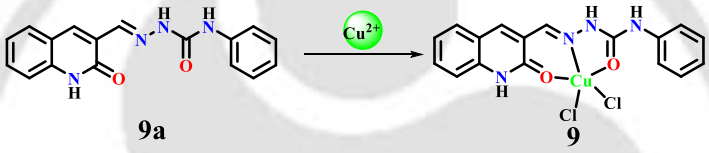

Scheme 9. Proposed mechanism of interaction between probe **9** with Cu^{2+} ion.

A coumarin appended napthol hydrazone chemosensor **10** was designed to detect two toxic metal ions with strong emission.[92] Fluorescence spectral analysis revealed probe **10** binds in 1:1 and 2:1 ratio with Hg^{2+} and Pb^{2+} ions, respectively with shorter response time, high sensitivity and very minimal interference in presence of other biological relevant metal ions. The turn-on reversible sensing mechanism was attributed due to ESIPT and C=N isomerization, upon addition of metal ions into the probe. Various practical applications like paper strip testing, natural water samples, and cell-imaging (in Hela cells and Zebrafish) were also performed for the specific recognition of detected metal ions.

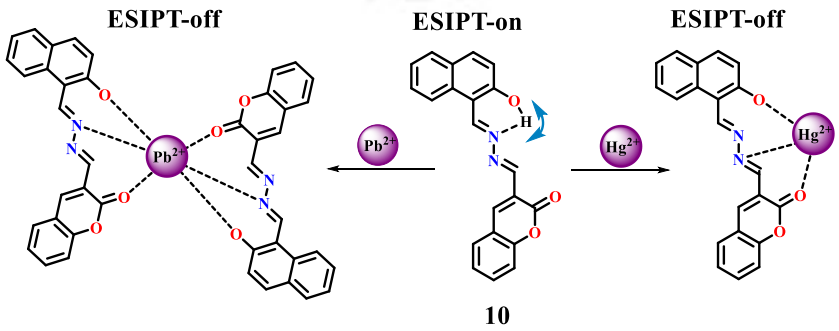

Scheme 10. Sensing of Hg^{2+} and Pb^{2+} ions through ESIPT mechanism.

Based on CHEF and FRET effects, a probe **11** containing a rhodamine unit as fluorophore and quinoline moiety was used for the selective detection of Bi^{3+} ion.[93] The chromogenic and fluorogenic sensor **11** showed a naked-eye colour change along with the increase of fluorescence intensity upon addition of Bi^{3+} ion. The distinct colour change allows easy discrimination of Bi^{3+} over other metal ions.

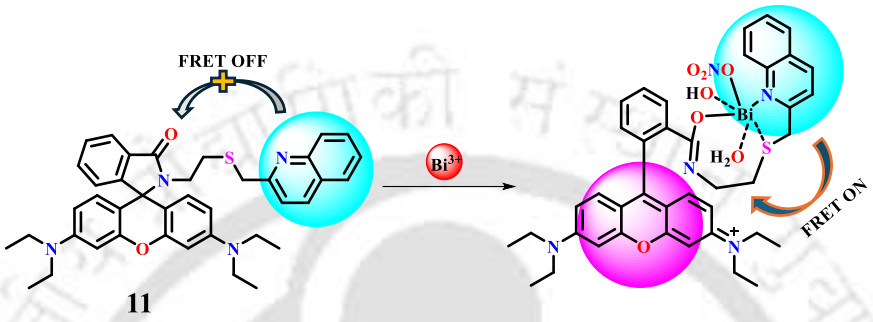

Scheme 11. FRET-based sensor **11** for the detection of Bi^{3+} ion.

Three rhodamine-naphthalimide conjugate fluorescent turn-on chemosensors were designed for Hg^{2+} ion sensing.[94–96] Probe **12a** functioned through a combination of CHEF, PET, and FRET mechanisms. Upon addition of Hg^{2+} ion, probe **12b** exhibited a typical FRET signal, indicating energy transfer from the naphthalimide moiety to the rhodamine group. This interaction also resulted in a distinct colour change from colorless to pink, facilitating naked-eye detection. In case of probe **12c**, the sensing mechanism was based on both FRET and PET pathways.

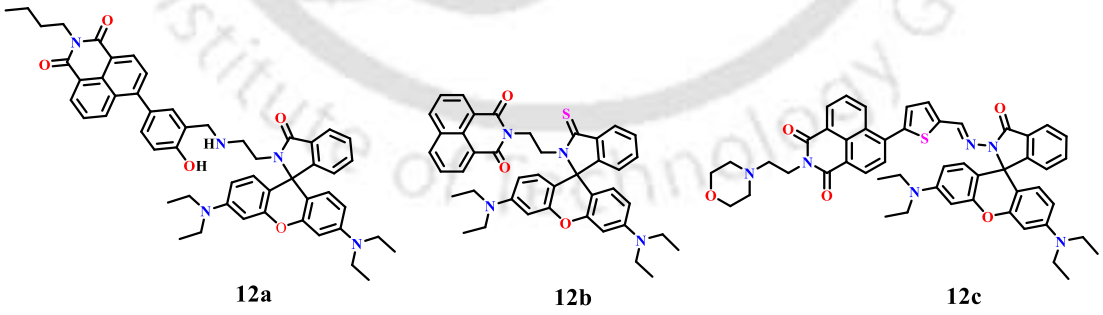

Scheme 12. Sensing of Hg^{2+} ion with three FRET-based chemosensors.

Diamino-benzophenone derivative-based probe **13** was employed for the selective recognition of Fe^{2+} ion.[97] The selectivity of sensor **13** was examined by colorimetric assay, indicating a distinct colour change from pale yellow to brown upon the gradual addition of Fe^{2+}. Also, **13**

exhibited a remarkable increase in fluorescence intensity towards Fe^{2+}, which was associated with the inhibition of PET and C=N isomerization mechanism.

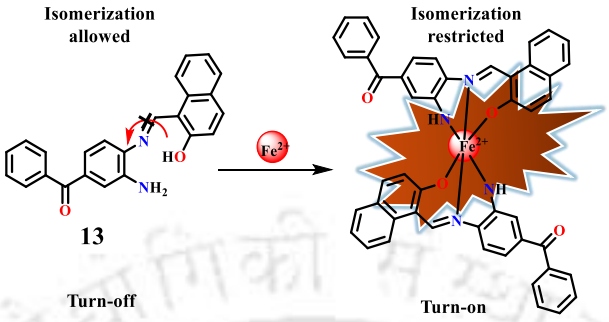

Scheme 13. Schematic representation of Fe^{2+} binding with probe **13** resulted an increment of fluorescence intensity by the restriction of C=N isomerization process.

Two xylofuranose-substituted probes **14a** and **14b** contain a triazole ring linked by pyrene fluorophore used for the detection of Au^{3+} ion.[98] The favourable coordination mode of each of the chemosensor was supported by DFT calculation. In presence of Au^{3+} both chemosensors exhibited fluorescence quenching, which might be explained due to spin-orbit interaction and energy transfer mechanism

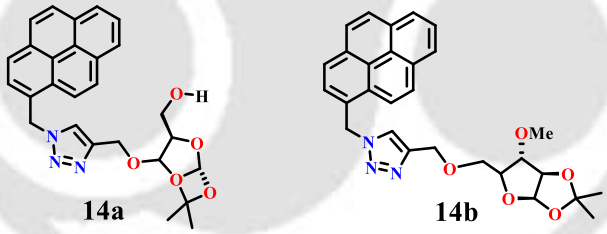

Scheme 14. Detection of Au^{3+} ion by probe **14a** and **14b**.

A non-emissive julolidine dihydrazone-based chemosensor **15** showed turn-on emission in presence of Zn^{2+} ion based on chelation enhanced emission effect.[99] The *in situ* formed Zn^{2+} complex utilised for the detection of pyrophosphate (PPi) over ATP and ADP through decomplexation mechanism. Since the binding affinity of PPi towards Zn^{2+} ion is higher than metal-ligand complex, demetallation leads to the formation of free probe and metal-PPi complex.

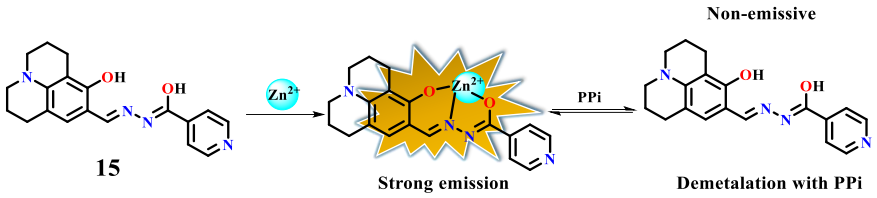

Scheme 15. Julolidine derivative as a chemosensor **15** for sensing of Zn^{2+} ion and PPi.

Probe **16** acts as a sensitive and selective chemosensor towards cysteine in presence of other biothiols like homocysteine and glutathione, which react through an intramolecular cyclization and conjugate addition reaction.[100] The reaction of **16** with cysteine resulted in a cleavage of the 7-position of acrylate moiety form **16a**, along with the formation of a lactum ring.

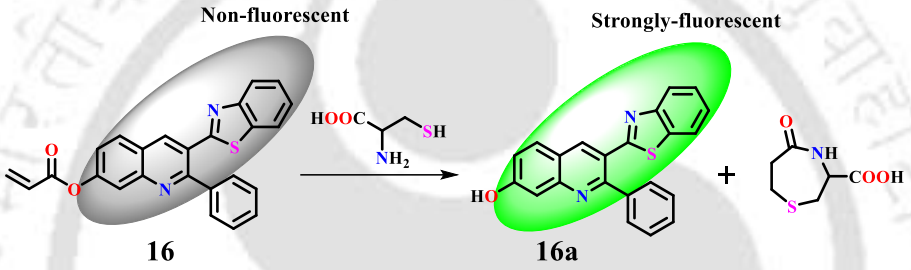

Scheme 16. Schematic showing the plausible interaction of **16** with cysteine.

A quinoline conjugate benzoxadiazole fluorophore **17** has been synthesized towards the detection of cysteine.[43] After the thiolysis of the 7-nitro-1,2,3-benzoxadiazole group, probe **17** forms a quinoline-substituted phenol ring, leading to an increase in fluorescence intensity. The sensing mechanism originated from the intramolecular charge transfer (ICT-OFF) and AIE pathway.

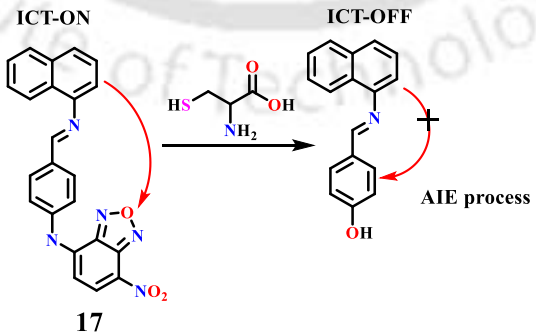

Scheme 17. Cysteine detection by probe **17** based on ICT and AIE pathway.

An amine-linked Schiff base morpholine-quinoline conjugate probe **18** used for the selective detection of Pb^{2+} ion.[101] The sensing pathway of **18** towards Pb^{2+} ion was exhibited *via* ICT

pathway through fluorescent enhancement. After the coordination of chemosensor with Pb^{2+}, rotation around the C-N single bond was restricted between quinoline and morpholine ring so that C=N isomerization was restricted.

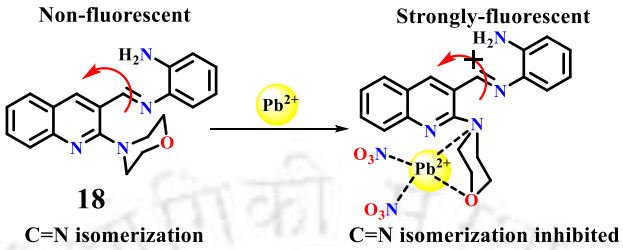

Scheme 18. Plausible binding model of **18** with $Pb(NO_3)_2$.

Based on FRET mechanism, two rhodamine-based probes **19a** and **19b** were synthesized which showed rapid selectivity towards ATP in presence of various biomolecules.[102] The thiourea group incorporated in the molecule helps to recognize tri-phosphate group by opening the spirocyclic ring of rhodamine moiety.

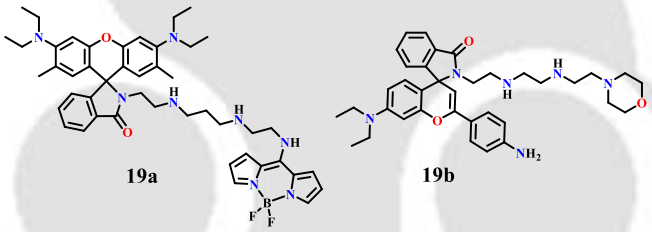

Scheme 19. FRET based chemosensors for the detection of ATP.

A newly synthesized tetra-phenyl carbazole porphyrin derivative **20** was treated as Cu^{2+} ion chelation-based fluorescent chemosensor for the detection of PO_4^{3-} ion.[103] The presence of symmetrical electron donating carbazole group increased the electron density of porphyrin ring, which helped in binding of the central metal with PO_4^{3-} ion and enhanced ICT pathway *via* a fluorescence turn-on mechanism.

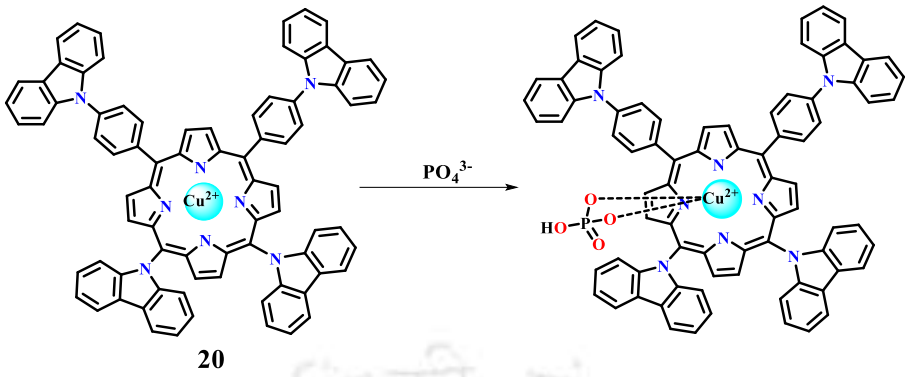

20

Scheme 20. Schematic representation for sensing of PO_4^{3-} ion.

A colorimetric and fluorometric probe **21** showed a selective detection of PO_4^{3-} ion.[104] The optical signaling behaviour of **21** after interaction of PO_4^{3-} enhanced the ICT pathway and leads to the disruption of ESIPT process due to the involvement of PO_4^{3-} ion induced deprotonation.

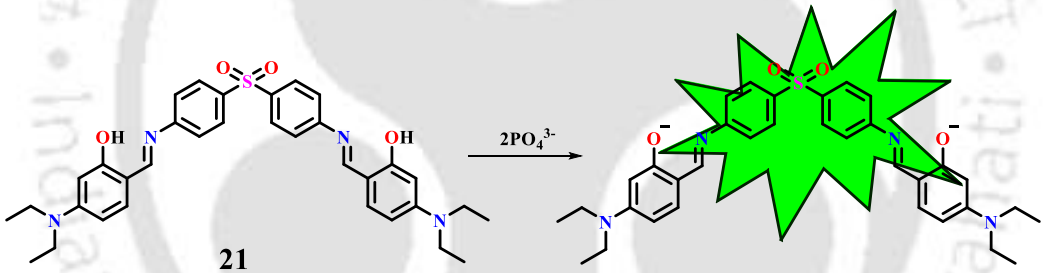

21

Scheme 21. The proposed turn-on sensing mechanism of **21** towards recognition of PO_4^{3-} ion.

A ninhydrin-based thiosemicarbazone effective chemosensor **22** distinguishes Zn^{2+} and Hg^{2+} ions from other metal ions.[105] Upon addition of the metal ions with probe **22,** a noticeable colour change of solution from yellow to reddish-orange was observed.

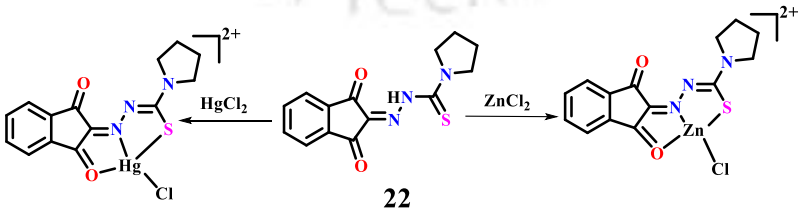

22

Scheme 22. Schematic illustration showing the coordination mode between probe **22** with Hg^{2+} and Zn^{2+} ions.

A 1H-benzo[d]imidazole moiety contains a substituted acrylate functional group, probe **23** used for specific and sensitive detection of cysteine with a fluorescence turn-on effect.[52] In presence of other bio-relevant analytes, only cysteine can eliminate the acrylate group of **23**. The thiol group of cysteine was added to the acrylate group on N-atom of benzimidazole ring followed by Michael addition reaction. The formation of a seven-member ring along with **23a** leads to the strong fluorescence enhancement. The acrylate group of **23** reduces π-electron density of benzimidazole moiety by triggering ICT pathway.

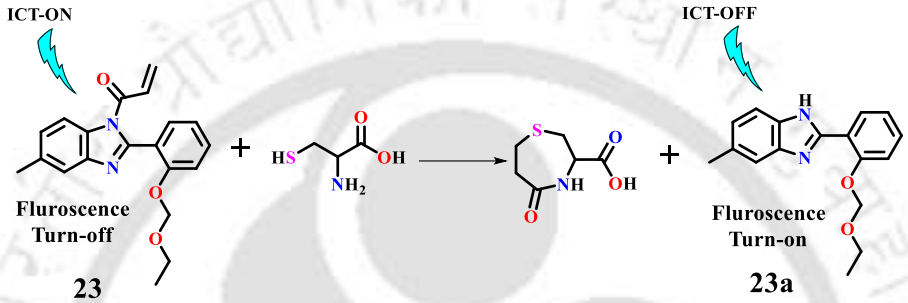

Scheme 23. The depicted scheme for detection of cysteine by **23**.

A quinazolinone-based probe **24** serves as a colorimetric chemosensor for specific detection of Cu^{2+} and Fe^{3+} ions in an aqueous medium.[106] The obtained results demonstrate the quenching of fluorescence, which is attributed the formation of stable complexation between the metal ions due to LMCT phenomenon.

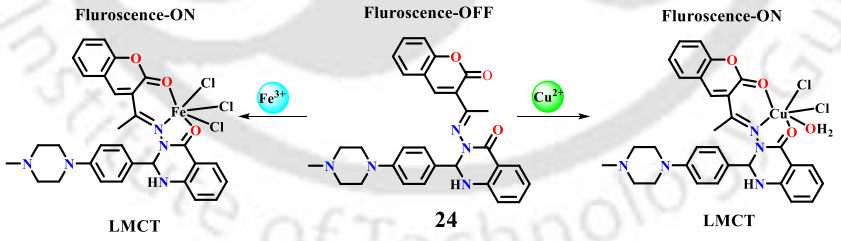

Scheme 24. Recognition of Fe^{3+} and Cu^{2+} *via* LMCT pathway.

A highly specific dipodal unsymmetrical fluorescent chemosensor **25** used for selective detection of Ag^{+} ion.[107] The probe **25** showed a 1:2 binding stoichiometry with Ag^{+} ion and the sensing mechanism involve a combination of PET and ICT mechanisms.

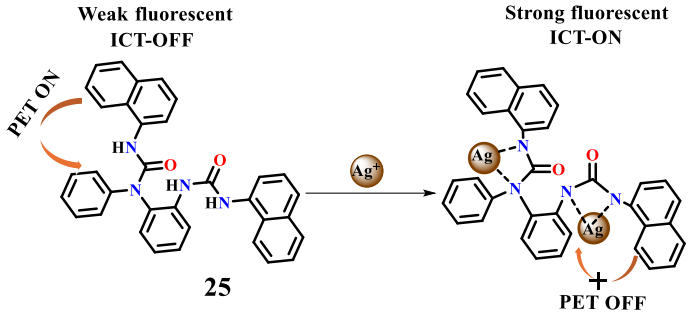

Scheme 25. The PET and ESIPT mechanism involved in **25** for the detection Ag^{+} ion.

A Salen type Schiff base chemosensor **26** possesses high selectivity and sensitivity towards Cr^{3+} ion in presence of different competitive metal ions by an enhancement of fluorescence emission intensity.[108] The possibility of restricted CHEF process of **26** on coordination of Cr^{3+} could contribute to the enhancement of fluorescence intensity along with PET mechanism.

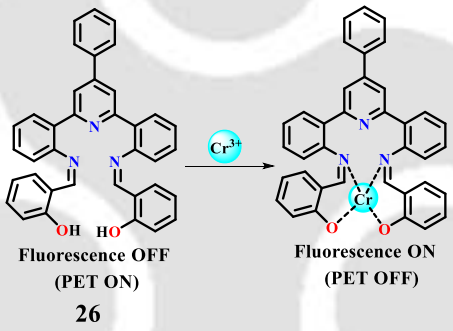

Scheme 26. Binding modes of chemosensor **26** to Cr^{3+} ion.

A chromene based fluorescent chemosensor **27** displayed high selectivity towards Cu^{2+} ion and glutathione (GSH).[109] Upon addition of Cu^{2+} with probe **27** showed a visual colour change along with obvious fluorescence quenching. The addition of GSH to **27**, produce compound **27a** and 7-(diethylamino)-2-oxo-2H-chromene-3-carbaldehyde.

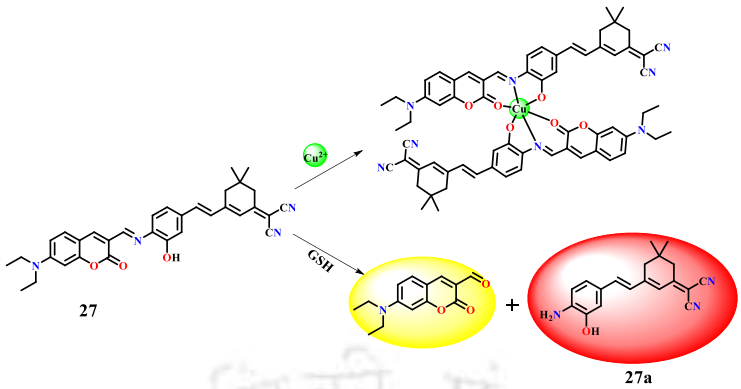

Scheme 27. Proposed binding of Cu^{2+} ion and GSH to probe **27**.

A 2,3-diphenyl-5,6,7,8-tetrahydroquinoxaline based potential optical chemosensor **28** was utilized for colorimetric and fluorescent detection of Ni^{2+} ion. The low fluorescence intensity of **28** can be ascribed to the PET and C=N isomerization mechanisim.[110] After, addition of Ni^{2+} ion to the probe resulted an enhancement of fluorescence intensity. In presence of Ni^{2+} ion, the PET process is blocked after coordination with nitrogen atoms of C=N group of the sensor. Additionally, the effective chelate complexation, resulting an efficient CHEF effect.

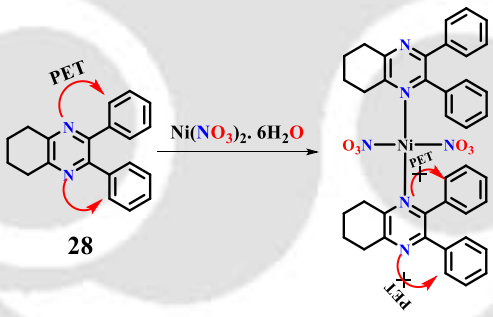

Scheme 28. PET mechanism involved in chemosensor **28** with Ni^{2+} ion.

An effective thiazole-coumarin-imidazole based chemosensor **29** was synthesized for the selective and sensitive detection of Cu^{2+} and Co^{2+} ions.[111] A visual colorimetric and turn-on sensing strategy were developed to identify the presence of both metal ions.

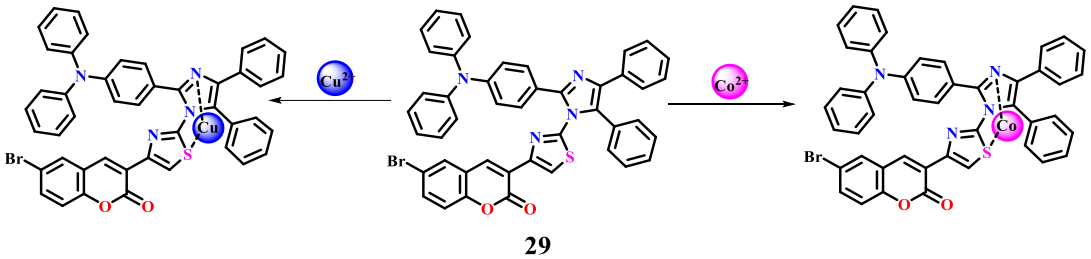

Scheme 29. Probable binding sites of **29** for complexation with Cu^{2+} and Co^{2+} ions.

A diaminomaleonitrile indole coupled chemosensor **30** has been designed for the selective detection of Zn^{2+} and Mn^{2+} ions.[112] Probe **30** selectively binds with the recognized metal ions *via* CHEF effect with an enhancement of fluorescence intensity.

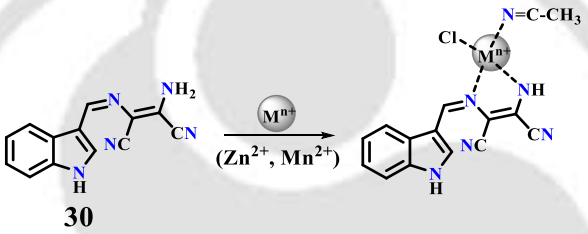

Scheme 30. Sensing response of chemosensor **30** towards Zn^{2+} and Mn^{2+} ions.

1.5 Objective of the Thesis

Inspired by the literature survey, an attempt has been made to design a ninhydrin-based O,O-donor chromogenic probe **LH** for selective detection of Cu^{2+} ion in Chapter 2. **LH** contains two oxygen atoms from carbonyl and phenolate groups of naphthoic-hydrazide moiety act as donor atoms for the formation of stable six-member $[Cu(\mathbf{L})Cl(H_2O)_2]$ complex **1**, which can be further utilized for the recognition of biothiols and phosphate ions. In other chapters, inspired by various examples of AIE-gens it was planned to synthesize three AIE-based probes in very simple steps, containing N,S-, N,N,N- and N,O- donor atoms. These probes can be used as effective chemosensors for metal ions sensing *via* colorimetric and fluorometric assay. The chemosensors can also be applied through real sample testing for environmental benefits. The output signals based on UV-Vis absorption and fluorescence emission spectra can also be utilized to construct molecular logic gate circuit.

1.6 Materials and Methods

1.6.1 Materials

All the chemical and spectroscopic grade solvents (MeOH, EtOH, DMSO, and MeCN) were purchased from Merck India. HEPES buffer, $CDCl_3$ and DMSO-d_6, naphthyl isothiocyanate, 1-pyrenecarboxaldehyde, 2-nitrobenzaldehyde, pyridine-2-carboxaldehyde, 4-(diethylamino)-2-hydroxybenzaldehyde, 2-hydroxynaphthaldehyde were purchased from Sigma Aldrich company and 1,2-phenylenediamine, 2-quinolinecarboxaldehyde, 2-aminobenzhydrazide from TCI Chemicals. All the chemicals and solvents were of reagent grade and were used without any further purification.

1.6.2 Instrumentation and Methods

HRMS spectra were recorded on an Agilent 6500 series Q-TOF mass spectrometer. FT-IR spectroscopic analysis was carried out by using Perkin Elmer Spectrum 2 IR spectroscopic instrument. Melting point of ligands were recorded by using the melting point apparatus of Stuart company. NMR spectra were recorded by Bruker Ascend 600 MHz NMR spectroscopic system and tetramethylsilane use [$Si(CH_3)_4$] used as residual solvent peak as reference. A Perkin-Elmer Lambda 365 UV-Visible spectrometer and an Agilent Cary 100 spectrometer were used to record the absorption spectra within the range of 200-600 nm in a quartz cuvette of path length 10 mm. The emission spectra were recorded with Horiba Fluoromax-4 spectrofluorometer with 10 mm pathlength quartz cuvette and having a slit width of 5 nm at room temperature with xenon lamp as excitation source. Field Emission Scanning Electron Microscopy (FESEM) images were obtained from Gemini 300 (Carl Zeiss) and Sigma 300 (10000KX) Microscopes. For the measurement of particle size DLS (Dynamic Light Scattering) experiments were performed with Malvern Zetasizer Nano ZS instrument which was equipped with 4.0 mW He–Ne laser having an operating wavelength of 633 nm. For monitoring fluorescence lifetime Pico Second Time Resolved Fluorimeter Lifespec II by Edinburgh Instruments used. The X-band electron paramagnetic resonance (EPR) spectrum was recorded on a JEOL JES-FA200 ESR spectrometer, with a microwave power of 0.998 mW and a microwave frequency of 9.14 GHz at 77 K. Inductively coupled plasma optical emission spectrometer (ICP-OES) measurements were recorded with Agilent 5800 ICP-OES spectrometer. X-ray diffraction spectral data were collected on Bruker D8Quest Single Crystal X-ray diffractometer (Diamond microfocus X-ray source). The structure was solved by using

smart software like SHELXS-20.[113] To further refine the data full-matrix least-square on F^2 with anisotropic displacement constraints by all non-hydrogen atoms were obtained. For the structural demonstration, ORTEP-3 window were used.[114] The packing diagram of the crystal lattice was obtained from Mercury 4.2.0 software.[115]

1.6.3 UV-Vis and Fluorescence Spectroscopic Studies

The spectroscopic experiments were performed in aqueous CTAB solution (3 mM), HEPES buffer, and solvent/HEPES buffer (5 mM, pH = 7.34, *v/v*) (solvent = EtOH, MeOH). All metal chloride, nitrate, sulphate salts, amino acids, and sodium salt of various anions were dissolved in deionised water to make 1 mM stock solution. However, $PdCl_2$ was first dissolved in modest volumes of DMSO before being diluted with deionized water. Stock solution of **LH** (1 mM) was prepared in DMSO and diluted to 1×10^{-5} M with CH_3OH/aqueous HEPES buffer for UV-Vis and fluorescence study. The probes **L_1**, **L2H**, and **L3H** solutions were prepared using similar methods. The UV-Visible and fluorescence titration experiments were carried out after mixing the probe solution with the metal solutions for one minute, all spectra were recorded at once. UV-Vis absorption spectra were recorded within a range of 200-600 nm. For the fluorescence studies, the excitation wavelength (λ_{ex}) of 380 nm (**L_1**), 354 nm (**L2H**), 372 nm (**L3H**) were used with a slit length of 2 nm.

1.6.4 Fluorescence Quantum Yield Calculation

1.6.4.1 Relative Method

The fluorescence quantum yield determination for **L_1** (15 μM) in different studied solvents and various EtOH/H_2O binary solvent mixtures (f_w = 0, 50, 70%) was performed using the following formula, and the reference solution used as standard Quinoline Sulphate solution in 0.1 M H_2SO_4 with a known value of $\Phi_{standard}$ = 0.546.

$$\phi_s = \phi_{std} \times \frac{G_s}{G_{std}} \times \frac{RI_{std}^2}{RI_s^2} \qquad (1)$$

where, ϕ_s and ϕ_{std} are the fluorescence quantum yield of the sample and reference, respectively. G_s and G_{std} are the areas of emission for the sample and reference, respectively, and RI is the refractive index of the corresponding solvents.

1.6.4.2 Absolute Method

The fluorescence quantum yield (φ) was measured by following the instructions mentioned in the operational manual of Edinburgh Instrument FLS1000 Fluorescence Spectrometer mentioned in the operational manual for **L2H** and **L3H**. The given equation to determine φ:

$$\varphi = \frac{E_C - E_A}{L_C - L_A} \times 100\% \qquad (2)$$

Here, E_c and L_C are the emission and light scattering of the samples, and E_A and L_C are the emission and light scattering of the used blank solvents.

1.6.5 Stern Volmer Equation

The quenching phenomenon between **L1** and Pd^{2+} can be described by a static quenching equation where a straight line is obtained by plotting I_0/I *vs* $[Pd^{2+}]$. So, the following equation can be written as

$$I/I_0 = Ksv\,[Pd^{2+}] + 1 \qquad (3)$$

I_0 and I were the fluorescence intensity of the **L1** in absence and presence of Pd^{2+}, and Ksv is the Stern-Volmer quenching constant.

1.6.6 Time-Resolved Photoluminescence Study

The fluorescence transients were measured by a time correlated single photon counting setup from Horiba. The laser diode 375 nm was used as a source with the excitation wavelengths of 380, 354, 372 nm. The fluorescence decay parameters were fitted using Origin software. The experimentally observed data were fitted using exponential decay function. For the average lifetime measurement (τ_{av}) bi-exponential decays (best-fitted curve) for every species were calculated by using the following equation:

$$\tau_{av} = \frac{\alpha_1\tau_1 + \alpha_2\tau_2}{\alpha_1 + \alpha_2} \qquad (4)$$

τ and α are the decay lifetimes and corresponding amplitude of the individual excited state-species, respectively. All the fluorescence decay lifetimes were fitted by using the exponential decay function. The radiative (*kr*) and non-radiative (*knr*) rate constants were calculated by using the following equation:

$$k_r = \frac{\varphi_f}{\tau_f} \qquad (5)$$

$$\frac{1}{\tau_f} = k_r + k_{nr} \qquad (6)$$

φ_f and τ_f are the fluorescence quantum yield and average lifetime.

1.6.7 Calculation of Limit of Detection (LOD) and Quantification (LOQ)

The LOD and LOQ values were calculated based on UV-Vis and fluorescence titrations profile.[116] The absorption and emission spectra of the probes were repeated 18/20 times, so that standard deviation (σ) of the blank samples were obtained. To obtain slope (k) of the fitted curve, fluorescence emission intensity of the probes was plotted against the concentration of the respective analyte solution. Both the detection limit and quantification limit were calculated by using the following equations:

$$LOD = \frac{3\sigma}{k} \qquad (7)$$

$$LOQ = \frac{10\sigma}{k} \qquad (8)$$

1.6.8 Determination of Binding Stoichiometry

Using Job's Plot and mass spectrometry, the binding stoichiometry of the probes (**LH**, **L1**, **L2H,** and **L3H**) with analytes were determined. The binding constants were calculated between the probes and the analytes from the Benesi-Hildebrand plot after plotting $1/I\text{-}I_0$ *vs* 1/[Analytes].[117]

$$\frac{1}{I-I_0} = \frac{1}{K_b(I_0-I_{min})}\frac{1}{[Analytes]} + \frac{1}{I_0-I_{min}} \qquad (9)$$

$$y = mx + c$$

I and I_0 are the emission intensities of the probes in presence and absence of analytes, I_{min} is the minimum intensity in presence of the guest analytes. The binding constant K_b was obtained by the ratio of intercept and slope of plot $1/(I\text{-}I_0)$ *vs* 1/[Analytes].

1.6.9 ^{1}H NMR Titration Experiment

LH, **L1** solution were prepared by dissolving 25 mg of 600 µL of DMSO-d_6, and metal chloride solution ($CuCl_2$, $PdCl_2$) were prepared in same solvent. The probes solution was titrated with the metal solutions under gradual addition of the same. For **L3H**, titration experiment was carried out in $CDCl_3$.

1.6.10 Aggregation Studies

For the aggregation study, FESEM imaging experiments were conducted separately with a solution of **L_1**, **L2H** and **L3H** (1 mM) and diluted to (1×10^{-5} M). The sample were prepared by drop casting (2 μL) **L_1** solution, water/EtOH mixture in respective solvents on glass plates covered with Al-foil, then coated with gold and dried under vacuum before imaging. For **L2H** (water/MeOH) and **L3H** (water/THF) solvent mixture were used. For DLS measurement, the probes solution (1 mM) was equilibrated for 60 minutes before taking the measurements. The samples along with the background were measured at room temperature (25 °C). The experiments were repeated for the sensing studies to determine the particle sizes of probes and detected analytes.

1.6.11 Computational Studies

The geometry optimisation was carried out using the density functional theory (DFT/TDDFT) method at B3LYP level for probes and the metal complexes of Cu^{2+}, Pd^{2+}, Al^{3+}, and As^{3+}. All the elements were assigned with LANL2DZ basic set. With the help of visualization program Gauss View, Gaussian09 program was used for all calculations.[118]

1.6.12 Molecular Docking Analysis

In silico docking simulations were done to investigate the molecular interactions of **LH**, **L3H** with the two albumins BSA and HSA with the Protein Data Bank (PDB) numbers of 4F5S and IE78, respectively.[119] The UCSF ChimeraX[120] software was employed in conjunction of Auto-Dock VINA[121] tools to show a significant binding ability for protein docking conformation. The 2D structure of the probes were created by using ChemDraw software. The structures of **LH** and **L3H** were optimized using Open Babel[122] with MMFF94 force field parameters for energy minimization. To perform the overall docking analysis, both the probe and biomolecule were converted in pdpqt format which was compatible with AutoDock software. Post-docking visualization and analysis of molecular interactions and binding orientations were performed using BIOVIA Discovery Studio 2021[123] software.

1.6.13 Appendices

An appendix containing relevant supporting information has been included after the references section of each chapter.

References:

1 P. R. Dongare and A. H. Gore, *ChemistrySelect*, 2021, **6**, 5657-5669.

2 A. Patil and S. Salunke-Gawali, *Inorg. Chim. Acta.*, 2018, **482**, 99-112.

3 Q. Li and Y. Zhou, *RSC Adv.*, 2023, **13**, 19429-19446.

4 A. Gupta and N. Kumar, *RSC Adv.*, 2016, **6**, 106413-106434.

5 F. Wang, X. Zhang, C. Huangfu, M. Zhu, C. Li and L. Feng, *Food Chem.*, 2022, **370**, 131033.

6 S. Kraithong, W. Panchan, A. Charoenpanich, J. Sirirak, S. Sahasithiwat, P. Swanglap, V. Promarak, P. Thamyongkit and N. Wanichacheva, *J. Photochem. Photobiol. A Chem.*, 2020, **389**, 112224.

7 J. Anastassopoulou and T. Theophanides, *Bioinorg. Chem.*, 1995, 209-218.

8 M. Stillman, *Angew. Chemie Int. Ed.*, 2007, **46**, 8741-8742.

9 P. Aisen, *Proteins*, **1**, 200-206.

10 T. A. Rouault, *Nat. Chem. Biol.*, 2006, **2**, 406-414.

11 J. Albretsen, *Vet. Med.*, 2006, **101**, 82-90.

12 B. L. Vallee and D. S. Auld, *Acc. Chem. Res.*, 1993, **26**, 543-551.

13 N. A. Webb and C. M. Wood, *Aquat. Toxicol.*, 2000, **49**, 111129.

14 S. Hite, C. D. La Barra, L. Tran, D. Riggan, S. Neynaber, C. Eng and R. W. Gen, *Clin. Chem.*, 2001, **47**, 763-766.

15 T. W. Purcell and J. J. Peters, *Environ. Toxicol. Chem.*, 1998, **17**, 539-546.

16 N. Tsipouras, C. J. Rix and P. H. Brady, *Clin. Chem.*, 1997, **43**, 290-301.

17 B. Das, M. Dolai, A. Dhara, A. Ghosh, S. Mabhai, A. Misra, S. Dey and A. Jana, *J. Phys. Chem. A*, 2021, **125**, 1490-1504.

18 G. Balamurugan, S. Velmathi, N. Thirumalaivasan and S. P. Wu, *Analyst*, 2017, **142**, 4721-4726.

19 V. Bhardwaj, K. Bhardwaj and S. K. Sahoo, *J. Fluoresc.*, 2023, **33**, 1157-1164.

20 L. N. Neupane, P. K. Mehta, S. Oh, S. H. Park and K. H. Lee, *Analyst*, 2018, **143**, 5285-5294.

21 A. Saravanan, S. Shyamsivappan, T. Suresh, G. Subashini, K. Kadirvelu, N. Bhuvanesh, R. Nandhakumar and P. S. Mohan, *Talanta*, 2019, **198**, 249-256.

22 A. Ullah, F. Shah, I. Khan, M. Anwar, K. Shah, M. T. Muhammad and F. Ahmad, *Spectrochim. Acta - Part A Mol. Biomol. Spectrosc.*, 2018, **192**, 188-193.

23 E. Zhang, P. Ju, Q. Li, X. Hou, H. Yang, X. Yang, Y. Zou and Y. Zhang, *Sensors Actuators, B Chem.*, 2018, **260**, 204-212.

24 N. Basu, M. Kwan and H. Man Chan, *J. Toxicol. Environ. Heal. - Part A Curr. Issues*, 2006, **69**, 1133-1143.

25 H. H. Harris, I. J. Pickering and G. N. George, *Science.*, 2003, **301**, 1203.

26 P. B. Tchounwou, W. K. Ayensu, N. Ninashvili and D. Sutton, *Environ. Toxicol.*, 2003, **18**, 149-175.

27 X. Z. Chen, X. D. Ma, H. M. Wang, M. Wang, Y. Y. Zhang, G. Gao, J. J. Liu and S. C. Hou, *New J. Chem.*, 2017, **41**, 8026-8030.

28 M. Wang, X. Liu, H. Lu, H. Wang and Z. Qin, *ACS Appl. Mater. Interfaces*, 2015, **7**, 1284-1289.

29 S. Erdemir, S. Malkondu and M. Oguz, *Talanta*, 2023, **252**, 123847.

30 A. Mukherjee and M. Chakravarty, *New J. Chem.*, 2020, **44**, 6173-6181.

31 C. F. S. Iii, *J. Inorg. Biochem.,*1999, **65**, 2589-2600.

32 I. Ott, *Coord. Chem. Rev.*, 2009, **253**, 1670-1681.

33 C. M. Goodman, C. D. McCusker, T. Yilmaz and V. M. Rotello, *Bioconjug. Chem.*, 2004, **15**, 897-900.

34 P. G. Sutariya, H. Soni, S. A. Gandhi and A. Pandya, *New J. Chem.*, 2019, **43**, 737-747.

35 S. Nag, A. Mondal, H. Hirani and P. Banerjee, *Mater. Adv.*, 2022, **3**, 4649-4658.

36 K. Nagaraj, A. Nityananda Shetty and D. R. Trivedi, *Microchem. J.*, 2024, **206**, 32-39.

37 D. Maity, S. Kumar Mandal, B. Guha and P. Roy, *Inorganica Chim. Acta*, 2021, **519**, 120258.

38 S. Negi, P. Takkar, P. Gahlyan and R. Kumar, *Anal. Methods*, 2024, **17**, 377-387.

39 C. K. Sen and L. Packer, *Am. J. Clin. Nutr.*, 2000, **72**, 653s.

40 D. Yu, Q. Zhang, S. Ding and G. Feng, *RSC Adv.*, 2014, **4**, 46561-46567.

41 L. Niu, Y. Luo, Y. Gan, Q. Cao, C. Zhu, M. Wang, J. Wang, W. Zhang and J. Wang, *Talanta*, 2020, **219**, 121291.

42 S. Gong, A. Qin, Y. Zhang, M. Li, X. Chen, Y. Liang, X. Xu, Z. Wang and S. Wang, *Food Chem.*, 2023, **400**, 134108.

43 S. Muthusamy, L. Zhao, K. Rajalakshmi, D. Zhu, R. Soy, J. Mack, T. Nyokong, S. Wang, K. B. Lee and W. Zhu, *Dye. Pigment.*, 2021, **193**, 109556.

44 J. Lin, I. M. Lee, Y. Song, N. R. Cook, J. Selhub, J. A. E. Manson, J. E. Buring and S. M. Zhang, *Cancer Res.*, 2010, **70**, 2397-2405.

45 E. Weerapana, C. Wang, G. M. Simon, F. Richter, S. Khare, M. B. D. Dillon, D. A. Bachovchin, K. Mowen, D. Baker and B. F. Cravatt, *Nature*, 2010, **468**, 790-797.

46 S. Ding, M. Liu and Y. Hong, *Sci. China Chem.*, 2018, **61**, 882-891.

47 X. Lou, Y. Hong, S. Chen, C. W. T. Leung, N. Zhao, B. Situ, J. W. Y. Lam and B. Z. Tang, *Sci. Rep.*, 2014, **4**, 1-6.

48 Y. Liu, S. Zhu, K. Gu, Z. Guo, X. Huang, M. Wang, H. M. Amin, W. Zhu and P. Shi, *ACS Appl. Mater. Interfaces*, 2017, **9**, 29496-29504.

49 X. Dai, Z. Y. Wang, Z. F. Du, J. Cui, J. Y. Miao and B. X. Zhao, *Anal. Chim. Acta*, 2015, **900**, 103-110.

50 A. Pastore, G. Federici, E. Bertini and F. Piemonte, *Clin. Chim. Acta*, 2003, **333**, 19-39.

51 K. Tayade, M. Sonawane, P. Torawane, A. Singh, N. Singh and A. Kuwar, *Sensors Actuators, B Chem.*, 2017, **246**, 563-569.

52 G. S. Yeom, I. ho Song, S. J. Park, A. Kuwar and S. B. Nimse, *J. Photochem. Photobiol. A Chem.*, 2022, **431**, 114074.

53 P. Kumar, S. Pachisia and R. Gupta, *Inorg. Chem. Front.*, 2021, **8**, 3587-3607.

54 Q. Wang, H. Sheng, L. Jin, Z. Zhang, W. Wang and X. Tang, *Spectrochim. Acta - Part A Mol. Biomol. Spectrosc.*, 2019, **207**, 96-104.

55 Y. W. Wang, S. B. Liu, Y. L. Yang, P. Z. Wang, A. J. Zhang and Y. Peng, *ACS Appl. Mater. Interfaces*, 2015, **7**, 4415-4422.

56 Q. Meng, Y. Wang, M. Yang, R. Zhang, R. Wang and Z. Zhang, *RSC Adv.*, 2015, **5**, 53189-53197.

57 S. Suresh, G. Prabakaran, J. Prabhu, P. S. Vijayanand, R. S. Kumar, R. Karthick, G. Velraj and R. Nandhakumar, *J. Food Compos. Anal.*, 2024, **132**, 106364.

58 A. Chowdhary, A. Dhawale and D. R. Trivedi, *Microchem. J.*, 2024, **204**, 111088.

59 A. Dhawale and D. R. Trivedi, *ChemPhysChem*, 2024, **25**, e202400803.

60 C. Warwick, A. Guerreiro, A. Soares, *Biosens. Bioelectron.,* 2024, **1306**, 137846.

61 Q. Zhao, F. Li and C. Huang, *Chem. Soc. Rev.*, 2010, **39**, 3007-3030.

62 R. M. Duke, E. B. Veale, F. M. Pfeffer, P. E. Kruger and T. Gunnlaugsson, *Chem. Soc. Rev.*, 2010, **39**, 3936-3953.

63 S. P. Wu, K. J. Du and Y. M. Sung, *Dalt. Trans.*, 2010, **39**, 4363-4368.

64 X. Zhang, J. Yin and J. Yoon, *Chem. Rev.*, 2014, **114**, 4918-4959.

65 Y. Wu, J. Feng, G. Hu, E. Zhang and H. H. Yu, *Sensors*, 2023, **23**, 2749.

66 B. Kaur, N. Kaur and S. Kumar, *Coord. Chem. Rev.*, 2018, **358**, 13-69.

67 A. P. De Silva, D. B. Fox, A. J. M. Huxley and T. S. Moody, *Coord. Chem. Rev.*, 2000, **205**, 41-57.

68 D. Galaris, V. Skiada and A. Barbouti, *Cancer Lett.*, 2008, **266**, 21-29.

69 K. P. Carter, A. M. Young and A. E. Palmer, *Chem. Rev.*, 2014, **114**, 4564-4601.

70 H. W. Ai, *Sensors*, 2014, **14**, 17829-17831.

71 A. P. De Silva, H. Q. N. Gunaratne, T. Gunnlaugsson, A. J. M. Huxley, C. P. McCoy, J. T. Rademacher and T. E. Rice, *Chem. Rev.*, 1997, **97**, 1515-1566.

72 T. Meyer and M. N. Teruel, *Trends Cell Biol.*, 2003, **13**, 101-106.

73 S. Saha, S. Paul, R. Debnath, N. Dey and B. Biswas, *Anal. Methods*, 2024, **9**, 1058-1068.

74 M. M. Henary and C. J. Fahrni, *J. Phys. Chem. A*, 2002, **106**, 5210-5220.

75 M. K. Goshisht, G. K. Patra and N. Tripathi, *Mater. Adv.*, 2022, **3**, 2612-2669.

76 S. Paul, K. Debsharma, S. Dey, S. Halder, K. Jana and C. Sinha, *Mater. Adv.*, 2023, **4**, 3874-3891.

77 L. Mao, Y. Liu, S. Yang, Y. Li, X. Zhang and Y. Wei, *Dye. Pigment.*, 2019, **162**, 611-623.

78 S. Dey and P. K. Sukul, *ACS Omega*, 2019, **4**, 16191-16200.

79 Y. Wu, X. Wen and Z. Fan, *Spectrochim. Acta Part A Mol. Biomol. Spectrosc.*, 2019, **223**, 117315.

80 P. Taya, B. Maiti, V. Kumar, P. De and S. Satapathi, *Sensors Actuators, B Chem.*, 2018, **255**, 2628-2634.

81 C. Fang, Y. Huang and Y. Zhao, *Am. J. Transl. Res.*, 2023, **15**, 694-709.

82 Z. Li, *J. Fluoresc.*, 1997, **7**, 237-242.

83 S. Zhang, Y. Wang and H. Xu, *Spectrochim. Acta - Part A Mol. Biomol. Spectrosc.*, 2022, **275**, 121193.

84 Z. Guo, T. Hu, X. Wang, T. Sun, T. Li and Q. Niu, *J. Photochem. Photobiol. A Chem.*, 2019, **371**, 50-58.

85 H. Li, X. Sun, T. Zheng, Z. Xu, Y. Song and X. Gu, *Sensors Actuators, B Chem.*, 2019, **279**, 400-409.

86 K. Dhanasekaran, R. Tamizhselvi, S. Mohandoss, M. Beena, A. Palaniappan and A. A. Napoleon, *Spectrochim. Acta - Part A Mol. Biomol. Spectrosc.*, 2024, **316**, 124325.

87 R. Naskar, S. Gharami, S. Mandal and T. K. Mondal, *New J. Chem.*, 2022, **46**, 17912-17917.

88 H. Song, Y. Zhou, H. Qu, C. Xu, X. Wang, X. Liu, Q. Zhang and X. Peng, *Ind. Eng. Chem. Res.*, 2018, **57**, 15216-15223.

89 B. Naskar, A. Dhara, D. K. Maiti, M. Kukułka, M. P. Mitoraj, M. S. Hooper, C. Prodhan, K. Chaudhuri and S. Goswami, *ChemPhysChem*, 2019, **20**, 1630-1639.

90 Y. B. Barot, V. Anand, S. Vyas and R. Mishra, *J. Mol. Liq.*, 2023, **376**, 121490.

91 C. Elamathi, R. J. Butcher, A. Mohankumar, P. Sundararaj, K. P. Elango, P. Kalaivani and R. Prabhakaran, *Dalt. Trans.*, 2021, **50**, 8820-8830.

92 B. Musikavanhu, T. Pan, Q. Ma, Y. Liang, Z. Xue, L. Feng and L. Zhao, *Spectrochim. Acta - Part A Mol. Biomol. Spectrosc.*, 2024, **313**, 124101.

93 S. Adhikari, S. Mandal, A. Ghosh, S. Guria, A. Pal, A. Adhikary and D. Das, *J. Photochem. Photobiol. A Chem.*, 2018, **360**, 26-33.

94 T. Mishra, S. Guria, J. Sadhukhan, D. Das, M. K. Das, S. S. Adhikari, S. Maity and P. Maiti, *J. Photochem. Photobiol. A Chem.*, 2024, **446**, 115168.

95 N. Z. Xu, M. M. Liu, M. A. Ye, Y. W. Yao, Y. Zhou, G. Z. Wu and C. Yao, *J. Lumin.*, 2017, **188**, 135-140.

96 X. Yuan, T. H. Leng, Z. Q. Guo, C. Y. Wang, J. Z. Li, W. W. Yang and W. H. Zhu, *Dye. Pigment.*, 2019, **161**, 403-410.

97 R. Kouser, S. Zehra, R. A. Khan, A. Alsalme, F. Arjmand and S. Tabassum, *Spectrochim. Acta - Part A Mol. Biomol. Spectrosc.*, 2021, **247**, 119156.

98 A. K. Atta, S. I. Hazarika, M. Loya and S. Giri, *J. Photochem. Photobiol. A Chem.*, 2022, **425**, 113723.

99 Megha, V. Kumar, P. Kaur and K. Singh, *Anal. Chim. Acta*, 2023, **1240**, 340758.

100 S. Manna, P. Karmakar, S. S. Ali, U. N. Guria, S. K. Samanta, R. Sarkar, P. Datta and A. K. Mahapatra, *Anal. Methods*, 2019, **11**, 1192-1198.

101 K. Velmurugan, R. Vickram, C. V. Jipsa, R. Karthick, G. Prabakaran, S. Suresh, J.

Prabhu, G. Velraj, L. Tang and R. Nandhakumar, *Food Chem.*, 2021, **348**, 129098.

102 K. M. K. Swamy, S. Eom, Y. Liu, G. Kim, D. Lee and J. Yoon, *Sensors Actuators, B Chem.*, 2019, **281**, 350-358.

103 S. Oncuoglu, T. Mumcu, C. G. Hizliates and K. Ertekin, *Spectrochim. Acta - Part A Mol. Biomol. Spectrosc.*, 2025, **339**, 126236.

104 A. D. Jaiswal, J. Chourasia, S. Ahamed, N. Tohora, M. Mahato, C. Debnath, S. Ghanta and S. K. Das, *J. Mol. Struct.*, 2025, **1319**, 139522.

105 P. Rasin, P. Prabhakaran, S. M. Basheer, V. Manakkadan, V. N. Vadakkedathu Palakkeezhill am and A. Sreekanth, *Anal. Chem.*, 2023, **95**, 6448-6457.

106 A. Raturi, M. M. Singh, Y. S. Meena, A. Rana, M. Yadav, R. Kumar, T. S. Khan, D. Tripathi, R. Kumar and G. Naik, *J. Mol. Struct.*, 2024, **1317**, 139140.

107 C. I. David, H. Jayaraj, G. Prabakaran, K. Velmurugan, D. P. Devi, R. Kayalvizhi, A. Abiram, V. R. Kannan and R. Nandhakumar, *Food Chem.*, 2022, **371**, 131130.

108 G. B. Chalmardi, M. Tajbakhsh, A. Bekhradnia and R. Hosseinzadeh, *Inorganica Chim. Acta*, 2017, **462**, 241-248.

109 K. Zhang, B. Zhao, Y. Song, H. Li, D. Du, H. Sun and W. Liu, *J. Photochem. Photobiol. A Chem.*, 2024, **453**, 115683.

110 S. Dutta, D. Kumar, A. Pandey, S. Manna, S. M. Choudhury, D. Sahu, V. Sharma, N. Kumari and G. K. Patra, *New J. Chem.*, 2025, 11906-11919.

111 A. R. Nesaragi, J. Nagalik, S. Chapi, M. Harshitha, K. D. Venuprasad, N. K. Kalagatur, C. H. Ravikumar, S. R. Inamdar, H. P. Shivarudrappa and N. Al-Zaqri, *New J. Chem.*, 2025, 12639-12650.

112 M. S. Kumar, A. K. Das, Y. Bylappa and A. Nag, *RSC Adv.*, 2025, **15**, 6708-6717.

113 G. M. Sheldrick, *Acta Crystallogr. Sect. A Found. Crystallogr.*, 2008, **64**, 112-122.

114 C. L. Barnes, *J. Appl. Crystallogr.*, 1997, **30**, 568.

115 C. F. Macrae, I. Sovago, S. J. Cottrell, P. T. A. Galek, P. McCabe, E. Pidcock, M. Platings, G. P. Shields, J. S. Stevens, M. Towler and P. A. Wood, *J. Appl. Crystallogr.*,

2020, **53**, 226-235.

116 L. A. Currie, *Anal. Chim. Acta*, 1999, **391**, 127-134.

117 I. D. Kuntz, F. P. Gasparro, M. D. Johnston and R. P. Taylor, *J. Am. Chem. Soc.*, 1968, **90**, 4778-4781.

118 M. Caricato, M. J. Frisch, J. Hiscocks and M. J. Frisch, *Gaussian 09: IOps Reference*, Gaussian Wallingford, CT, USA, 2009.

119 P. Mulimani, M. P. Bhat, P. Patil, S. Aralekallu, R. Kapavarapu, J. Yu, M. Kurkuri and R. G. Kalkhambkar, *J. Water Process Eng.*, 2024, **59**, 105030.

120 E. F. Pettersen, T. D. Goddard, C. C. Huang, E. C. Meng, G. S. Couch, T. I. Croll, J. H. Morris and T. E. Ferrin, *Protein Sci.*, 2021, **30**, 70-82.

121 M. S. V. Tresanco, M. E. V. Tresanco, P. A. Valiente and E. Moreno, *Biol. Direct*, 2020, **15**, 1012.

122 T. Dovramadjiev, *Science. Business. Society*, 2018, **7**, 6-7.

123 U. Baroroh, M. Biotek, Z. S. Muscifa, W. Destiarani, F. G. Rohmatullah and M. Yusuf, *Indones. J. Comput. Biol.*, 2023, **2**, 22-30.

Chapter 2

A Naphthyl Appended Ninhydrin Based Colorimetric Chemosensor for Cu^{2+} ion: Detection of Cysteine and ATP *

Abstract:

A ninhydrin-based colorimetric chemosensor (**LH**) was synthesized using 3-hydroxy-2-naphthoic hydrazide and 11*H*-indeno[1,2-*b*]quinoxalin-11-one. It was characterized by spectroscopic and single crystal X-ray diffraction techniques. In a semi-aqueous (MeOH/HEPES) system, **LH** displayed a characteristic chromogenic change from colorless to yellow upon adding Cu^{2+} ion, with the appearance of a new peak at λ_{max} = 460 nm. A 1:1 binding stoichiometry between **LH** and Cu^{2+} ion had been found, with LOD = 2.3 μM (145 ppb) and LOQ = 8 μM (504 ppb). Based on experimental results, the formula of $[Cu(\mathbf{L})Cl(H_2O)_2]$ (**1**) was assigned and this *in situ* generated **1** was found to exhibit a discoloration of upon gradual addition of cysteine (LOD = 60 nM) as well as ATP (LOD = 130 nM) having 1:2 and 1:1 stoichiometry respectively. The **LH** was useful for recognition of Cu^{2+} ion in real water samples and on filter paper strips. A two-input-two-output logic gate circuitry was also constructed by employing **1** and cysteine. The DFT/TDDFT calculations performed on **LH** and **1** were consistent with experimental findings. The binding affinity of **LH** towards HSA and BSA were determined with HSA having greater affinity than BSA, which was also supported by theoretical calculations.

* This work has been published in:

A. Mondal, V. Manivannan, *Spectrochim. Acta A Mol. Biomol. Spectrosc*., 2024, **322**, 124734.

2.1 Introduction:

Synthesis of colorimetric chemosensors for the selective recognition of target analytes like metal ions, and biomolecules have attained immense interest.[1–4] These chemosensors have found enormous applications in environmental, analytical, and biomedical sciences.[5,6] Among the various metal ions, copper plays a crucial role in functioning of many biological systems and acts as a cofactor in enzymes like cytochrome c oxidase, ceruloplasmin, superoxide dismutase, dopamine β monooxygenase, and so on.[7–9] But this metal ion can be hazardous if it is consumed excessively and can create neurodegenerative disorder such as Alzheimer's, Wilson's and Parkinson's disease as well as Menkes syndrome.[10–12] Problems like liver cirrhosis and kidney damage can also occur due to the long-term accumulation of copper in excess.[13,14] The World Health Organization (WHO) has declared 2 ppm as the allowable limit of copper in drinking water. So, the development of highly selective and sensitive chromogenic probe for recognition of Cu^{2+} ion with short response time and low detection limit is significantly important.[15]

Thiol-containing amino acid *viz*., cysteine is considered a semi-essential amino acid, which plays a crucial role in a variety of processes like irreversible detoxification in order to maintain healthy conditions within the cell. It is also utilized as an additive in food preservation and used in pharmaceutical industry.[16] It was well known that an optimal level of any analyte is crucial for efficient function in human body and disruption of normal balance of cysteine (500 mg per day) can create several health issues *viz*., cardiovascular disorder, neurotoxicity effects, depigmentation on human hair, delayed growth of children, loss of fat muscle, and so on.[17,18] Investigations were directed towards organic receptors for rapid detection and quantification of cysteine.[19,20] However, limited number of colorimetric sensors with the ability to detect cysteine selectively, in the presence of glutathione, homocysteine and other amino acids were reported. So, sensors for rapid detection of cysteine in all biologically relevant substances continue to be on search.

Adenosine 5' -triphosphate (ATP), one of the most prevalent anions among all nucleotides, plays a vital role in vast range of biological processes [21–23] and store chemical energy in living cells.[24,25] ATP deficiency in the human body has been known to cause kidney damage, hypoglycemia, and cardiovascular disorders.[26] ATP helps to perform numerous cellular activities which include cell signaling, respiration, DNA transcription, and replication.[27] The

motivation to synthesize a chemosensor that can selectively and sensitively detect ATP still continues.

The Bovine Serum Albumin (BSA) has outstanding similarity to Human Serum Albumin (HSA)[28] that has been regularly used in the colorimetric sensor-based system.[29,30] Studies on the binding interactions of BSA and HSA with several organic ligands[31,32] has been utilized to understand the interaction of drug molecules with amino acid residues and to design pharmacokinetic drug profiles.[33,34]

This Chapter describes the synthesis of a ninhydrin-based naphthyl appended probe **LH** having the potential for sensitive and selective chromogenic/visual recognition of Cu^{2+} ion. In addition, the utility of *in situ* generated Cu(II) complex of **LH** as a chromogenic sensor for detecting cysteine and ATP along with *in silico* docking studies on binding of **LH** with BSA and HSA have been described.

2.2 Experimental Section:

Synthesis

3-hydroxy-N'-(11H-indeno[1,2-b]quinoxalin-11-ylidene)-2-naphthohydrazide (**LH**)

The chemoreceptor **LH** was synthesized by reacting 11*H*-indeno[1,2-*b*]quinoxalin-11-one (**1a**, which was prepared by the literature procedure)[35] and 3-hydroxy-2-naphthoic hydrazide as shown in Scheme 1. Typically, to **1a** (0.236 g, 1.02 mmol) dissolved in ethanol (15 mL), 3-hydroxy-2-naphthoic hydrazide (0.303 g, 1.5 mmol) and 2-3 drops of conc. sulfuric acid was added and heated at reflux for 5 h. The solution was allowed to cool to room temperature, deep-yellow precipitate deposited was filtered and thoroughly washed with cold ethanol. The product was confirmed by ^{1}H,^{13}C NMR, ESI MS, IR spectra and SXCRD analysis (Figure A1-A4). Yield: 0.310 g (74%), M.P.: 310 °C. 600 MHz ^{1}H NMR ($CDCl_3$, δ (J, Hz)): 14.68 (OH, s), 11.46 (NH, s), 8.24 (1H, m, 12.0), 8.18 (1H, m), 8 (1H, d, 12.0), 7.92 (2H, d, 6.0), 7.78 (1H, d, 6.0), 7.65 (2H, d, 6.0), 7.59 (1H, t, 6.0), 7.48 (1H, t, 6.0), 7.45 (1H, s). 600 MHz ^{13}C NMR ($CDCl_3$, δ): 207.4, 158.8, 157.6, 146.6, 142.5, 138.7, 137.5, 134.4, 132.8, 132.0, 130.7, 130.5, 129.6, 129.5, 128.7, 128.3, 127.3, 127.2, 126.9, 125.3, 124.8, 123.7, 123.1, 122.9, 120.9, 113.6. ESI Mass *m*/*z* calcd. for $C_{26}H_{16}N_4O_2$, 416.1273; found: 417.1344 (**LH** + H^+). Selected IR (ATR mode, cm^{-1}): 3656(s), 3196(m), 1658(s), 1629(m), 1599(m), 1506(s), 1461(s), 1332(w), 1197(m).

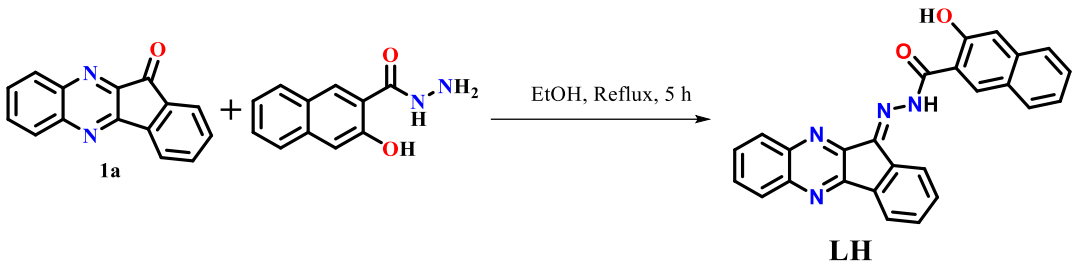

Scheme 1. Synthesis of **LH**.

2.3 Results and Discussion:

2.3.1 Molecular Structure

The probe crystallized as a thin needle-shaped yellow coloured solvate **LH**·$CHCl_3$ when its solution in 1:1 $CHCl_3$-hexane mixture was allowed to evaporate slowly. Single crystal X-ray diffraction data was collected, and it crystallized in $P2_1/n$ space group. The molecular structure of **LH** is shown in Figure 1 and the crystallographic data are listed in Table A1. The naphthyl and quinoxaline rings are nearly planar while the ninhydrin moiety deviates slightly from planarity. Intramolecular H-bonding interactions have been found to exist between phenol-OH and keto form of hydrazone moiety O1–H1···O2 (O1···O2 = 2.552(4) Å) and quinoxaline-N with hydrazone-NH, N1–H1a···N3 (N1···N3 = 2.825(4) Å) through which formation of supramolecular polymeric chain in **LH** was facilitated (Figure A5).

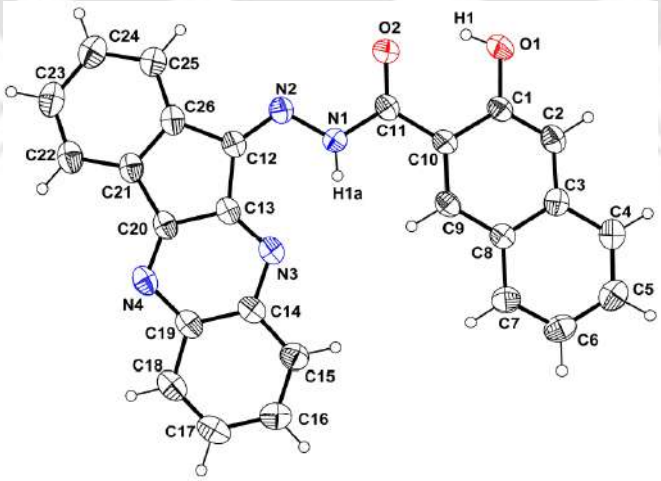

Figure 1. ORTEP diagram of **LH** (30% probability).

2.3.2 UV-Visible Spectra

The behaviour of **LH** in seven different solvents of varying polarity (DCM < THF < Dioxane < MeOH < CH_3CN < DMF < DMSO) was checked (Figure A6, Table A2). With the change in the polarity of solvents, the absorption maxima at 338 and 397 nm remained unaffected, except that the 338 nm peak (in DCM) exhibited a small change by appearing at 353 nm (in DMSO). However, the solution colour changed from colorless to pale yellow in DMF and DMSO possibly due to formation of $\mathbf{L}^-$ ion (Figure A7). These peaks at 338 and 397 nm may be of $\pi \rightarrow \pi^*$ transition origin. The **LH** was weakly fluorescent in all the solvents noted above, with λ_{ex} = 338 nm fluorescence was observed at 446 nm in DCM, while in all other solvent emission peak appeared in the range 426-436 nm.

Pure **LH** exhibited an absorption band at λ_{max} = 351 nm along with a shoulder at 393 nm in MeOH-HEPES (1:1, *v*/*v*, pH = 7.4) buffer solution (Figure A8) and all the UV-Vis spectra were recorded in this buffer. The result indicates an allowed π-π^* transition between two π-conjugated aromatic rings in the ligand framework, namely naphthalene and quinoxaline moiety. The selectivity of **LH** has been examined by recording the electronic spectra in presence of different metal ions *viz*., Na^+, K^+, Li^+, Be^{2+}, Ca^{2+}, Mg^{2+}, Mn^{2+}, Fe^{2+}, Co^{2+}, Ni^{2+}, Cu^{2+}, Zn^{2+}, Cd^{2+}, Hg^{2+}, Pb^{2+}, Fe^{3+}, Cr^{3+}, Al^{3+}, Pd^{2+}, Pt^{2+} and Au^{3+} (Figure 2A). The solution of **LH** was originally colorless but upon addition of aqueous solution of Cu(II) salts (up to 3 equivalents), the colour changed to yellow and no other metal ions listed above imparted such change. This colour change was specific to Cu^{2+} ion which occurred due to its binding to **LH** by exhibiting characteristic bands at 387 and 460 nm. With the addition of an excessive amount of other metal ions no such colour change occurred, which indicated that the chemoreceptor exhibited colour change only with copper(II) salts and hence is selective towards Cu(II) ions only (Figure 2B).

Upon gradual addition of $CuCl_2$ to **LH**, the intensity of the band at 338 nm got decreased while that of the 397 nm peak grew gradually (Figure 2C) and a new band with λ_{max} = 460 nm appeared whose intensity also increased gradually. The presence of a distinct isosbestic point at 374 nm indicated that only two species were present during the entire titration *viz*., **LH** and Cu(II) complex. To check the effect of counter anions, absorption spectra of **LH** was tested with $Cu(OAC)_2$, $Cu(NO_3)_2$, $Cu(ClO_4)_2$, and $CuSO_4$, all of which showed the same absorption spectrum as that of $CuCl_2$ (Figure A9). From this titration data, the detection limit for Cu^{2+} ion

was found to be 2.3 μM, which is less than the permissible limit in drinking water mentioned by WHO. The limit of quantification (LOQ) value was 8.0 μM (Figure A10). From the Job's plot, it was found that **LH** bound with the Cu^{2+} ion in 1:1 ratio (Figure A11) and for this stoichiometry, the binding constant was determined to be 1.13×10^4 M^{-1}, by using the modified Benesi-Hildebrand equation (Figure A12). In the ESI mass spectrum (Figure A13) of the sample containing 1:1 mixture of **LH** and $CuCl_2$, a peak observed at m/z = 586.8729 fitted with the formula $[Cu(\mathbf{L})Cl(DMF)]^+$ (m/z calcd. = 586.0707). This supported the 1:1 stoichiometry observed in Job's plot.

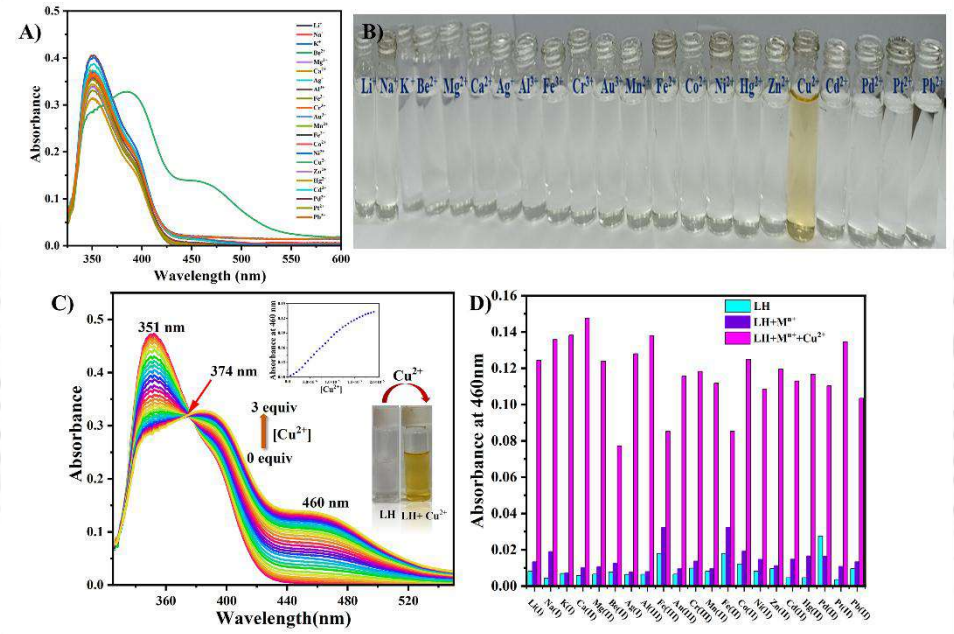

Figure 2. (A) The UV-Vis spectra of **LH** with different metal chlorides along with $CuCl_2$, (B) colorimetric response of **LH** after addition of other metal (C) the titration of **LH** in presence of $CuCl_2$ (inset: visuals), and (D) bar diagram of absorbance of **LH** with Cu^{2+} ion and other metal ions.

To investigate the selectivity of **LH**, competitive experiments were performed by adding 10 equivalents of competitive metal ion (listed above) to **LH** followed by 10 equivalents of Cu^{2+} ion. From the bar diagram (Figure 2D), it was clear that the value of the peak at 460 nm of probe **LH** with Cu^{2+} reached the maximum absorbance in presence of another metal ion. So, these metal ions did not show any significant effect on the absorption spectra of **LH**. The interaction of **LH** with several amino acids (Figure A14) were also checked and no spectral absorption change was observed. Hence, it may be proposed that the probe **LH** can be a handy

tool for the naked eye discrimination of Cu^{2+} ion in the presence of several co-existing metal ions.

2.3.3 pH Effect, Response Time and Reversibility Test

Most of the chemosensor involved in metal ion detection have heteroatoms and/or dissociable protons in the framework and hence the overall process can be affected by pH of the solution.[36] Evaluation of the desirable pH range for the recognition of metal ions and the effect of pH in presence of guest analyte Cu^{2+} ion is mandatory. The stability of **LH** has been determined in the pH range of 1-12 by following the absorbance value of the peak at 460 nm (Figure 3A). In the range pH = 1-4, no change was observed which indicated that Cu^{2+} ion remained unbound while in the range 5-10, the yellow colour developed and persisted. But in the basic range of 10-12, turbidity developed due to precipitation of copper (II) as hydroxide. Thus, the optimum pH range for the detection of Cu(II) ion by **LH** lies in the range 5-10.

Response time was an important sensing parameter[37] and for **LH** it was determined by following the absorbance value at 460 nm. In this kinetic study at room temperature, to the solution of **LH** 3.5 equivalents of $CuCl_2$ were added and the absorbance was recorded (Figure 3B), and the absorption maximum was attained within ~50 sec. This response time is significantly faster for real-time Cu^{2+} ion detection.

The stability/reversibility of **LH** for using it multiple times, was determined by using a strong chelating agent like $EDTA^{4-}$ ion.[38] The absorbance value of 460 nm peak of the complex **1** became nearly zero upon adding $EDTA^{4-}$ ion, which released the free **LH** due to formation of $[Cu(EDTA)]^{2-}$ ion. Noticeably, the colour of the solution was reversible upon the sequential addition of Cu^{2+} ion and Na_2EDTA solution, as depicted in (Figure 3C) and repeated several times.

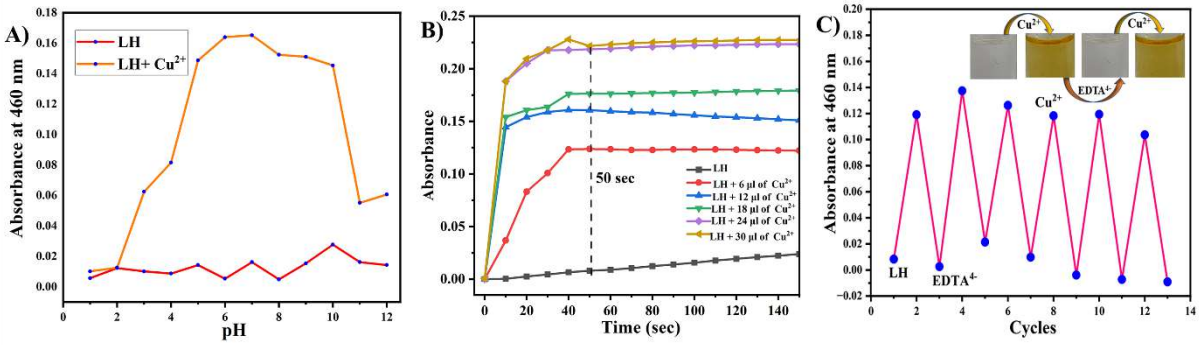

Figure 3. (A) Effect of pH, (B) determination of response time at 460 nm, (C) addition of Cu^{2+} ion and $EDTA^{4-}$ into **LH**.

2.3.4 IR and ^{1}H NMR Titration

In the IR spectrum, **LH** exhibited a peak at 1677 cm^{-1} due to $\nu_{C=O}$ which got shifted to 1665 cm^{-1} and the ν_{O-H} peak at 3651 cm^{-1} disappeared in presence of Cu^{2+} ion (Figure A15) indicating involvement of the carbonyl-O and phenolate-O atoms in coordination having a bidentate six-membered chelate ring. Thus, the formula [Cu(**L**)Cl(H_2O)] (**1**) has been assigned based on spectral data. The morphologies of **LH** and **l** in solution were studied by FESEM analysis (Figure 4). A clear morphological transition occurred between **LH** and **1**.[39] Initially, **LH** formed block-shaped aggregate but after adding $CuCl_2$ into the solution, the degree of agglomeration increased which resulted in the formation of a rod-shaped structure that authenticated the binding of **LH** and guest analyte Cu^{2+} ion which is in support of complex formation between **LH** and Cu^{2+} ion.

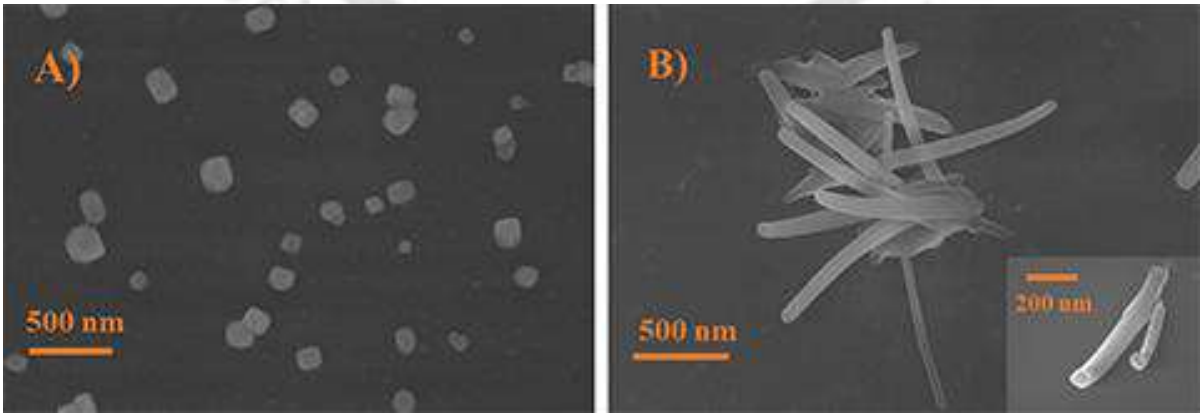

Figure 4. FESEM images of (A) **LH** (1.0×10^{-5} M) in MeOH/HEPES buffer (1:1, *v/v*, pH = 7.4), (B) **LH** + $CuCl_2$ (inset: higher magnification image of single rod-shaped structure).

The binding of **LH** to Cu(II) ion was followed by a ^{1}H NMR titration study (Figure 5). Pure ligand exhibited two distinct peaks at 14.68 and 11.46 ppm which are attributed to the phenolic-OH and hydrazinyl-NH proton respectively. Upon gradual addition of $CuCl_2$, the changes observed were (i) the intensity of the peak due to -OH proton deceased slowly which eventually disappeared after the addition of one equivalent of $CuCl_2$, (ii) the peak of -NH proton shifted to 11.30 ppm and broadened slightly, (iii) all other peaks broadened slightly and the singlet (C-H) peak of the naphthyl group also shifted from 8.51 to 8.62 ppm. Thus, **LH** has lost its -OH proton upon binding to the Cu^{2+} ion which indicated that conjugate base $\mathbf{L}^-$ has bonded to the Cu(II) center.

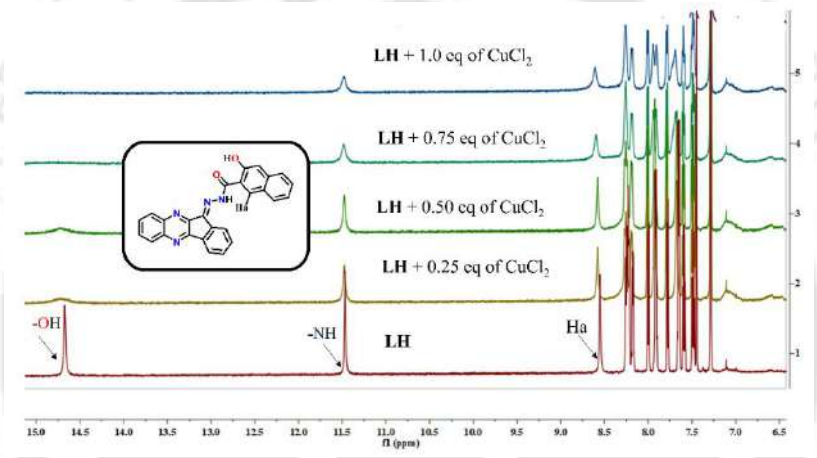

Figure 5. ^{1}H NMR titration plot of **LH** with the gradual addition of $CuCl_2$.

2.3.5 Detection of Cysteine by 1

The complex **1** had been tested for a potential chromogenic sensor for sensing various amino acids *viz*., alanine, glycine, leucine, lysine, histidine, arginine, methionine, tyrosine, phenylalanine, isoleucine, valine, tryptophan, asparagine, aspartic acid, glutamic acid, homocysteine (Hcy), glutathione (GSH) and cysteine (Figure 6A). Upon adding amino acids into the solution of **1** formed *in situ*, only cysteine showed the colour change from yellow to colorless. All other amino acids did not show any colour change and hence **1** was selective for the detection of cysteine. The pK_a value of -SH group present in the side chain of cysteine was 8.0, which was lower than other thiol-containing amino acids namely Hcy (8.87) and GSH (9.20). Cys exists mostly in its thiolate form at pH 7.4 and is sterically less hindered than Hcy and GSH,[40–42] making it an effective ligand for Cu^{2+} than the other two biothiols. The aforementioned biothiols did not affect the spectral absorbance change on **1** (Figure A16).

From the UV-Vis spectral titration of **1** with cysteine (up to 2 equivalents) the intensity of peaks at 460 and 380 nm decreased and the peak at 350 nm grew in intensity (Figure 6B). The absorption intensity of complex **1** was increased from (60-75%) in presence of 10 equivalents of other competitive amino acid mentioned earlier (Figure 6C). Job's plot data revealed a Cu^{2+} ion to cysteine ratio of 1:2 (Figure A17). With the addition of 2 equivalents of cysteine to **1** the $\nu_{C=O}$ peak shifted to 1761 cm^{-1} (Figure A18) which had appeared at 1665 cm^{-1} in **1**, along with the new peak at 622 cm^{-1} due to ν_{C-S}. In the ESI MS spectra of the sample of Cys + **1**, the peak at *m*/*z* = 586.8729 due to $[Cu(\mathbf{L})Cl(DMF)]^+$ got completely vanished and peak due free **LH** + H^+ was observed at *m*/*z* = 417.1347. Another peak at *m*/*z* = 241.0300 calculated *m*/*z* = 241.0311 for cystine $[C_6H_{12}N_2O_4S_2+H]^+$ was observed (Figure A19). Thus, in the presence of two equivalents of cysteine, Cu(II) ion in **1** was reduced to Cu(0) accompanied by the release of free **LH** and cystine (Scheme 2). From the spectral titration data, the reaction constant (K_b, calculated using the Benesi-Hildebrand equation), LOD, and LOQ were calculated to be 1.03 × 10^9 M^{-2}, 60 nM, and 0.2 μM respectively (Figure A20). Since the ligand **LH** was weakly fluorescent and the *in situ* generated complex **1** also had very weak fluorescence intensity, with the addition of various amino acids no spectral emission change was observed (Figure A21).

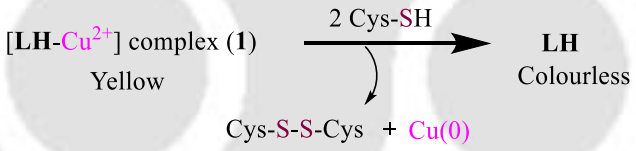

Scheme 2. Detection of cysteine by **1**.

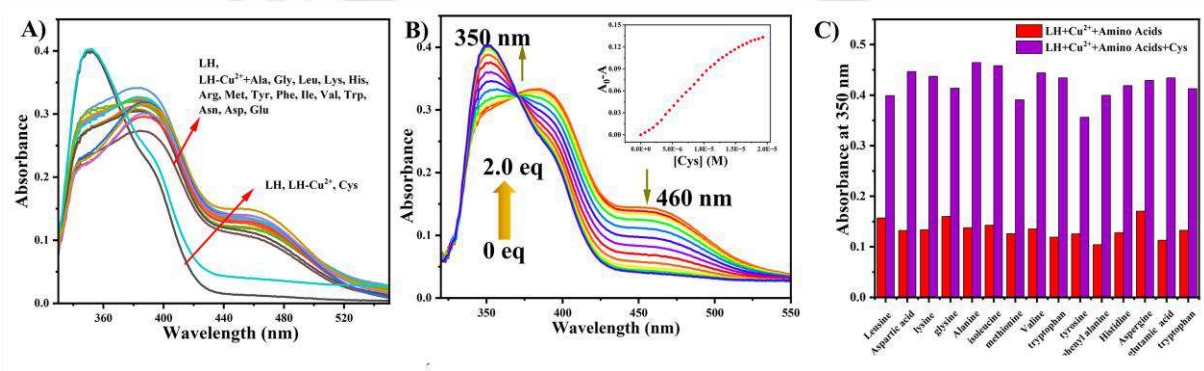

Figure 6. (A) The UV-Vis spectral change in **1** with the addition of several amino acids. (B) titration of *in situ* formed **1** with cysteine (inset: calibration curve at 350 nm), (C) competitive experiment of **1** with different amino acids in presence of cysteine at 350 nm.

2.3.6 Detection of ATP by 1

Since ATP was known to have high affinity towards Cu^{2+} ion,[43] an attempt was made to determine the ability of **1** formed *in situ* for the detection of ATP (Scheme 3). In MeOH/HEPES buffer, upon addition of anions like F^-, Cl^-, Br^-, I^-, CN^-, SCN^-, PO_4^{3-}, S^{2-}, $S_2O_3^{2-}$, CO_3^{2-}, HCO_3^-, CH_3COO^-, ClO_4^-, $H_2PO_4^-$, HPO_4^{2-}, NO_3^-, SO_4^{2-}, $P_3O_7^{4-}$, HSO_4^-, ADP and AMP, no perceptible change in the spectra of **1** was observed (Figure 7A). But only in the presence of ATP, the colour changed from yellow to colorless (Figure A22). The UV-Vis titration experiment was subsequently carried out by a gradual addition of ATP to **1**, the absorbance value of 383 nm peak gradually decreased while that of 343 nm increased with saturation point reached after addition of 3 equivalents of ATP (Figure 7B). From the calibration plot (Figure A23), the calculated LOD and LOQ values were 130 nM and 460 nM respectively. Again, to check the counter anion test competitive bar diagram experiment in presence of other anion was also carried out in complex **1** which showed an increase of absorbance intensity of about (53-86%) in presence of ATP (Figure 7C).

A 1:1 binding ratio between **1** and ATP was obtained from the Job's plot (Figure A24) which was supported by the presence of *m*/*z* peak at 603.2224 in the mass spectrum, calculated value of 603.8864 for $^{63}CuC_{10}H_{15}N_5O_{13}P_3Cl$ due to $[Cu(ATP)Cl(H)]^+$ (Figure A25), and the calculated binding constant (K_b) value being 8.9×10^4 M^{-1} (Figure A26). The binding constant value clearly suggested that *in situ* generated complex **1** has four times higher affinity than **LH**, indicating that ATP can quickly snatch Cu^{2+} ion from **1**.

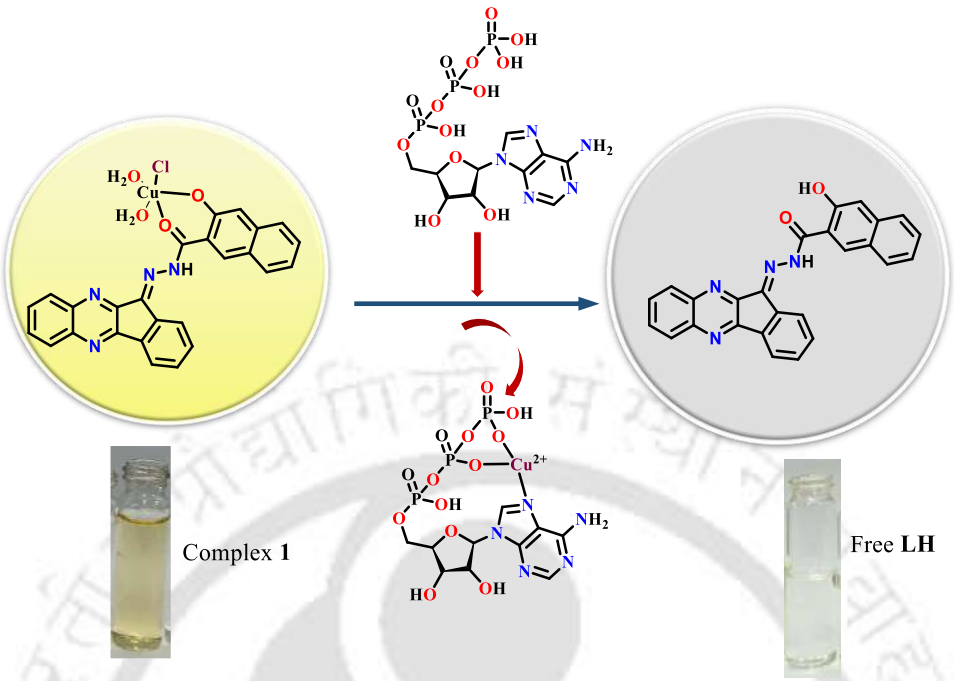

Scheme 3. Detection of ATP by **1**.

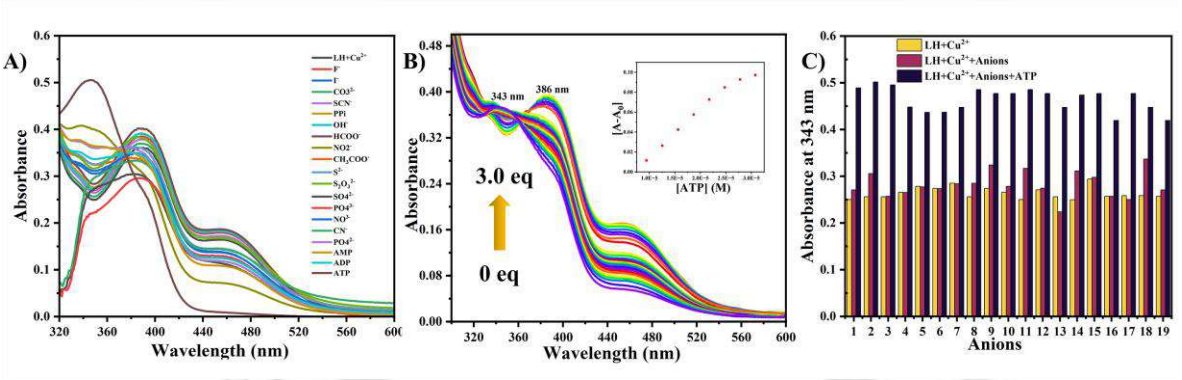

Figure 7. (A) Spectra of **1** with the addition of various anions, (B) titration of *in situ* formed **1** with ATP (inset: absorbance changes at 343 nm), (C) bar graph representing spectral absorbance change in **1** with anion addition in presence of ATP at 343 nm.

2.3.7 DFT-TDDFT Calculations

To support the UV-Vis spectral absorption studies, DFT/TDDFT calculations were carried out on **LH** and **1**. In the optimized structure (Figure A27I), the central copper atom was bound by $\mathbf{L}^-$ in a bidentate chelating manner through phenolate-O and carbonyl-O atoms, forming a six-membered chelate ring. These two are the most favourable binding site as inferred from the red colour around oxygen atoms in molecular electrostatic potential map (MEP) diagrams (Figure A27II). In **LH**, HOMO is localized on the naphthyl ring and LUMO is concentrated on

hydrazide and indeno[1,2-*b*]quinoxalinylidene moieties. For **1**, the Frontier Molecular Orbitals split into alpha and beta MOs due to the presence of unpaired electron of Cu^{2+} center.[44,45] The alpha and beta HOMO mainly reside over the central metal Cu^{2+} ion and the naphthyl ring (Figure 8). The alpha LUMO was distributed on the hydrazide and indeno[1,2-*b*]quinoxalinylidene moieties, while the beta LUMO was concentrated over the metal center and co-ligands. Figure A28, A29 represent energy level diagram of selected HOMO-LUMO of **LH** and **1**. The calculated energy level in **LH** having the highest oscillator frequency (f = 0.4329) and **1** (f = 0.0620) in MeOH were listed in Table A3, A4. The HOMO-LUMO energy gap in **LH** was observed to be 3.14 eV, which decreased in both alpha (2.85 eV) and beta (2.30 eV). This result supported the red shift in the absorption maximum observed experimentally (Figure A30). As the result, Intramolecular Charge Transfer (ICT)[46,47] between the donor group 3-hydroxynaphthyl and the acceptor group indeno[1,2-*b*]quinoxalinylidene moieties was much more efficient for these complexations which reflected from the red shift in absorption peak (Scheme 4).

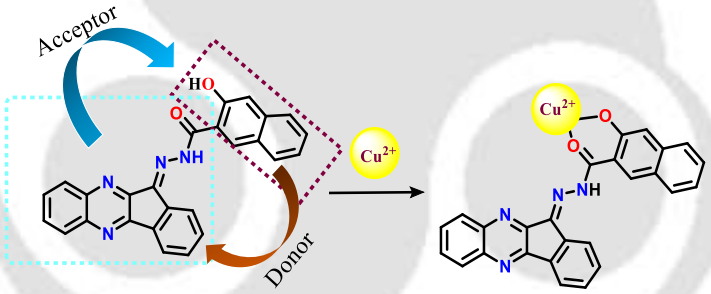

Scheme 4. Binding of **LH** with Cu^{2+} ion.

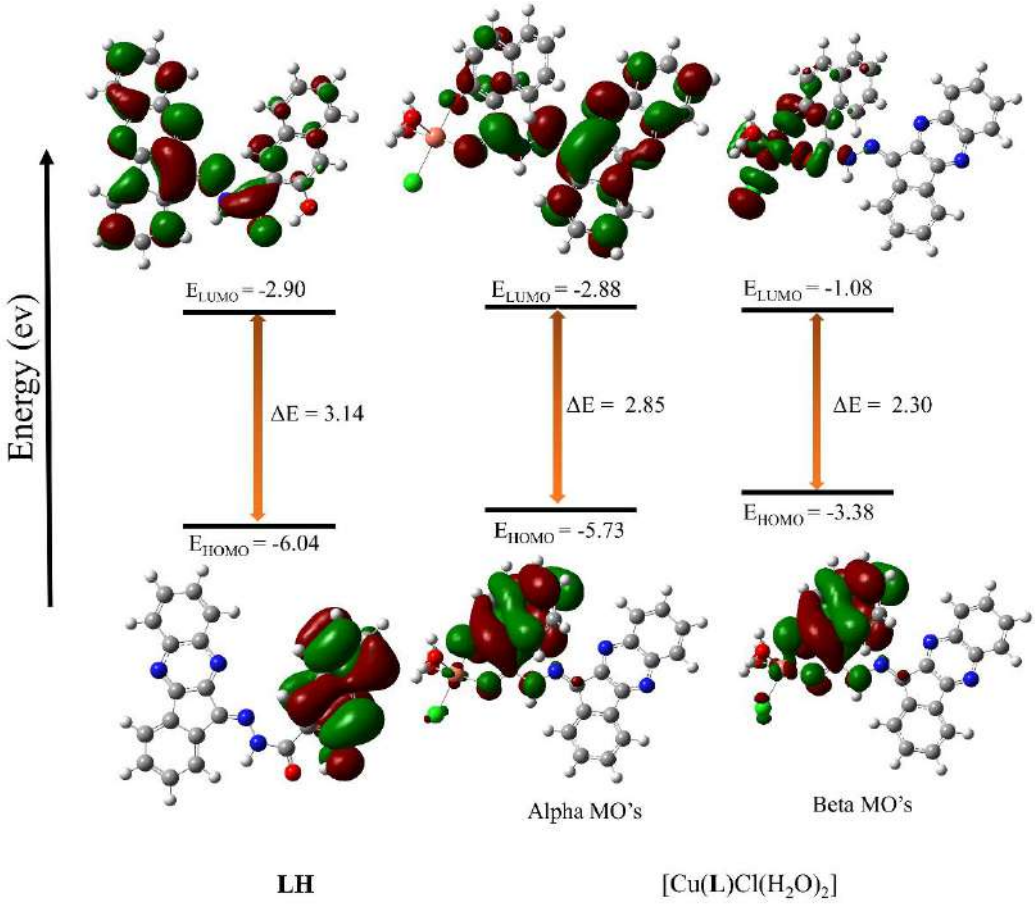

Figure 8. HOMO and LUMO in **LH** and **1**.

2.3.8 Real Water Sample and Paper Test Strips

Ability of **LH** for detecting Cu^{2+} ion, using water taken from river, domestic supply, and drinking water facility were also examined. All the water samples were collected from common facilities of IIT Guwahati and the adjacent Brahmaputra River. Sample water was filtered through membrane filter paper (0.22 μm pore size) and the pH was adjusted from 7.2 to 7.4, prior to further analysis. A fixed concentration of Cu^{2+} (15 μM) was put into the resultant solution of **LH** and the absorbance change at 460 nm was recorded (Figure 9A). Real water sample analysis and calculated recovery percentage of Cu^{2+} ion data were given in Table A5. The LOD values of Cu^{2+} were determined by using the UV-Vis titration data (Figure A31) and the calibration plot is given in Figure A32. A comparative list of multiple analyte detection involving Cu^{2+} ion, cysteine, and ATP reported in the literature study has been shown in Table A6.

Filter paper strips-based experiments play the most important role in rapid metal ion detection owing to its immense selectivity and sensitivity.[48] To examine the practical application of chemosensor **LH**, six Whatman 40 filter paper strips (2 × 8) cm was dipped in a MeOH/HEPES buffer solution of **LH** (10 μM). The resulting paper strips were air dried, and different concentration of $CuCl_2$ solution (0-30 μM) was drop cast. The mean intensity of the colour of all filter paper strips were analyzed by using ImageJ software.[49] The detection limit of the filter paper strips-based **LH** ligand for naked eye visualization was found to be 3.39 μM (Figure 9B). The colour changed from colorless to pale yellow in the filter paper strips can be observed instantly (Figure 9C). So, the detection of Cu^{2+} ion can be done on-spot by using test strips without the help of any sophisticated instrument.

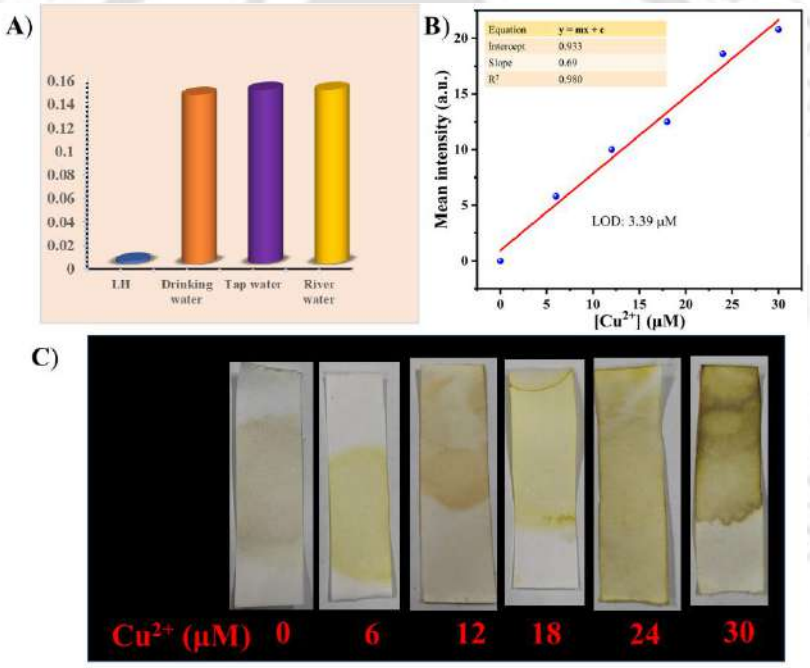

Figure 9. (A) Bar diagram of **LH** absorbance at 460 nm with spiked $CuCl_2$ (1mM) in MeOH + real water sample, (B) colour change in filter paper strips by addition various concentration of $CuCl_2$.

2.3.9 Molecular Logic Gate Circuits

Currently, many researchers are interested in the construction of molecular logic gates based upon the supramolecular sensing behaviour and chemically inscribe the information as input and the absorption results as output. By determining the observed spectroscopic results of **1** in the presence of cysteine, it was quite logical to interpret the chemical outcomes with molecular logic gate electronic circuit which is extremely helpful to conserve information for the next

generation.[50,51] For the construction of the molecular logic gate, **1** and cysteine were considered as two inputs, IN1 and IN2 respectively and their corresponding absorbance values at 460 and 350 nm taken as two outputs as OUT1 and OUT2 respectively. The absorbance spectra of **1**, IN1 show the absorption maximum at 460 nm which is treated as OUT1 should be "ON" state *i.e.,* (OUT1 = 1) while OUT2 should be in OFF state *i.e.,* (OUT2 = 0). Again, with the presence of cysteine (IN2 = 1), we get OUT2 as in "ON" state *i.e.,* (OUT2 = 1), the absorbance peak at 350 nm will begin to rise and the initial absorption peak at 460 nm decreases rapidly *i.e.,* (OUT1 = 0). Based on the following outcomes, a two-of-two logic gate circuitry has been designed (Figure 10) and correspondingly, the produced truth table has been displayed in Table 1. The designed logic gate circuitry reflected the present sensing skill would be an added value for the wide range of molecular logic gate scaffolds.

Table 1. Representing the UV-Vis absorption data by using a truth table for complex **1** with the presence of cysteine.

IN1 Complex 1	IN2 Cysteine	OUT1 (460 nm)	OUT2 (350 nm)
0	0	0	0
1	0	1	0
0	1	0	0
1	1	0	1

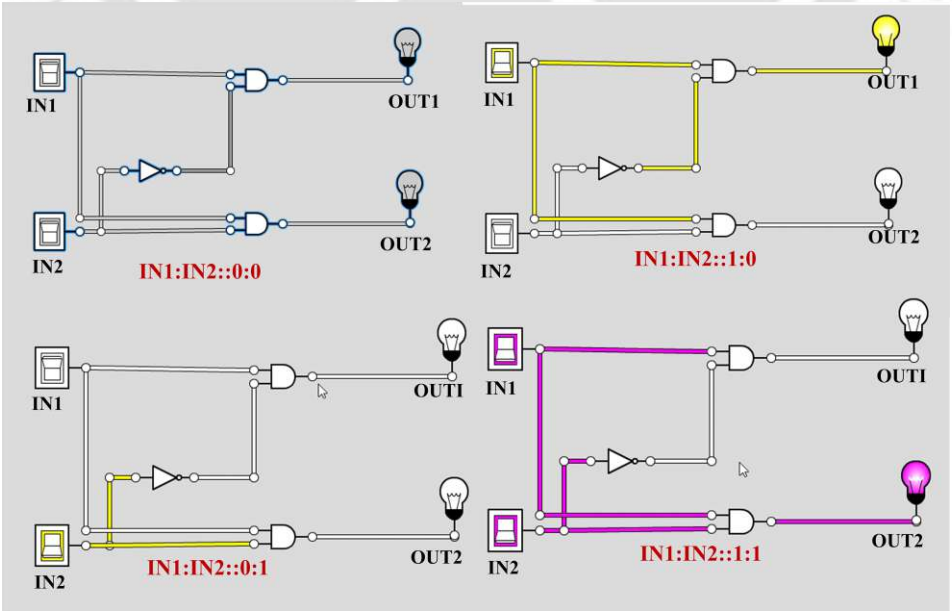

Figure 10. Construction of two input logic gate ensembles by **1** and Cysteine.

2.3.10 LH Towards Biomolecules

Serum albumin (SA), a plasma protein that typically transports various ions and medications through the blood to the cells and different tissues. The favourable interaction between the drug and serum albumin helps in the transport of the drug.[30,52] The ability of the probe **LH** to bind with BSA and HSA was determined by the UV-Vis spectroscopic method in MeOH/Tris-HCl buffer (1:1, *v/v*, pH = 7.4) (Figure 11A, 11B). The probe **LH** (25 μM) exhibited an absorption band with a peak at 353 nm, which upon gradual addition aliquots of BSA/HSA (0-200 μM) resulted in bathochromic shift of the band with the peak at 408 nm (BSA) and 413 nm (HSA). An isosbestic point observed in both cases (372 nm in BSA and 374 nm in HSA) indicated the involvement of only **LH** and SA proteins. The K_a values (Figure A33) calculated using Benesi-Hildebrand equation (Equation A1) were 9.41×10^4 M^{-1} (BSA) and 1.83×10^5 M^{-1} (HSA), which indicated a favourable binding between the BSA/HSA and **LH**.

Tryptophan residues present in BSA (Trp-134, Trp -212) and HSA (Trp-134, Trp-214) has been known to exhibit fluorescence with λ_{em} = 347 nm upon excitation with 300 nm light .[53,54] Upon incremental addition of **LH** (10 μL of 0-200 μM) to BSA/HSA (10 μM) in Tris-HCl buffer medium, the fluorescence intensity decreased which got completely quenched after addition of about half equivalent (Figure 11C, Figure 11D). For the calculation of quenching constant (K_{SV}) Stern-Volmer equation was used (Equation A_{2I}). Since here static quenching takes place so the binding constant (K_b) was calculated by using Scatchard equation (Equation A_{2II}). The calculated K_b, K_{SV}, and K_q values were listed in Table 2 and the Scatchard plot was included in (Figure A34). Large values of K_b indicated a stronger interaction between the ligand and these protein molecules, but HSA had stronger binding ability than BSA.

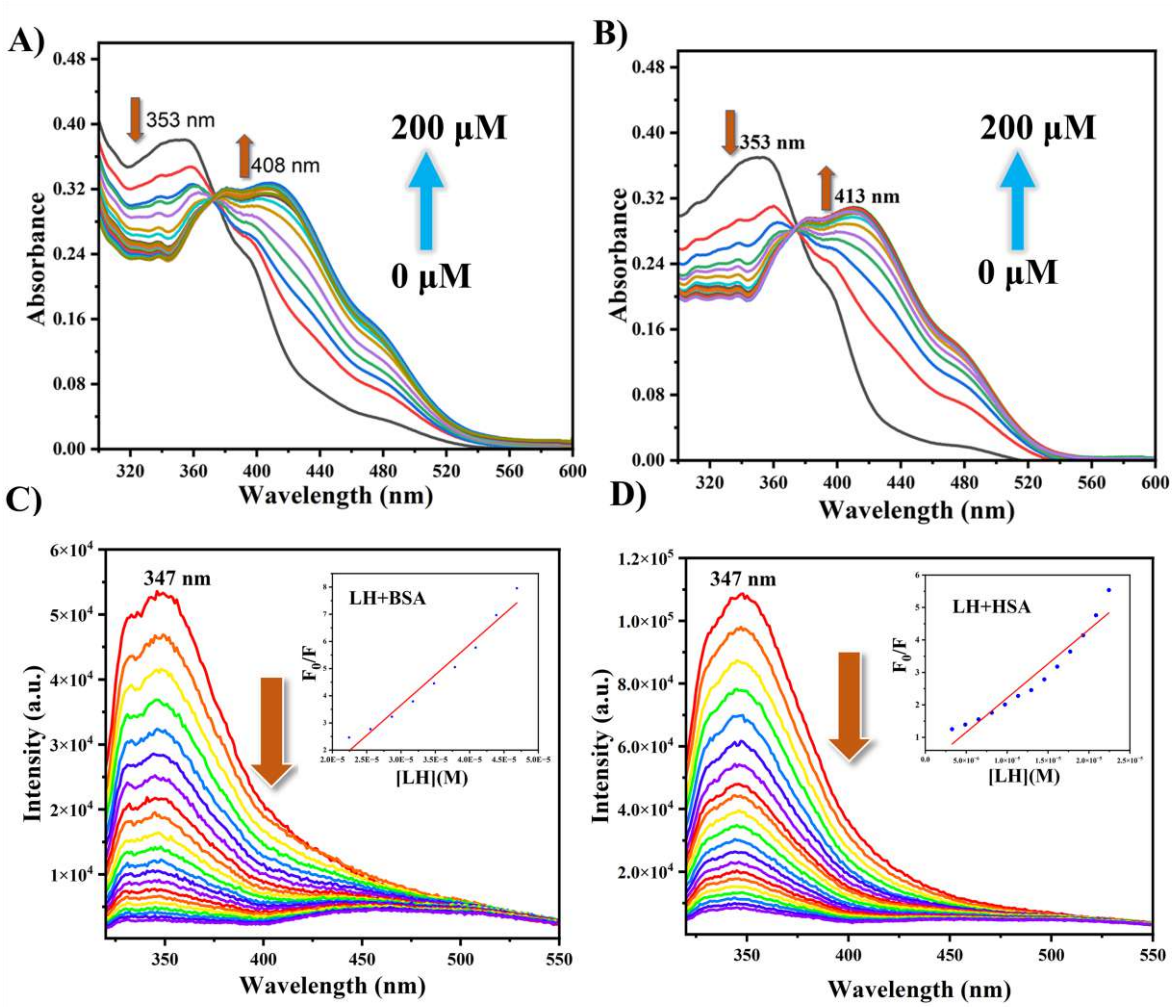

Figure 11. UV-Vis spectra of **LH** (25 µM) with increasing concentration of (A) BSA and (B) HSA (0-200 µM) in MeOH/Tris-HCl buffer medium (1:1, *v/v*, pH = 7.4). Emission spectra of (C) BSA (D) HSA (25 µM) in MeOH/Tris-HCl buffer medium (1/1, *v/v*) with the increasing concentration of **LH** (0-200 µM) (inset: Stern-Volmer plots).

Table 2. Spectral information regarding the interaction of the probe **LH** with BSA and HSA.

	Fluorescence method			
Biomolecule	**K_b (M^{-1})**	**K_{SV} ($M^{-1}s^{-1}$)**	**K_q (M^{-1})**	***n***
BSA	4.2×10^7	2.2×10^5	2.2×10^{13}	1.59
HSA	3.4×10^8	4.4×10^5	4.4×10^{13}	1.70

2.3.11 *In silico* Molecular Docking Studies

For understanding the binding site and intermolecular interaction of **LH** with BSA and HSA, *in silico* blind molecular docking studies were performed.[53,54] Chemosensor **LH** was not only useful as colorimetric sensor for Cu^{2+} ion but it showed a favourable interaction with BSA and HSA (Figure 12). The binding energy for docking of **LH** with BSA and HSA were respectively -7.12 and -8.39 kcal/mol indicating that HSA has a stronger affinity with the **LH**. Interaction with various amino acid residues were listed in Table A7. In BSA, interaction with **LH** include (i) hydrogen bond between imine nitrogen and Lys 114 (ii) π-alkyl between quinazoline moiety and Val 423, Pro 420 (iii) π-alkyl between naphthyl moiety and Arg 144, Pro 110, (iv) π-sigma between quinazoline moiety and Ile 522 (v) π-anionic involving quinazoline moiety as well as imine nitrogen with Glu 424 (Figure A35I**)**. In HSA, interaction with **LH** includes (i) H-bond between hydrazinyl (N-H) and Leu 45, as well as carbonyl oxygen and Trp 47 (ii) aromatic ring π-π interactions with Trp 62, and (iii) π-alkyl involving naphthyl ring as well as quinazoline moiety with Ala 60 and Lys 43 (Figure A35II).

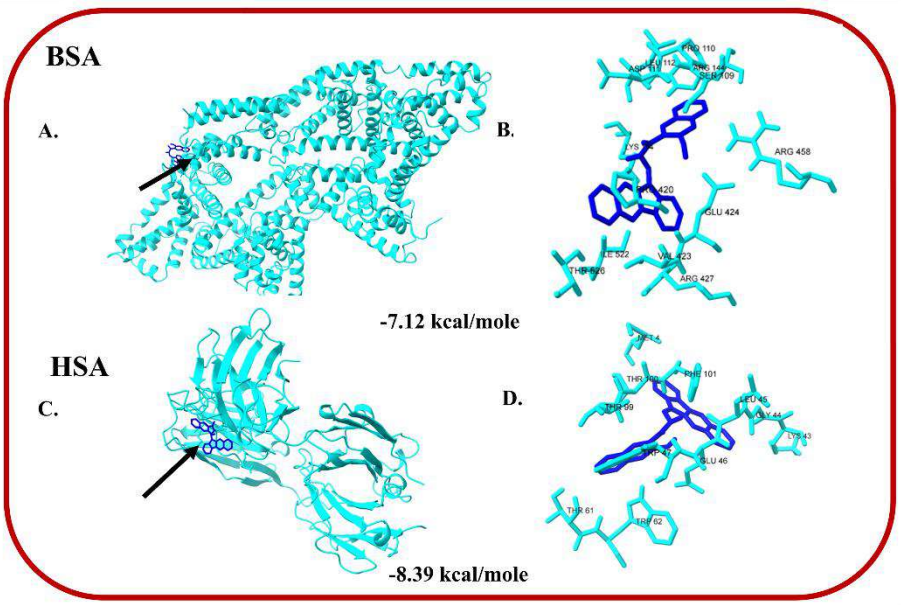

Figure 12. Possible binding mode of the interaction of **LH** with (A) BSA and (B) HSA protein model, and 3D zoomed picture for showing the favourable interactions between **LH** and (C) BSA, (D) HSA.

2.4 Conclusion:

In summary, a new chemosensor **LH** bearing quinoxaline and hydroxynaphthyl group has been synthesized and characterized thoroughly with different spectroscopic techniques and SCXRD analysis. The probe **LH** was exceptionally specific and selective for the colorimetric detection of Cu^{2+} ion over other tested metal ions, and it also displayed an instantaneous prominent colour change from colorless to yellow in aqueous MeOH/ HEPPS buffer medium (1:1, *v/v*, pH = 7.4). A 1:1 binding stoichiometry of **LH** towards Cu^{2+} was confirmed by ESI Mass spectral analysis, ^{1}H NMR titration experiment and Job's plot analysis. The sensing response is rapid (50 sec response time), good pH tolerance (5-10) and maintained reversibility with the addition of Na_2EDTA. The calculated detection limit for Cu^{2+} ion was 2.3 μM, which was far less than the acceptable limit of Cu^{2+} in drinking water. The *in situ* formed **1** was useful in the selective detection of cysteine and ATP over other interfering amino acids and anions. The practical application of **LH** was also ascertained through real water samples and filter paper strips which can used for on-spot detection of Cu^{2+} ion. The sensing activity of **1** towards cysteine was studied using molecular logic gate operation. Theoretical calculations showed that **LH** after coordinating with Cu^{2+} ion caused a red shift in the absorption band. Molecular docking studies have shown that **LH** exhibited a strong binding interaction with BSA and HSA molecules, with binding energies of -7.12 and -8.39 kcal/mol, respectively.

References:

1 S. Paul, R. Das, M. Seth, H. Hirani, N. C. Murmu and P. Banerjee, *Ind. Eng. Chem. Res.*, 2020, **59**, 19077-19092.

2 D. Vashisht, S. Sharma, R. Kumar, V. Saini, V. Saini, A. Ibhadon, S. C. Sahoo, S. Sharma, S. K. Mehta and R. Kataria, *Microchem. J.*, 2020, **155**, 104705.

3 M. Sahu, A. K. Manna, S. Chowdhury and G. K. Patra, *RSC Adv.*, 2020, **10**, 44860-44875.

4 D. P. Dominguez, M. Rodriguez, G. R. Ortiz, J. L. Maldonado, D. L. Moreno, M. O. Gutierrez and V. Barba, *Sensors Actuators, B Chem.*, 2016, **225**, 221-227.

5 M. Sahu, A. K. Manna, K. Rout, J. Mondal and G. K. Patra, *Inorg. Chim. Acta*, 2020, **508**, 119633.

6 W. Lin, L. Yuan, Z. Cao, J. Feng and Y. Feng, *Dye. Pigment.*, 2009, **83**, 14-20.

7 S. Mahata, S. Dey, B. B. Mandal and V. Manivannan, *J. Photochem. Photobiol. A Chem.*, 2022, **427**, 113795.

8 H. Kim, Y. J. Na, E. J. Song, K. B. Kim, J. M. Bae and C. Kim, *RSC Adv.*, 2014, **4**, 22463-22469.

9 A. Bhattacharya, S. Mahata, A. Bandyopadhyay, B. B. Mandal and V. Manivannan, *Luminescence*, **2022**, 37, 883-891.

10 I. Bertini and A. Rosato, *Cell. Mol. Life Sci.*, 2008, **65**, 89-91.

11 Y. H. Hung, A. I. Bush and R. A. Cherny, *J. Biol. Inorg. Chem.*, 2010, **15**, 61-76.

12 E. Gaggelli, H. Kozlowski, D. Valensin and G. Valensin, *Chem. Rev.*, 2006, **106**, 1995-2044.

13 M. S. Tanner, *Am. J. Clin. Nutr.*, 1998, **67**, 1074S-1081S.

14 R. Mehta, D. M. Templeton and P. J. O'Brien, *Chem. Biol. Interact.*, 2006, **163**, 77-85.

15 S. Paul, P. Ghosh, S. Bhuyan, S. K. Mukhopadhyay and P. Banerjee, *Dalt. Trans.*, 2018, **47**, 1082-1091.

16 Z. Wu, W. Li, J. Chen and C. Yu, *Talanta*, 2014, **119**, 538-543.

17 Y. M. Go and D. P. Jones, *Free Radic. Biol. Med.*, 2011, **50**, 495-509.

18 A. Pastore, A. Alisi, G. Di Giovamberardino, A. Crudele, S. Ceccarelli, N. Panera, C. D. Vici and V. Nobili, *Int. J. Mol. Sci.*, 2014, **15**, 21202-21214.

19 R. Singh and G. Das, *Analyst*, 2019, **144**, 567-572.

20 S. K. Pandit, S. Das and G. Das, *Sensors and Diagnostics*, 2024, **3**, 440-447.

21 W. W. Wang, Y. Wang, W. N. Wu, X. L. Zhao, Z. Q. Xu, Z. H. Xu, X. X. Li and Y. C. Fan, *Spectrochim. Acta Part A Mol. Biomol. Spectrosc.*, 2020, **226**, 117592.

22 C. Park and J. I. Hong, *Tetrahedron Lett.*, 2010, **51**, 1960-1962.

23 S. Mishra, S. M. Hossain and A. K. Singh, *Spectrochim. Acta Part A Mol. Biomol. Spectrosc.*, 2020, **240**, 118600.

24 R. V. V. Castillo, M. K. S. Flores, A. O. V. Posadas, I. J. B. Rodriguez, C. B. Brito, J.

M. B. Renedo, N. G. Rivas, L. D. R. Vazquez and A. D. Gonzalez, *Dye. Pigment.*, 2021, **196**, 109827.

25 Y. Zhou, Z. Xu and J. Yoon, *Chem. Soc. Rev.*, 2011, **40**, 2222.

26 S. M. Cardoso, I. Santana, R. H. Swerdlow and C. R. Oliveira, *J. Neurochem.*, 2004, **89**, 1417-1426.

27 C. Speck, *EMBO J.*, 1999, **18**, 6169-6176.

28 T. Bayraktutan, B. Gur and Y. Onganer, *J. Mol. Struct.*, 2022, **1256**, 132448.

29 H. Swaminathan and K. Balasubramanian, *Sensors Actuators B Chem.*, 2018, **264**, 337-343.

30 B. X. Huang, H. Y. Kim and C. Dass, *J. Am. Soc. Mass Spectrom.*, 2004, **15**, 1237-1247.

31 M. Akram, F. Ansari, I. A. Bhat and Kabir-ud-Din, *J. Mol. Liq.*, 2019, **276**, 519-528.

32 S. Karthikeyan, G. Bharanidharan, S. Ragavan, S. Kandasamy, S. Chinnathambi, K. Udayakumar, R. Mangaiyarkarasi, R. Suganya, P. Aruna and S. Ganesan, *Mol. Pharm.*, 2019, **16**, 669-681.

33 M. A. Neelakantan, K. Balamurugan, C. Balakrishnan and L. Subha, *Appl. Organomet. Chem.*, 2018, **32**, e4259.

34 F. Abyar and L. Tabrizi, *J. Biomol. Struct. Dyn.*, 2020, **38**, 474-487.

35 G. Balamurugan and S. Velmathi, *ChemistrySelect*, 2017, **2**, 10946-10950.

36 S. Mahata, A. Bhattacharya, J. P. Kumar, B. B. Mandal and V. Manivannan, *J. Photochem. Photobiol. A Chem.*, 2020, **394**, 112441.

37 D. Aydin, S. N. K. Elmas and F. N. Arslan, *Food Chem.*, 2023, **402**, 134439.

38 B. Wang, W. Xu, K. Gan, K. Xu, Q. Chen, W. Wei and W. Wu, *Spectrochim. Acta Part A Mol. Biomol. Spectrosc.*, 2022, **277**, 121245.

39 R. Das, S. Bej, D. Ghosh, N. C. Murmu, H. Hirani and P. Banerjee, *Sensors Actuators, B Chem.*, 2021, **341**, 129925.

40 Y. Wang, Q. Meng, Q. Han, G. He, Y. Hu, H. Feng, H. Jia, R. Zhang and Z. Zhang, *New*

J. Chem., 2018, **42**, 15839-15846.

41 A. K. Manna, J. Mondal, K. Rout and G. K. Patra, *J. Photochem. Photobiol. A Chem.*, 2018, **367**, 74-82.

42 Y. S. Kim, G. J. Park, S. A. Lee and C. Kim, *RSC Adv.*, 2015, **5**, 31179-31188.

43 C. Wang, Q. Qi, W. Li, J. Dang, M. Hao, S. Lv, X. Dong, Y. Gu, P. Wu, W. Zhang, Y. Chen and J. S. Hartig, *Nat. Commun.*, 2020, **11**, 4792.

44 Y. F. Ding, L. L. Man, L. Tong, X. Li, W. K. Dong and Y. J. Ding, *J. Mol. Struct.*, 2024, **1301**, 137341.

45 M. Azam, S. I. Al-Resayes, M. Alam, A. Trzesowska-Kruszynska, R. Kruszynski and M. R. H. Siddiqui, *Polyhedron*, 2019, **170**, 287-293.

46 N. Mergu and V. K. Gupta, *Sensors Actuators B Chem.*, 2015, **210**, 408-417.

47 M. S. Kim, T. G. Jo, H. M. Ahn and C. Kim, *J. Fluoresc.*, 2017, **27**, 357-367.

48 G. H. Liu, Z. Z. Chen, Y. H. Deng and W. K. Dong, *J. Photochem. Photobiol. A Chem.*, 2021, **414**, 113271.

49 C. Staudter, C. V. Hugo, P. Bosselmann, J. P. Mollenhauer, R. Meran and O. Roenpage, *Manag. Prof.*, 2013, **Part F411**, 203-346.

50 A. Palta, G. Kumar and V. Luxami, *J. Photochem. Photobiol. A Chem.*, 2022, **433**, 114198.

51 P. Rasin, J. Haribabu, K. M. Malappuram, V. Manakkadan, V. N. V. Palakkeezhillam, C. Echeverria and A. Sreekanth, *J. Photochem. Photobiol. A Chem.*, 2023, **437**, 114493.

52 P. Sonderby, J. T. Bukrinski, M. Hebditch, G. H. J. Peters, R. A. Curtis and P. Harris, *ACS Omega*, 2018, **3**, 16105-16117.

53 S. Gurusamy, K. Krishnaveni, M. Sankarganesh, V. Sathish, P. Thanasekaran and A. Mathavan, *J. Mol. Liq.*, 2021, **325**, 115190.

54 S. Gurusamy, M. Sankarganesh, V. Sathish, P. Thanasekaran and A. Mathavan, *J. Photochem. Photobiol. A Chem.*, 2022, **425**, 113674.

55 H. Tavallali, G. D. Rad, M. A. Karimi, E. Rahimy, *Anal. Biochemistry*, 2019, **583**, 113376.

56 A. Puni, C. J. Chang, J. Chen, S. R. Hsieh, M. C. Lee, *Spectrochim. Acta - Part A Mol. Biomol. Spectrosc.*, 2022, **274**, 121108.

57 T. Anand, G. Sivaraman, D. Chellappa, *J. Photochem. Photobiol. Chem.*, 2014, **281**, 47-52.

58 M. Ranjani, P. Kalaivani, F. Dallemer, S. Selvakumar, T. Kalpana, R. Prabhakaran, *Inorganica Chim. Acta*, 2022, **530**, 120683.

59 A. K. Manna, J. Mondal, K. Rout, G. K. Patra, *J. Photochem. Photobiol. Chem.*, 2018, **367**, 74-82.

60 S. Jiang, J. Qiu, S. Chen, H. Guo, F. Yang, *Spectrochim. Acta - Part A Mol. Biomol. Spectrosc.*, 2020, **227**, 117568.

61 P. Xia, Z. Su, J. Sun, D. Li, X. Huang, *ChemistrySelect*, 2017, **2**, 11620-11625.

62 W. Sun, G. Liu, M. Tong, H. Wang, S. Liu, *Analyst*, 2021, **146**, 1892-1896.

63 L. Y. Geng, Y. Zhao, E. Kamya, J. T. Guo, B. Sun, Y. K. Feng, M. F. Zhu, X. K. Ren, *J. Mater. Chem. C*, 2019, **7**, 2640-2645.

64 X. Jin, J. Gao, P. Xie, M. Yu, T. Wang, H. Zhou, A. Ma, Q. Wang, X. Leng, X. Zhang, *Spectrochim. Acta - Part A Mol. Biomol. Spectrosc.*, 2018, **204**, 657-664.

65 B. Zha, S. Fang, H. Chen, H. Guo, F. Yang, *Spectrochim. Acta - Part A Mol. Biomol. Spectrosc.*, 2022, **269**, 120765.

Appendix

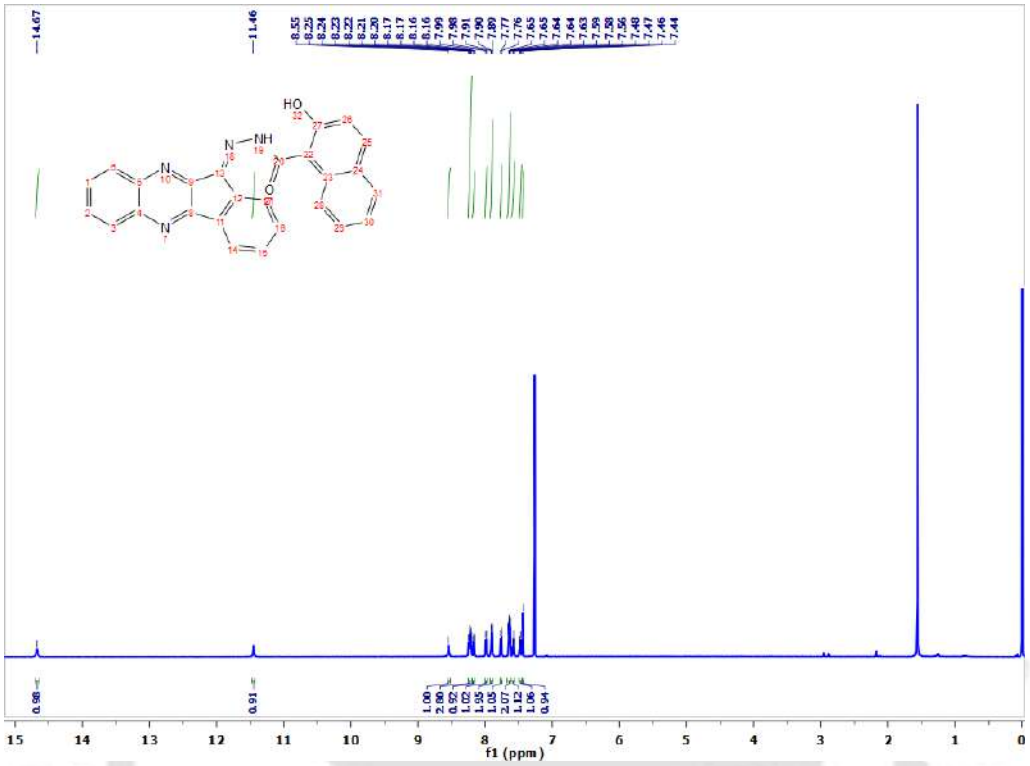

Figure A1. ^{1}H NMR (600 MHz) spectrum of **LH** in $CDCl_3$.

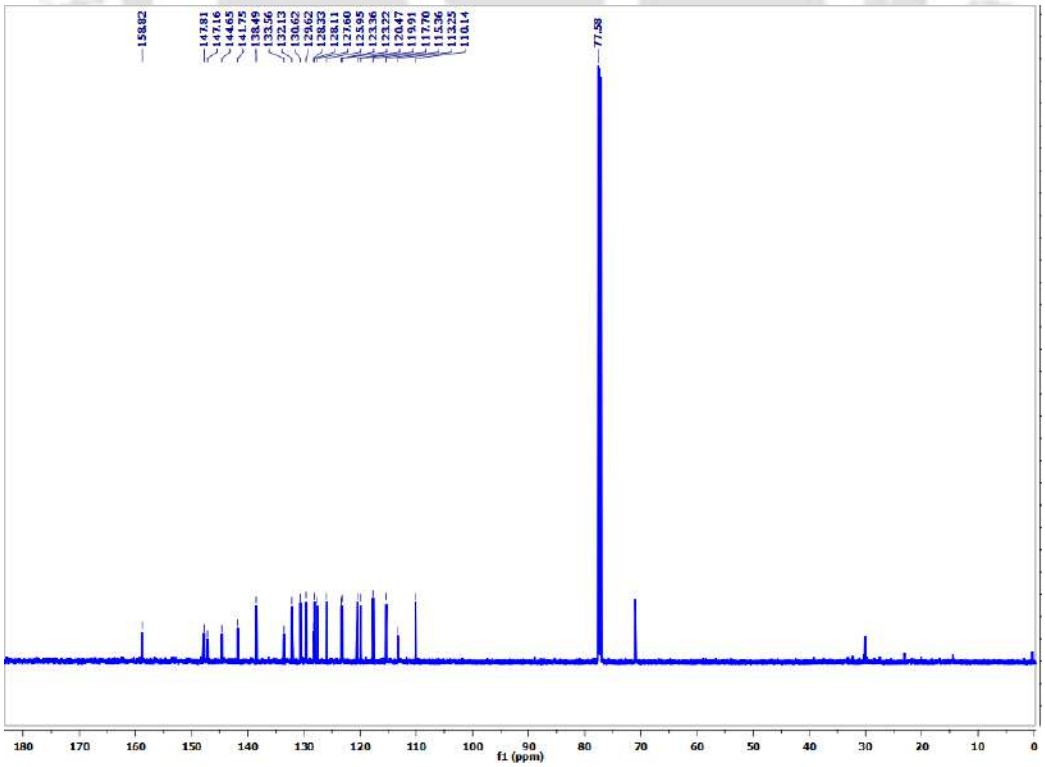

Figure A2. ^{13}C NMR (600 MHz) spectrum of **LH** in $CDCl_3$.

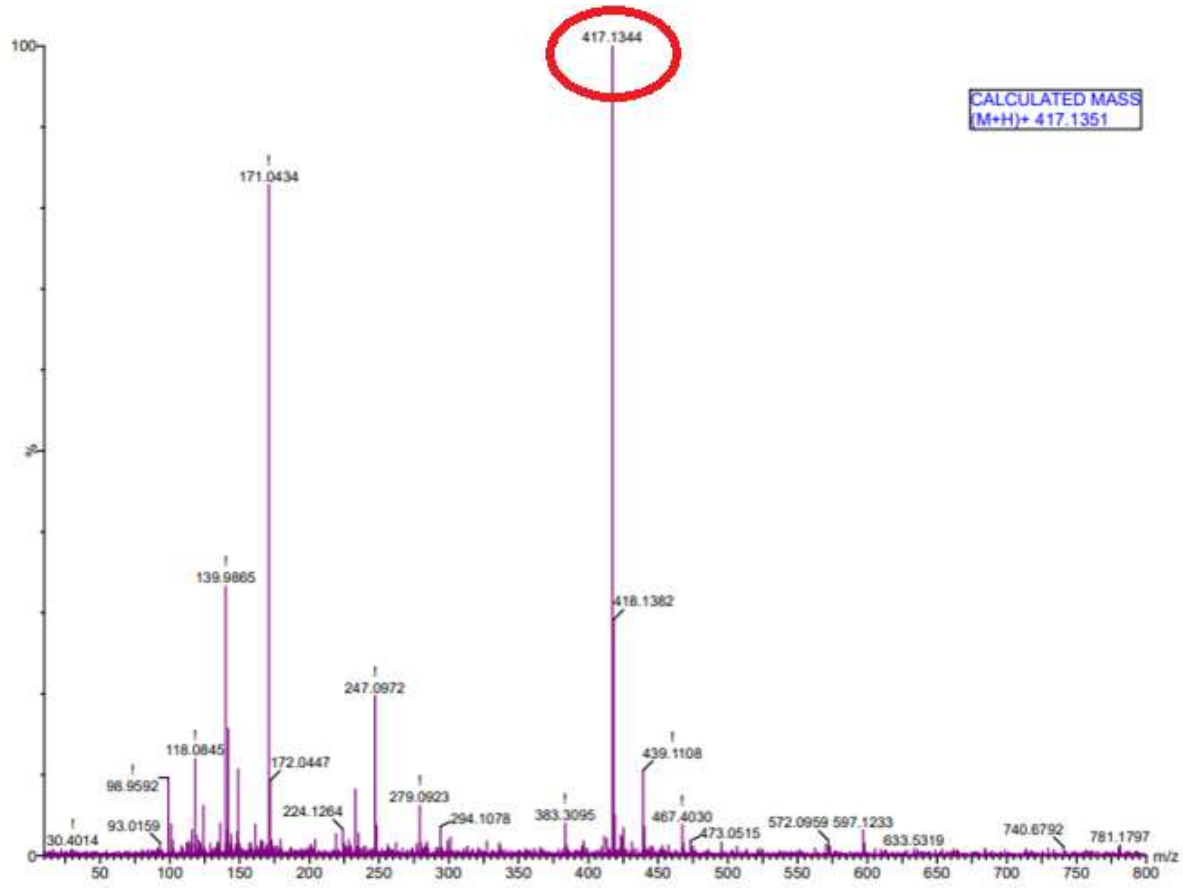

Figure A3. ESI Mass spectrum of **LH**.

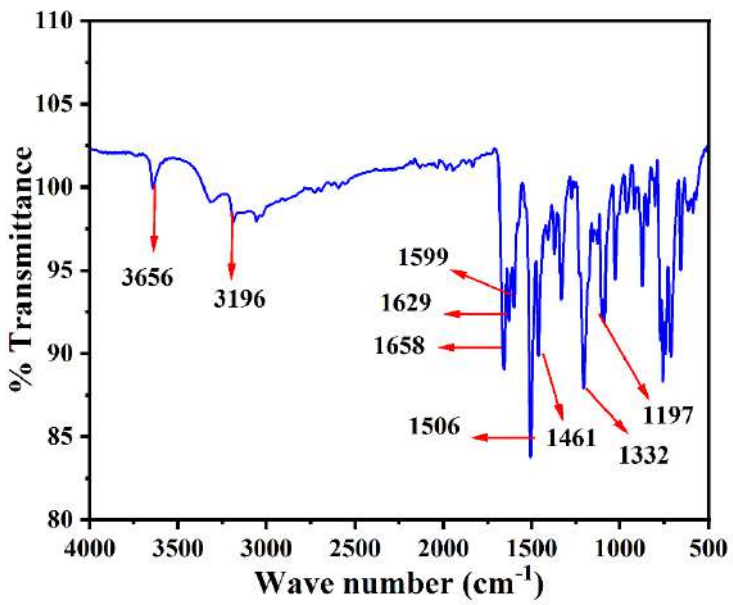

Figure A4. IR spectrum of **LH** in acetonitrile.

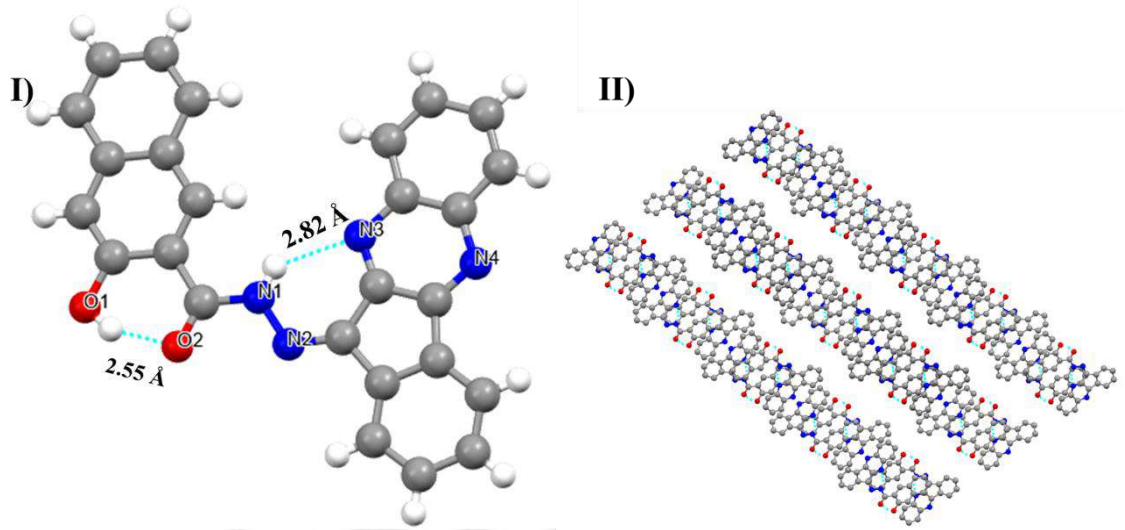

Figure A5. Intramolecular H-bonding interaction within **LH** (I), supramolecular 2D chain of **LH** (II).

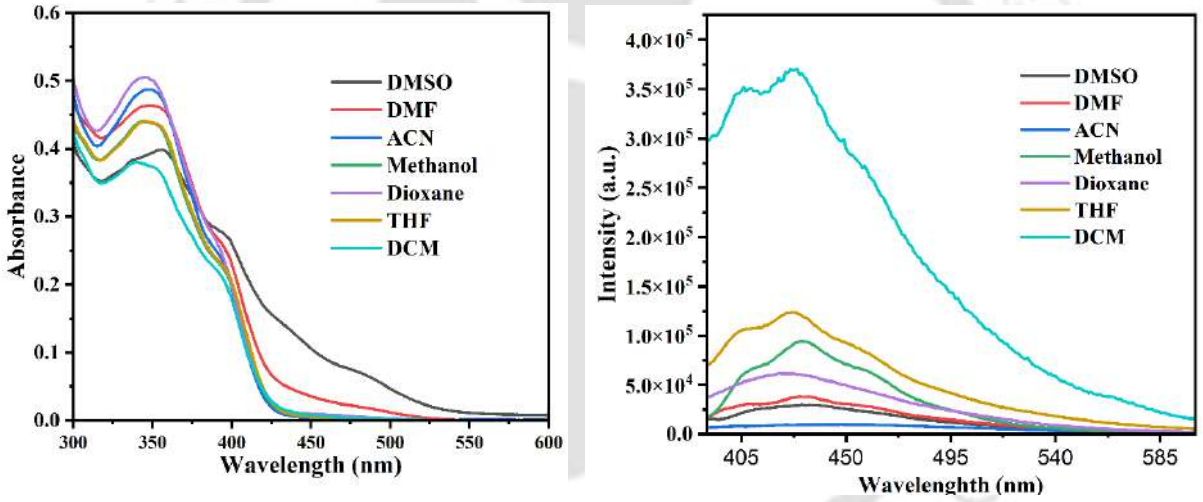

(I) **(II)**

Figure A6. Both (I) absorption and (II) emission spectra of **LH** in various solvents.

Figure A7. Photographs of the spectral colour change of ligand **LH** capture in various solvents.

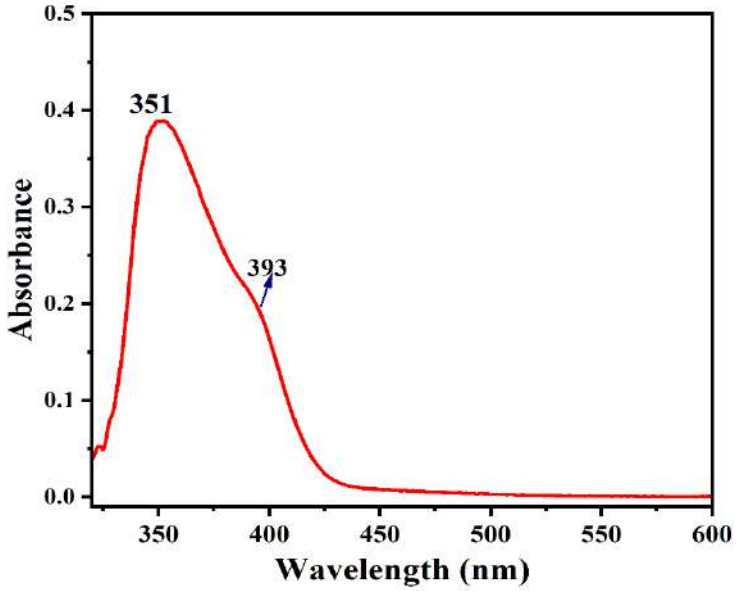

Figure A8. UV-Vis spectrum of chemosensor **LH** in MeOH /HEPES (1:1, *v*/*v*, pH = 7.4).

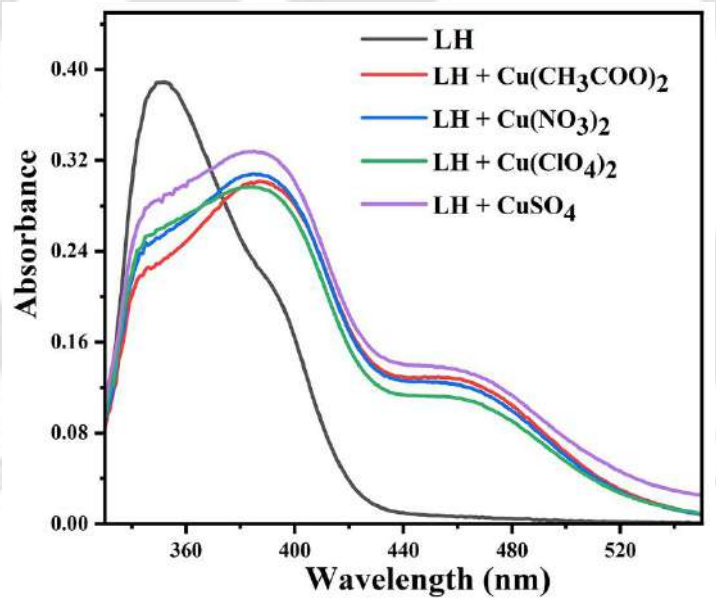

Figure A9. Effect of the presence of different counter ions of Cu^{2+} towards **LH**.

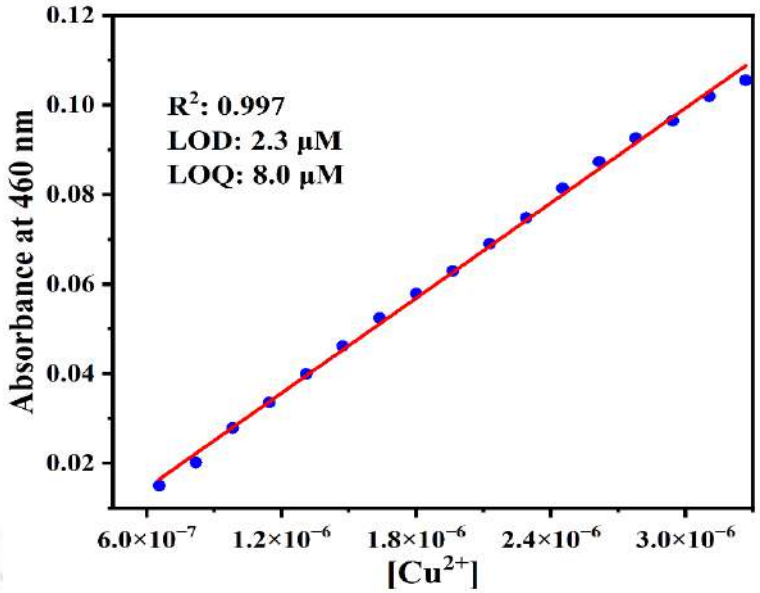

Figure A10. Calculation of LOD and LOQ of **LH** towards Cu^{2+} ion.

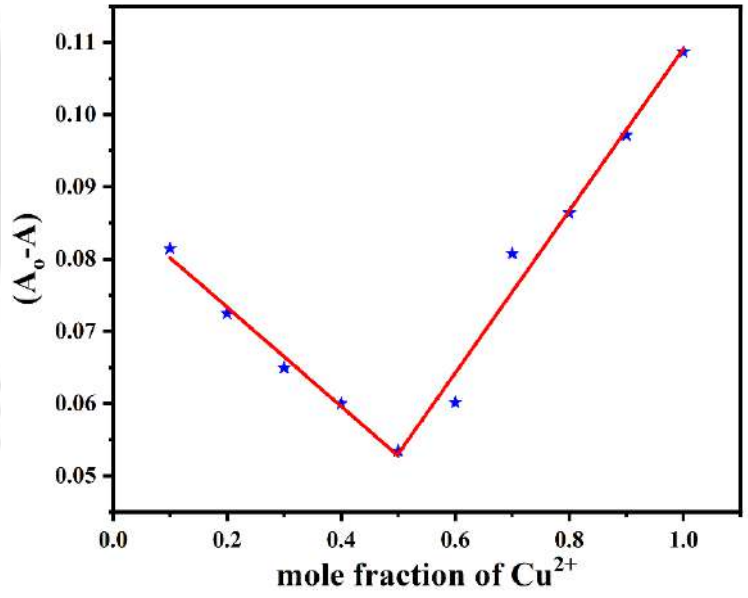

Figure A11. Job's plot of **LH** with Cu^{2+} for the stoichiometry determination monitoring the change of absorbance maximum at 460 nm.

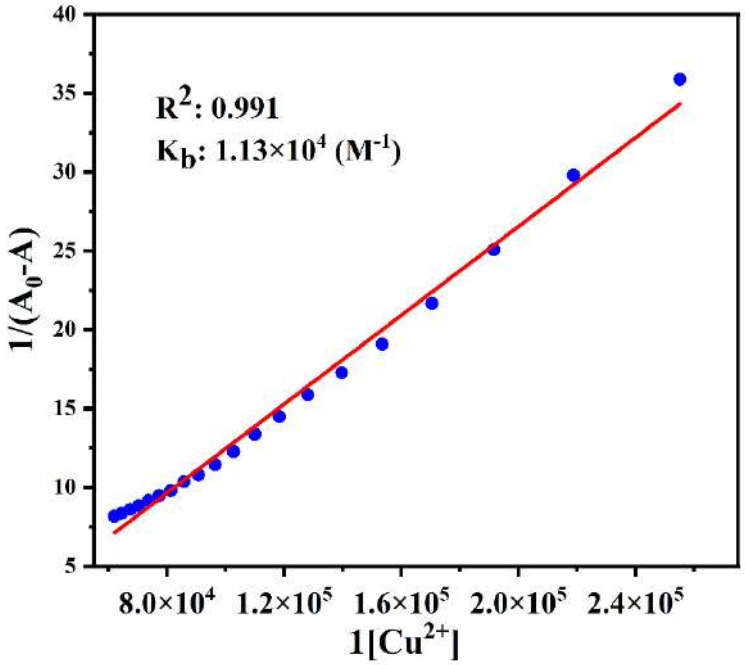

Figure A12. Bensi-Hildebrand plot to determine the association constant of **LH** + Cu^{2+} complex.

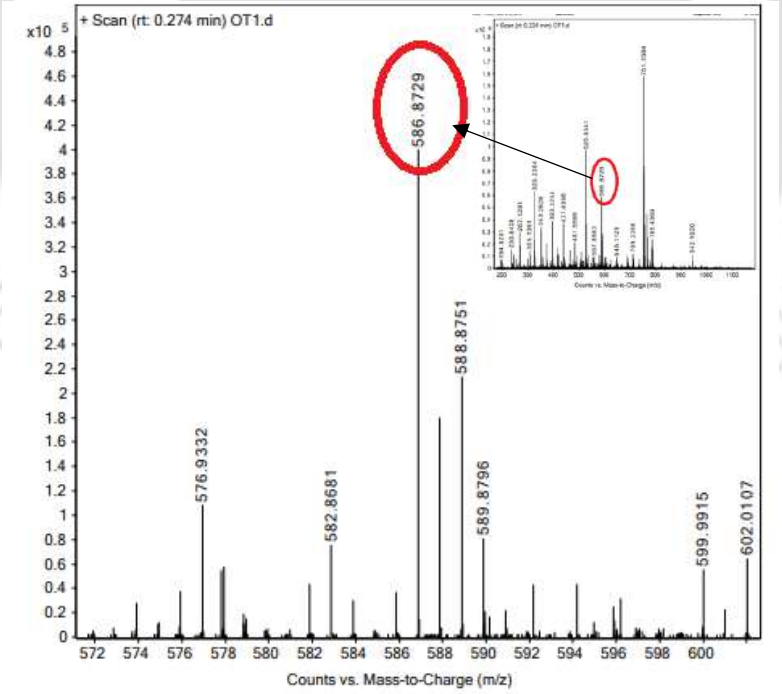

Figure A13. ESI MS mass spectrum (Calcd. *m/z* = 586.0707 for $[Cu(\mathbf{L})Cl(DMF)]^+$ complex ion.

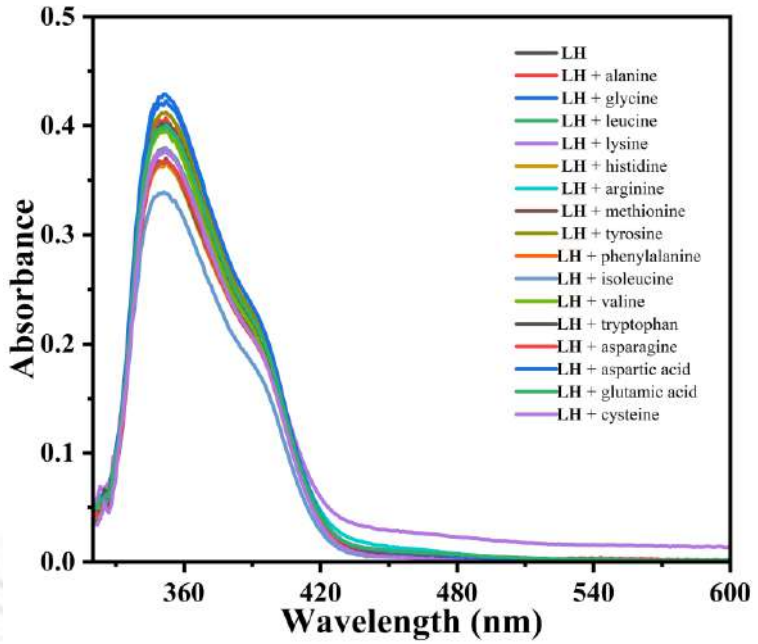

Figure A14. UV-Vis spectral response of **LH** with various amino acids.

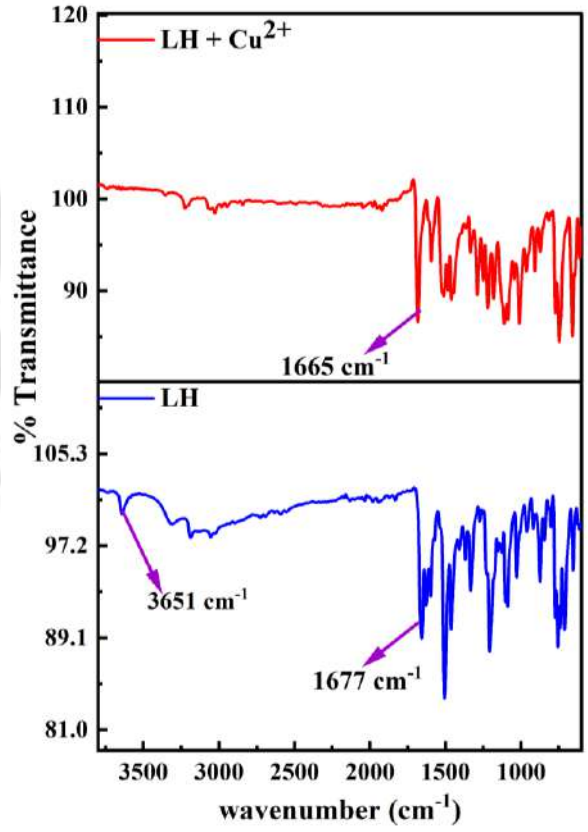

Figure A15. Combined IR spectra of **LH** and **LH** + Cu^{2+} complex.

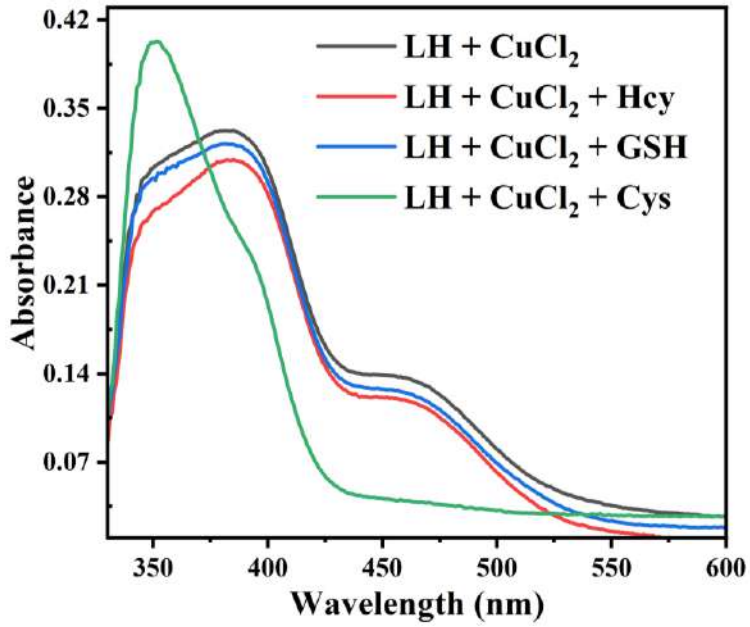

Figure A16. Effect of thiol-containing amino acids on complex **1**.

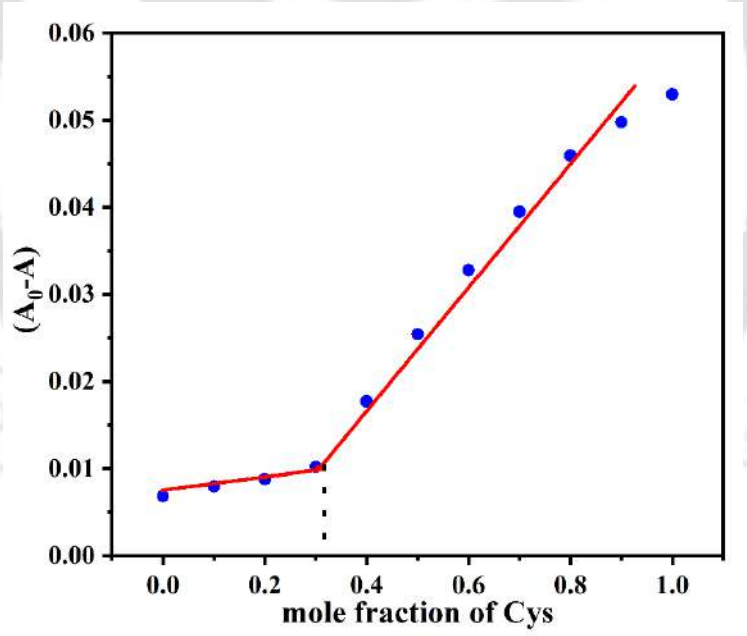

Figure A17. Job's plot of complex **1** with cysteine.

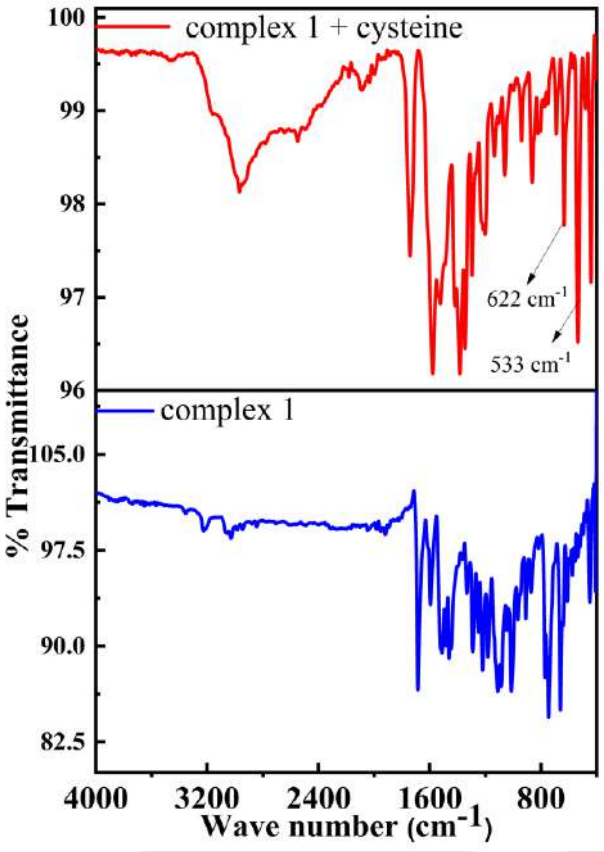

Figure A18. Infrared spectrogram of complex **1** *versus* cysteine.

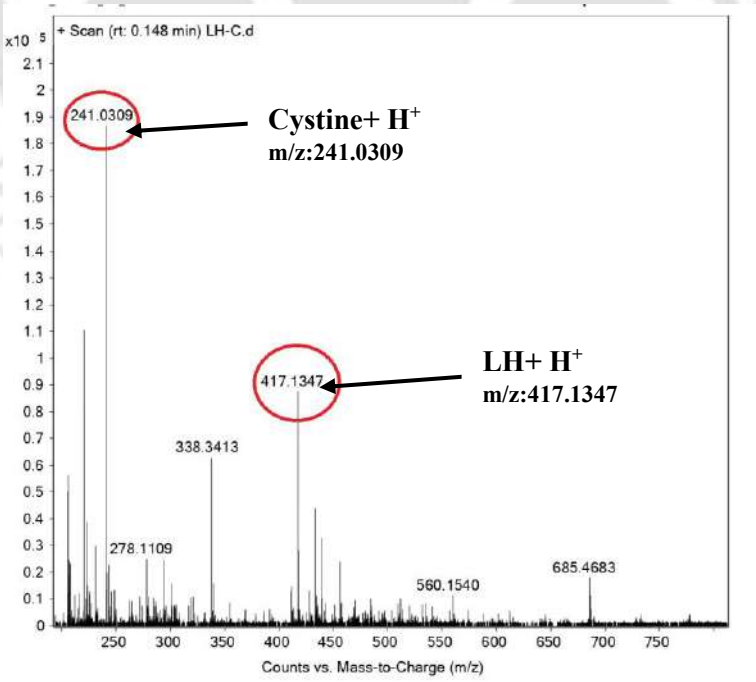

Figure A19. ESI mass spectrum of **1** + cysteine solution.

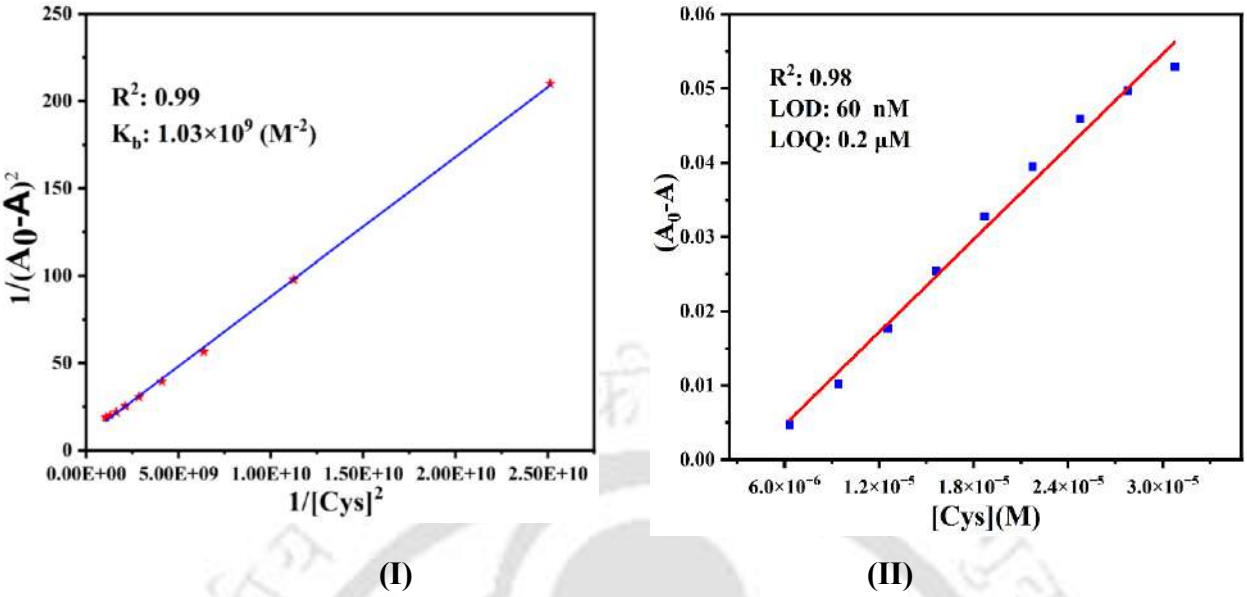

(I) **(II)**

Figure A20. Determination of (I) reaction constant and (II) LOD and LOQ of cysteine with complex **1**.

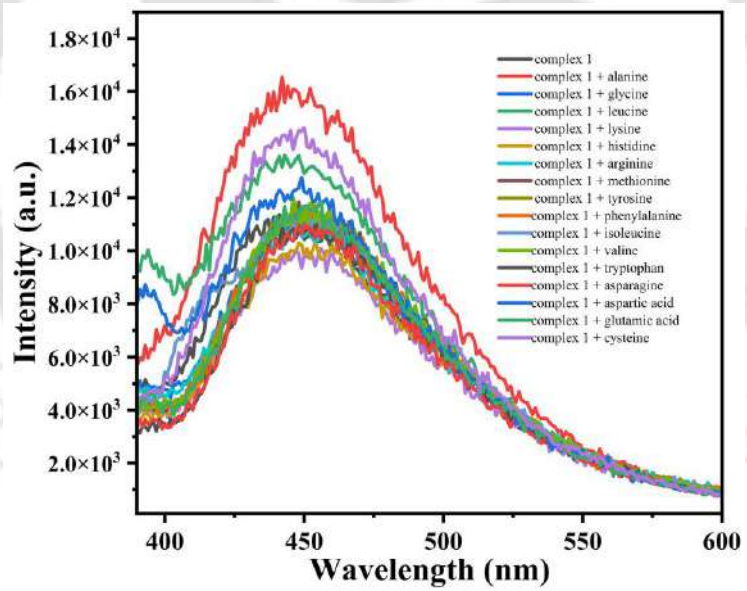

Figure A21. Fluorescence emission spectra of complex **1** against various amino acids.

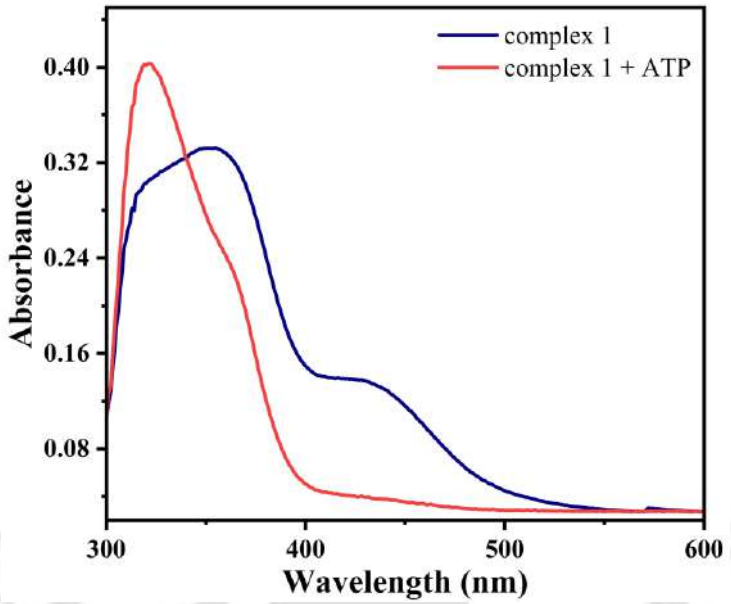

Figure A22. UV-Vis spectra of complex **1** with ATP.

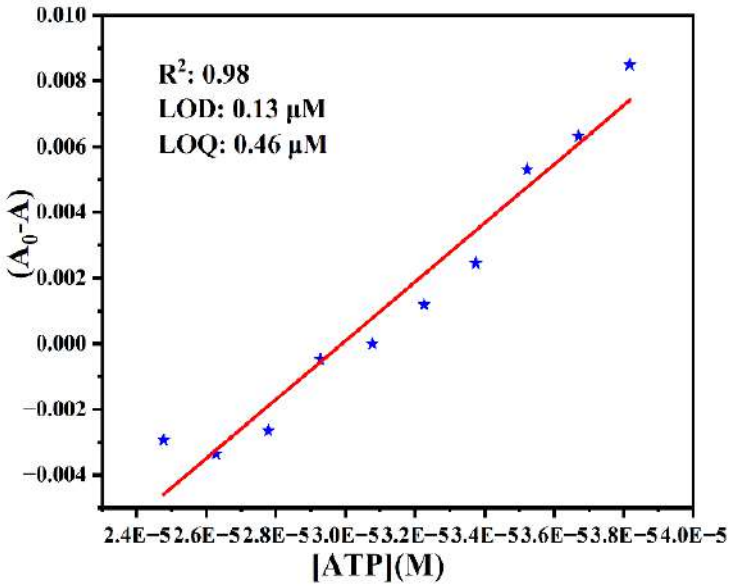

Figure A23. Calculation of LOD and LOQ of ATP.

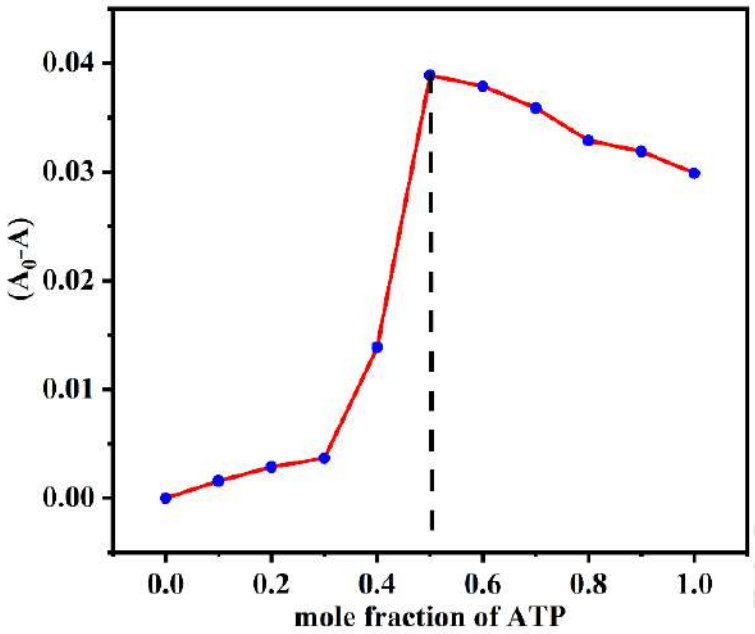

Figure A24. Job's plot of complex **1** with ATP.

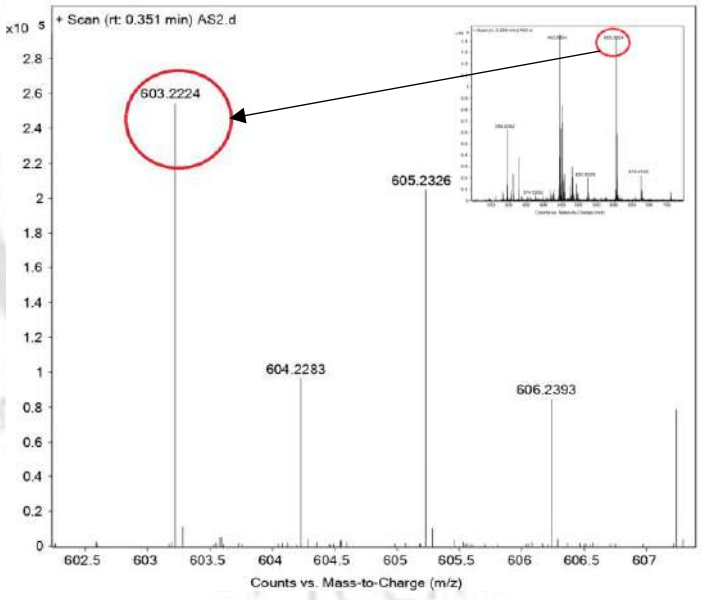

Figure A25. ESI mass spectra Cu-ATP complex. Found = 603.2224, Calculated = 603.2114. (Full range of Cu-ATP complex is shown in the inset).

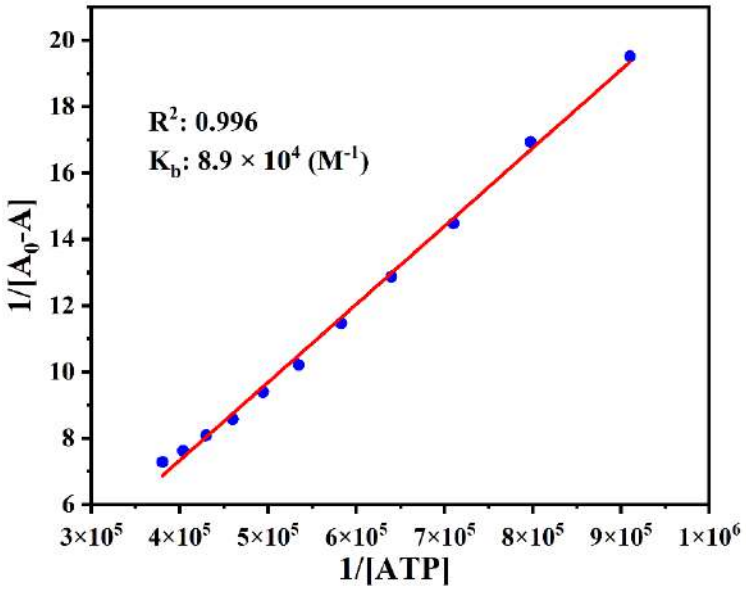

Figure A26. Determination of binding constant of ATP with complex **1**.

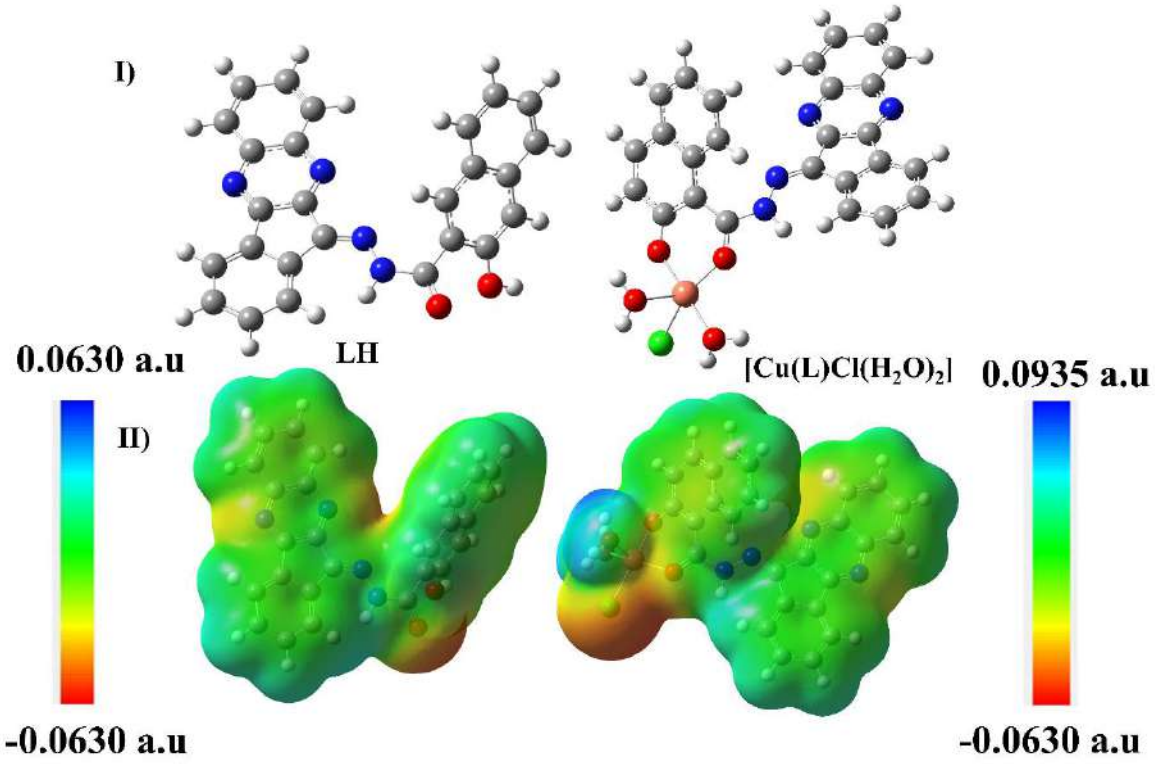

Figure A27. Optimized structure of **LH** and [Cu(**L**)Cl(H_2O)$_2$] complex (I) with its MEP diagrams (II).

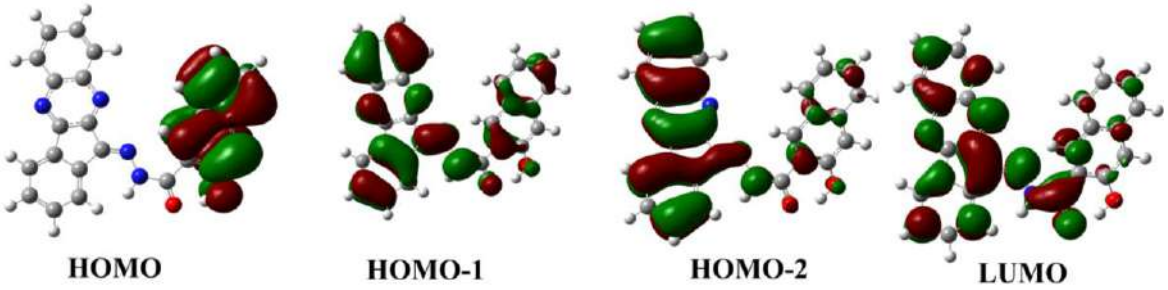

Figure A28. FMOs of **LH** involved in electronic transition.

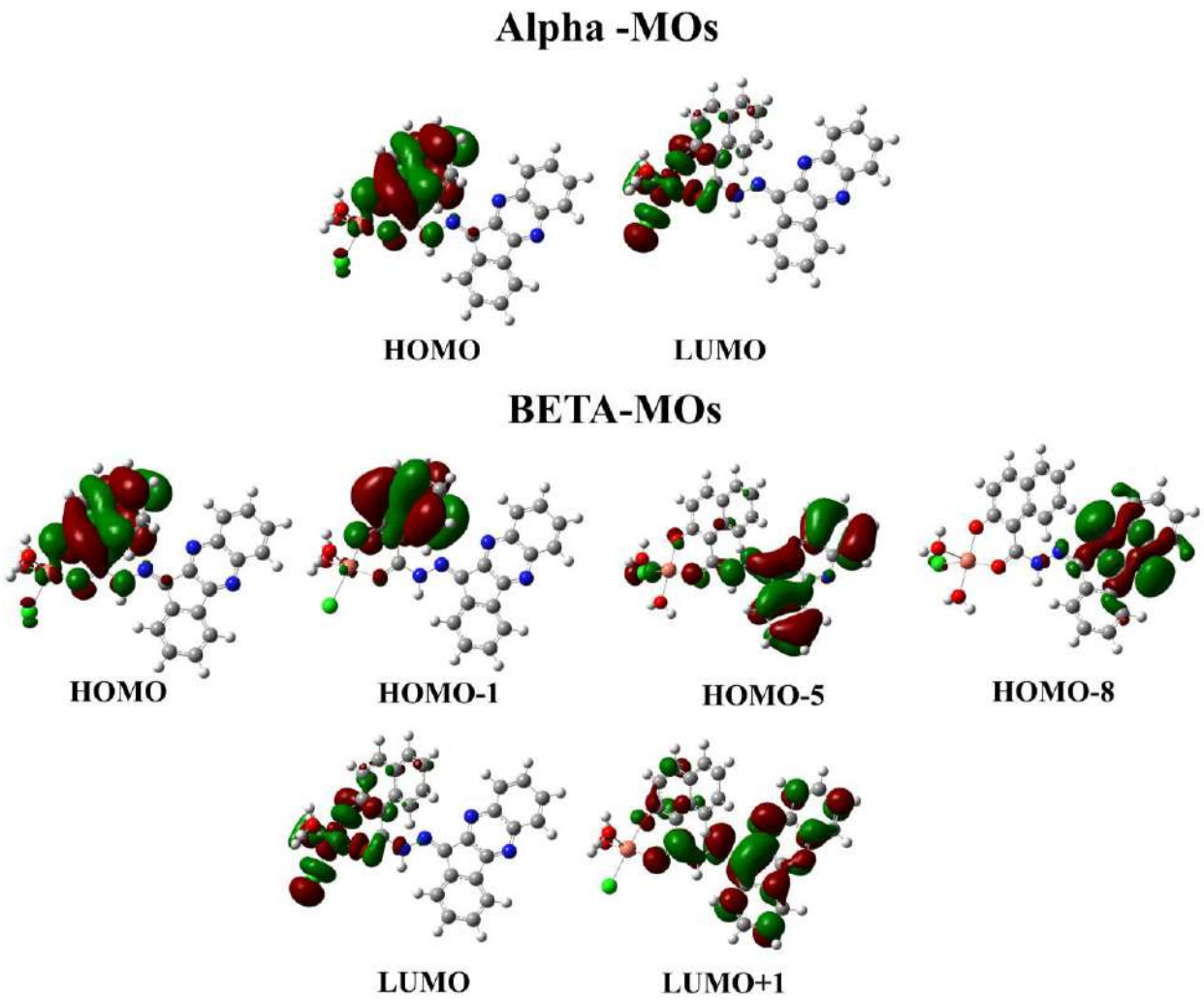

Figure A29. FMOs of [Cu(**L**)Cl(H_2O)$_2$] complex involved in electronic transition.

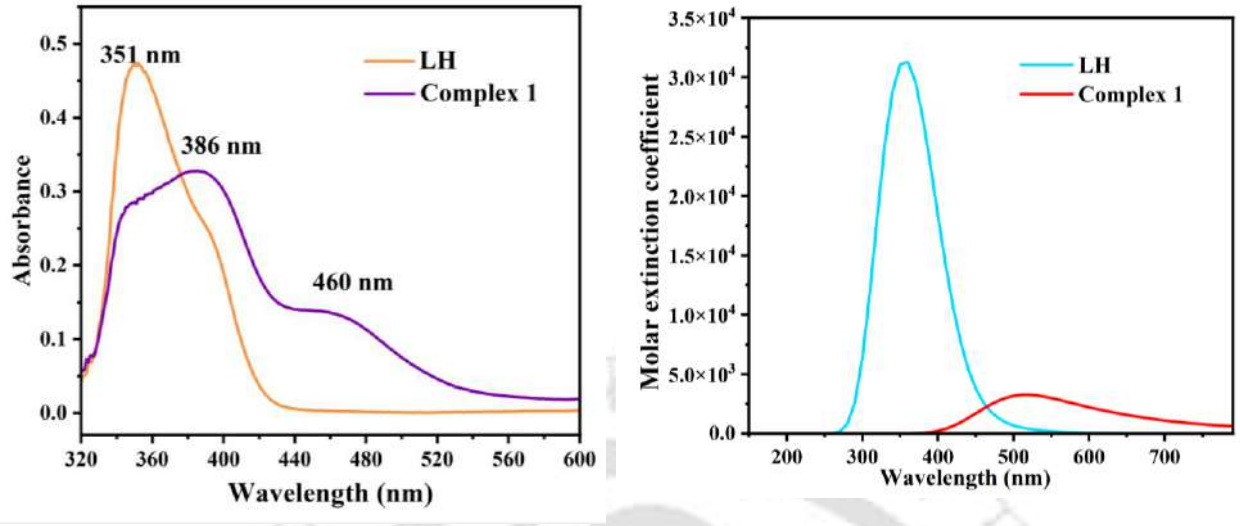

(I) **(II)**

Figure A30. Experimental and theoretical UV-Vis spectrum of (I) **LH** and its (II) [Cu(**L**)Cl(H_2O)$_2$] complex **1**.

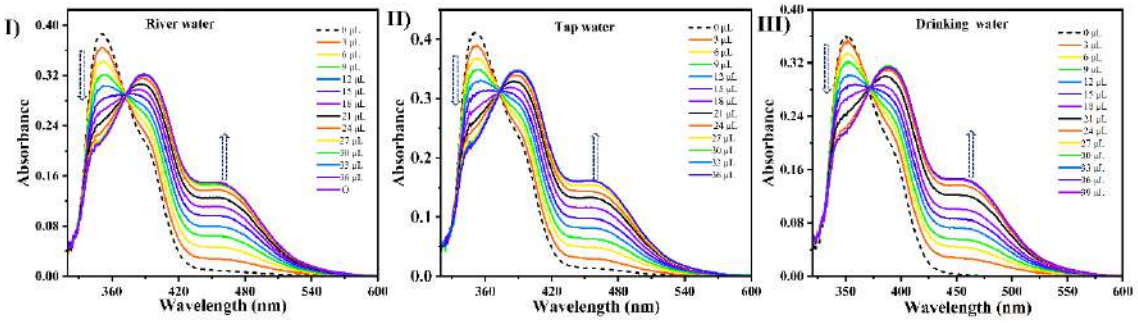

Figure A31. UV-Vis spectral titration of **LH** with $CuCl_2$ in various real water samples like (I) river, (II) Tap, and (III) drinking water.

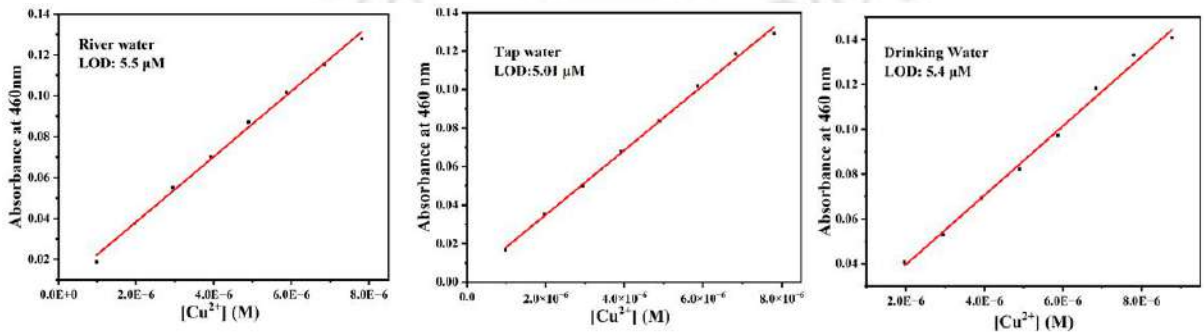

Figure A32. Determination of LOD of Cu^{2+} in all real water samples.

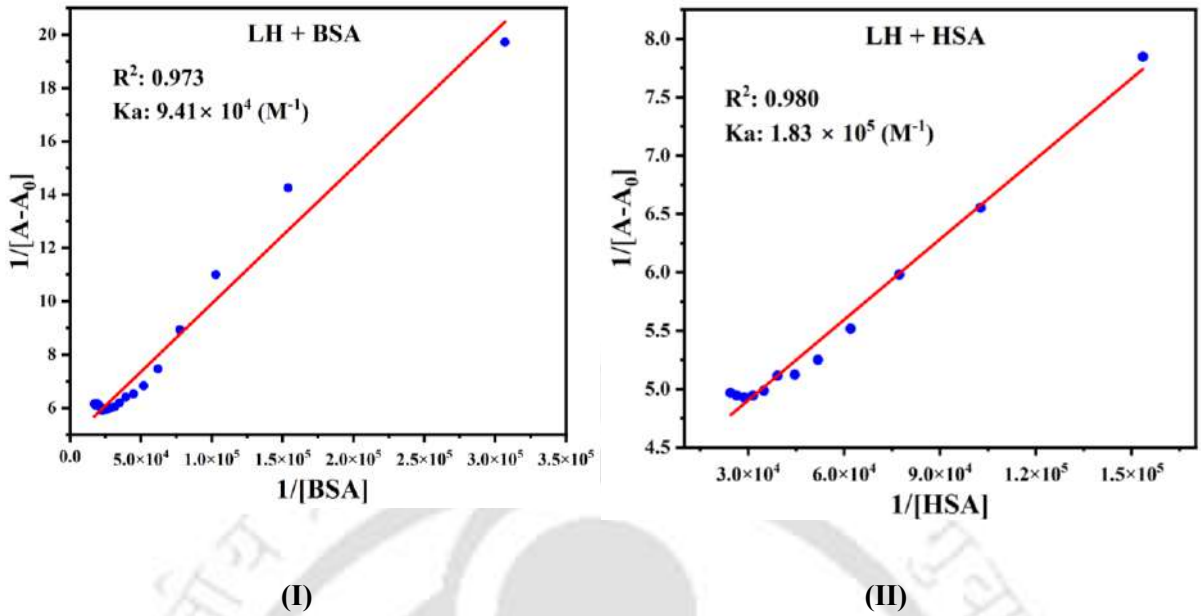

(I) **(II)**

Figure A33. Binding constant calculation for (I) BSA and (II) HSA by using B-H plot.

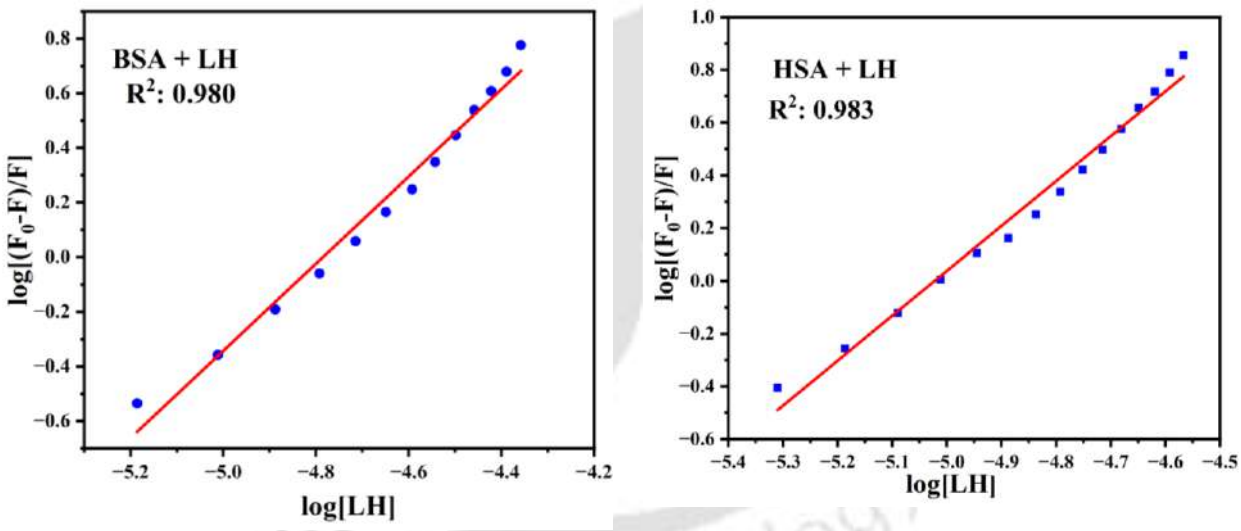

(I) **(II)**

Figure A34. Scatchard plot of log [(F_0 - F)/F] *vs.* log [**LH**] for (I) BSA and (II) HSA with **LH**.

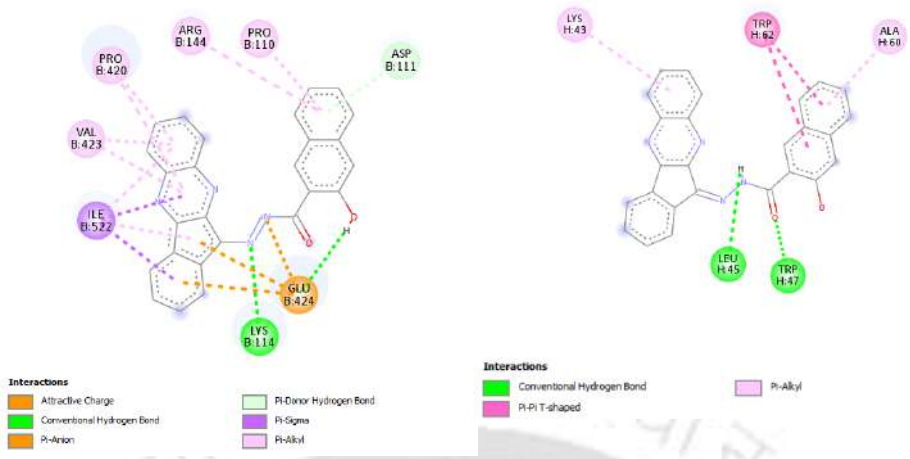

(I) **(II)**

Figure A35. 2D molecular interaction of **LH** with (I) BSA and (II) HSA.

Equation A1 Binding constant calculation for BSA and HSA.

The binding constant (K_b) was calculated by using Bensi-Hildebrand equation from the UV-Vis absorption study:

$$[Biomolecule]/(A-A_0) = 1/ K_b (A_0-A_{min}) [Biomolecule] + 1/ (A_0-A_{min})$$

Where, [Biomolecule] are [BSA] and [HSA], A and A_0 are the absorbance of **LH** in presence and absence of biomolecule and A_{min} is the minimum absorbance of **LH** in presence of biomolecule. K_b was obtained by the ratio of intercept and slope from the plot of $1/(A-A_0)$ *vs.* 1/[Biomolecule].

Equation A2 Quenching constant calculation for BSA and HSA.

The quenching constant (K_q) was calculated by using Stern-Volmer equation from fluorescence study

$$F_0/F = 1+ K_{sv} = [q] + K_q\tau_0[q]\ldots\ldots\text{.}\mathbf{Equation\ A_{2I}}$$

Where F_0 and F are the fluorescence intensity in the absence and presence of probe **LH,** K_q is the bimolecular quenching constant, τ_0 is the average lifetime of BSA/HSA without the probe **LH** which is 10^{-8} sec, [q] is the concentration of biomolecule, and K_{sv} ($M^{-1}s^{-1}$) is the Stern-Volmer quenching constant.

The binding constant (K_b) was calculated by using Scatchard equation from the fluorescence titration study

$\log[(F_0\text{-}F)/F] = n\log[q] + \log K_b$ …….. **Equation A_{2II}**

Where F_0 is the fluorescence intensity of BSA/HSA in the absence of absence of **LH**, F is the fluorescence intensity of BSA in presence of **LH**, [q] is the concentration of **LH**, K_b is the binding constant and n is the no of binding sites.

Table A1. Crystallographic data and structure refinement parameters of **LH**.

Ligand	***LH·CHCl₃***
Empirical formula	$C_{27}H_{17}N_4O_2Cl_3$
Formula weight	535.80
Temperature/K	296 K
Crystal system	Monoclinic
Space group	P 1 21/n 1
a/Å	20.5659(6)
b/Å	7.7381(3)
c/Å	20.5659(8)
α/°	90
β/°	95.418(1)
γ/°	90
Volume/Å^3	2436
Z	4
ρ_{calc}g/cm^3	1.461
μ/mm^{-1}	410
F (000)	1096.0
2Θ range for data collection/°	0.697 to 0.745
Reflections collected	62443
Goodness-of-fit on F^2	1.173
Final R indexes [I>=2σ (I)]	R_1 = 0.0584, wR_2 = 0.1819.

[a]GOF (Goodness-of-fit) = $[\sum[w(F_0^2 - F_c^2)^2] / M - N]^{1/2}$ (M =number of reflections, N = number of parameters refined). [b] $R_1 = \sum \| F_0 | - | Fc \| / \sum | F_0 |$. [c]$wR_2 = [\sum[w(F_0^2 - F_c^2)^2] / \sum[w(F_0^2)^2]]$.

Table A2. Changes in (λ_{abs}) and (λ_{emi}) with stokes shift value of **LH** in various solvents.

Solvents	*λ_{abs} (nm)*	*λ_{em} (nm)*	*Stokes shift (nm)*
DMSO	353, 395	433	80
DMF	349, 397	436	87
Acetonitrile	348, 394	432	84
MeOH	345, 393	428	83
Dioxane	343, 390	426	83
THF	340, 395	428	88
DCM	338, 393	446	108

Table A3. Calculated energy level having higher oscillator strength (f = 0.4329) in **LH**.

Electronic transition	*Assignment*		*Transition contribution (%)*	*Energy (ev)*	*Wavelength (nm)*
	from	**to**			
$S_0 \rightarrow S_4$	HOMO-1	LUMO	45%	3.2970	376.06
	HOMO-2	LUMO	51%		

Table A4. Calculated energy level having higher oscillator strength (f = 0.0620) in [Cu(**L**)Cl(H_2O)$_2$] complex.

Electronic transition	*MOs*	*Assignment*		*Transition contribution (%)*	*Energy (eV)*	*Wavelength (nm)*
		from	*to*			
$S_0 \rightarrow S_9$	Alpha	HOMO	LUMO	66.12%	2.4575	504.52
		HOMO-8	LUMO	12.67%		
	Beta	HOMO-5	LUMO	16.77%		
		HOMO-1	LUMO	32.50%		
		HOMO	LUMO+1	61.71%		

Table A5. Measured data of various real water samples.

Real water Sample	*Cu^{2+} spiked (μM)*	*Recover %*
River	6	92
Tap	6	99
Drinking	6	98

Table A6. A comparison table of recently published chemosensors suitable for detecting analyte like Cu^{2+}, cysteine and ATP.

SL NO	*Structure of chemosensor*	*Analyte detected*	*LOD*	*Response time*	*Paper -strip test*	*Logic gate fabrication*	*Biomolecule interaction*	*Ref*
1	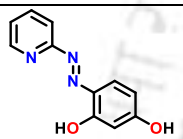	Cu^{2+} Cys	31.5 nM 72.0 nM	No data	NO	Yes	NO	55
2	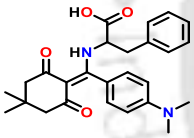	Cu^{2+} Fe^{3+} Cys Trp	6.37 μM 2.29 μM 2.29 μM 9.35 μM	No data	NO	NO	NO	56
3	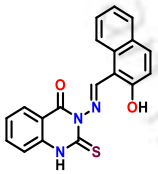	Cu^{2+} Cys	20 nM -	No data	NO	NO	NO	57
4	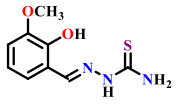	Cu^{2+} Hg^{2+} Asp	17 nM 0.13 μM 87 nM	No data	NO	NO	NO	58
5	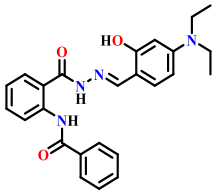	Cu^{2+} Cys	0.37μM 5.86 μM	No data	NO	Yes	NO	59
6	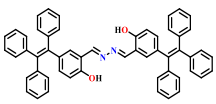	Cu^{2+} Zn^{2+} ATP	0.25μM 5.86 μM 0.42 μM	No data	Yes	No	NO	60

7	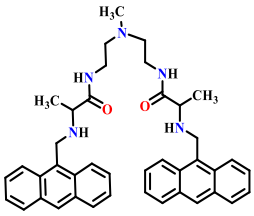	Cu^{2+} ATP	- 11 μM	No data	No	No	NO	61
8	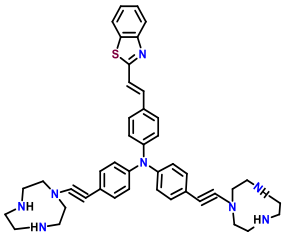	Cu^{2+} ATP	40 nM 43 nM	No data	No	No	NO	62
9	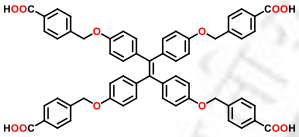	Cu^{2+} ATP	4.5nM 42.3nM	No data	Yes	No	NO	63
10	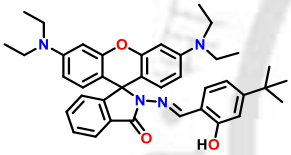	Cu^{2+} ATP	0.1 μM 1 μM	No data	No	No	NO	64
11	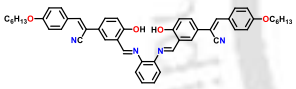	Cu^{2+} ATP	0.1 μM 1 μM	No data	No	No	NO	65
12	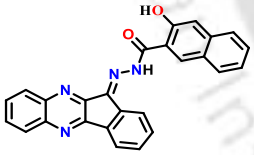	Cu^{2+} Cys ATP	2.3 μM 60 nM 0.13 μM	50 sec for Cu^{2+}	Yes	Yes	Yes	This work

Table A7. Docking results for the favourable conformer.

Biomolecule	***Amino Acid Residue***	***Binding energy (kcal/mol)***
BSA	PRO 492, ARG 412, LYS 413, ARG 409, SER 488	-7.12
HSA	LEU 189, ILE 141, ARG 144, LEU 112, LYS 114, LEU 115, LYS 116, ARG 185	-8.39

Chapter 3

Aggregation Induced Emission Active Pyrene Scaffold for Real-Time Chromogenic and Fluorogenic Selective Detection of Pd^{2+} Ion and Device Fabrication*

Abstract:

A fluorogenic and chromogenic probe (**L_1**) bearing pyrenyl and naphthyl group was synthesized using 4-(naphthalen-1-yl) thiosemicarbazide and pyrene-1-carboxaldehyde. Sensor (**L_1**) exhibited significant aggregation induced emission (AIE) property in 7:3 water-EtOH mixture and the aggregated form exhibited a yellowish-green fluorescence upon excitation with 380 nm light. Upon adding Pd^{2+} ion, colorless EtOH/aqueous HEPES buffer (3:7, *v/v*) solution of **L_1** showed a sharp change to bright yellow as well as fluorescence turn-off response. Probe displayed high selectivity, sensitivity, rapid response time (50 s) and good pH tolerance range (5-8). Sensing was reversed in presence of triphenylphosphine. The detection limit of Pd^{2+} was 41 nM (7.2 ppb) which was lower than the WHO recommended value. Mass spectrum and Job's plot revealed 1:1 binding ratio. Both FESEM and DLS studies manifested the decrease of particle size upon interaction of **L_1** with Pd^{2+}. ^{1}H NMR titration data were consistent with binding of Pd^{2+} to nitrogen atom of (–CH=N–) group and IR spectra revealed coordination by sulphur of carbothioamide group. DFT/TDDFT calculations performed on **L_1** and [Pd(**L_1**)$(NO_3)_2$] supported the experimental results very well. Probe **L_1** was also found to be suitable for the recognition of Pd^{2+} in real water and pharmaceutical drug samples. Paper strips for on-spot analysis and testing and a symmetric 2D sensor device were also constructed.

* This work has been published in:

A. Mondal, V. Manivannan, *Spectrochim. Acta A Mol. Biomol. Spectrosc.*, 2025, **333**, 125865.

3.1 Introduction:

The development of organic fluorophores displaying aggregation-induced emission (AIE) behaviour either in solid or exhibiting aggregation in solution has gathered attention because of their utility in solar cells, OLEDs, OFETs, laser dyes, and so on.[1–4] AIE based fluorophores were usually weakly emissive in good solvents (usually organic solvents) but exhibited intense emission in poor solvents like water or buffer due to molecular aggregation.[5–7] For such AIE active molecules, the primary mechanism of AIE was the restriction of intermolecular motion (RIM),[8] which included both vibrational and rotational motion (RIV and RIR).[9] Many Schiff base compounds exhibiting AIE behaviour have not only been exploited for the detection of transition metal ions[10] and biomolecules, but also been used in bio-imaging and as phototheranostic agents in cancer treatment.[11–13]

Heavy metal ions like Cd(II), Hg(II), As(III), and Pd(II) were reported to be toxic and cause carcinogenicity.[14,15] Palladium has been used in a variety of sectors including electronics, medical devices, dentistry, fuel cells, and jewellery[16–20] also as an essential industrial catalyst for coupling reactions. Presence of Pd^{2+} in the environment was linked to cause diseases because it can easily form complexes with proteins, biomolecules, and enzymes[21] resulting in memory loss, allergic reactions, severe skin infection, gum disease and others.[22–24] According to the World Health Organisation (WHO), the permissible concentration of Pd^{2+} in any pharmaceutical products was 5-10 ppm and tolerable intake was 2 µg per day.[25,26]

Recently, probes bearing chromone,[27] benzothiazole,[28] coumarin,[29] rhodamine,[30] and fluorescein[31] functions have been explored as optical chemosensors based on fluorometric and colorimetric techniques for Pd^{2+} detection, due to its less cost, easily affordable, straightforward, and field employable methodology.[31,32] Compounds having pyrenyl group were found to act as a AIE based sensor and gained attention because this ring can show increased chemical stability,[33] high fluorescence lifetime,[34] higher charge carrier potentiality,[35] quick response time[36,37] and can display π–π stacking interactions by virtue of its planar ring.[38,39] In this Chapter, an AIE active probe **L_1** having pyrenyl and napthyl rings for the selective recognition of Pd^{2+} ion has been described along with its practical utility.

3.2 Experimental Section:

3.2.1 Synthesis

*4-(naphthalene-1-yl) thiosemicarbazide (**L**)*

Compound **L** was synthesized using the previous literature procedure.[40] In a 100 mL round-bottom flask, 1.85 g (10 mmol) of naphthyl isothiocyanate was dissolved in 50 mL of dry ethanol. After that, excess hydrazine hydrate (30 mmol, 0.9 mL) was added to the solution all at once. The mixture was stirred under ice-cold conditions for 3 hours, then the precipitate was filtered and washed three times with 6 mL of diethyl ether. A colorless solid was obtained by drying the precipitate under vacuum over silica gel. Yield 85%.

N-(naphthalen-1-yl)-2-(pyren-1-ylmethylene)hydrazine-1-carbothioamide (**L_1**)

L_1 has been prepared by a slight modification of the literature procedure[41] and shown in Scheme 1. To 4-(naphthalene-1-yl) thiosemicarbazide (**L**) (0.217 g, 1 mmol) dissolved in methanol (15 mL), pyrene-1-carboxaldehyde (0.230 g, 1 mmol) was added and refluxed for 4 h. The mixture was left at room temperature over-night, pale-yellow precipitate deposited was recovered by filtration and washed with ice-cold methanol, dried in a desiccator. Yield: 0.415 g (83%). M.P.: 302 °C. 600 MHz ^{1}H NMR (δ (J, Hz), DMSO-d_6): 12.03 (1H, s), 11.60 (1H, s), 9.45 (1H, s), 9.12 (1H, d, J = 9.5), 8.55 (1H, d, J = 11.1), 8.37 (3H, m), 8.32 (1H, d, J = 9.9), 8.25 (2H, q), 8.12 (1H, t, J = 9.18), 8.01 (1H, m), 7.94 (2H, m), 7.57 (4H, m). 600 MHz ^{13}C NMR (δ, DMSO-d_6): 178.2, 140.9, 136.2, 134.1, 132.3, 131.3, 131.0, 130.6, 129.3, 129.2, 128.7, 128.5, 127.9, 127.4, 127.3, 127.0, 126.9, 126.6, 126.5, 126.5, 126.2, 125.9, 125.6, 124.8, 124.5, 124.3, 123.9, 122.0. MS (ESI +ve) *m/z* calcd. For $C_{28}H_{19}N_3S$ $[M+H]^+$ 430.1355; found: 430.1382. Selected IR (ATR mode, cm^{-1}): 3313 (ν_{N-H}), 3181 (ν_{C-H}), 1549 ($\nu_{C=N}$), 823 ($\nu_{C=S}$) (Figure A1-A4).

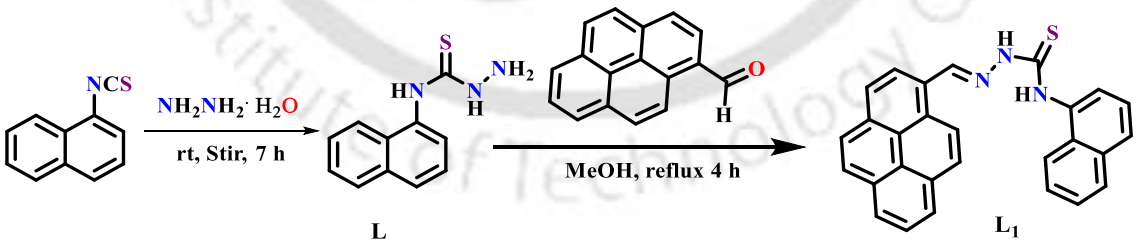

Scheme 1. Synthesis route of **L_1**.

3.2.2 Preparation of Drug Samples

Different active pharmaceutical ingredients (API) like telmisartan, valsartan, olmesartan medoxomil, and losartan potassium were purchased from commercial source and used without any further purification. All drug samples were prepared by 10 mg of the drug in HPLC grade DMSO. The overall UV-Vis titration experiment was carried out in 70% EtOH-HEPES buffer

solution in the four test samples of the drug (0.5 mg) to obtain the calibration plots. To perform the recovery test, 150 µL of predetermined $PdCl_2$ solution was spiked into the drug solution, followed by the addition **L1** (1 mM) solution. By recording the following absorbance value, the unknown concentration of Pd^{2+} was calculated in the corresponding spiked solutions. Besides these other practical applications of **L1** were also monitored in different real water samples like river, lake, and tap water respectively. A series of Pd^{2+} solutions were prepared from (7.0 and 9.0 µM) to acquire the recovery test for Pd^{2+} detection. The absorbance values were measured at 451 nm.

3.2.3 Device Fabrication Technique

The two terminal electrical devices were fabricated on Si/SiO_2 substrate. Firstly, the Si/SiO_2 substrate was cleaned in acetone, propanol, and distilled water sequentially in ultra-sonication bath for 10 min each. Then the two gold (Au) contact pads were deposited using a thermal evaporation system (Auto 500, HHV) at 4.0×10^{-6} mbar pressure and shadow mask. The probe solution (1 mM/ 2 µL) with and without Pd^{2+} ion was drop cast several times between the contact pads to ensure proper contact. Finally, electrical measurements of the fabricated device were carried out using a Keithley 4200 SCS source meter under room light illumination in the voltage range -20 to +20 V at room temperature.

3.3 Results and Discussion:

3.3.1 X-Ray Crystallographic Study

The single crystals of **L1** was obtained by slow evaporation of its DMF solution, which crystallized in $P2_1/c$ space group (Table A1). The hydrazine-1-carbothioamide moiety separated two aromatic pyrene and naphthalene rings, rendering them delinked from each other. In this moiety, bond distances C17–N1, 1.271(4) Å (C=N) and C18–S1, 1.677(3) Å (C=S) were comparable with reported values.[42,43] Within **L1**, two planar pyrene and naphthalene rings were tilted by an angle of 50.98° with respect to each other. Intermolecular π···π stacking interactions were present between two pyrene and two naphthalene rings with an inter-planar distance of 3.43 and 3.47 Å, respectively. Two **L1** molecules were juxtaposed such that intermolecular H-bonding interactions existed involving hydrazonyl-NH and -C=S groups with N2···S1 = 3.388(3) Å. This also resulted in formation of a H-bonded dimer (Figure A5I) and a wave-like supramolecular pattern was also observed (Figure A5II). The ORTEP diagram of **L1** has been provided in Figure 1.

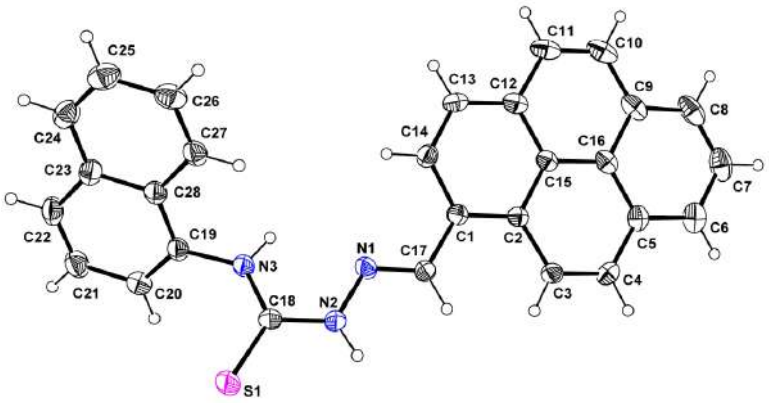

Figure 1. ORTEP plot of **L1** with 30% probability.

3.3.2 Spectra

The UV-Vis spectral absorption and photoluminescence properties of **L1** have been monitored in eight different solvents with varying polarity and observed spectral details were provided in Table A2 and Figure A6. The probe **L1** was highly soluble in DMSO and DMF but was only sparingly soluble in THF, chloroform, methanol, acetonitrile, ethanol and dioxane, but was insoluble in water. In EtOH, **L1** exhibited two bands having their peaks at 381 and 405 nm which are due to π–π* transitions originating from naphthyl and pyrenyl rings respectively. There were no noticeable changes in the spectrum when recorded in other solvents noted above except for water. However aliquot of DMF solution of **L1**, when diluted with water, two peaks originally observed at 381 and 405 nm got shifted to 393 and 425 nm. Spectra were also recorded in varying ratios of EtOH:H_2O (in increments of 10% starting from 10:0). The 3:7 EtOH:H_2O ratio was found to be best suited with a significant change in the spectra was observed *viz*., with the peaks shifted to 370, 397 and 434 nm (Figure 2A), due to formation of nano-aggregates of **L1** and the light scattering phenomenon getting developed in the semi-aqueous medium.[44,45] In pure ethanol, **L1** exhibited a weak fluorescence with the maximum at 445 nm (λ_{ex} = 380 nm), having the quantum yield of 0.5%. Upon increasing water content gradually (in increments of 10%) from 10:0 EtOH:H_2O to 3:7, the emission maximum shifted to 465 nm (Figure 2B) accompanied by an increase in the fluorescence intensity to an extent of 2.8 times having the quantum yield of 2.2% (Figure A7). The reason behind the enhancement of emission intensity was due to aggregation induced restriction of intramolecular rotation around the imine group resulting in increased number of intermolecular interaction which in turn suppressed the non-radiative pathway.[46,47] Formation of J-type nano-aggregates[48] in 3:7 EtOH:H_2O mixture was inferred from the distinct bathochromic shift of 445 nm peak to

465 nm ($\Delta\lambda$ = 20 nm). Such aggregates were found in the crystal packing diagram as non-parallel head to tail stacking of individual molecules (Figure A8). Thus in combination of good solvent (ethanol) and bad solvent (water), **L_1** can be a potential AIE active probe for detection of analytes using UV-Vis and fluorescence spectroscopies.[49] Fluorescence time-resolved photoluminescence (TRPL) plots and changes observed visually as a yellow-green fluorescence were provided in Figures 2C and 2D. Notably, the measured fluorescence lifetime was increased from 0.08 ns (in 0% H_2O) to 1.58 ns (in 50% H_2O) to 2.05 ns (in 70% H_2O) as in Table A3. Thus, the above-mentioned photophysical measurements showed a positive AIE effect. In DLS measurements average particle size diameter (Figure A9) of **L_1** increased from 110 nm (EtOH) to reach the maximum of 1231 nm (3:7 EtOH:H_2O) which decreased to 927 nm (2:8) and finally to 110 nm (H_2O), and such observation was also reported earlier.[50] To explain the patterns of aggregation, the FESEM images for **L_1** in various H_2O-EtOH mixtures was collected (Figure 3). In EtOH, **L_1** exhibited "thin root" like morphology and in 3:7 H_2O-EtOH mixture, the morphology changed to fibrous ribbon shape which further aggregated in 7:3 H_2O-EtOH to extensive fibrous network. The average particle size of **L_1** was 49 nm (in pure EtOH), which increased to 86 nm (in 3:7 H_2O-EtOH) and further increased to a maximum of 128 nm (in 7:3 H_2O-EtOH), as highlighted in Figure 3 and Figure A10. Thus, **L_1** became fluorescent due to formation of the AIE aggregates in 7:3 mixture and hence can be potential turn-off fluorescent sensor for metal ions in solution.

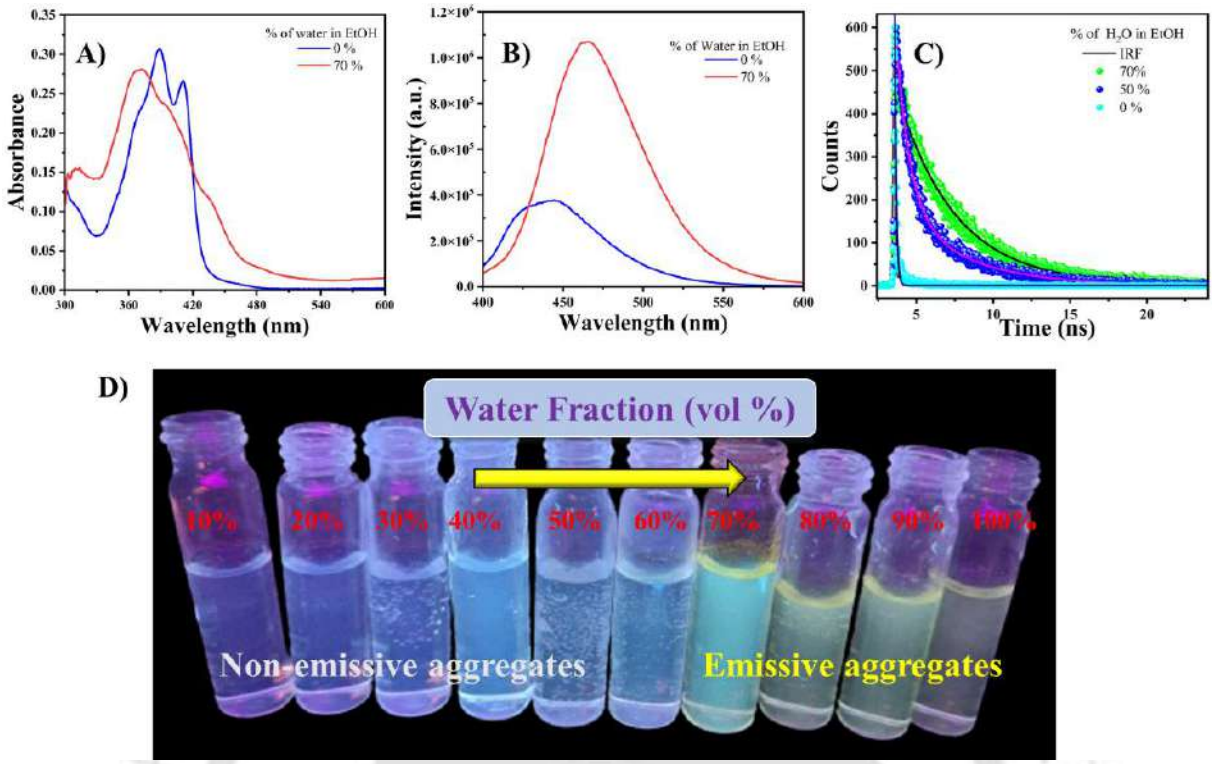

Figure 2. (A) Absorption, (B) fluorescence spectra of **L1** recorded in (0,70) % EtOH-H_2O mixture, (C) fluorescence lifetime measurement of **L1** in various water fractions (0, 50, 70) %, and (D) fluorescence images of **L1** taken with a long UV light at increasing water from (10-100) %.

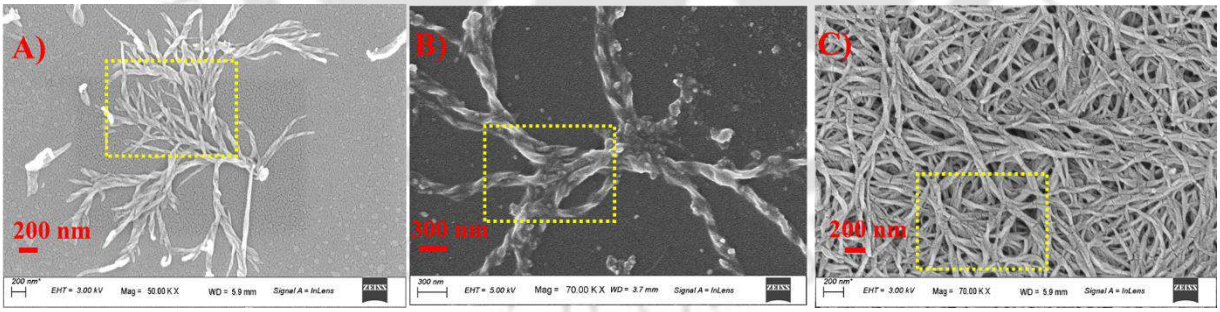

Figure 3. FESEM images of **L1** in (A) pure EtOH, (B) 3:7 and (C) 7:3 H_2O-EtOH mixture.

3.3.3 Sensing of Pd^{2+} Ion

The probe **L1** in addition to having napthyl and pyrenyl rings, can chelate metal ions through the nitrogen atom of (-C=N) and the sulphur atom of (C=S) groups present in the hydrazinecarbothioamide linkage. **L1** when treated with various metal chlorides of Na^+, Li^+, K^+, Ca^{2+}, Co^{2+}, Zn^{2+}, Cd^{2+}, Hg^{2+}, Fe^{2+}, Pb^{2+}, Ni^{2+}, Cu^{2+}, Pt^{2+}, Al^{3+}, Fe^{3+}, Au^{3+} and Cr^{3+}, nitrates of Pb^{2+}, Ag^+, sulfates of Be^{2+}, Mg^{2+}, Ag^+ and acetate of Mn^{2+} (up to 8 equivalents), the peak

values at 379 and 406 nm remained unchanged but some decrease in the intensity was observed (Figure 4A). However, while adding $PdCl_2$ solution (up to 1.5 equivalents), the intensities of 379 and 406 nm peak steadily decreased and split to peaks at 345, 362, 379 and 397 nm along with a new broad band having a peak 451 nm which grew gradually in intensity. Isosbestic points at 344 and 417 nm (Figure 4B), suggested that only two species are engaged in the solution *viz.,* free **L1** and Pd^{2+} bound **L1**. A considerable change from colorless to bright yellow was observed with the naked eye due to shift toward longer wavelength of intra-ligand charge transfer (ILCT) upon chelation with palladium(II) ion. So **L1** permitted visual detection of Pd^{2+} ion because the colour change is observable with the naked eye. For the other metal ions, the absorption intensity (i) remained unaltered for Li^+, K^+, Be^{2+}, Cr^{3+}, Mn^{2+}, Cd^{2+}, and Hg^{2+} ions (ii) decreased slightly for (2 – 10%) for Mg^{2+}, Au^{3+}, Co^{2+}, Ni^{2+}, Cu^{2+} and Zn^{2+} ions and (iii) increased from (10 – 35%) for Na^+, Ca^{2+}, Ag^+, Al^{3+}, Fe^{3+} and Pt^{2+} ions. No such spectral change was observed with the other metal ions, which indicated that **L1** was very selective and sensitive to Pd^{2+} ion only (Figure 4C). Same spectral pattern was observed when **L1** was tested with $Pd(CH_3COO)_2$ and $Pd(NO_3)_2$ (Figure A11).

The selectivity of **L1** towards Pd(II) ion was consistent with the Pearson's HSAB principle that by having a borderline nitrogen from (-C=N) and soft sulphur from (C=S) donor atom can quickly sense the kinetically faster soft Pd(II) ion.[51] The absorbance value at 451 nm was followed with gradual addition of Pd^{2+} salts, and from the reaction kinetic profile (Figure A12) it has been found that reaction attained completion within 50 sec which was very advantageous for on-site detection of Pd^{2+} ions in samples. Again, the UV-Vis spectral response of **L1** in the absence and presence of Pd^{2+} in EtOH/H_2O (3:7, *v/v*) solution at various pH values was determined at ambient temperature and the optimum pH range was found to be 5-8 (Figure A13). The reversibility was evaluated by adding triphenylphosphine (15 μM) to the *in situ* generated **L1** + Pd^{2+} complex (Figure A14), which rendered the colour of the solution getting changed from yellow to colorless. The colour reversed to yellow after addition of Pd^{2+} and this process was recycled five times. The cation interference study was carried out by following the absorbance value at λ = 451 nm. The absorbance values of solutions (EtOH/HEPES) of (a) **L1** (b) **L1** + M^{n+} (10 equivalents of each metal chlorides) (c) **L1** + M^{n+} (10 equivalents) + Pd^{2+} were recorded (Figure A15). A 70-90 % increased absorbance values with Pd^{2+} in presence of the tested metal ion indicated that Pd(II) ion can be selectively colorimetrically recognized by **L1**.

Experiment performed by adding cysteine, homocysteine and glutathione to $\mathbf{L_1}$ + Pd^{2+} solution did not show any effect (Figure A16).

As catalysts containing palladium in 0, and +4 oxidation states were also used, the sensing capability of $\mathbf{L_1}$ was carried out by using $Pd(PPh_3)_4$ and $(NH_4)_2PdCl_6$ (Figure A17I and 17II). About 90% increase in the absorbance value at λ = 451 nm was observed upon adding these two compounds to $\mathbf{L_1}$ and thus this probe has the efficiency in detecting Pd across various oxidation states.

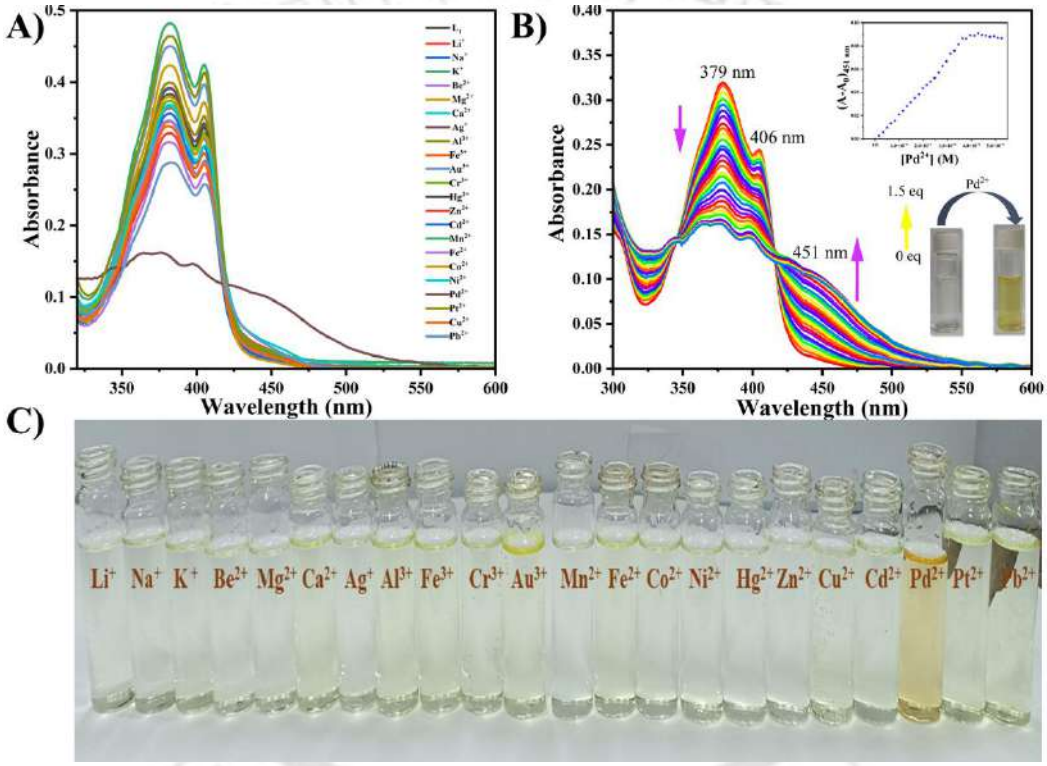

Figure 4. (A) UV-Vis spectra of probe $\mathbf{L_1}$ with different metal ion solutions, (B) UV-Vis titration of probe $\mathbf{L_1}$ on gradually adding Pd^{2+} in EtOH-HEPES buffered solution (pH = 7.4, 3:7, *v/v*) (inset: change in spectral absorbance with the concentration of Pd^{2+} at 451 nm), and (C) chromogenic response of $\mathbf{L_1}$ with different metal ions visibly observed by our naked eyes.

Since best values of maximum fluorescence intensity were observed in EtOH/HEPES (3:7, *v/v*) buffer system (Figure A18), same medium was adopted for performing sensing experiments and on irradiation of $\mathbf{L_1}$ (λ_{ex} = 380 nm), a moderately intense green emission band was observed at 465 nm. Addition of metal ions listed earlier, only Cu^{2+} ion exhibited ~10% reduction in intensity while all others exhibited negligible effect (Figure 5A). The only major exception was Pd^{2+} ion, which caused a drastic reduction (~90%) in intensity (Figure 5B). The fluorescent

aggregates after chelation with Pd^{2+} ion turned into a non-fluorescent complex through disaggregation of **L1** (Scheme 2), a chelation enhanced quenching effect (CHEQ).[52,53]

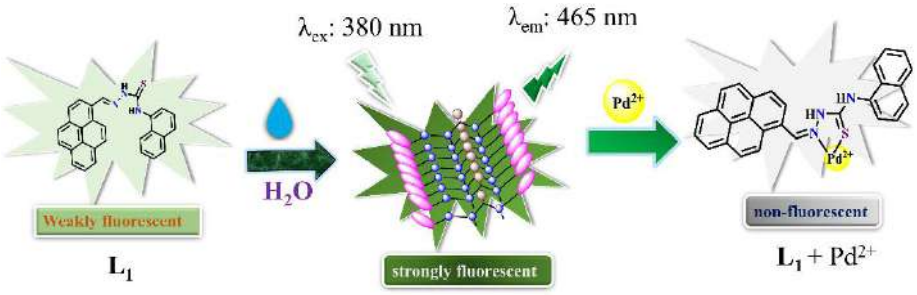

Scheme 2. Proposed sensing mechanism of **L1** with Pd^{2+}.

Both the binding stoichiometry and binding constant of **L1** with Pd^{2+} ion was calculated from fluorescence titration plot considering the intensity value at λ_{em} = 465 nm. The obtained binding ratio was 1:1 having a deviation point at 0.48 mole fraction and the binding constant was determined to be 2.65×10^5 M^{-1} as given in Figures A19 and A20. In the ESI MS mass spectrum of a solution of **L1** and $Pd(NO_3)_2$, the peak at *m/z* = 651.0580 corresponding to the composition of {[Pd(**L1**)(NO_3)(CH_3OH)]+Na^+} (calculated for $^{107}PdC_{29}H_{22}NaO_4S^+$ = 651.0596, Figure A21) supported the 1:1 stoichiometry. It may be noted that **L1** can exhibit thione-thiol tautomerism but was found to be in thione form in the solid state.[54,55] The calculated limit of detection (LOD) and limit of quantification (LOQ) obtained from the fluorescence spectral titration were 41 and 136 nM respectively (Figure 5C). This LOD value was far less than the permissible threshold level of Pd^{2+} (about 47–94 μM) as prescribed by US EPA and WHO guidelines.[56] The Stern-Volmer plot revealed a quenching constant of 7.2×10^5 M^{-1} (Figure A22), indicating the formation of a stable complex between **L1** and Pd^{2+} ion.

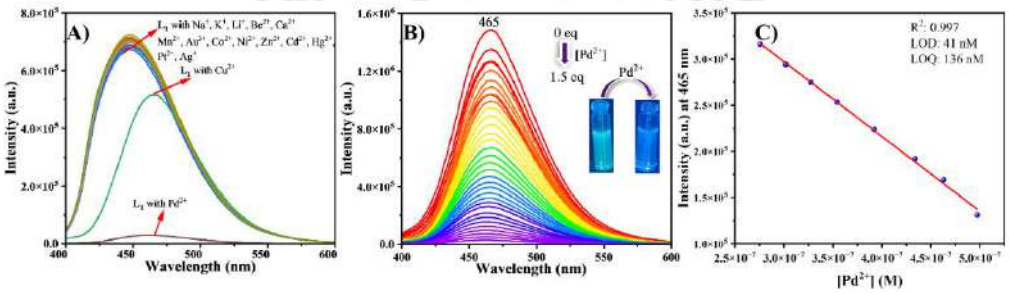

Figure 5. (A) Emission spectral change of **L1** upon the addition of different metal ions, (B) spectral emission change of **L1** with the progressive addition of $PdCl_2$ (0–1.5) equivalents, and (C) detection limit plot for Pd^{2+} ion.

3.3.4 Interaction of Pd^{2+} with L_1

Comparing the IR spectra of free **L1** and with that of **L1** + $PdCl_2$, $\nu_{C=S}$ at 823 cm^{-1} and $\nu_{C=N}$ at 1549 cm^{-1}) in **L1** got shifted to 807 and 1537 cm^{-1} in the latter (Figure 6) and Figure A23 which indicated that the most probable mode binding were through sulphur and nitrogen atoms of C=S and C=N groups.[57–59]

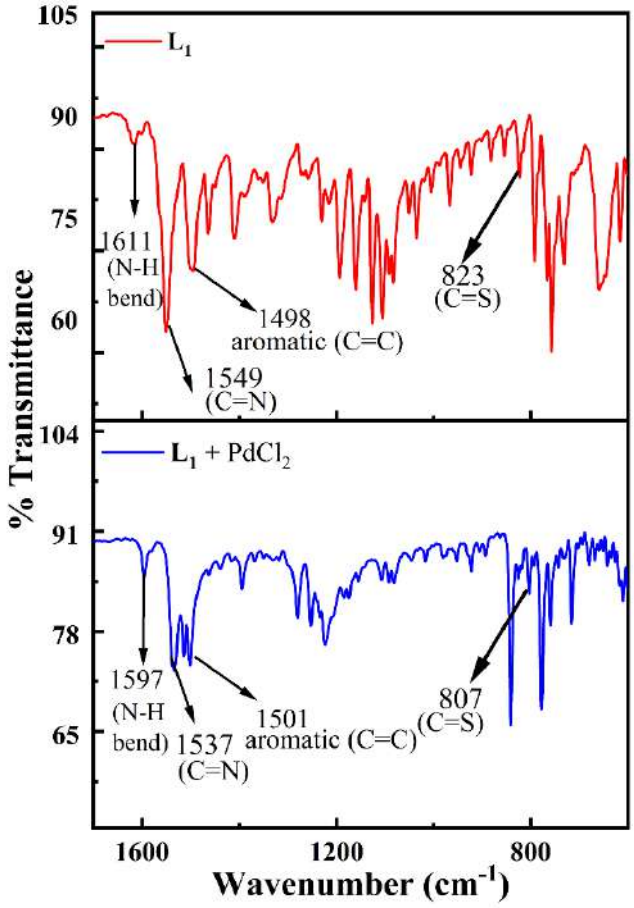

Figure 6. IR spectra of **L1** and **L1** + $PdCl_2$.

FESEM image (2 µm) of **L1** (in EtOH/HEPES) displayed circular flower-shaped agglomerated networks, which after addition of $PdCl_2$ changed to a thin needle-like morphology. The average particle size of **L1** decreased from 360 to 154 nm in the presence of Pd^{2+}, as shown in Figure 7 and Figure A24. So, the variation of surface morphology clearly revealed the effective complexation between the probe and Pd^{2+} ion. Furthermore, the average particle diameter (Z_{avg}) determined from the DLS studies confirmed the drastic decrease from 320 nm (in **L1**) to 75 nm after adding Pd^{2+} ion, verified a favourable disaggregation after interaction (Figure 7B).[60] The Energy Dispersive X-Ray spectra (Figure A25) was used to calculate the elemental

composition, which were found to be C, 75.13%; N, 23.55%; S, 1.32% (in **L1**) and C, 71.70%; N, 19.53%; S, 2.72%; Pd, 2.05% (in Pd-complex). The ^{1}H NMR titration was performed in DMSO-*d*$_6$ (Figure A26) by adding 0.33 equivalent increments of $PdCl_2$ to **L1** solution. In general, it was observed that all the peaks got broader while peak-to-peak ratios remained constant and peak at 9.43 ppm due to proton of –CH=N– got shifted to 9.67 ppm (marked as *a*). This is consistent with involvement of nitrogen atom present in –CH=N– and no loss of proton in **L1** occurred during the complex formation.

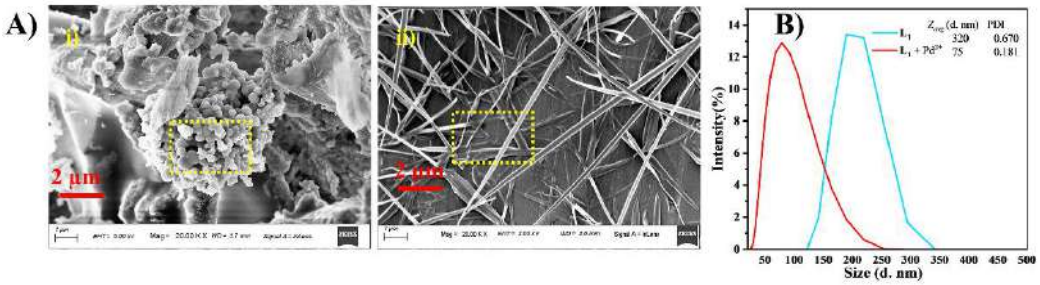

Figure 7. FESEM images of A(i) **L1**, A(ii) **L1** + Pd^{2+} complex, and (B) DLS particle size measurement of **L1** in (3:7, *v/v*) EtOH-HEPES buffered media before and after the addition of Pd^{2+}.

3.3.5 Lifetime and Quantum Yield

Lifetime decay measurements were carried out on free **L1** and in presence of Pd^{2+} indicated quenching of emission intensity (Figure 8, Table A4) and from the bi-exponential decay profiles, τ_{av} value was found to be 4.04 ns (for **L1**) which dropped down 2.80 ns after addition of $PdCl_2$. This result signified that quenching of emission intensity of aggregated **L1** by $PdCl_2$ was due formation of a non-fluorescent complex. The quantum yields for **L1** and **L1** + Pd^{2+} were found to be 4.53 and 0.73% respectively, consistent with fluorescence turn-off mechanism.

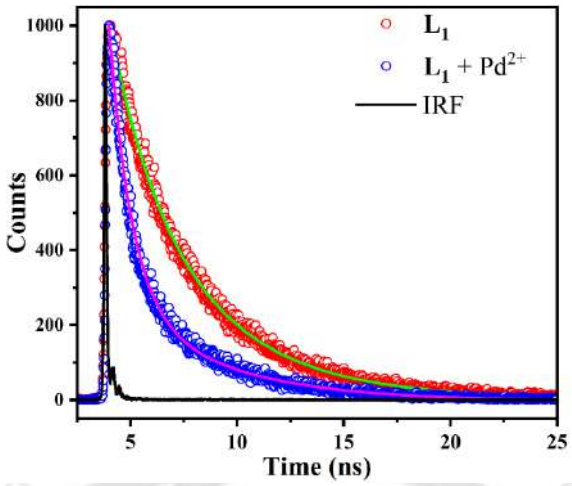

Figure 8. The decay lifetime profile of **L1** with the presence and absence of Pd^{2+} (λ_{ex} = 380 nm, measured at 465 nm).

3.3.6 Theoretical studies

To determine the most stable conformers of **L1**, the potential energy surface plot was carried out by using Gaussian 09 program. Out of the 20 dihedral rotations, the dihedral angle was varied for 10° around 1N, 21N, 3C, 4S atoms. It was depicted in Figure A27 that conformer 'a' had the lowest energy, so conformer 'a' was selected for further studies. The DFT/TDDFT calculation was carried out on **L1** and [Pd(**L1**)$(NO_3)_2$], the composition for the complex was assigned based on results of Job's plot, mass spectrum, and ^{1}H NMR titration. The optimized structures of **L1** and [Pd(**L1**)$(NO_3)_2$] were shown in Figure A28I and 28II. The palladium center was coordinated by neutral molecule **L1** in a bidentate fashion through nitrogen and sulphur atom forming five-membered chelate ring and other two coordination sites were completed by oxygen atoms of two nitrate ions. Overall palladium center has distorted pseudo square planar geometry. Charge distribution in molecular electrostatic potentials (MEP) map of **L1**, indicated that most electron rich center for coordination were S and N atoms which decreased in [Pd(**L1**)$(NO_3)_2$] (Figure A28III, 28IV).

The energy level diagram for HOMO and LUMO has been provided in Figure 10. The energies of HOMO and LUMO (in **L1**) were -6.84 eV and -3.49 eV, having a difference of 3.35 eV. In HOMO of **L1**, electron density was localized mostly on thiohydrazide function and pyrene ring, while in LUMO on hydrazinecarbothioamide and pyrene moiety. But in [Pd(**L1**)$(NO_3)_2$] the HOMO was distributed over pyrene ring and Pd^{2+} ion, whereas the LUMO was mainly concentrated on Pd^{2+} center, pyrene ring and thiohydrazide unit (Figure 9). After complexation

with Pd^{2+}, the HOMO to LUMO energy gap reduced to 2.31 eV consistent with the red shift observed in absorption bands observed experimentally. Relevant MO contour diagrams of **L1** and [Pd(**L1**)$(NO_3)_2$] were provided in (Figure A29). Using TDDFT calculation results electronic absorption spectra of **L1** and [Pd(**L1**)$(NO_3)_2$] both were generated and compared with the experimentally observed results (Table A5, A6). The stimulated and experimental UV-Vis spectra of both correlated well (Figure A30).

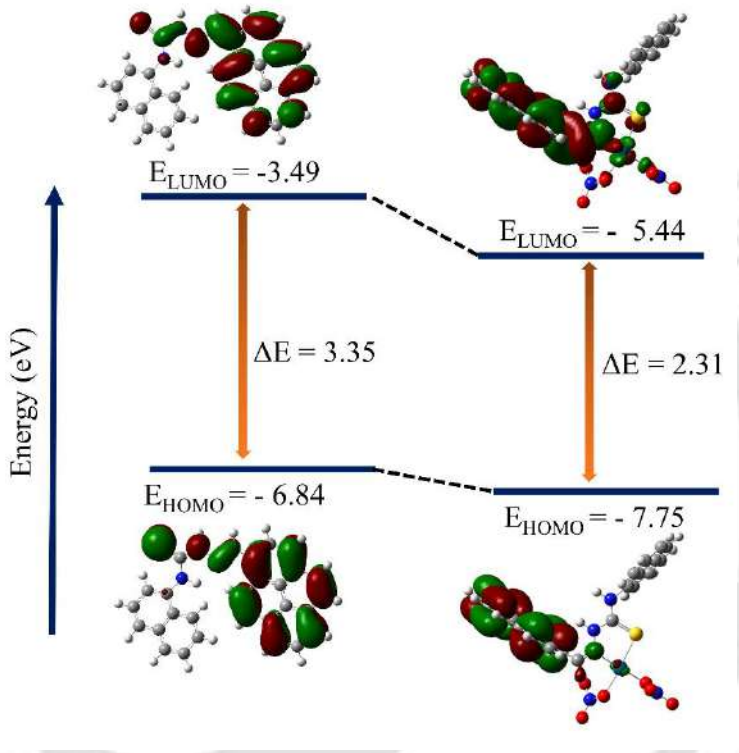

Figure 9. FMO in **L1** and [Pd(**L1**)$(NO_3)_2$].

3.3.7 Practical Utility

Simply a rectangular piece filter paper was dipped in 0.1 mM aqueous solution of **L1** and dried. To this coated colorless filter paper, when few drops of freshly prepared solution of Pd^{2+} (1 mM) was applied, a deep yellow developed immediately (Figure 10A). This characteristic colouration makes the chemosensor suitable for the quick detection of Pd^{2+} ion.

To realize the practical ability of **L1** in various natural water specimens, water samples were collected from Brahmaputra river, Serpentine lake of IIT Guwahati campus and tap water from the laboratory. The water samples were filtered through a 0.22 μm filter paper and pH was adjusted to 7.4.[61] Then, **L1** was titrated by adding Pd^{2+} (ranging from 0–1.5 μM) and absorbance value at 451 nm after each addition were recorded. A calibration plot of absorbance *versus* Pd^{2+}

concentration was obtained (Figure A31) and from bar diagram, it was evident that **L1** was able to detect Pd^{2+} from solution the spiked 60% (river), 85% (lake) and 68% (tap) water samples (Figure 10B). Additionally, the calculated recovery percentage of un-spiked/spiked Pd^{2+} water samples was within acceptable consistency and the significant recovery rate also compared well with the ICP-OES analysis. The real water sample analysis data are listed in Table A7. All the experiments were performed in triplicate and recovery rates were calculated with reference to the ICP-OES observations. This result suggested that probe **L1** is a promising candidate for rapid Pd^{2+} ion detection in environmental water samples without using any sophisticated analytical tools.

Using Tauc's plot,[62] the bandgap in **L1** was calculated to be 3.28 eV (Figure A32) which matched well with the HOMO-LUMO bandgap of 3.35 eV obtained through TDDFT calculations.[63] This demonstrated the consistency between experimental and theoretical results. This high bandgap resulted in lower current of 0.8 nano-amphere (nA) range at 10 V bias. From the electrical characteristics, it can be observed that Schottky junction[62,64] exist between the Au electrodes and semiconducting probe resulting in a sharp increase in the current after 2 V external bias. To understand, the effect of changing concentration of Pd^{2+} to **L1**, on electrical parameters upon, we have added (0.5 to 2 equivalents of Pd^{2+}) and studied the electrical sweeping. The current increased from 7.5 to 30 nA with increasing Pd^{2+} concentrations (Figure 10C). Hence a systematic linear enhancement of current observed (Figure A33). So, this probe can be used for the construction of an electrical device to recognize Pd^{2+} ion (Figure 10D). This enhancement in conductivity upon Pd^{2+} interaction makes it a promising candidate for real-time electrical detection.

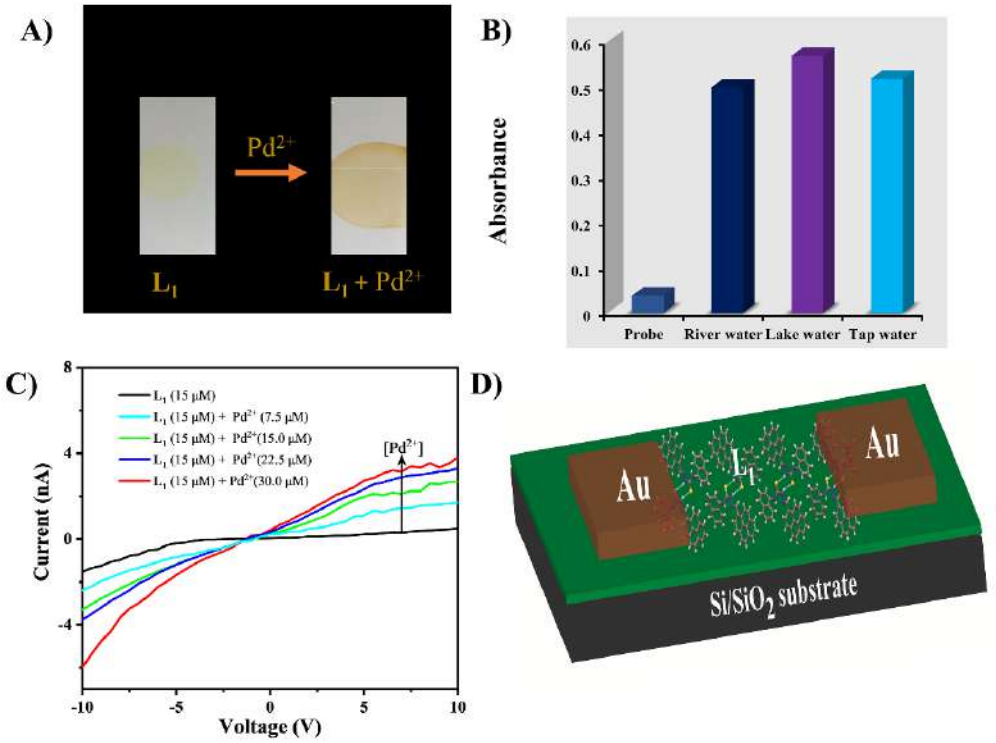

Figure 10. (A) Paper strip test before and after addition of Pd^{2+} ion, (B) absorbance at 451 nm in real water samples, (C) current-Voltage plot of probe **L1** (15 μM) with increasing Pd^{2+} ion concentration from (0–30 μM), and (D) fabricated device.

Palladium compounds were used as catalyst in reactions involved in the manufacture of drug molecules and residual palladium, if any, in API mandated to be maintained below 5 to 10 ppm level.[65] So, to test capability of **L1** to detect the residual palladium, APIs (Figure A34) like Telmisartan, Valsartan, Olmesartan and Losartan were evaluated. Known concentrations of $PdCl_2$ were added (150 μL) to each of the drug samples (0.5 mg) and calibration plots were obtained (Figure A35) by titrating the resultant spiked solution with **L1** solution. The absorbance values at 451 nm of **L1** was used for detection, absorbance due to API did not interfere, since they lied in the range 200–300 nm. The recovery test was performed following a standard protocol of spiking known concentration of $PdCl_2$ and absorbance value of **L1** was recorded for spiked solution. As shown in Figure A36, Table A8 the recycling rates and relative standard deviation (RSDs) of Pd^{2+} in the spiked sample varied from 93% to 102%, and 0.5% to 4.8% respectively. Each was analyzed three times and the results compared well with those obtained from ICP-OES methods. Thus, **L1** can detect Pd^{2+} in presence of all four-drug sample, and calculated LOD values were in the range $1.0–2.0 \times 10^{-7}$ M (Table A9, Figure A37). So, the

results suggested that **L1** was applicable to detect Pd^{2+} in presence of all anti-hypertensive drugs. The analytical performance of **L1** was compared with other reported colorimetric and fluorometric sensors in Table A10 for ready reference.

3.4 Conclusion:

An AIE active probe **L1** had been evaluated for the selective and sensitive detection of Pd^{2+} in presence of other interfering metal ions. Determination of molecular structure revealed presence of J-type nano-aggregates of **L1** in the packing diagram. FESEM studies confirmed their nano-structure formation and DLS analysis showed increased particle size in 7:3 water-EtOH mixture. Coordination of **L1** as bidentate N, S donor ligand resulted in recognition of Pd^{2+} ion both colorimetrically and fluorometrically. The yellowish-green fluorescent aggregates of **L1** turned into a non-fluorescent complex after chelation with Pd^{2+} *via* a CHEQ process. The 1:1 binding stoichiometry of **L1** toward Pd^{2+} was confirmed by Job's plot, Benesi-Hildebrand (B-H) plot, ESI MS mass spectrum and ^1H NMR titration. FESEM images displayed flower and needle-like morphology before and after the addition of Pd^{2+} ion into **L1** solution. TRPL decay profile suggested the lifetime of the non-fluorescent Pd complex had decreased by half compared to free **L1**, indicating static quenching. Theoretical calculations supported the observed experimental red shift of the UV-Vis absorption band. The practical utility of **L1** was analyzed in various real water specimens and commercially available drug samples, with a recovery rate of over 83%. The rectangular filter paper strips for on-site Pd^{2+} detection and a two terminal electrical device was fabricated for real-time recognition.

References:

1 M. Wu, D. D. Yang, H. W. Zheng, Q. F. Liang, J. B. Li, Y. Kang, S. Li, C. Jiao, X. J. Zheng and L. P. Jin, *Dalt. Trans.*, 2021, **50**, 1507-1513.

2 W. Z. Yuan, Y. Gong, S. Chen, X. Y. Shen, J. W. Y. Lam, P. Lu, Y. Lu, Z. Wang, R. Hu, N. Xie, H. S. Kwok, Y. Zhang, J. Z. Sun and B. Z. Tang, *Chem. Mater.*, 2012, **24**, 1518-1528.

3 J. Xiao, B. Yang, J. I. Wong, Y. Liu, F. Wei, K. J. Tan, X. Teng, Y. Wu, L. Huang, C. Kloc, F. Boey, J. Ma, H. Zhang, H. Y. Yang and Q. Zhang, *Org. Lett.*, 2011, **13**, 3004-3007.

4 S. Samanta, S. Goswami, M. N. Hoque, A. Ramesh and G. Das, *Chem. Commun.*, 2014,

50, 11833-11836.

5 J. Mei, N. L. C. Leung, R. T. K. Kwok, J. W. Y. Lam and B. Z. Tang, *Chem. Rev.*, 2015, **115**, 11718-11940.

6 Y. Hong, J. W. Y. Lam and B. Z. Tang, *Chem. Commun.*, 2009, 4332.

7 J. Mei, Y. Hong, J. W. Y. Lam, A. Qin, Y. Tang and B. Z. Tang, *Adv. Mater.*, 2014, **26**, 5429-5479.

8 N. L. C. Leung, N. Xie, W. Yuan, Y. Liu, Q. Wu, Q. Peng, Q. Miao, J. W. Y. Lam and B. Z. Tang, *Chem. - A Eur. J.*, 2014, **20**, 15349-15353.

9 M. H. Chua, B. Y. K. Hui, K. L. O. Chin, Q. Zhu, X. Liu and J. Xu, *Mater. Chem. Front.*, 2023, **7**, 5561-5660.

10 J. Zhou, S. Xu, Z. Yu, X. Ye, X. Dong and W. Zhao, *Dye. Pigment.*, 2019, **170**, 107656.

11 N. Gupta, T. Kaur, V. Bhalla, R. D. Parihar, P. Ohri, G. Kaur and M. Kumar, *Chem. Commun.*, 2017, **53**, 12646-12649.

12 C. Chen, H. Ou, R. Liu and D. Ding, *Adv. Mater.*, 2020, **32**, 1-6.

13 J. Qi, C. Chen, X. Zhang, X. Hu, S. Ji, R. T. K. Kwok, J. W. Y. Lam, D. Ding and B. Z. Tang, *Nat. Commun.*, 2018, **9**, 1-12.

14 M. Li, H. Gou, I. Al-Ogaidi and N. Wu, *ACS Sustain. Chem. Eng.*, 2013, **1**, 713-723.

15 P. Chakraborty, A. Rana, S. Mukherjee and S. Biswas, *Inorg. Chem.*, 2023, **62**, 802-809.

16 W. Zhou, Q. Gao, D. Liu, C. Li, S. Liu, K. Xia, B. Han and C. Zhou, *Spectrochim. Acta Part A Mol. Biomol. Spectrosc.*, 2020, **237**, 118365.

17 G. Wu, Z. Wang, W. Zhang, W. Chen, X. Jin and H. Lu, *Inorg. Chem. Commun.*, 2019, **102**, 233-239.

18 Q. Huang, Y. Zhou, Q. Zhang, E. Wang, Y. Min, H. Qiao, J. Zhang and T. Ma, *Sensors Actuators B Chem.*, 2015, **208**, 22-29.

19 A. A. S. Paulino, L. Giroldo, N. A. Pradie, J. S. Reis, D. F. Back, A. A. C. Braga, H. A. Stefani, C. Lodeiro and A. A. Dos Santos, *Dye. Pigment.*, 2020, **179**, 108355.

20 A. Bhattacharya and V. Manivannan, *Microchem. J.*, 2024, **200**, 110440.

21 H. Li, J. Fan, M. Hu, G. Cheng, D. Zhou, T. Wu, F. Song, S. Sun, C. Duan and X. Peng, *Chem. - A Eur. J.*, 2012, **18**, 12242-12250.

22 T. Z. Liu, S. D. Lee and R. S. Bhatnagar, *Toxicol. Lett.*, 1979, **4**, 469-473.

23 J. C. Wataha and C. T. Hanks, *J. Oral Rehabil.*, 1996, **23**, 309-320.

24 J. Kielhorn, C. Melber, D. Keller and I. Mangelsdorf, *Int. J. Hyg. Environ. Health*, 2002, **205**, 417-432.

25 C. E. Garrett and K. Prasad, *Adv. Synth. Catal.*, 2004, **346**, 889-900.

26 F. K. Tang, S. M. Chan, T. Wang, C. S. Kwan, R. Huang, Z. Cai and K. C. F. Leung, *Talanta*, 2020, **210**, 120634.

27 X. Chen, H. Wang, X. Ma, M. Wang, Y. Zhang, G. Gao, J. Liu and S. Hou, *Dye. Pigment.*, 2018, **148**, 286-291.

28 T. Chen, T. Wei, Z. Zhang, Y. Chen, J. Qiang, F. Wang and X. Chen, *Dye. Pigment.*, 2017, **140**, 392-398.

29 X. Z. Chen, X. D. Ma, H. M. Wang, M. Wang, Y. Y. Zhang, G. Gao, J. J. Liu and S. C. Hou, *New J. Chem.*, 2017, **41**, 8026-8030.

30 H. Li, J. Fan and X. Peng, *Chem. Soc. Rev.*, 2013, **42**, 7943.

31 M. G. Choi, J. Y. Seo, E. J. Cho and S. K. Chang, *J. Photochem. Photobiol. A Chem.*, 2022, **429**, 113920.

32 Q. Xia, S. Feng, D. Liu and G. Feng, *Sensors Actuators B Chem.*, 2018, **258**, 98-104.

33 S. Wang, Z. Zhang, Z. Huang, X. Lei, Y. Wang, L. Li, L. Yang, H. Liu, F. Sun and L. J. Ma, *J. Photochem. Photobiol. A Chem.*, 2021, **418**, 113438.

34 K. Ayyavoo and P. Velusamy, *New J. Chem.*, 2021, **45**, 10997-11017.

35 M. Shellaiah, Y. T. Chen, N. Thirumalaivasan, B. Aazaad, K. Awasthi, K. W. Sun, S. P. Wu, M. C. Lin and N. Ohta, *ACS Appl. Mater. Interfaces*, 2021, **13**, 28610-28626.

36 Y. Wu, X. Wen and Z. Fan, *Spectrochim. Acta Part A Mol. Biomol. Spectrosc.*, 2019,

223, 117315.

37 W. N. Wu, P. D. Mao, Y. Wang, X. J. Mao, Z. Q. Xu, Z. H. Xu, X. L. Zhao, Y. C. Fan and X. F. Hou, *Sensors Actuators B Chem.*, 2018, **258**, 393-401.

38 A. Panigrahi, B. P. Sahu, S. Mandani, D. Nayak, S. Giri and T. K. Sarma, *J. Photochem. Photobiol. A Chem.*, 2019, **374**, 194-205.

39 K. A. Zachariasse, A. L. Maçanita and W. Kuhnle, *J. Phys. Chem. B*, 1999, **103**, 9356-9365.

40 Z. Li, Y. Xiang and A. Tong, *Anal. Chim. Acta*, 2008, **619**, 75-80.

41 D. Udhayakumari, S. Velmathi, P. Venkatesan and S. P. Wu, *J. Lumin.*, 2015, **161**, 411-416.

42 A. R. Chowdhury, B. G. Roy, S. Jana, T. Weyhermuller and P. Banerjee, *Sensors Actuators, B Chem.*, 2017, **241**, 706-715.

43 M. Ashfaq, A. Ali, M. N. Tahir, A. Kuznetsov, K. S. Munawar and S. Muhammad, *J. Mol. Struct.*, 2022, **1262**, 133088.

44 H. Yin, B. Zhao, W. Kan, L. Ding, L. Wang, B. Song, W. Wang and Q. Deng, *Dye. Pigment.*, 2020, **173**, 107916.

45 T. Mondal, S. Roy, I. Mondal, M. V Mane and S. S. Panja, *J. Photochem. Photobiol. A Chem.*, 2021, **406**, 112998.

46 M. Shyamal, S. Maity, P. Mazumdar, G. P. Sahoo, R. Maity and A. Misra, *J. Photochem. Photobiol. A Chem.*, 2017, **342**, 1-14.

47 A. Kathiravan, K. Sundaravel, M. Jaccob, G. Dhinagaran, A. Rameshkumar, D. Arul Ananth and T. Sivasudha, *J. Phys. Chem. B*, 2014, **118**, 13573-13581.

48 Khadija, H. Irshad, S. Rafique, A. M. Khan, S. Nawazish, H. ur Rehman, M. Imran, S. A. Shahzad and U. Farooq, *Spectrochim. Acta Part A Mol. Biomol. Spectrosc.*, 2023, **290**, 122273.

49 Z. F. Hu, Z. L. Chai, Y. R. Zheng, Y. F. Ding, W. K. Dong and Y. J. Ding, *Microchem. J.*, 2023, **190**, 108736.

50 X. Feng, J. Zhang, Z. Hu, Q. Wang, M. M. Islam, J. S. Ni, M. R. J. Elsegood, J. W. Y. Lam, E. Zhou and B. Z. Tang, *J. Mater. Chem. C*, 2019, **7**, 6932-6940.

51 R. T. Myers, *Inorg. Chem.*, 1974, **13**, 2040-2041.

52 B. Musikavanhu, S. Muthusamy, D. Zhu, Z. Xue, Q. Yu, C. N. Chiyumba, J. Mack, T. Nyokong, S. Wang and L. Zhao, *Spectrochim. Acta - Part A Mol. Biomol. Spectrosc.*, 2022, **264**, 120338.

53 L. Gustavo, T. Alves, F. Lange, F. Berbigier, F. Severo, G. Gamino and D. Zambon, 2020, **181**, 1-7.

54 J. Baruah, R. Gogoi, N. Gogoi and G. Borah, *Transit. Met. Chem.*, 2017, **42**, 683-692.

55 A. A. Aly, E. M. Abdallah, S. A. Ahmed, M. M. Rabee, O. Fuhr, M. A. A. Ibrahim, H. Ali Alzahrani and B. G. M. Youssif, *Polyhedron*, 2024, **251**, 116851.

56 S. Mahata, A. Bhattacharya, J. P. Kumar, B. B. Mandal and V. Manivannan, *J. Photochem. Photobiol. A Chem.*, 2020, **394**, 112441.

57 L. Fuks, N. S. Sosnowska, K. Samochocka and W. Starosta, *J. Mol. Struct.*, 2005, **740**, 229-235.

58 T. A. Yousef, O. K. Alduaij, G. M. Abu El-Reash and R. M. El Morshedy, *J. Mol. Liq.*, 2016, **222**, 762-776.

59 D. Fabra, A. I. Matesanz, J. M. Herrero, C. Alvarez, Lucia. M. Balsa, I. E. Leon, *Eur. J Inorg Chem.*, 2021, **11**, 1041-1049.

60 S. Saha, S. Paul, R. Debnath, N. Dey and B. Biswas, *Anal. Methods*, 2024, **9**, 1058-1068.

61 A. Mondal and V. Manivannan, *Spectrochim. Acta - Part A Mol. Biomol. Spectrosc.*, 2024, **322**, 124734.

62 A. Panja, M. Das, N. C. Jana, P. Brandao, R. M. Gomila, J. O. Castro, A. Frontera and P. P. Ray, *CrystEngComm*, 2023, **25**, 2133-2143.

63 L. Harynski, A. Olejnik, K. Grochowska, K. Siuzdak, *Opt. Mat.*, 2022, **127**, 112205.

64 N. Honnappa, A. G. Anil, S. Shekar, S. K. Behera and P. C. Ramamurthy, *Inorg. Chem.*,

2022, **61**, 15085-15097.

65 S. Erdemir, S. Malkondu and M. Oguz, *Talanta*, 2023, **252**, 123847.

66 D. Wang, H. Hou, W. Chen, Y. Wu, X. Peng and F. Song, *Tetrahedron Lett.*, 2022, **102**, 153932.

67 P. Sharma, S. Kaur, S. Kaur and P. Singh, *Photochem. Photobiol. Sci.*, 2020, **19**, 504-514.

68 L. Wang, X. Y. Zheng, X. Zhang and Z. J. Zhu, *Spectrochim. Acta Part A Mol. Biomol. Spectrosc.*, 2021, **249**, 119283.

69 B. C. M. A. Ashwin, G. Sivaraman, T. Stalin, R. Yuvakkumar and P. M. Mareeswaran, *J. Photochem. Photobiol. B Biol.*, 2018, **183**, 302-308.

70 A. Higashi, N. Kishikawa, K. Ohyama and N. Kuroda, *Tetrahedron Lett.*, 2017, **58**, 2774-2778.

71 L. Tang, S. Ding and X. Yan, *Inorg. Chem. Commun.*, 2016, **74**, 35-38.

72 A. Kumar, Virender, B. Mohan, A. A. Solovev, M. Saini and H. K. Sharma, *Microchem. J.*, 2022, **180**, 107561.

Appendix

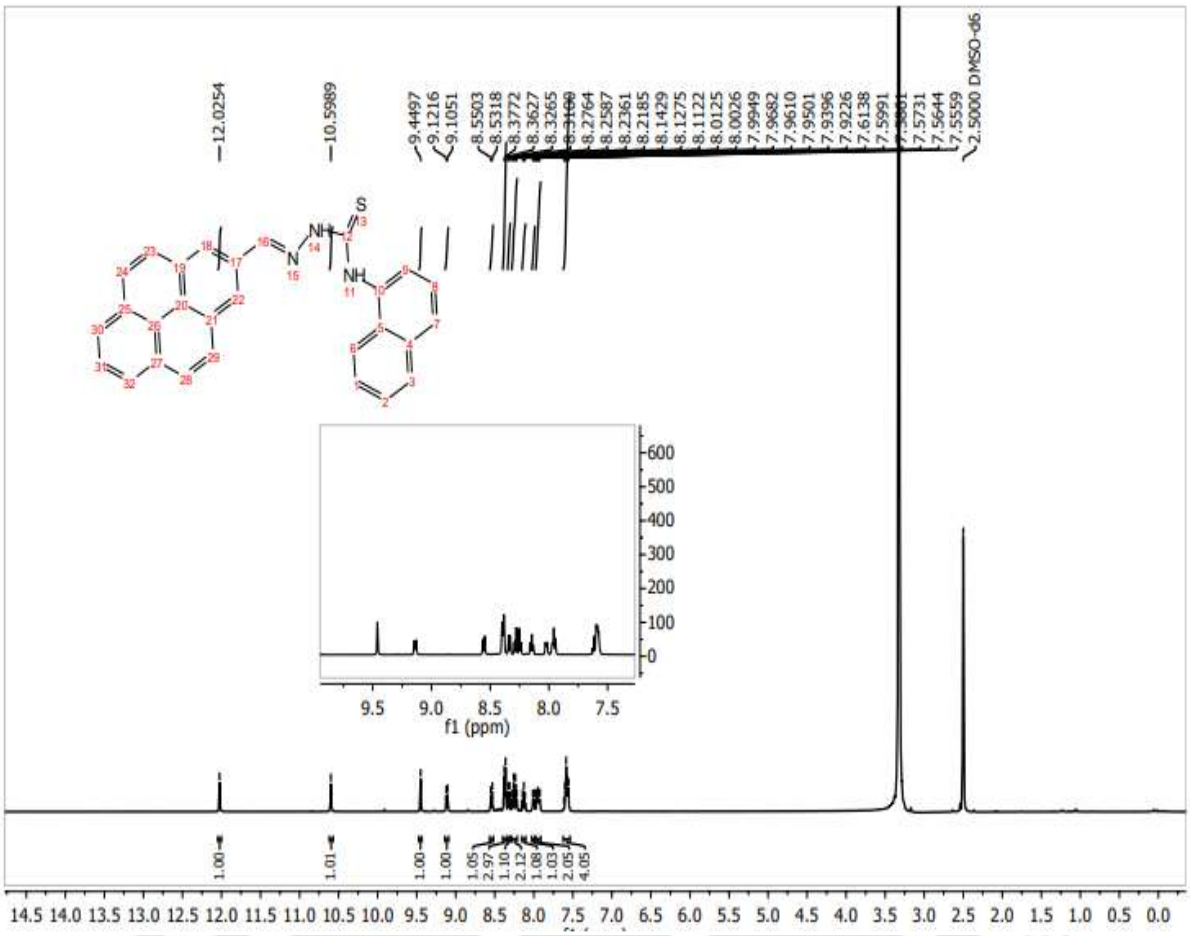

Figure A1. ^{1}H NMR (600 MHz) of **L1** in DMSO-d_6.

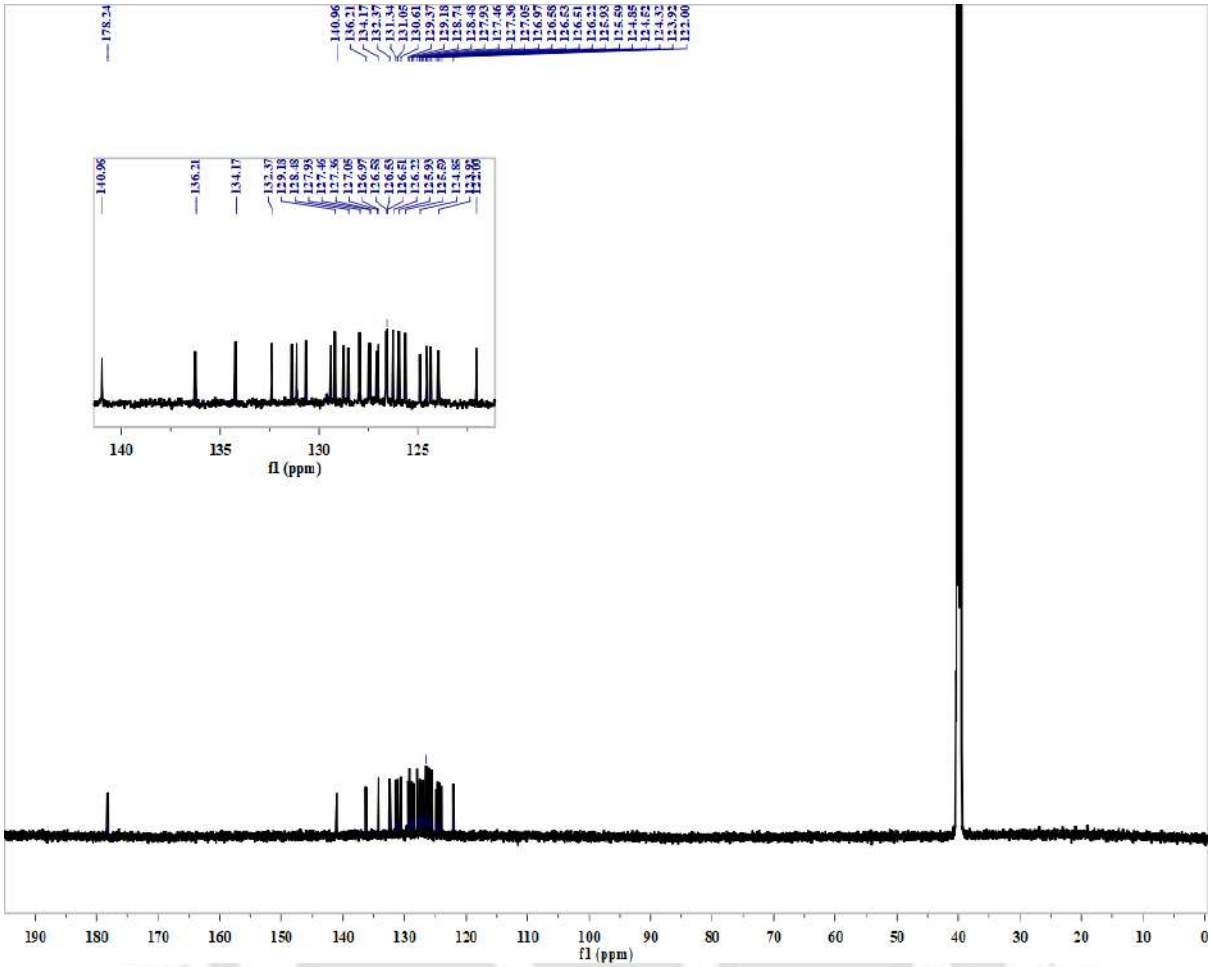

Figure A2. ^{13}C NMR (600 MHz) of **L$_1$** in DMSO-d_6.

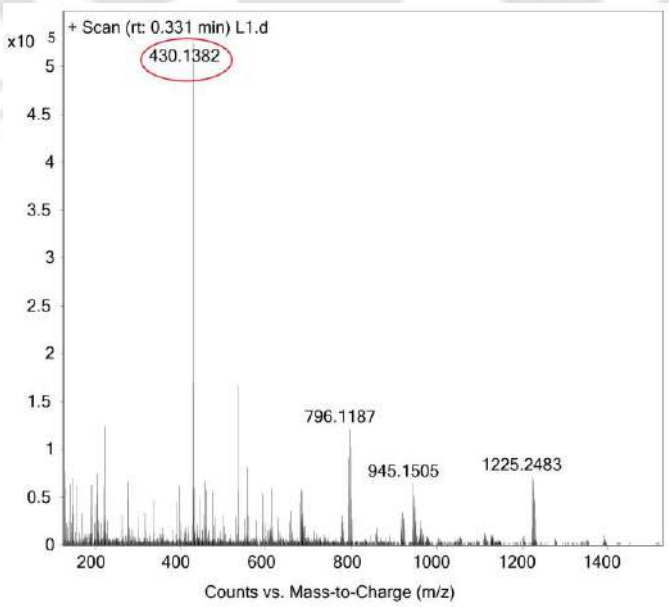

Figure A3. ESI Mass spectrum of **L$_1$** in acetonitrile.

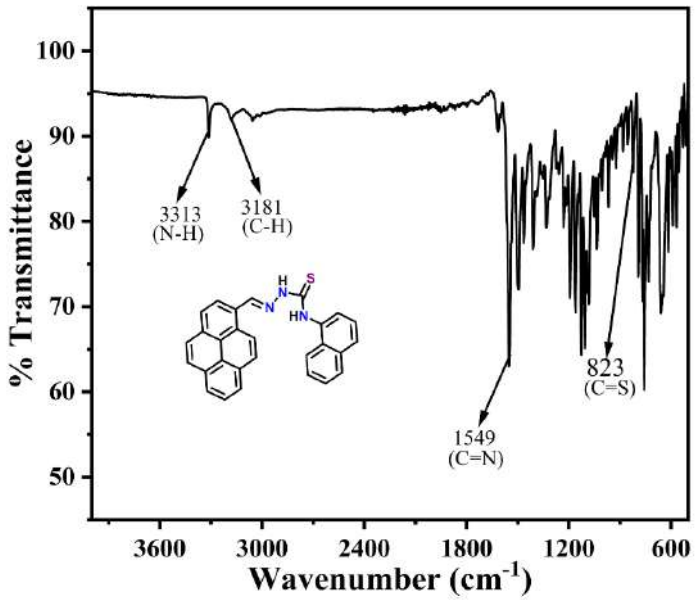

Figure A4. IR spectrum of $\mathbf{L_1}$.

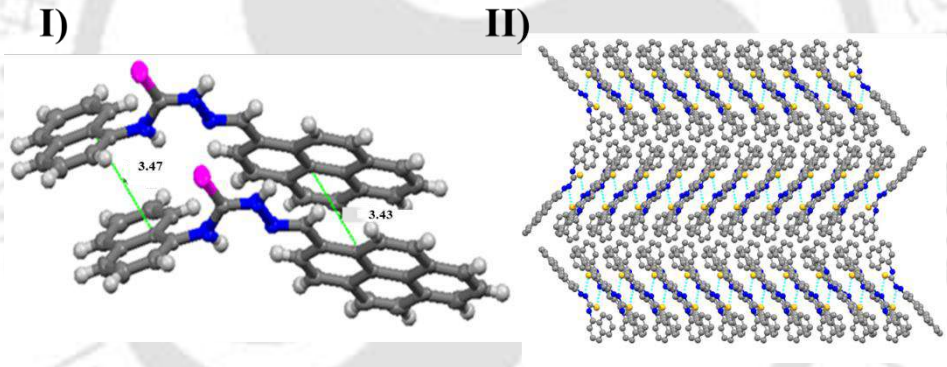

Figure A5. (I) Intermolecular H-bonding interactions of $\mathbf{L_1}$ view along *b*-axes, and (II) extended 2D supramolecular chain-like structure of $\mathbf{L_1}$.

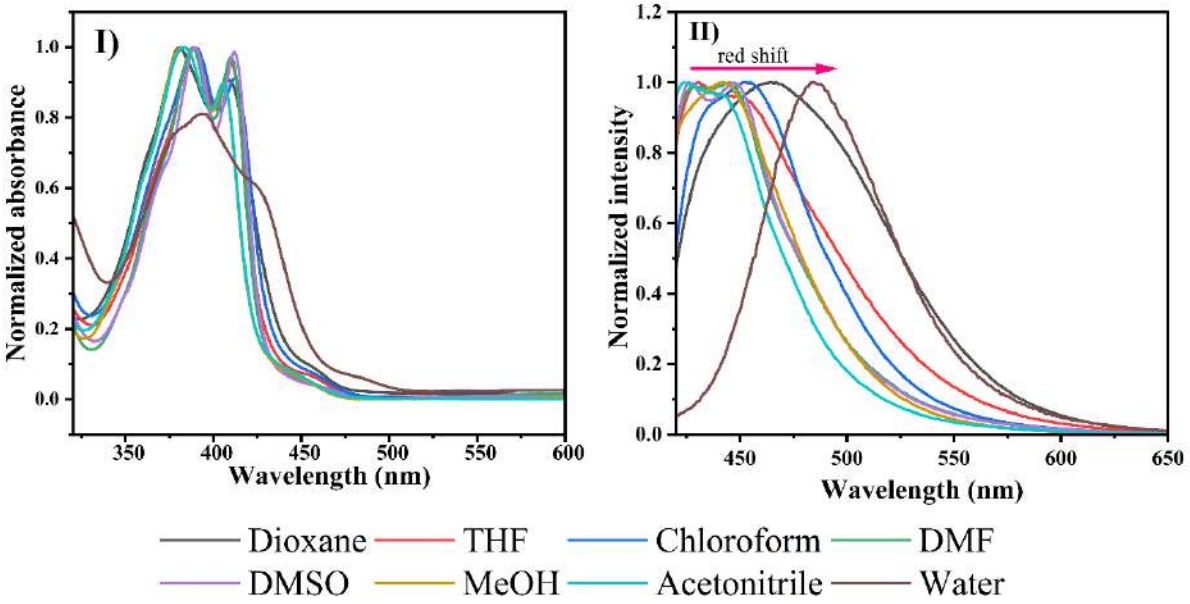

Figure A6. (I) Normalized absorbance and, (II) emission spectral behaviour of **L1** in various solvents.

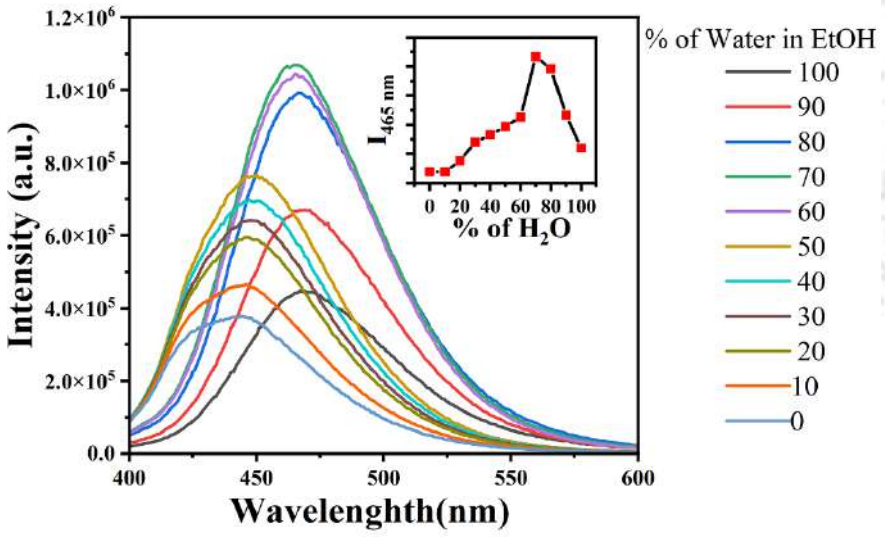

Figure A7. Fluorescence spectra of **L1** recorded in EtOH-H_2O mixture (λ_{em}: 465 nm are in inset).

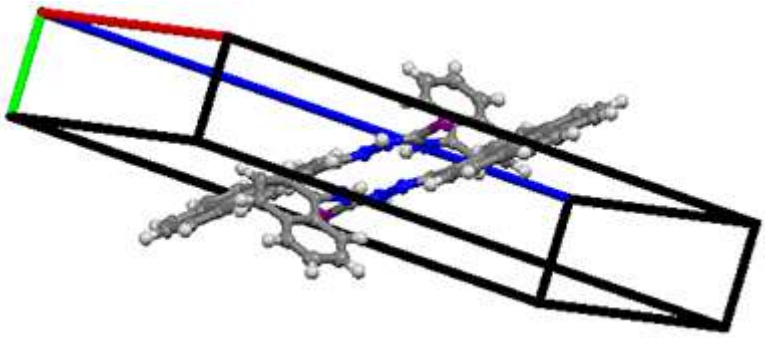

Figure A8. Single crystal unit cell packing diagram of **L1** view along *b*-axes.

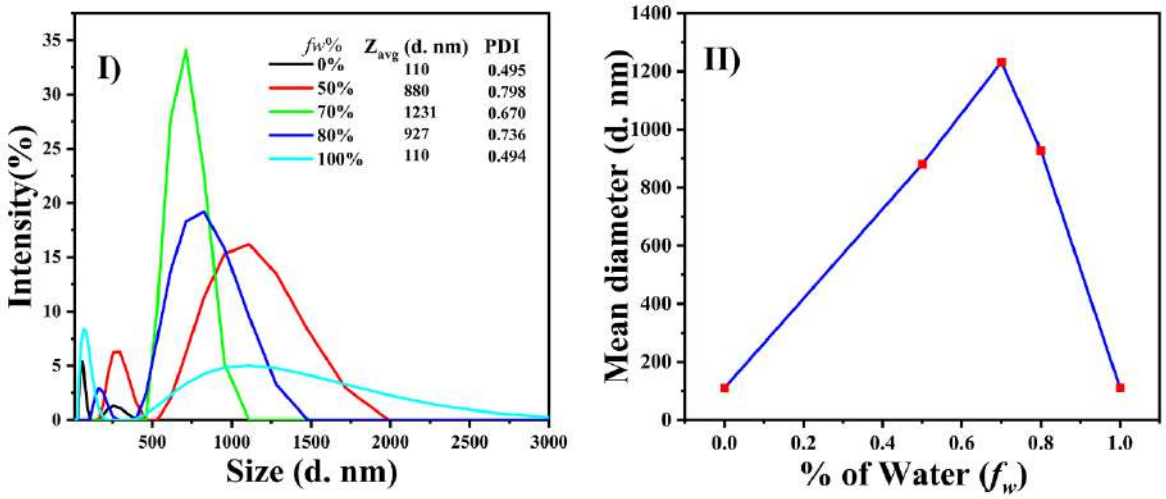

Figure A9. (I) Particle size distribution of **L1** (15 μM) in EtOH/H_2O mixtures and (II) variation of the mean diameter of **L1** nano-aggregates, determined by using DLS experiments.

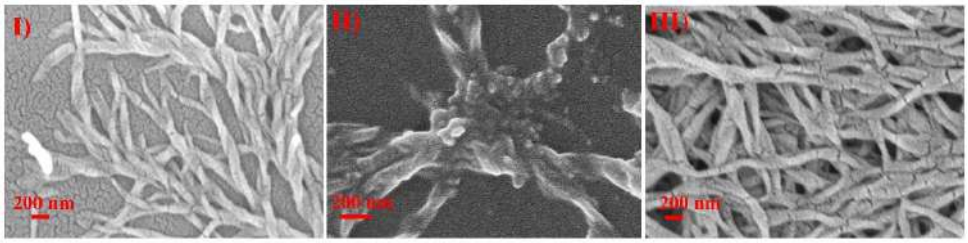

Figure A10. Higher magnification FESEM images of **L1** (scale bar = 200 nm) in (I) pure EtOH, (II) 3:7 and (III) 7:3 H_2O-EtOH mixture.

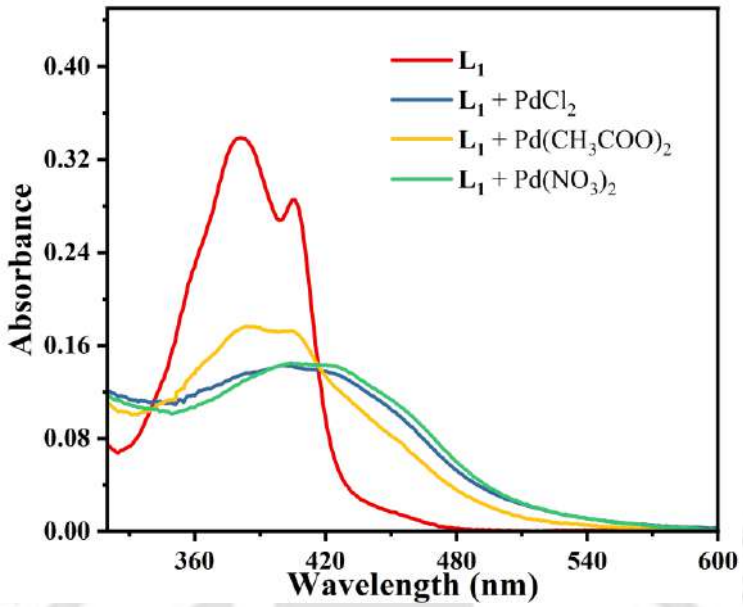

Figure A11. Absorption spectra of **L1** (15 μM) upon addition of different counter anion of palladium, in EtOH-HEPES buffer mixture (3:7, *v/v*).

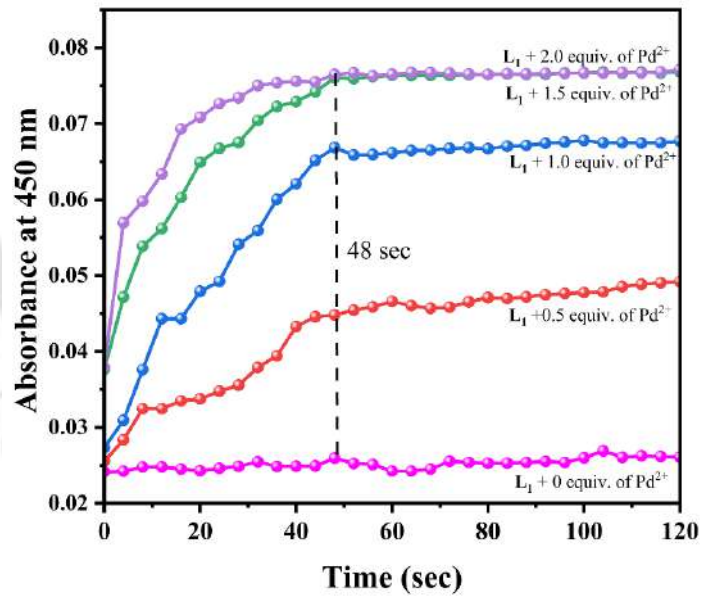

Figure A12. Variation of response time of **L1** with increasing concentration of Pd^{2+} by monitoring the absorbance maximum at 451 nm.

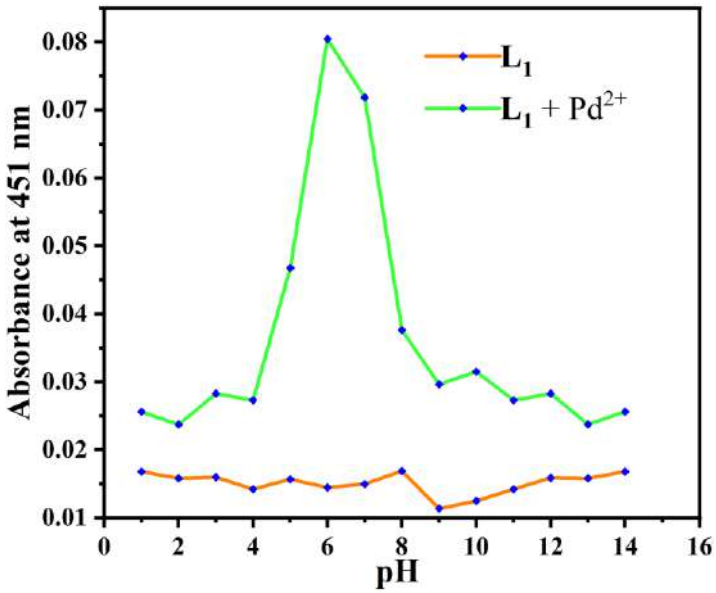

Figure A13. Plot of absorbance intensity *versus* pH in EtOH-H_2O mixture (3:7, *v/v*).

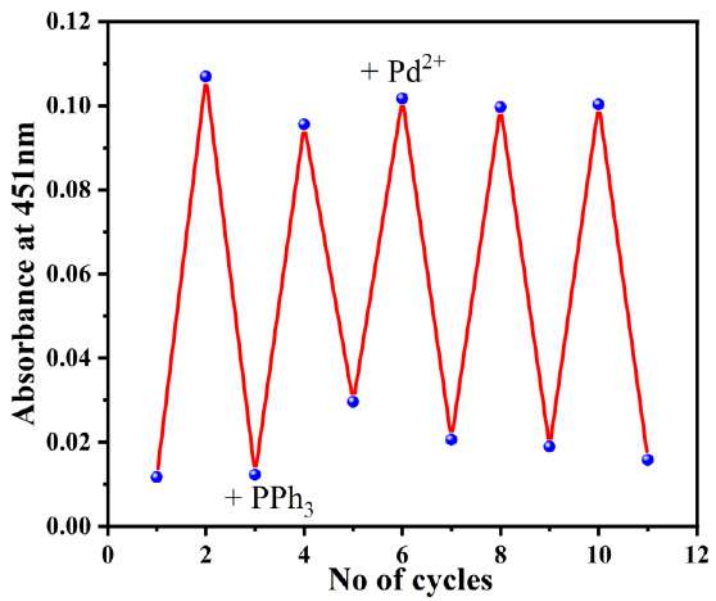

Figure A14. Plot of absorbance intensity (451 nm) against no of cycles for the reversible addition of Pd^{2+} with PPh_3 to **L_1** (with five cycles).

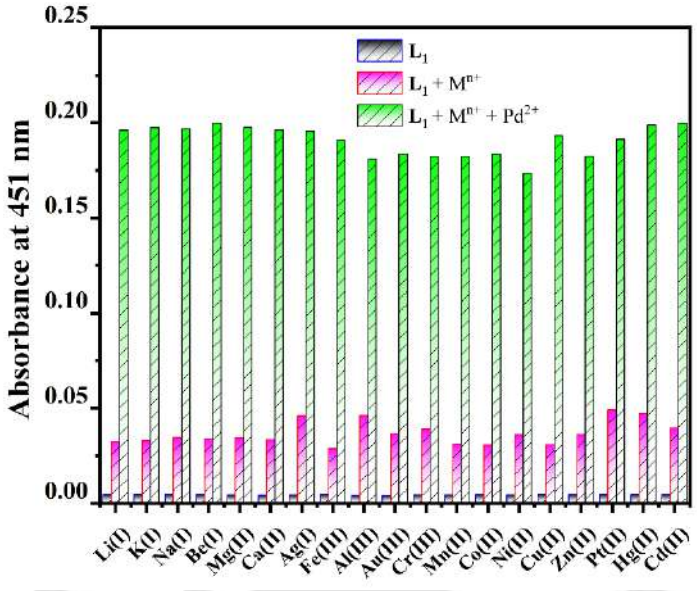

Figure A15. Bar diagram plot of **L1** with various cationic analytes in EtOH/HEPPS buffer solvent medium.

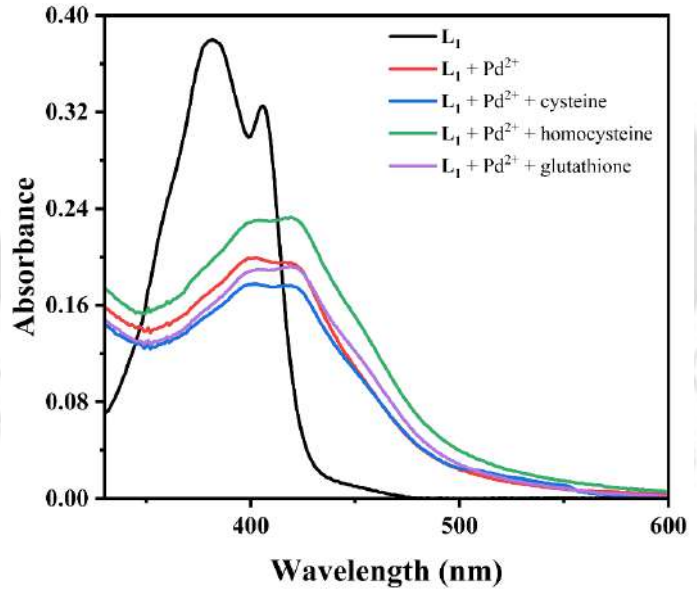

Figure A16. UV-Vis spectral response of **L1** + Pd^{2+} towards cysteine, homocysteine, and glutathione.

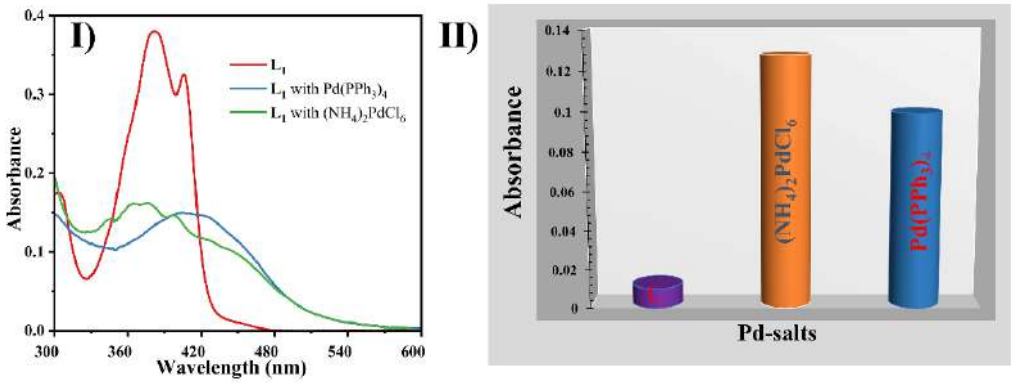

Figure A17. (I) Selective colorimetric responses of Palladium with **L1** in various oxidation states (0, +4) along its (II) bar diagram.

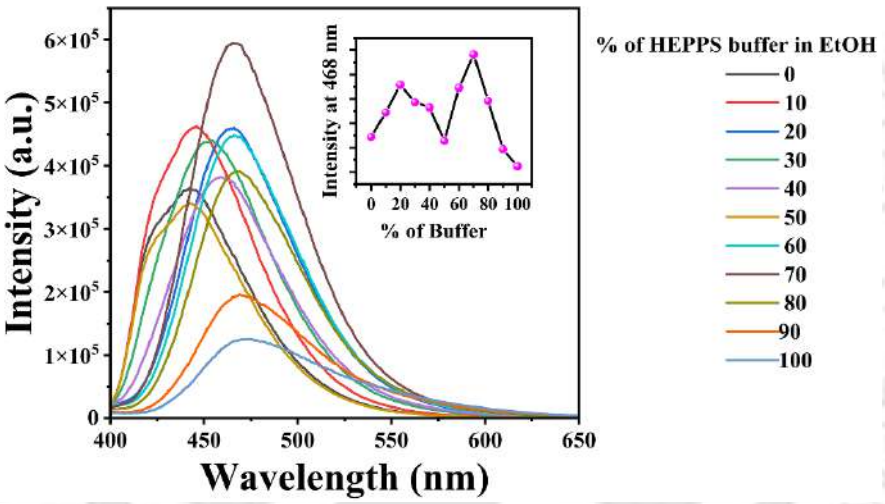

Figure A18. Fluorescence spectral behaviour of **L1** in various fractions of *fw* (0–100) % in EtOH-HEPES buffer system.

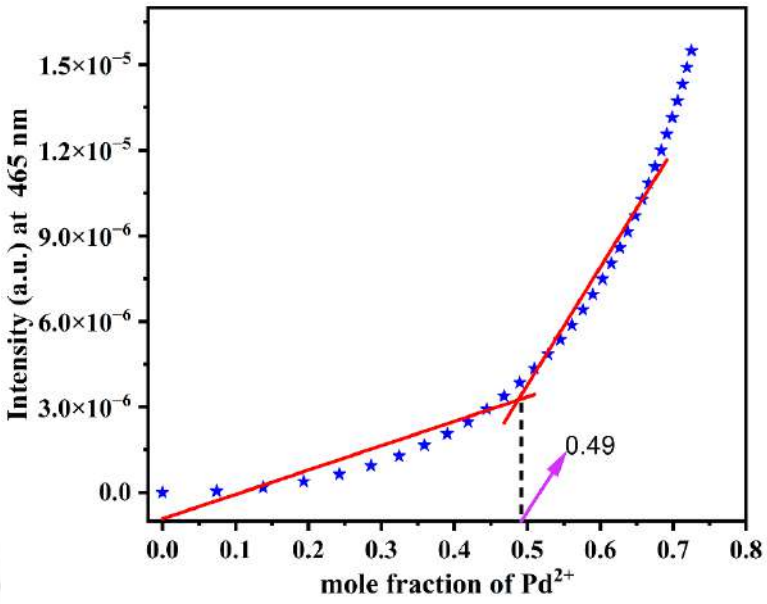

Figure A19. Job's plot for determining the binding stoichiometry between **L1** (15 μM) and $PdCl_2$ in EtOH-HEPES buffer mixture (3:7, *v/v*, pH = 7.4) at λ_{em}: 465 nm.

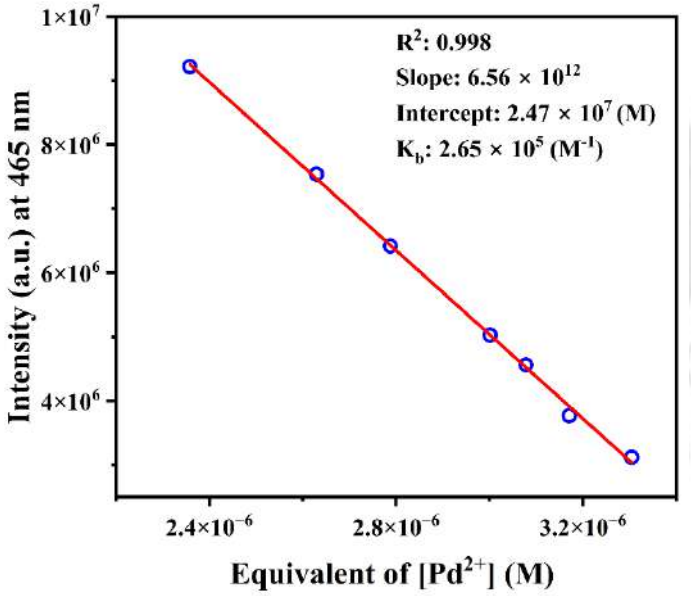

Figure A20. Determination of binding constants (K_b) of **L1** + Pd^{2+} complex based on Benesi-Hildebrand (B-H) method.

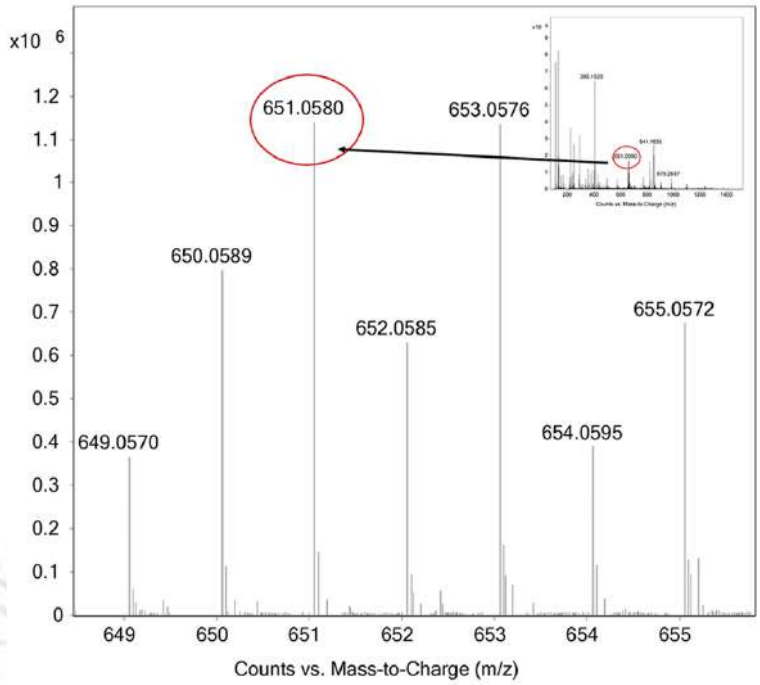

Figure A21. Mass spectrum of $\mathbf{L_1}$ with $Pd(NO_3)_2$ in methanol (inset: full range).

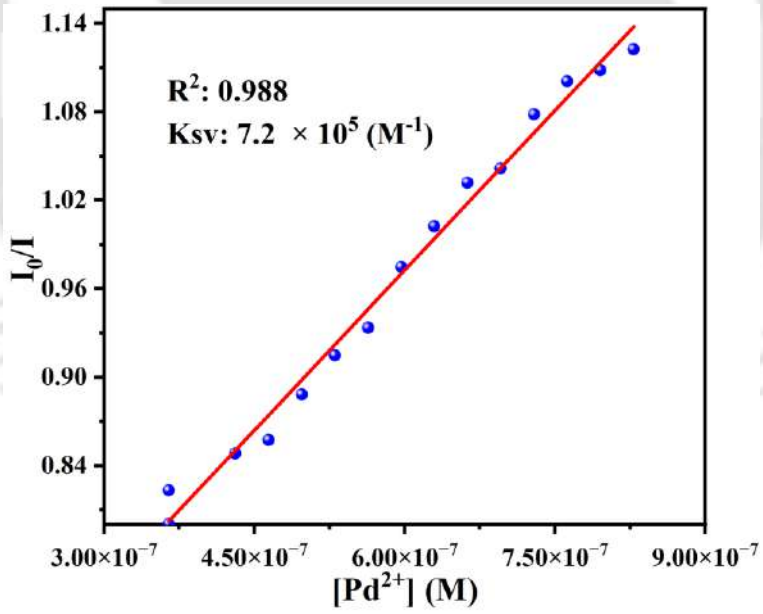

Figure A22. The Stern-Volmer plot obtained for $\mathbf{L_1}$ (15 μM) by gradual addition of $PdCl_2$ (0–22 μM) to determine the quenching constant (Ksv).

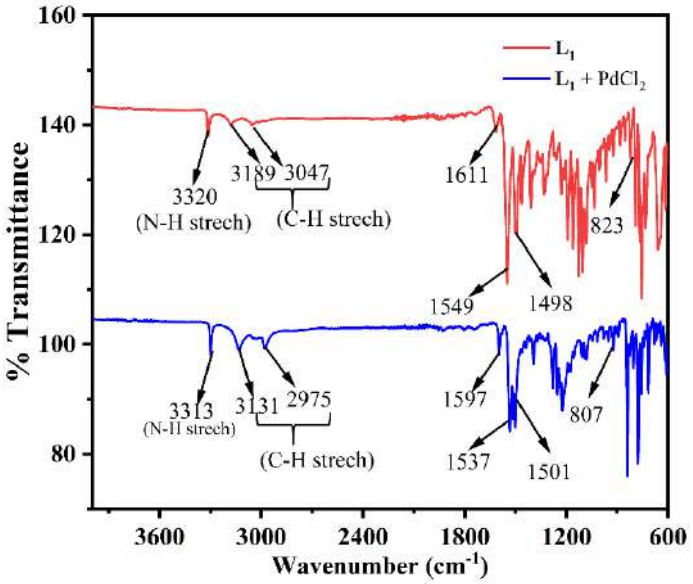

Figure A23. Full range (400-4000) cm^{-1} IR spectra of **L1** and **L1** + Pd^{2+} complex.

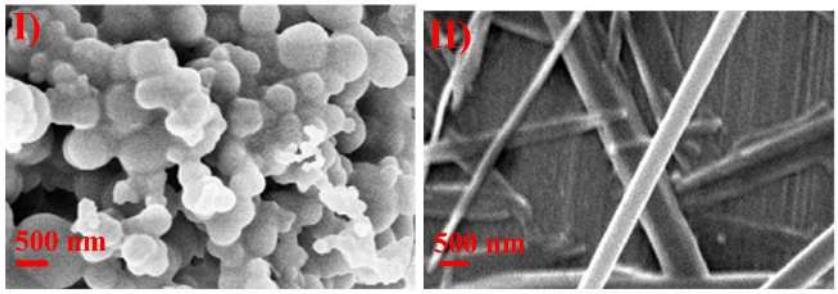

Figure A24. Higher magnification FESEM images of (I) **L1** and (II) **L1** + Pd^{2+}complex (scale bar = 500 nm) in (3:7, *v/v*) EtOH-HEPES medium.

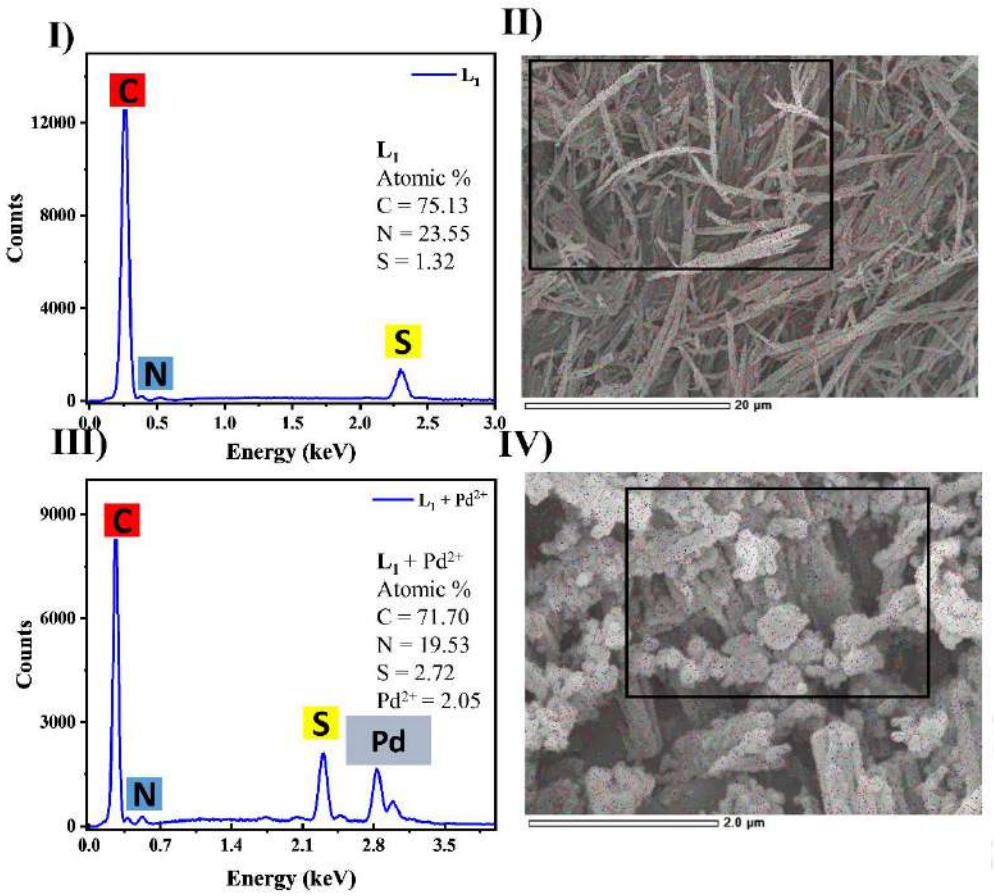

Figure A25. (I, III) EDX spectra and its corresponding area of the (II, IV) SEM images for **L1** and **L1** + Pd^{2+} complex.

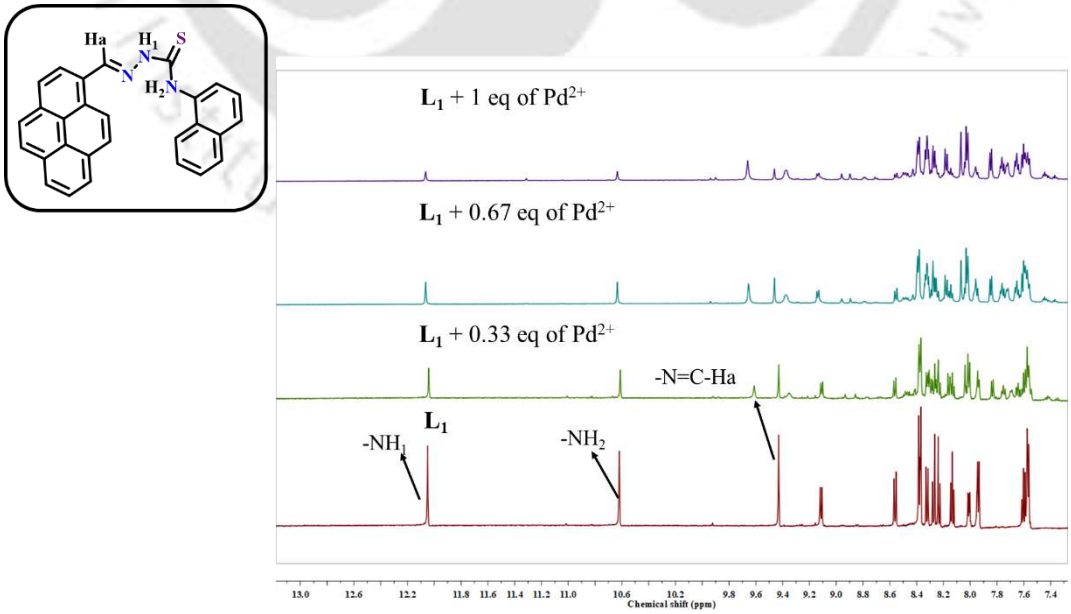

Figure A26. ^{1}H NMR titration study of **L1** with the incremental addition of $PdCl_2$ in DMSO-d_6.

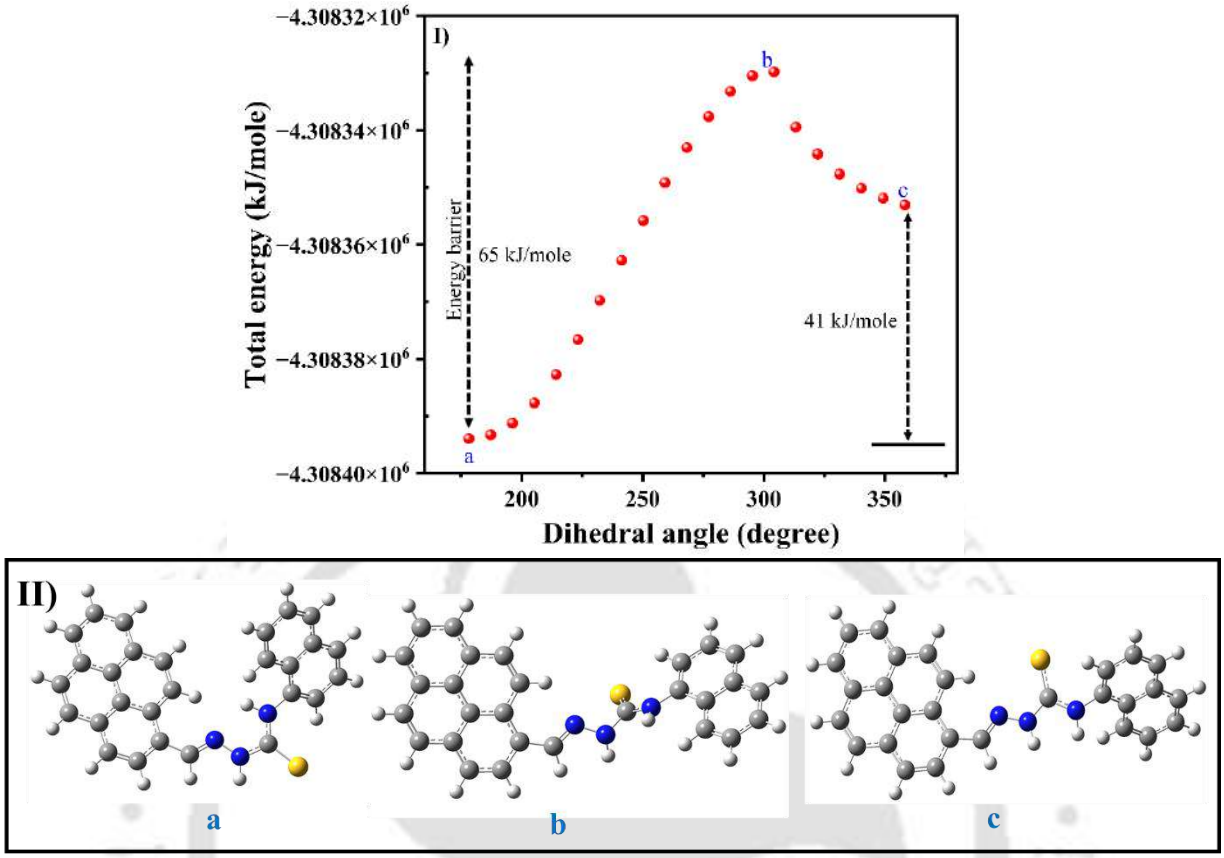

Figure A27. (I) The potential energy scan plot and (II) 3 conformers of $\mathbf{L_1}$ rotating the 1N-21N-3C-4S axis from +180° to +360° calculated involving the DFT/CAM-B3LYP/6-31G theoretical model.

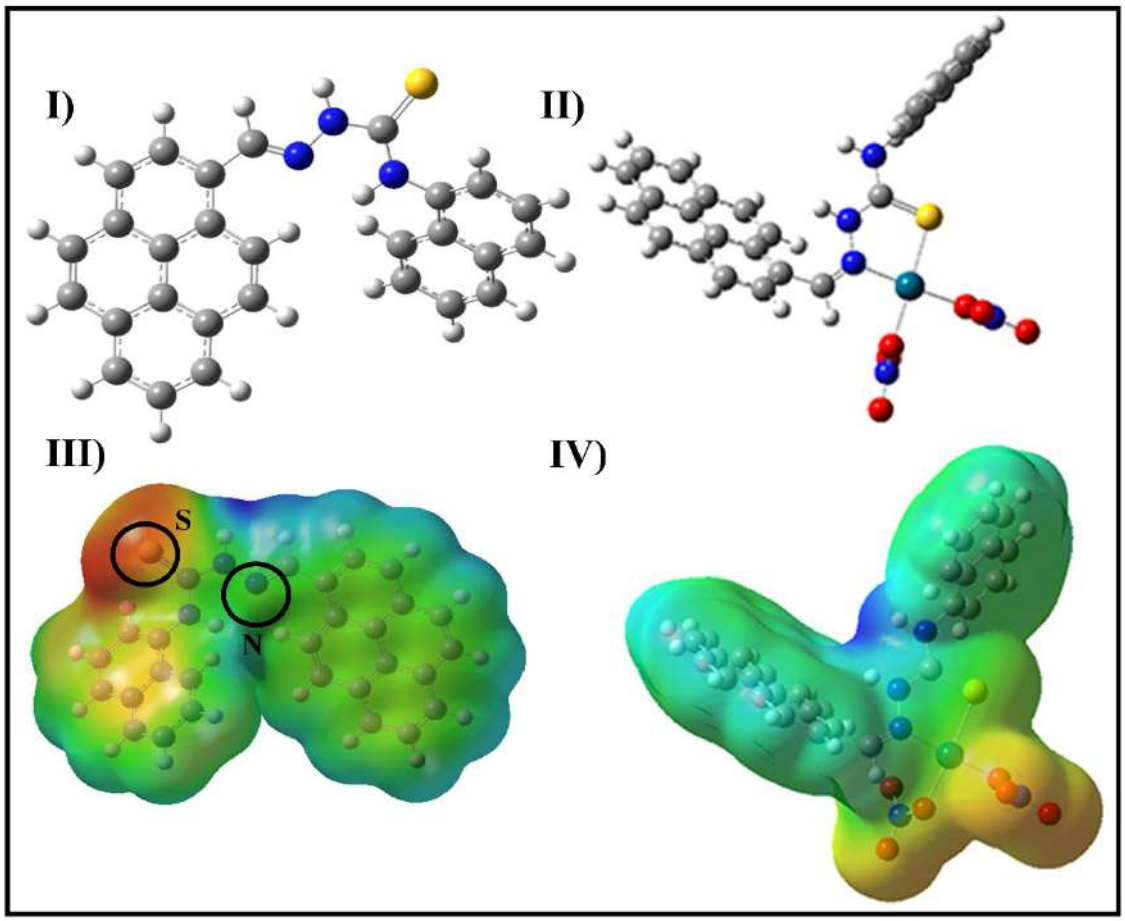

Figure A28. Energy optimized structure and ESP maps of (I), (III) **L**$_1$ and (II), (IV) [Pd(**L**$_1$)(NO_3)$_2$] complex.

L_1	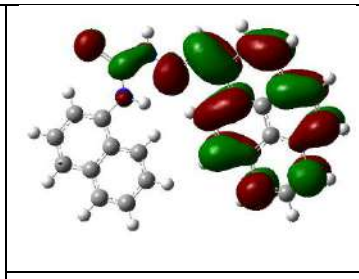	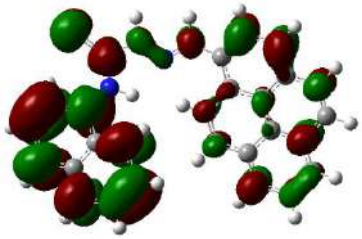	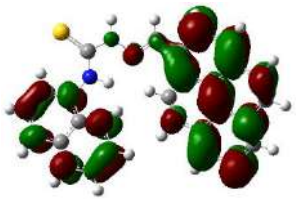	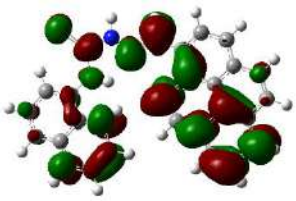
	LUMO	LUMO+1	LUMO+2	LUMO+3
	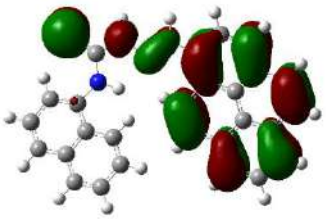	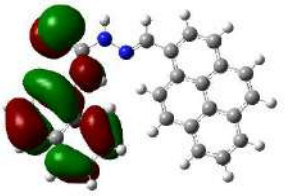	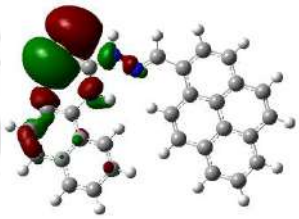	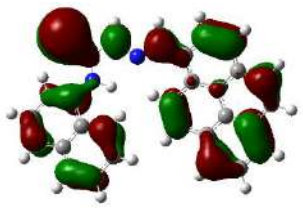
	HOMO	HOMO-1	HOMO-2	HOMO-3
$L_1 + Pd^{2+}$	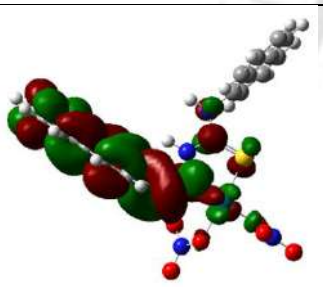	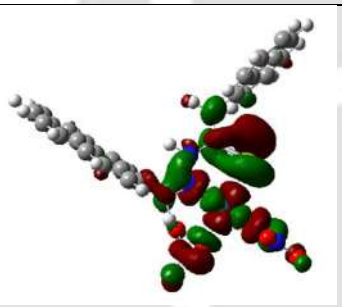	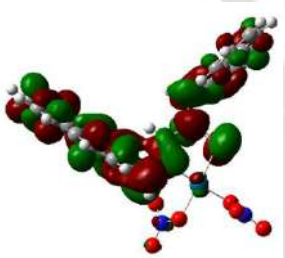	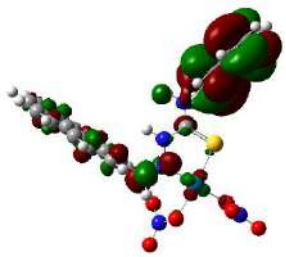
	LUMO	LUMO+1	LUMO+2	LUMO+3
	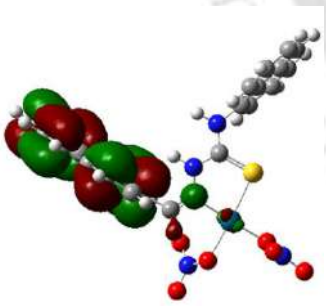	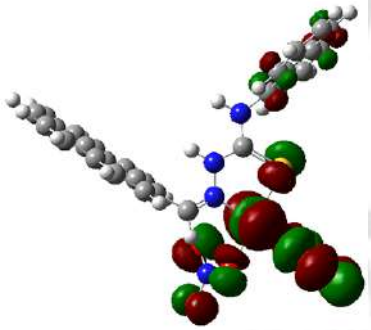	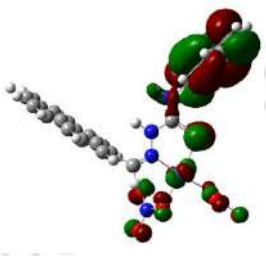	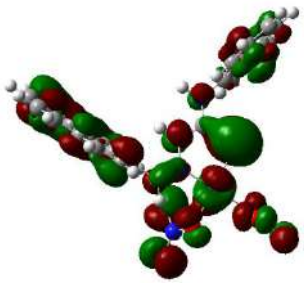
	HOMO	HOMO-1	HOMO-2	HOMO-3

Figure A29. Plausible HOMOs and LUMOs of **L_1** and its Pd^{2+} complex involved in electronic transition. The positive values of the counter map are represented in red colour (0.02 a.u.) and the negative values are represented in green colour (-0.02 a.u.).

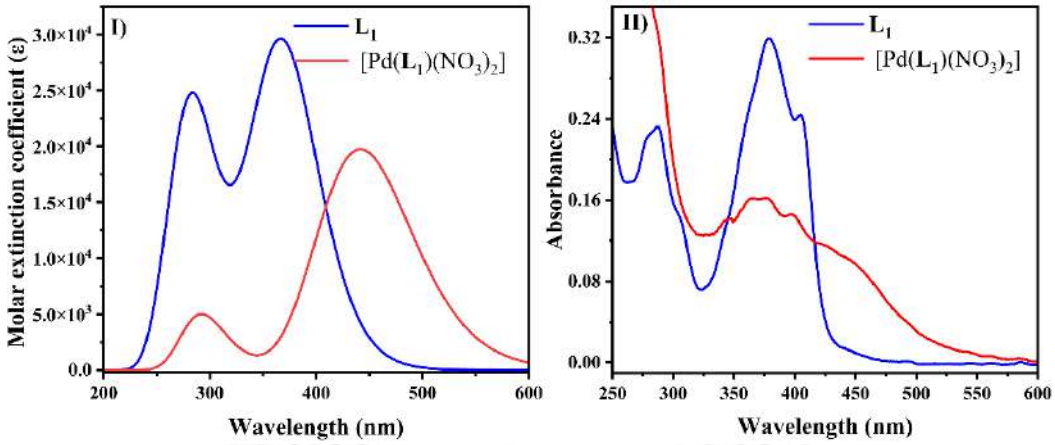

Figure A30. (I) Theoretical and (II) experimental UV-Vis spectra of **L1** and $[Pd(L_1)(NO_3)_2]$ complex.

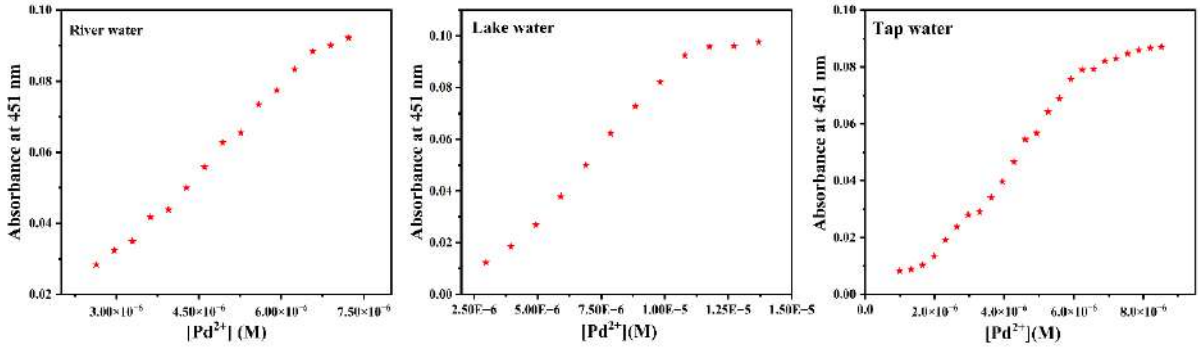

Figure A31. Absorbance intensity changes of **L1** with the gradual addition of Pd^{2+} solution in real water samples.

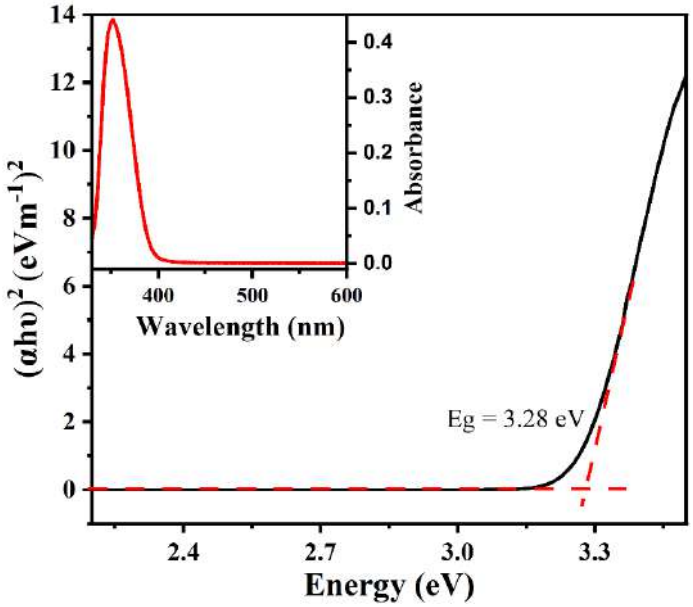

Figure A32. Tauc's plot of **L1** (inset: UV-Vis absorbance spectrum).

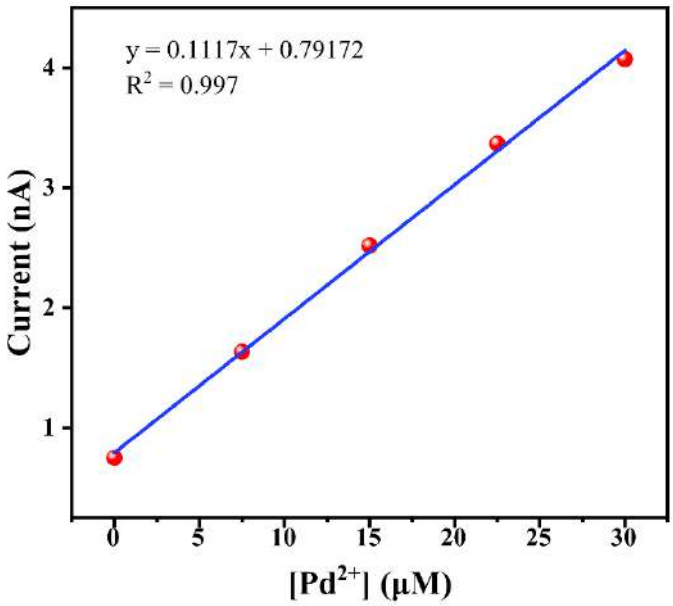

Figure A33. Variation of current with increasing Pd^{2+} concentration.

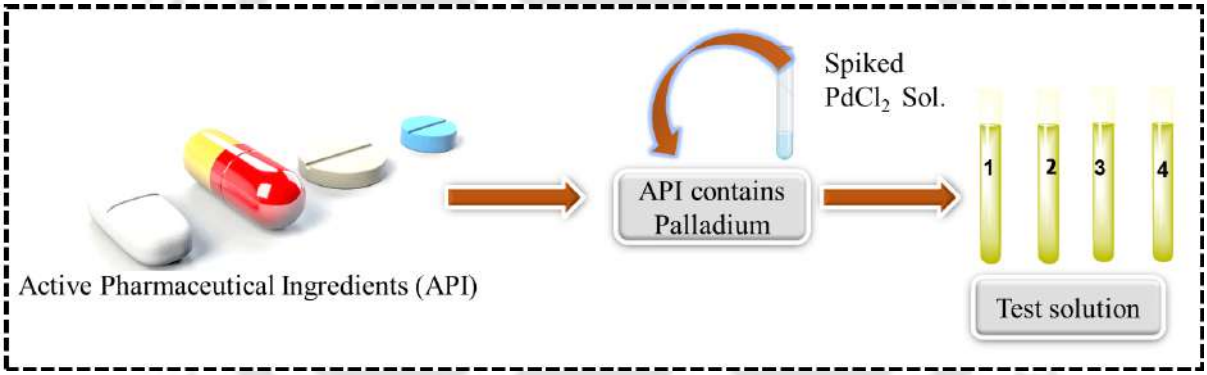

Figure A34. Schematic representation for drug sample analysis.

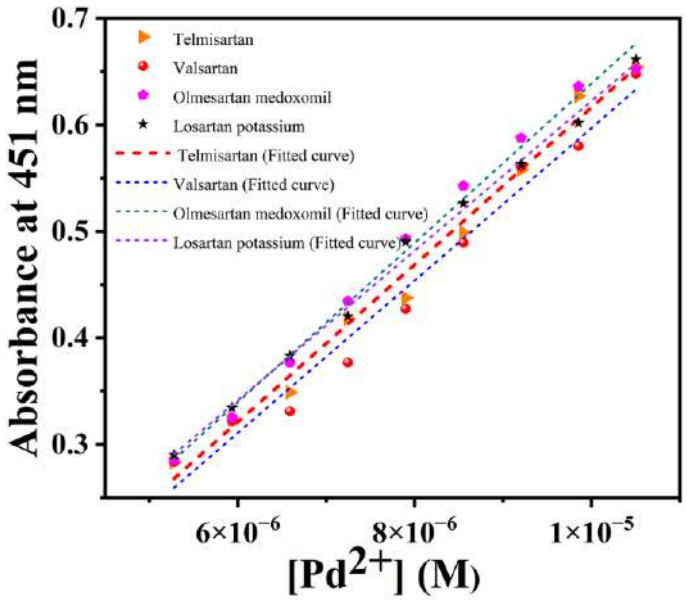

Figure A35. Linear fitted calibration curve with all used drug samples.

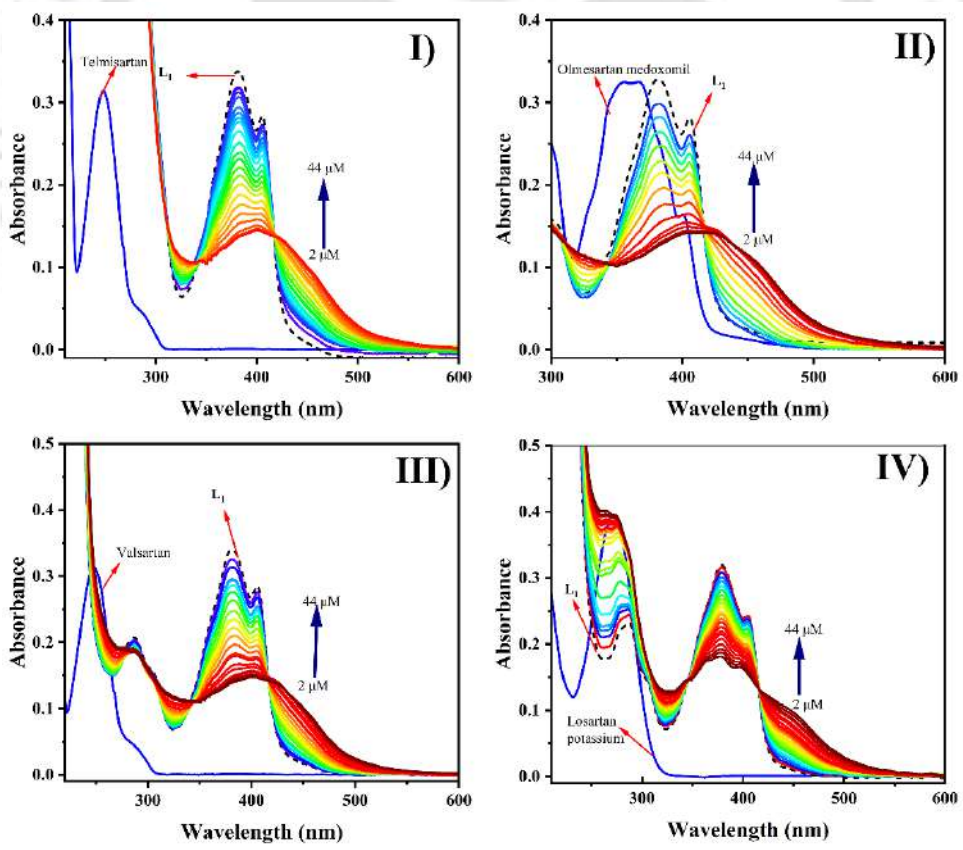

Figure A36. UV-Vis spectral titration of **L1** with $PdCl_2$ in presence of (I) Telmisartan, (II) Valsartan, (III) Olmesartan medoxomil, (IV) Losartan potassium.

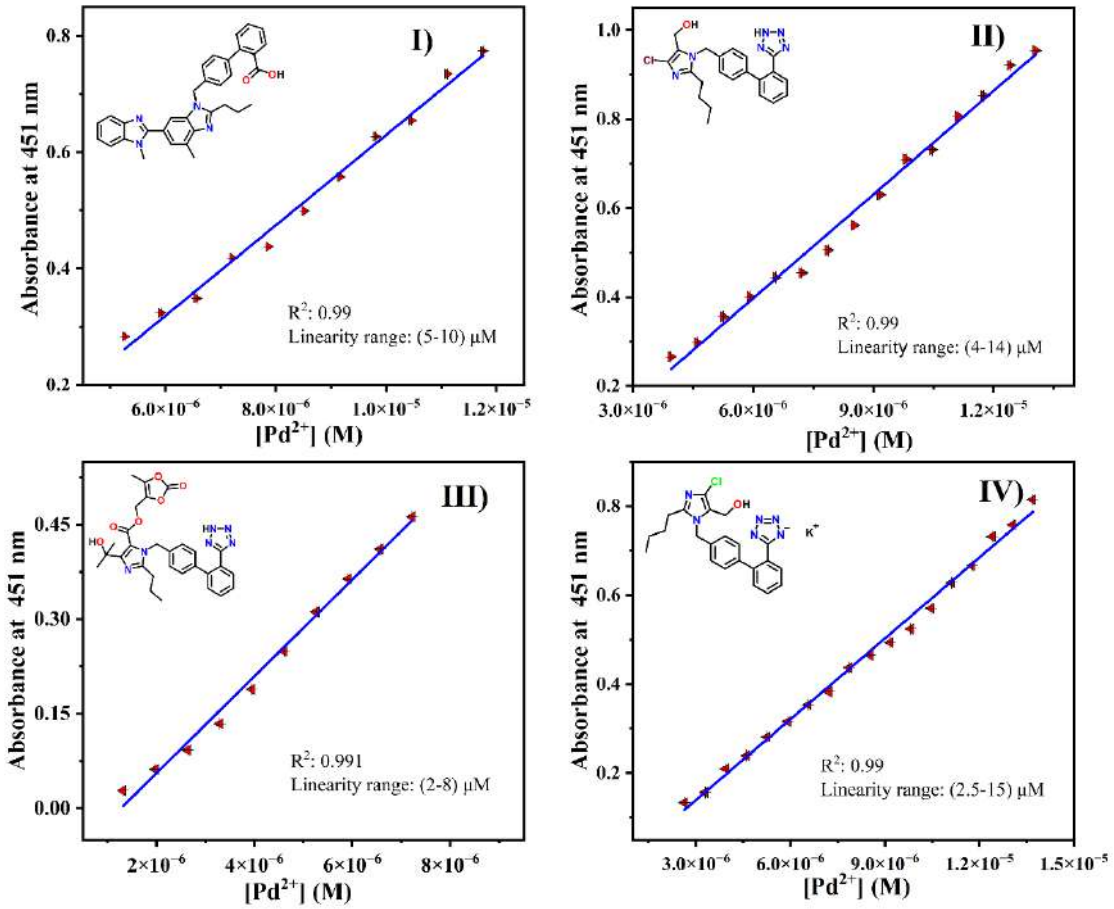

Figure A37. The calibration curve obtained from UV-Vis titration of **L1** with Pd^{2+} in the presence of (I) Telmisartan, (II) Valsartan, (III) Olmesartan medoxomil, (IV) Losartan potassium.

Table A1. Crystallographic data and refinement parameter of **L1**.

Formula	$C_{28}H_{19}N_3S$
CCDC NO	2347084
Mol. wt.	429.52
Cryst. color, habit	Yellow, Needle
T, K	298
Cryst. syst.	monoclinic
Space group	P21/c
a, Å	17.360(12)
b, Å	4.452(3)
c, Å	27.2861(19)
α, deg	90
β, deg	90.821(2)

γ, deg	90
V, Å^3	2094.1(2)
Z	4
Dcalcd, g cm^{-3}	1.362
μ, mm^{-1}	0.177
GOF[a] on F^2	1.217
F(000)	896
Reflection collected	2403
Unique reflections	3327
R_1[b], wR_2[c] ($I \geq 2\sigma(I)$)	0.0610, 0.1499
R_1[b], wR_2[c] (all data)	0.0698, 0.1656

[a]GOF (Goodness-of-fit) = $[\sum[w(F_0^2 - F_c^2)^2] / M - N]^{1/2}$ (M = number of reflections, N = number of parameters refined). [b]$R_1 = \sum \| F_0 | - | Fc \| / \sum | F_0 |$. [c]$wR_2 = [\sum[w(F_0^2 - F_c^2)^2] / \sum[w(F_0^2)^2]]$.

Table A2. Photophysical properties of **L1** in different solvents.

Solvents	***λ_{abs} (nm)***	***λ_{emi} (nm)***	***Stokes shift (nm)***	***Polarity***
Dioxane	380, 408	464	84	0.164
THF	388, 410	431, 450	62	0.207
Chloroform	389, 413	452	63	0.259
DMF	388, 410	445	57	0.386
DMSO	388, 411	427, 448	39	0.444
EtOH	381, 405	441	60	0.464
Acetonitrile	382, 406	423	41	0.654
Water	394. 425	484	90	1.000

Table A3. Fluorescence decay parameters of **L1** in EtOH-water mixture with various water fractions.

% of H_2O	***τ_1(ns)***	***τ_2 (ns)***	***α_1 (%)***	***α_2 (%)***	***τ(ns)***	***χ^2***	***Φ (%)***
0%	0.10	0.08	6.27	8.57	0.08	0.96	0.5
50%	0.88	4.31	4.33	1.86	1.58	0.99	1.4
70%	0.14	3.77	4.28	4.77	2.05	0.99	2.2

Table A4. Decay lifetime parameters of $\mathbf{L_1}$ in presence and absence of Pd^{2+}.

Entry	τ_1*(ns)*	τ_2 *(ns)*	α_1 *(%)*	α_2 *(%)*	τ*(ns)*	χ^2	Φ *(%)*
$\mathbf{L_1}$	2.36	4.88	0.33	0.66	4.04	1.02	4.53
$\mathbf{L_1}$ + Pd^{2+}	0.67	3.79	0.31	0.68	2.80	1.01	0.73

Table A5. TDDFT spectral outcomes of $\mathbf{L_1}$.

Electronic transition	*Theoretical λ (nm)*	*E (eV)*	*Oscillator strength*	*Major transition*	*coefficient*	*Experimental λ (nm)*
$S_0 \rightarrow S_1$	369.14	3.35	0.6986	HOMO→ LUMO	67 %	
				HOMO-4 → LUMO	45 %	
$S_0 \rightarrow S_3$	321.38	3.85	0.0207	HOMO-4 → LUMO+2	11 %	
				HOMO → LUMO+1	36 %	
				HOMO-2 → LUMO+1	12 %	379
$S_0 \rightarrow S_4$	314.12	3.94	0.1377	HOMO-1→ LUMO	59 %	
				HOMO → LUMO	11 %	
				HOMO-6 → LUMO	20 %	
$S_0 \rightarrow S_5$	285.41	4.34	0.3592	HOMO-3 → LUMO	54 %	
				HOMO → LUMO+1	15 %	
				HOMO-3 → LUMO	14 %	
				HOMO-1 → LUMO	21 %	
$S_0 \rightarrow S_6$	282.27	4.3925	0.1202	HOMO-1 → LUMO+1	55 %	
				HOMO-1 → LUMO+2	25 %	
				HOMO-7 → LUMO	41 %	
$S_0 \rightarrow S_8$	263.26	4.7096	0.1420	HOMO-1 → LUMO	26 %	
				HOMO → LUMO+2	14 %	288
				HOMO-7 → LUMO	33 %	
				HOMO-1 → LUMO	16 %	
				HOMO-3 → LUMO+4	12 %	
$S_0 \rightarrow S_{10}$	258.21	4.8017	0.0308	HOMO → LUMO+1	21 %	
				HOMO → LUMO+3	27 %	
				HOMO → LUMO+4	35 %	

Table A6. TDDFT spectral outcomes of [Pd($\mathbf{L_1}$)(NO_3)$_2$] complex.

Electronic transition	*Theoretical λ (nm)*	*E (eV)*	*Oscillator strength*	*Major transition*	*coefficient*	*Experimental λ (nm)*
$S_0 \rightarrow S_1$	442	2.80	0.4722	HOMO →LUMO	66 %	451
				HOMO-4→LUMO+2	15 %	
$S_0 \rightarrow S_9$	312	3.96	0.0287	HOMO-3→LUMO	22 %	345
				HOMO→LUMO+4	43 %	
$S_0 \rightarrow S_{10}$	288	4.29	0.1068	HOMO-4→LUMO	18 %	293
				HOMO-4→LUMO+2	12 %	
				HOMO-3→LUMO	37 %	
				HOMO-3→LUMO+2	23 %	
				HOMO-2→LUMO	24 %	
				HOMO-2→LUMO+2	19%	

Table A7. Comparative analysis of Pd^{2+} in different real water samples by using UV-Vis spectroscopy and ICP-OES method.

Test sample	*UV-Vis spectroscopy*				*Inductively coupled plasma optical emission spectroscopy (ICP-OES)*			
	Added (μM)	*Found (μM)*	*% of Recovery*	*RSD %*	*Added (μM)*	*Found (μM)*	*% of Recovery*	*RSD %*
River water	0	-	-	-	0	-	-	-
	3	2.88	96	6.7	3	2.82	106	0.7
	5	4.59	92	5.5	5	5.25	95	0.5
Lake water	0	-	-	-	0	-	-	-
	3	2.62	86	2.64	3	3.39	94	5.6
	5	4.16	83	0.63	5	5.12	97	2.7
Tap water	0	-	-	-	0	-	-	-
	3	2.69	89	3.9	3	3.39	88	2.4
	5	4.20	84	2.0	5	5.57	89	1.4

Table A8. Comparative recovery study results of Pd^{2+} ion detection using probe $\mathbf{L_1}$.

Test sample	*UV-Vis spectroscopy*				*Inductively coupled plasma optical emission spectroscopy (ICP-OES)*			
	Added (μM)	*Found (μM)*	*% of Recovery*	*RSD %*	*Added (μM)*	*Found (μM)*	*% of Recovery*	*RSD %*
	0	-	-	-	0	-	-	-
A + $PdCl_2$	7	7.06	99	0.6	7	7.07	101	0.5
	9	9.20	97	4.8	9	8.37	93	2.4
	0	-	-	-	0	-	-	-
B + $PdCl_2$	7	7.03	99	3.1	7	7.13	101	3.5
	9	9.11	98	0.5	9	8.55	95	0.4
	0	-	-	-	0	-	-	-
C + $PdCl_2$	7	7.49	93	4.2	7	6.78	96	4.8
	9	8.96	99	2.0	9	8.89	98	2.2
	0	-	-	-	0	-	-	-
D + $PdCl_2$	7	7.49	93	3.3	7	6.30	95	4.7
	9	8.82	102	0.6	9	9.18	102	6.3

[#] A = Telmisartan; B = Valsartan; C = Olmesartan Medoxomil; D = Losartan Potassium.

Table A9. LOD values for $\mathbf{L_1}$ towards Pd^{2+} ion in presence of all drug samples.

Test sample	*Linearity range (μM)*	*LOD (M)*
A + $PdCl_2$	5-11	1.3×10^{-7}
B + $PdCl_2$	6.5-11	1.2×10^{-7}
C + $PdCl_2$	6.0-10	1.0×10^{-7}
D + $PdCl_2$	6.5-11	2.0×10^{-7}

Table A10. Comparative literature survey of L_1 with another reported chemoreceptor.

Chemosensor Structure	*Detection method*	*Sensing solvent*	*Analytes detected*	*Potential application of chemosensor*	*LOD*	Ref
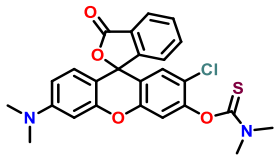	Colorimetry, Fluorescence	pH 7.0 phosphate buffered 50% aq. DMSO	Pd^{2+}	Detection of residual Pd in ibuprofen and another drugs sample.	10 nM	31
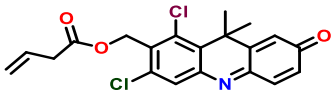	Colorimetry, Fluorescence	PBS buffer (10 mM, pH = 7.4)	Pd^{0}	Pd detection in drugs, living cell	2.2 nM	32
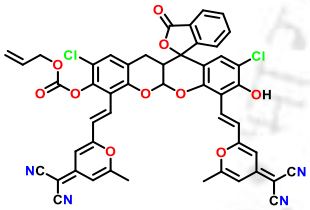	Fluorescence	EtOH-PBS buffer solution (10 mM, 1:1, *v/v*, pH = 7.4)	Pd^{2+}	Lysosomes targeting ability	37 nM	66
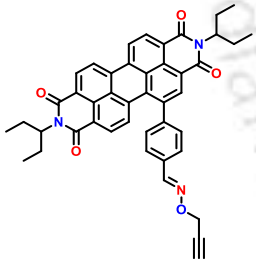	Fluorescence	90% HEPPS Buffer/DMSO (pH = 7.2)	Cu^{2+} Pd^{0}	Paper strips, in-vitro cell studies	79 nM	67
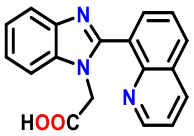	Fluorescence	1:1 (*v/v*) DMSO/PBS (pH = 6.0)	Pd^{2+}	-	0.2 µM	68
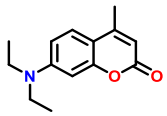	Fluorescence and naked eye	-	Pd^{2+}	Paper strips, in-vitro cell imaging	0.25 µM	69

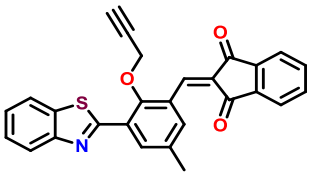	Fluorescence	H_2O-THF (2:5, *v/v*)	Pd^{2+}	Filter Paper strips	14.6 nM	28
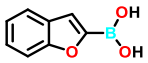	Fluorescence	Acetonitrile	Pd^{2+}	-	9.8 n M	70
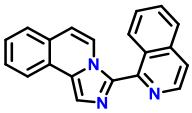	Fluorescence and naked eye	MeOH/ HEPES buffered aqueous solution (5 mM, pH = 7.4, 6:4, *v/v*)	Pd^{2+}	Biological cell imaging	0.21 µM	56
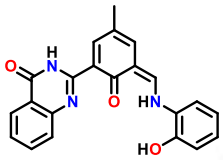	Fluorescence	PBS buffer (10 mM, pH = 7.4)	Pd^{2+}	Living cell imaging	0.48 µM	71
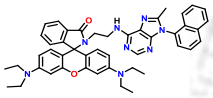	Fluorescence	EtOH/HEPES buffer (3/2, *v/v*, pH = 7.4)	Pd^{2+}	Filter paper strips	49.5 nM	17
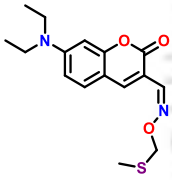	Fluorescence	EtOH/H_2O (4:6, *v/v*)	Pd^{2+}	In-vitro cell imaging	41.5 nM	27
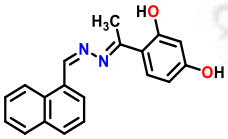	Colorimetric	MeOH/H_2O (1:1, *v/v*)	Pd^{2+}	test kit (paper, cotton, and N-95 mask)	0.98 µM 0.49 µM	72
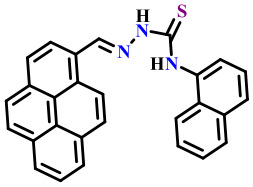	Colorimetric and Fluorescence	EtOH/HEPES buffered aqueous solution (5 mM, pH = 7.4, 4:6, *v/v*)	Pd^{2+}	i) TLC paper strips. ii) Pd^{2+} detection in presence of API and real water sample. iii) Real-time electrical detection	41 nM	This work

Chapter 4

Solvent-Tuned Fluorometric Detection of Al^{3+} ion and Cysteine by a Benzimidazole-Linked AIE Active Sensor in Solution and Solid Matrix*

Abstract:

The probe 6-(quinolin-2-yl)-5,6-dihydrobenzo[4,5]imidazo[1,2-*c*]quinazoline (**L2H**) was synthesized and found to exhibit weak fluorescence in pure methanol but exhibited typical AIE phenomenon in 90% H_2O-MeOH mixture. Formation of a larger agglomerated hetero structure of **L2H** was confirmed by FESEM image. This probe was found to detect Al^{3+} ion and cysteine in three aqueous solvents *viz*., (i) MeOH/HEPES buffer (8:2, pH = 7.4, rt), (ii) water and (iii) aqueous CTAB medium. The sensitivity as well as selectivity of Al^{3+} ion and cysteine got enhanced in surfactant environment, having very low detection limit of 2.75 nM (for Al^{3+}) and 2.65 nM (for cysteine). Upon binding to Al^{3+}, cyclic bidentate **L2H** was converted to tridentate **L2′**, having an open structure. Cysteine converted **L2H** to fluorescent **L2–L2** *via* formation of **L2•** which was detected using EPR spectroscopy at 77 K. Molecular ion peaks due to cystine and **L2–L2** were found in ESI(-) mass spectrometry. Larger aggregates of **L2H** formed through AIE activity in presence of these two analytes were observed in FESEM and DLS experiments. Outcome of DFT/TDDFT calculation performed on **L2H**, [Al(**L2'**)$(NO_3)_3$], and **L2–L2** supported experimental findings. On-site detection in solution and solid-state matrix as well as reversible fluorometric outcomes were formulated to construct a logic gate circuit.

* This work has been published in:

A. Mondal, V. Manivannan, *ChemistrySelect*, 2025, **10**, e03977.

4.1 Introduction:

With the ever increasing environmental pollution created by hazardous metal ions, it has become a serious threat to our ecosystem, receiving a lot of attention because of its negative impacts on the biosphere.[1–5] Since aluminium is the most widely used element in our daily life, extensively used in various textiles, food additives, pharmaceuticals and paper-industry.[6–8] But even a very less amount of aluminium in the brain can lead to illnesses like Parkinson's disease, loss of memory, dysfunction of the central nervous system, Irritable Bowel Syndrome (IBS) and so on.[9–13] So, by utilizing affordable and effective methods for the selective detection of Al^{3+}, it became of utmost importance to address this pressing problem.

In presence of various other biological amino acids, the selective recognition of cysteine (Cys) over homocysteine (Hcy) gained significant attention among researchers working on amino acid detection using selective functional group bearing chemosensors.[14] Since cysteine contains only a thiol residue, it participates in various physiological processes, by maintaining proper redox homeostasis and stabilizing proteins structurally through disulfide bonds.[15,16] Additionally, cysteine also helps to regulate various nervous system and cardiovascular functions.[17] Excessive levels of Cys can cause Parkinson's, Alzheimer's disease, AIDS, cardiovascular dysfunction and numerous disorders like liver and skin damage, depigmentation of hair, shrinkage of muscle cells and others. Again, a greater risk of various tumour regeneration has been tightly linked to the total cellular Cys content.[18,19] Although there are numerous fluorogenic probes for the detection of biologically important metal ions and neutral biothiols in only aqueous medium are reported, the use of surfactant molecule for such analyte detection has been very less explored. The presence of surfactant media enhances the selectivity, sensitivity, and rapid response time of the probe, which can function as suitable sensors for analyte detection.[20,21] Based on these advantages, we focused our interest on the detection of Al^{3+} and cysteine in a surfactant-assisted CTAB medium.

Various small molecular probes proposed until then possessed a planar geometry and emitted light in dilute solution. However, π-π stacking interaction that cause aggregation-caused quenching (ACQ) quenches their emission intensity in a compact solid-state.[22] Aggregation-induced emission (AIE), a unique fluorescence phenomenon of fluorogenic probes, was first reported by Tang's group.[23] AIE-based luminogens showed strong emission in their aggregated state and were non-emissive as discrete molecules in solution.[24] AIEgens, are widely studied for applications in liquid crystals,[25] OLEDs,[26] photoluminescence,[27] sensing, and biomolecule

recognition.[28] Benzimidazole analogue acted as a multifunctional structural component which was used in the synthesis of various novel heterocyclic compounds to develop new therapeutic agents.[29] Also due to the excellent fluorescent properties of fused benzimidazole probe, they can be used as organic luminophores, chemosensors/chemodosimeters, optoelectronics, optical lasers. However, an AIE active sensor on a benzimidazole unit is very rare which promotes the intramolecular charge transfer (ICT) between a donor and an acceptor group and exhibits AIE property.[30,31] In this Chapter 4, we describe a benzimidazole appended quinoline linked AIE active sensor (**L2H**) for the detection of Al^{3+} ion and cysteine.

4.2 Experimental Section:

4.2.1 Synthesis

6-(quinolin-2-yl)-5,6-dihydrobenzo[4,5]imidazo[1,2-c]quinazoline (**L2H**)

A solution of 2-(2-aminophenyl)-1H-benzimidazole[32] (0.212 g, 1 mmol) and 2-quinolinecarboxaldehyde (0.172 g, 1 mmol) in methanol (50 mL) was heated at reflux for 12 h (Scheme 1). Solution was concentrated to 25 mL and was kept at 5 °C to facilitate slow evaporation. A yellow solid material separated out which was filtered and washed with cold methanol three times. Yield: 0.261 g (75%), M.P.: 323 °C. 600 MHz ^{1}H NMR (DMSO-d_6, δ (J, Hz)): 8.37 (s, 1H), 8.04 (1H, d, 6.0), 7.98 (2H, dd, 12.0, 6.0), 7.91 (1H, s), 7.82 (1H, t, 6.0), 7.70 (1H, d, 6.0), 7.65 (1H, t, 6.0), 7.30 (4H, dd, 12.0, 6.0), 7.22 (1H, t, 6.0), 7.13 (2H, m 12.0, 6.0). 600 MHz ^{13}C NMR ($CDCl_3$, δ): 159.11, 147.02, 146.83, 144.18, 143.10, 138.57, 133.38, 132.18, 130.68, 129.27, 128.31, 127.92, 127.56, 125.08, 122.76, 122.62, 119.02, 118.64, 118.25, 115.06, 111.91, 110.79, 70.00. ESI Mass *m/z* calcd. for $C_{23}H_{16}N_4O_2$, 349.1568; found: 349.1576 (**L2H** + H^+). Selected IR peaks (ATR mode, cm^{-1}): 3317(m), 3182(w), 1492(s), 1413(m), 1198(s) (Figure A1-A4).

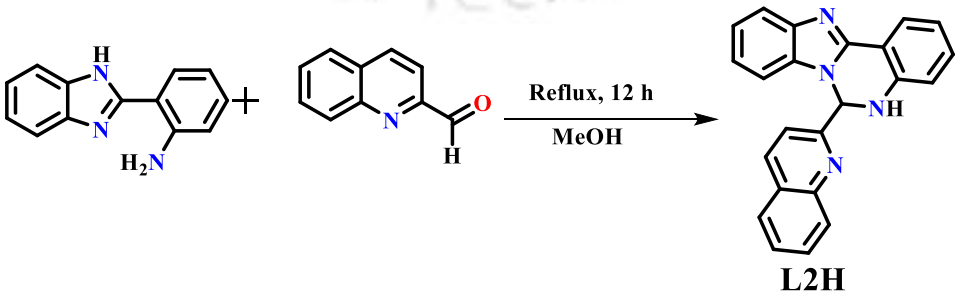

Scheme 1. Synthesis route of **L2H**.

4.2.2 Fluorescence Microscopy

Freshly prepared **L2H** (1×10^{-5} M) solution and **L2H** mixed with 10 equivalents of Al^{3+} and cysteine solution, drop cast on a glass slide. After drying the sample at room temperature, the images were captured using Olympus fluorescence microscope under UV light.

4.3 Results and Discussion:

4.3.1 Molecular Structure of L2H

The single crystal of **L2H** was obtained by diffusion of Et_2O vapours into its acetonitrile solution, which crystallized in space group $P2_1/n$ (Table A1). The lattice consisted of a 1:1 mixture of two enantiomers consistent with the presence of an asymmetric carbon at C1 and ORTEP plot of one enantiomer is provided in Figure 1. The plane formed by all carbon and nitrogen atoms of 5,6-dihydrobenzo[4,5]imidazo[1,2-*c*]quinazoline moiety is nearly planar which is also nearly vertical with the plane formed by the atoms of quinoline ring and the angle calculated between these two planes being 88.93°. Packing diagram also revealed the presence of π···π interactions with the distance of 3.237 Å between two 5,6-dihydrobenzo[4,5]imidazo[1,2-*c*]quinazoline moieties and 3.530 Å between two quinoline rings (Figure A5I). Furthermore, crystals of **L2H** exhibited greenish yellow colour when observed under the fluorescence microscope (Figure A5II).

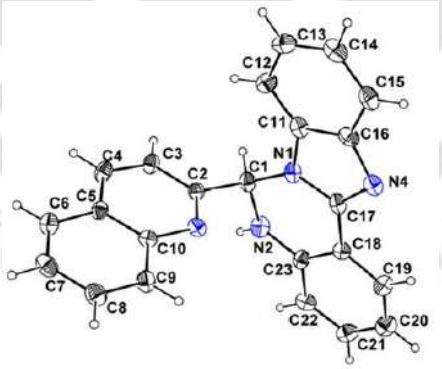

Figure 1. ORTEP plot of **L2H** with 30% ellipsoid probability.

4.3.2 Spectral Behaviour of L2H in Various Solvents

The spectral absorption properties of **L2H** has been monitored in nine different solvents and the observed spectral details are presented in Figure A6 and Table A2. In all tested solvents, **L2H** showed absorption maximum at 341 nm (half-width lying in the range 50–70 nm), but only in water the peak was broader (half-width = 94 nm) having a long tail which may be due

to poor solubility in water. The fluorescence spectra recorded (λ_{ex} = 354 nm) in these solvents indicated that **L2H** is weakly fluorescent in nature with the emission maximum lying in the range 407 nm (in hexane) to 523 nm (in water). This polarity dependent spectral red shift confirmed a moderate ICT transition between the donor and acceptor moieties present in the compound.

As evident from the packing diagram of **L2H** wherein molecules were stacked in a face-to-face arrangement and two sets of π-π stacking interactions were found between two kinds of planar moieties present in the probe, aggregate formation in solution was also expected (Figure A7). The aggregation behaviour of **L2H** was investigated with the help of UV-Vis and fluorescence study by using a binary solvent of MeOH and water. In pure MeOH, **L2H** exhibited a well-defined absorbance band at around 345 nm which remained nearly the same till 80% water-MeOH mixture beyond which lead to peak broadening accompanied by upliftment of baseline with 90% and 100% water (Figure 2A). This observation suggested the aggregate formation in this mixed solvent system. In MeOH, **L2H** was weakly emissive (λ_{em} = 422 nm, φ = 0.16%) upon gradual addition of water, fluorescence intensity decreased up to 50%. With further addition of water, intensity increased rapidly and reached a maximum at 90% (λ_{em} = 476 nm, φ = 5.00%) and decreased slightly in 100% water. Thus ~7 times enhancement of intensity accompanied by a red shift of ~54 nm on changing the solvent from MeOH to 90% water-methanol (Figure 2B, 2C) indicated formation of J-type aggregates.[33] So, probe **L2H** was confirmed to exhibit aggregation induced emission behaviour in 9:1 (H_2O:MeOH) solution (Figure 2D). A Drop in emission intensity with water content greater than 90% was due to aggregated matter becoming insoluble.[34,35] The fluorescence lifetime measurement also confirmed that on increasing the water fraction, the fluorescence lifetime enhanced from 0.08 ns (*fw* = 60%) to 5.02 ns (*fw* = 90%) (Figure 2E, Table A3). In 90% water, the intermolecular rotation was restricted due to molecular aggregation which blocked the non-radiative pathway due to which the molecule stayed longer in the excited state. In 9:1 (H_2O:MeOH) mixture, the intensity was recorded by increasing the concentration of **L2H** gradually from 0.5 to 10 μM, a systematic growth in emission intensity abruptly levelled off, revealing a critical aggregation concentration (CAC) of 3.4 μM (Figure A8). The aggregation pattern was further analyzed by DLS and FESEM experiments. The DLS output revealed that the average particle size (Z_{avg}) of the respective aggregate in 0%, 40% and 90% water were 453, 537 and 687 nm, respectively (Figure 3A). The result concluded that the particle size increased with the increase of water

fraction in MeOH medium. FESEM images of same solutions revealed a smooth circular disc shaped particles (0%) (particle size 178 nm) which turned into oval shaped spine likes particles of average size 250 nm (40%) in micro-meter range and finally in 90% water, a massive agglomerated hetero structure was formed with considerably increased of particle size of 664 nm (Figure 3B, A9). So, the morphology of the AIE-gen can be easily controlled by solvent switching.

Twisted Intramolecular Charge Transfer (TICT) behaviour of **L2H** was also measured by altering the viscosity by varying amount of glycerol in MeOH. Probe had a lower emission intensity in pure MeOH, but upon increasing the percentage of glycerol the emission intensity increased. Thus in 100% glycerol, the twisted state of **L2H** got stabilized, resulting in maximum AIE emission at 419 nm (Figure A10). This was ascribed to the TICT phenomenon[36,37] due to the restriction of intramolecular rotation of the quinoline ring with respect to 5,6-dihydrobenzo[4,5]imidazo[1,2-*c*]quinazoline moiety in a viscous medium.

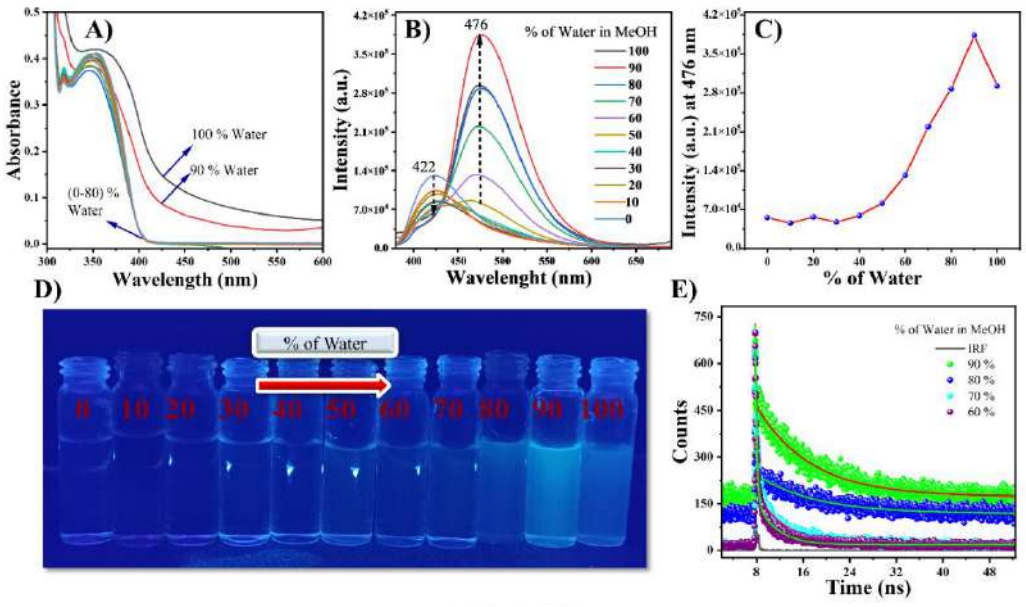

Figure 2. (A) Absorption and (B) emission of spectra of **L2H** with increasing water percentage in MeOH, (C) the plot of fluorescence intensity *versus* various water content in MeOH/water mixture for **L2H**, (D) fluorescence photographs of **L2H** with increasing *fw* (0–100%) under long UV lamp, and (E) fluorescence decay profile of **L2H** by varying water content in MeOH *fw* (60–90%).

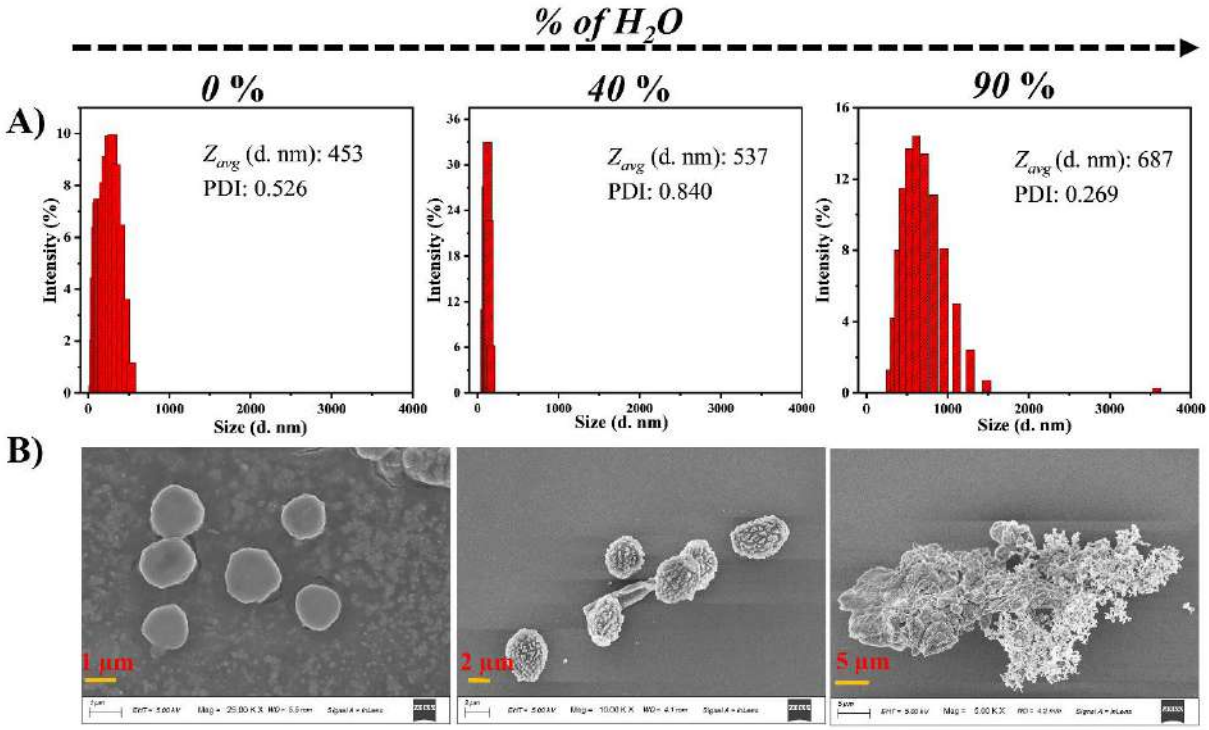

Figure 3. (A) Particle size distribution and (B) FESEM images of **L2H** (4 µM) by varying the solvent ratio in MeOH/water mixture.

4.3.3 Spectral Response with Various Metal Ions and Amino Acids

In MeOH/HEPES buffer (1 mM, pH = 7.4, 8/2, *v/v*) **L2H** exhibited prominent absorption at λ_{max} = 353 nm, due to n→π^* transition. After addition of metal ion (2 equivalents) solution like Li^+, Na^+, K^+, Ca^{2+}, Cu^{2+}, Cr^{3+}, Co^{2+}, Fe^{3+}, Zn^{2+}, Ni^{2+}, Fe^{2+}, Pd^{2+}, Pt^{2+}, Au^{3+} (chloride salts), Ag^+, Mg^{2+}, Be^{2+} (sulphate salts), Mn^{2+} (acetate salt), Pb^{2+}, Ag^+ (nitrate salts) no change in spectra was observed (Figure A11I). Upon the gradual addition of 2 equivalents of $Al(NO_3)_3{\cdot}9H_2O$ solution, the intensity of the absorption band at 353 nm decreased with the appearance of shoulder at around 376 nm and a broad band around 415 nm. A distinct isosbestic point at 368 nm indicated the presence of **L2H** and **L2H** bound to Al^{3+} ion, confirming the formation of a complex species (Figure A11II). Among the other tested metal ions the absorbance intensity i) remain unchanged for Li^+, Na^+, Pt^{2+} , Mn^{2+}, Mg^{2+}, ii) decreased by (1 – 3%) at 353 nm for Pb^{2+}, K^+ and Ag^+ and iii) slightly increased (3 – 7%) for Fe^{3+}, Cr^{3+}, Au^{3+}, Be^{2+}, Mn^{2+}, Co^{2+}, Ni^{2+}, Cu^{2+}, Zn^{2+}, Cd^{2+}, Hg^{2+}, Pd^{2+} metal ions.

The UV-vis spectral response of **L2H** towards various amino acids *viz*., alanine, glycine, leucine, homocysteine, cysteine, arginine, methionine, tyrosine, phenylalanine, lysine,

isoleucine, valine, tryptophan, asparagine and aspartic acid (Figure A12) has been recorded in MeOH/HEPES buffer medium. Only with addition of cysteine, intensity of 353 nm band decreased and shifted to 367 nm, while all other amino acids imparted no significant spectral absorbance change (Figure A13I). The titration experiments were performed with the gradual addition of cysteine (up to 2 equivalents) into **L2H** solution, and an isosbestic point appeared at 370 nm closer to the 367 nm band (Figure A13II). A visual colour change from colorless to greenish yellow was observable through naked-eye for both Al^{3+} and cysteine, which confirmed the red shift of the absorption band. So, we can conclude that **L2H** enabled naked-eye detection of Al^{3+} ions and cysteine in solution.

To enhance the sensing efficiency of **L2H**, the spectral behaviour of **L2H** was evaluated in aqueous surfactant medium (3 mmol CTAB, CMC = 1 mmol). However, no distinct spectral shift was observed in the UV-Vis spectra of **L2H** in both aqueous and aqueous surfactant media upon adding Al^{3+} and cysteine (Figure A14). On excitation with 354 nm light, **L2H** showed an emission peak at around 423 nm in MeOH/HEPES buffer, while at 464 nm in pure water and aqueous CTAB medium (Figure A15). The CTAB micelles provide a well-defined hydrophobic microenvironment that facilitates strong interactions between **L2H** and target analytes. So, we chose a cationic surfactant cetyltrimethylammonium bromide (CTAB) medium for selective and sensitive detection of metal ions and amino acids.

In MEOH/HEPES medium out of the selected metal ions and amino acids, a selective turn-on response was observed for the trivalent metal ions Al^{3+}, Fe^{3+}, Cr^{3+} and biothiols like cysteine, glutathione, homocysteine (Figure A16I, II). But in aqueous medium, **L2H** was selective towards Al^{3+}, Fe^{3+}, Cys and Hcy along with noticeable red shift of 15, 9, 56, 38 nm respectively (Figure A16III, IV). The titration experiments were carried out by increasing concentration of Al^{3+} and cysteine to determine the detection limit values (Figure A17). Finally, on tuning the aqueous system with the assistance CTAB, **L2H** showed higher selectivity and sensitivity towards only Al^{3+} ion and cysteine (Figure 4A, 4B). The colour of the solution changed from colorless to cyan blue towards Al^{3+} ion in presence of several metal ions and cysteine among all other amino acids as depicted in Figure A18. A similar fluorescence spectral pattern was observed when **L2H** was tested with aluminium chloride, aluminium sulfate and dihydroxyaluminum acetate (Figure A19). The fluorescence titration profile showed an increase in fluorescence intensity of ~ 14 fold for Al^{3+} and ~ 3.5 fold for cysteine (Figure 4C-4F) as well as a red shift of 13 nm (Al^{3+}) and 11 nm (cysteine). No such emission spectral change was observed when **L2H** was treated with various sodium anion salts of F^-, Cl^-, CN^-,

SCN^-, PO_4^{3-}, S^{2-}, N_3^-, NO_3^-, NO_2^-, ClO_4^-, $H_2PO_4^-$, CH_3COO^-, HSO_4^- and OH^- ions (Figure A20).

In MeOH/HEPES, water and aqueous CTAB medium, the emission intensities at λ_{em} = 478, 468, 477 nm (for Al^{3+}) and λ_{em} = 476, 479, 475 nm (for Cys) were considered for constructing the calibration plots to determine the LOD and LOQ values (inset: Figure A16, 4D, 4E). From Table 1, aqueous CTAB demonstrated the highest sensitivity for the detection of Al^{3+} and Cys, with the lowest LODs (2.75 nM for Al^{3+} and 2.65 nM for Cys) and LOQs (6.58 nM and 8.85 nM, respectively). On comparison, water showed moderate sensitivity performing significantly better than semi-aqueous medium, particularly for Cys, where the LOD decreased from 540 nM (MeOH/HEPES) to 3.23 nM. The lowest LOD and LOQ values were observed in aqueous CTAB for both the analytes, where the detection limit for Cys is 200 times lower than MeOH/HEPES buffer. Hence, the detection limit was best in CTAB medium compared to the other two media, even though water was comparable only for cysteine.

Table 1. Comparison table of LOD and LOQ.

Solvent	***LOD** (nM)*		***LOQ** (nM)*	
	Al^{3+}	Cys	Al^{3+}	Cys
MeOH/HEPES	33.37	540	110	1860
Water	13.83	3.23	46.32	10.77
Aq. CTAB	2.75	2.65	6.58	8.85

The pH range for the surfactant medium was evaluated for range of 2–14 by adjusting with NaOH and HCl solutions. It was observed that **L2H** solution remained weakly emissive (Figure A21) in this range and a significant enhancement of fluorescence intensity occurred in the range 6–9 (for Al^{3+} ion) and 5–9 (for Cys), thus these could be the suitable pH in CTAB medium.

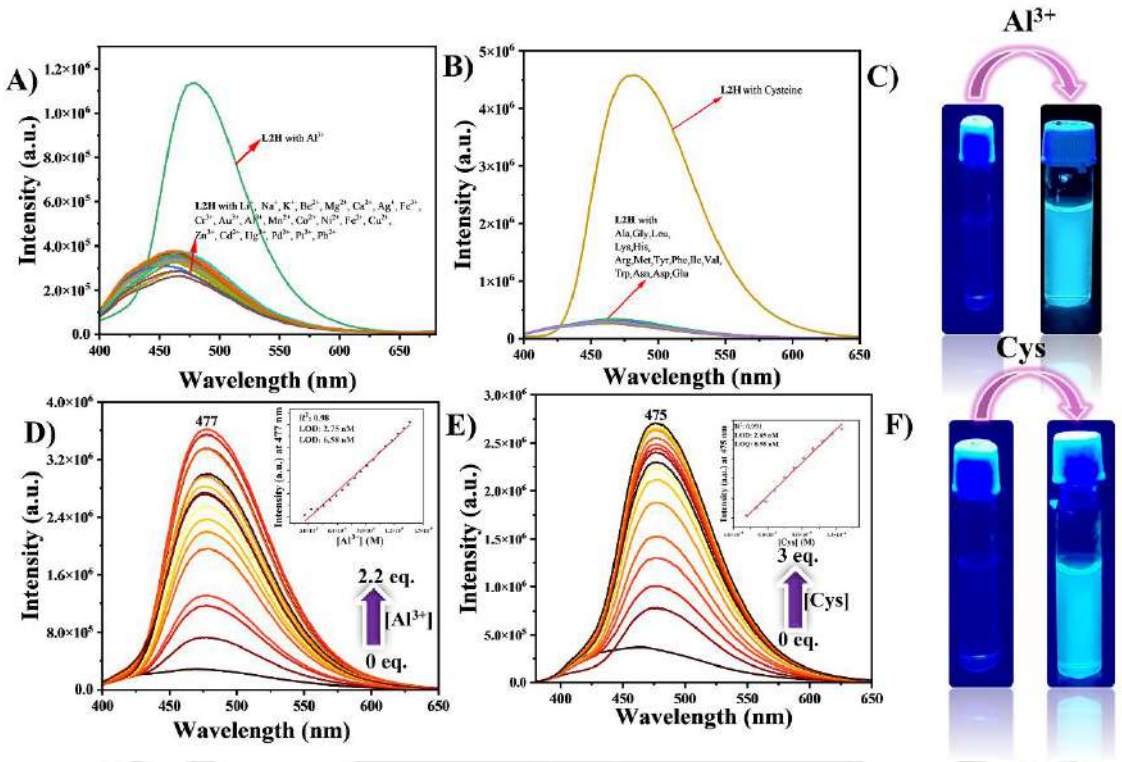

Figure 4. Emission spectra of **L2H** in presence of different (A) metal ions and (D) amino acids, fluorescence titration profile of **L2H** with incremental addition of (B) Al^{3+} and (E) Cysteine, and images under long UV light of **L2H** solution upon addition of (C) Al^{3+} and (F) Cysteine.

4.3.4 Response time, Competitive Study, and Reversibility Test

The kinetic study was performed at room temperature in aqueous CTAB as well as water medium by monitoring the intensity at 476 nm with a time interval of 4 sec. As depicted in Figure 5A-5B in aq. CTAB, upon the addition of 2 equivalents of Al^{3+} fluorescence intensity increased rapidly within ~ 20 s and similarly, upon addition of 3 equivalents of cysteine maximum intensity was reached within ~ 90 s. Same experimental protocol was adopted to evaluate the response time of Al^{3+} and cysteine in aqueous medium and the same were found to be (Figure A22) 80 s (for Al^{3+}) and 450 s (for Cys). So, in surfactant medium detection of **L2H** became fast, making it an ultrafast sensor.

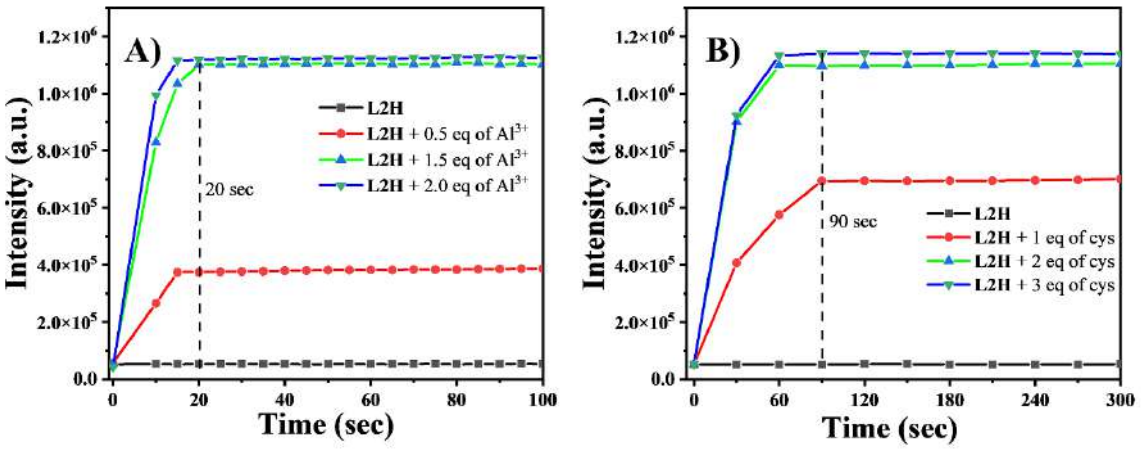

Figure 5. Response time measurement of (A) Al^{3+} and (B) cysteine with **L2H**.

The competitive study was performed by adding 10 equivalents of Al^{3+} and cysteine separately to **L2H** in MeOH/HEPES, water, and aqueous CTAB solutions, alongside the same equivalents of competing metal ions and amino acids / biothiols. In the semi-aqueous medium, Fe^{3+} and Cr^{3+} interfered, while in the aqueous medium, only Cr^{3+} caused interference with the detection of Al^{3+} ion. Among the tested amino acids and biothiols, fluorescence intensity increased significantly for homocysteine and glutathione in the semi-aqueous medium, whereas in pure water, only homocysteine showed enhancement (Figure A23). However, no spectral interference was observed in the surfactant medium (Figure 6A, 6B). Thus, in the aqueous CTAB medium, none of the metal ions interfered with the detection of Al^{3+} ion while none of the amino acids / biothiols with Cys.

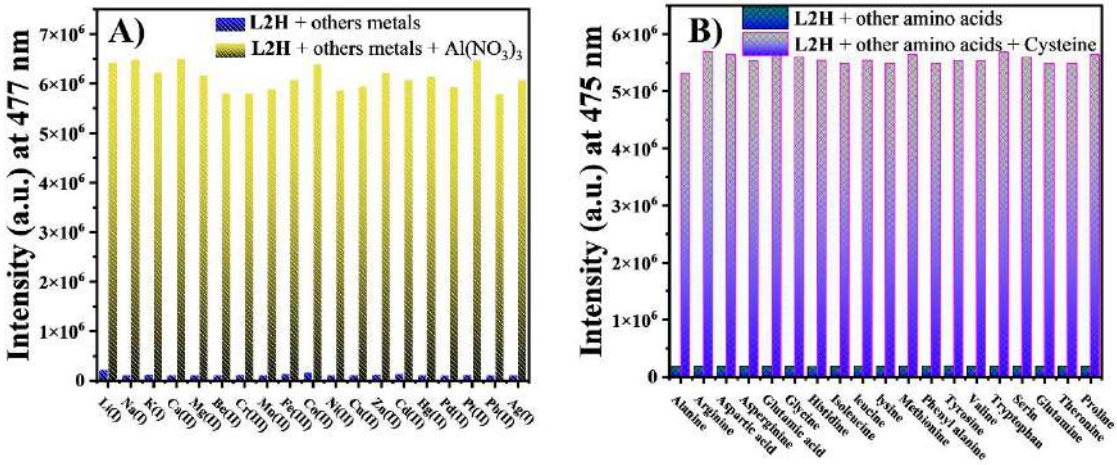

Figure 6. Bar diagram competitive experiment for (A) metal ions and (B) amino acids showing the change of fluorescence intensity of **L2H**.

The reversible "ON-OFF" switch in fluorescence property of **L2H** was observed after the addition of an equivalent amount of aqueous solution of Na_3PO_4 to the *in situ* generated **L2H** + Al^{3+} complex. It was observed (Figure A24I) that with the addition of various anions such as F^-, Cl^-, Br^-, I^-, CN^-, SCN^-, S^{2-}, NO_3^-, ClO_4^-, CH_3COO^-, HSO_4^- and SO_4^{2-} to the resulting **L2H** + Al^{3+} complex no such interference occurred except for PO_4^{3-}. With the gradual addition of PO_4^{3-} solution, the fluorescence intensity was abruptly decreased to similar level of **L2H** at 464 nm (Figure A24II). These results suggested that PO_4^{3-} abstracts Al^{3+} ion from **L2H** + Al^{3+} complex to form $AlPO_4$ salt having very low solubility. The calculated binding constant and detection limit of **L2H** + Al^{3+} complex toward PO_4^{3-} are found to be 1.78×10^5 (M^{-1}) and 59 nM (Figure A25). Meanwhile, the *in situ* generated **L2H** + Al^{3+} complex selectively detected PO_4^{3-} ion, effectively overcoming interference from other common anions (Figure A26).

4.3.5 Binding of L2H with Al^{3+} Ion and Cysteine

To understand the binding interaction between the probe with Al^{3+} ion and cysteine, various spectroscopic studies were carried out. Job's plot analysis indicated a 1:1 binding stoichiometry between **L2H** and Al^{3+} ion (Figure A27I). For 1:1 binding interaction, the binding constant was calculated as 2.30×10^4 (M^{-1}) by using Bensi-Hildebrand equation (Figure A27II).

IR spectrum of free **L2H** displayed bands 3317 (υ_{N-H}), and 1492 ($\upsilon_{C=C}$) cm^{-1} (Figure A28). Upon addition of 1 equivalent of $Al(NO_3)_3$, in addition to bands 3224 (υ_{N-H}) and 1461 ($\upsilon_{C=C}$) cm^{-1}, a sharp peak at 1678 ($\upsilon_{C=N}$) cm^{-1} was present, indicative of conversion of **L2H** to **L2'** through a [1,5]-sigmatropic hydrogen shift and coordination of **L2'** with Al^{3+} ion. Also, a weak peak observed at 3014 cm^{-1} corresponding to the C–H (υ_{C-H}) at the unique tertiary carbon shifted to 3033 cm^{-1} upon conversion to C–H of imine group. The existence of a new band at 1316 cm^{-1} was attributed to monocoordinated NO_3^- ion.[38–40] After the addition of cysteine to **L2H**, two new bands at 1076 (υ_{N-N}) and 640 (υ_{S-S}) cm^{-1} were observed (Figure A29) indicating formation of **L2–L2** dimer and cystine.[41,42]

The ESI(+) mass spectrum of a 1:1 mixture of **L2H** and $Al(NO_3)_3$ contained a peak at m/z = 540.1216 (calculated for $C_{25}H_{19}AlN_7O_6^+$, 540.1212 corresponding to the formula $[Al(\mathbf{L2H})(NO_3)_2(CH_3CN)]^+$ ion (Figure A30). Mixture of **L2H** and cysteine in their mass spectrum (ESI(-), Figure A31) exhibited characteristic (m/z) peaks at (i) 346.1224 assignable to $\mathbf{L2}^-$ ($[C_{23}H_{15}N_4–H]^-$ calculated 346.1223) (ii) 239.0391 due to Cys-S-S-Cys

($[C_6H_{12}N_2O_4S_2-H]^-$, calculated 239.0390) and (iii) 693.2522 due to **L2–L2** dimer ($[C_{46}H_{30}N_8-H]^-$), calculated 693.2520). At 77 K, the X-band EPR spectrum recorded instantaneously after adding cysteine to acetonitrile solution of **L2H** showed a sharp signal of three lines at g = 1.960. Three lines were due to hyperfine splitting by ^{14}N (I = 1),[43,44] which indicated formation of a radical centered at the nitrogen atom (Figure A32). Thus, **L2H** had reacted with cysteine producing, **L2•** and hydrogen molecule. The cysteine thiyl radical (Cys–S•) could not be detected in the EPR spectrum may be due to its quick dimerization to cystine (Cys-S-S-Cys) and **L2•** was only detected, which was unstable as the room-temperature EPR spectrum was blank. Based on these results sensing mechanism for Al^{3+} ion has been shown in Scheme AI and that of cysteine in Scheme AII.

To figure out the variation in surface morphology, FESEM and DLS measurements were carried out on **L2H** before and after the addition of Al^{3+} as well as cysteine solutions with CTAB. It was evident from Figure 7A, **L2H** (2 μm) displayed feather-shaped particles having average particle size (d) of 86 nm, which completely changed to spherical shaped structure with spikes (d, 140 nm) in presence of 20 equivalents of Al^{3+} ions. With cysteine (20 equiv.) a large spherical agglomerated clumps were formed (d, 152 nm), clearly indicating that the analytes influenced aggregation. Particle sizes of the aggregates in surfactant medium determined from DLS experiments were Z_{avg} increased to 476 nm and 572 nm compared to free **L2H** (255 nm) the addition of excess (20 equiv.) Al^{3+} and Cys to **L2H**, which strongly corroborated FESEM result (Figure A33). Fluorescence microscope images (Figure 7B) clearly showed the emission of intense blue and red fluorescence light with the presence of Al^{3+} and Cys compared to free **L2H**. From Scheme 2, it can be clearly stated that presence of Al^{3+} and Cys triggered the AIE behaviour into the ligand framework to enable fluorescence turn-on response.

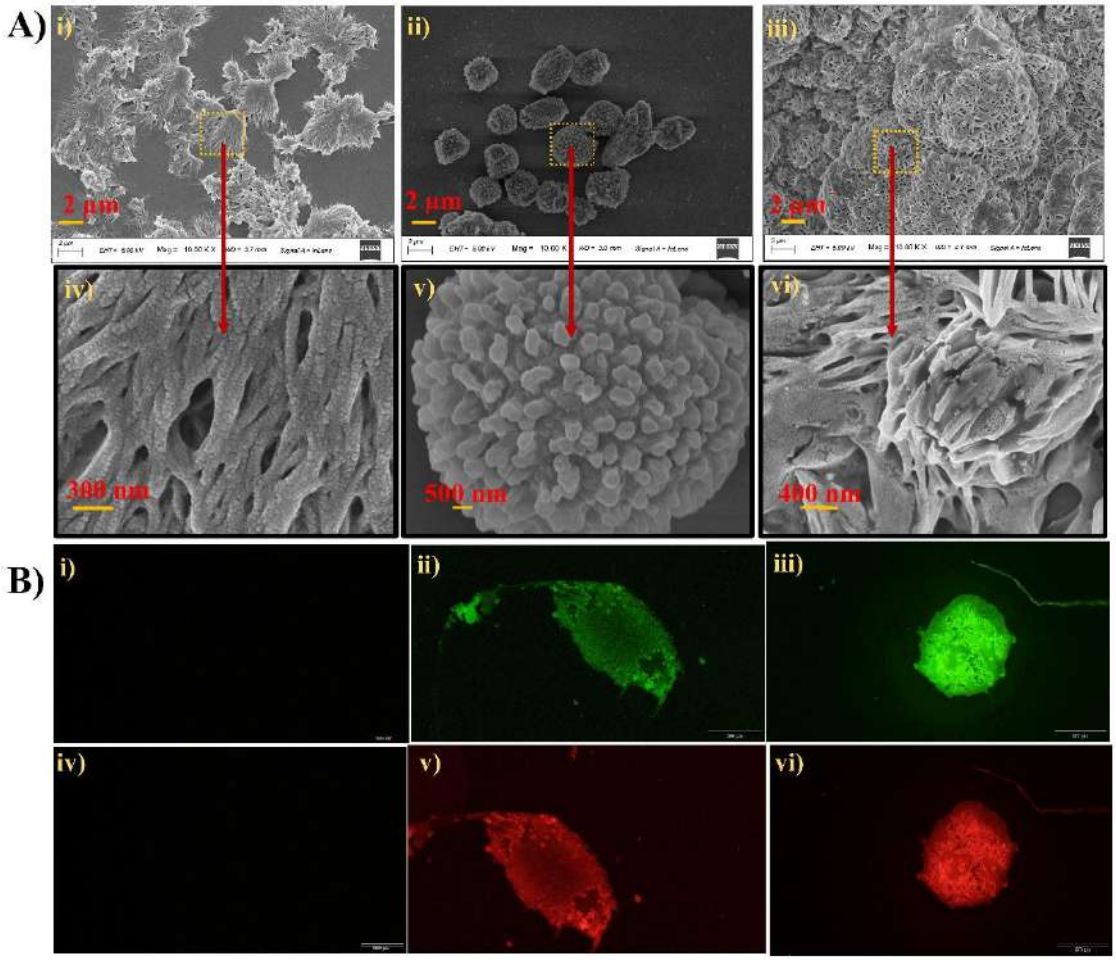

Figure 7. (A) FESEM images of (i) **L2H** with (ii) Al^{3+} and (iii) cysteine and the higher magnification (iv, v, vi) respectively, and (B) bright field fluorescence microscopic images of (i), (iv) **L2H** with (ii), (v) Al^{3+} and (iii), (vi) cysteine.

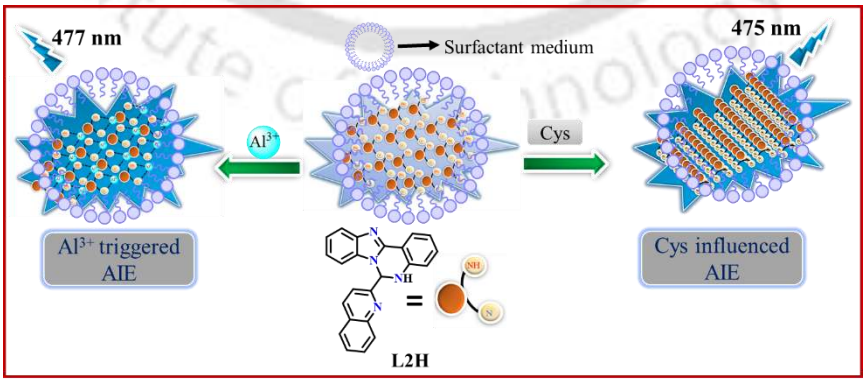

Scheme 2. Schematic representation of the sensing mechanism of **L2H** towards Al^{3+} and cysteine.

4.3.6 Lifetime Photoluminescence Studies and Quantum Yield Measurement

Time-resolved photoluminescence studies were carried out to understand the turn-on sensing response of **L2H** towards Al^{3+} and cysteine (Figure 8). The radiative (*kr*) and non-radiative (*knr*) rate constants were calculated using Equations 5 and 6. Photophysical parameters are listed in Table A4. The average lifetime of **L2H** (0.55 ns) increased to 9.61 ns with Al^{3+} and to 4.65 ns with cysteine. This indicated a 17-fold enhancement in fluorescence lifetime with 1 equivalents of $Al(NO_3)_3$ and 8-fold enhancement with cysteine. The increase in *kr* and decrease in *knr* in presence of analyte suggested enhancement of both radiative decay and fluorescence intensity after complexation. Since the probe **L2H** exhibited a turn-on response in the CTAB medium, its quantum yield (φ) significantly increased to 57.91% and 26.13% in the presence of Al^{3+} ions and cysteine, respectively, from 8.82% for free **L2H**. Table A5 shows a similar trend in a pure aqueous medium, where φ of **L2H** (2.05%) increased to 43.00% with Al^{3+} and 20.69% with cysteine. In the semi-aqueous medium, the enhancement was relatively lower due to a decrease in emission intensity after the addition of Al^{3+} and cysteine.

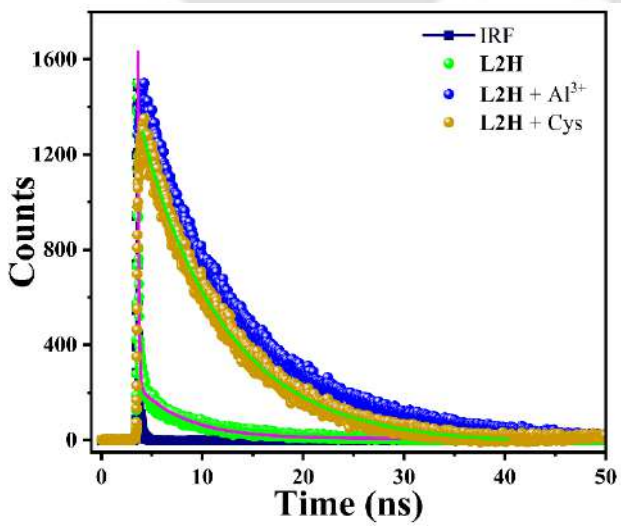

Figure 8. Photoluminescence spectra of **L2H** with Al^{3+} ions and cysteine.

4.3.7 Theoretical Studies

To determine the stable conformers of **L2H**, a potential energy surface diagram was generated using the Gaussian 09 program. A total of 38 dihedral rotations were set around N2–C1–C2–N3 to predict the most stable conformers. Conformer 1 had the lowest energy of 3.01 eV (Figure A34) which was calculated to have a dihedral angle of 81.82° and the same was selected for

further calculations. DFT calculations were performed on [Al(**L2'**)$(NO_3)_3$] and the formula was adopted based on the results of Job's plot, ESI-MS spectrometry. The optimized structures were shown in Figure A35. Aqueous solution of Al^{3+} ion has been known to exhibit acidic behaviour and release proton.[45] In presence of proton, **L2H** can undergo 1,5-sigmatropic shift and convert to **L2'** which can act as a tridentate ligand by coordinating through quinoline-N, imine-N, and benzimidazole-N. The other three coordination sites were satisfied by oxygen atom from three nitrate ions. Thus upon binding to Al^{3+} ion, **L2H** got converted to **L2'** which inhibited the PET process and resulted in enhancement of fluorescence intensity. The HOMO was spread over the 5,6-dihydrobenzo[4,5]imidazo[1,2-*c*]quinazoline moiety, whereas the LUMO was dispersed over the quinoline ring (Figure 9). In [Al(**L2'**)$(NO_3)_3$], the HOMO remained similar to that of **L2H**, while the LUMO in addition to quinoline ring, was partially located over phenyl ring of 5,6-dihydrobenzo[4,5]imidazo[1,2-*c*]quinazoline framework. Upon binding to Al^{3+}, energies of both HOMO and LUMO decreased respectively by 3.09 and 3.59 eV. The calculated HOMO-LUMO energy gap (ΔE) decreased from 3.82 eV (in **L2H**) to 3.32 eV (in [Al(**L2'**)$(NO_3)_3$]. In presence of cysteine, **L2H** underwent dimerization to form **L2–L2** and the energy of HOMO was increased while that of LUMO decreased. The HOMO of dimer was predominantly distributed over one of the monomer units of the imidazo[1,2-*c*]quinazoline framework, while the LUMO was mainly localized on one of the quinoline moieties. The HOMO-LUMO energy gap for **L2–L2** was calculated to be 3.36 eV (Figure A36). Relative to the free **L2H**, the reduced energy gap by 0.50 eV (for Al^{3+}) and 0.46 eV (for Cys) aligned well with the red shift observed in the UV-Vis spectrum following interaction with Al^{3+} and cysteine.

From the TDDFT study, the calculated wavelength value of λ_{max} = 373 nm for electronic transition of **L2H** matched closely with the experimental value of 351 nm. The absorption band was assigned to the $S_0 \rightarrow S_{10}$ transition with the highest oscillator frequency of f = 0.1790. For [Al(**L2'**)$(NO_3)_3$], observed λ_{max} value at 355 nm in MeOH/HEPES buffered medium (*v/v*, 8/2), also lied closer to the value of 380 nm (f = 0.3156) found in simulated spectrum, due to the $S_0 \rightarrow S_2$ electronic transition. **L2–L2** exhibited an absorption band at 381 nm, with a corresponding calculated band at 406 nm (f = 0.6861), assigned to the $S_0 \rightarrow S_5$ transition. The involvement of various transitions between HOMOs and LUMOs having highest f value for **L2H**, [Al(**L2'**)$(NO_3)_3$] and **L2–L2** were depicted in Figure A37, with the relevant output of TDDFT results listed in Table A6. All calculated spectra were found to be in good agreement with experimental findings (Figure A38).

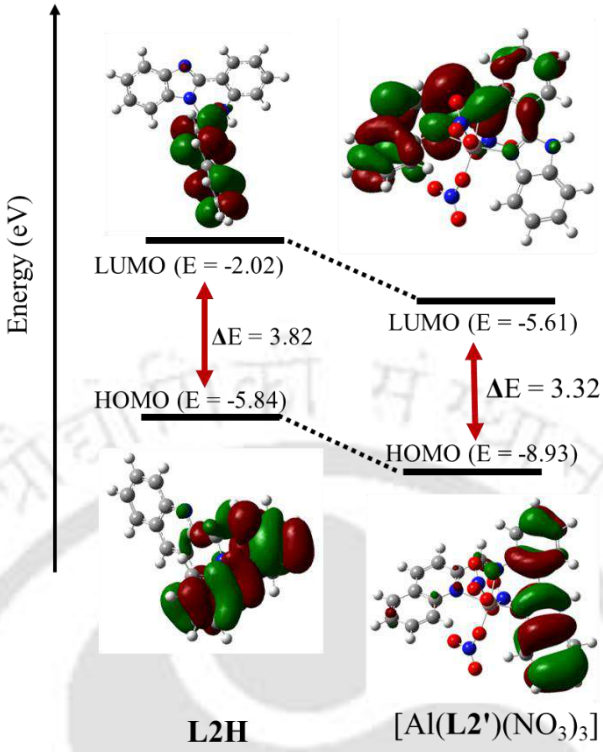

Figure 9. Energy levels profile depicting HOMO and LUMO in **L2H** and [Al(**L2'**)$(NO_3)_3$] complex.

4.3.8 Practical Application of L2H

4.3.8.1 Solid Phase Detection Strategy

A portable, cost-effective filter paper strip and silica gel-based assay experiments for solid phase analysis have been designed. For the preparation of paper test strips, Whatman filter paper of 1 cm × 2 cm size was dipped into **L2H** solution and dried in air. A 0.1 mM stock solution of Al^{3+} and Cys was drop casted on paper strips which were noticeable as dark spots under 365 nm light in photographs (Figure 10A). With increasing concentration of Al^{3+} and Cys from 0 to 20 μM intensity of the paper strips got enhanced. These paper strips were analyzed using ImageJ software to calculate the mean intensity,[46] calculated detection limits of the filter paper-based sensor were 1.5 μM for Al^{3+} and 1.2 μM for Cys (Figure 10B). These coated paper strips can be used for real-time on-location detection of Al^{3+} and Cys.

For performing silica gel-based experiment, 2 g of 60-120 mesh silica gel was soaked with (15 mg, 0.04 mmol) solution of **L2H** and dried. One was used as reference and each of other two, $Al(NO_3)_3{\cdot}9H_2O$ (16 mg, 0.4 mmol) and Cys (5.2 mg, 0.4 mmol) solution were added separately and dried to remove solvents. A cyan blue colour was imparted to both samples loaded with

Al^{3+} and Cys which was observed under a long UV lamp (inset: Figure 10B). The solid-state emission spectra of three silica samples were recorded using λ_{ex} = 354 nm, **L2H**, **L2H** + Al^{3+} and **L2H** + Cys showed maximum intensity respectively at (λ_{em}) 466, 496 and 482 nm. A five- and three-fold increase in intensity was observed for the two loaded with Al^{3+} and Cys, respectively (Figure 10C). Thus, **L2H** could be employed as a ready-made tool for solid-state detection of Al^{3+} and Cys.

For further application, **L2H** functionalised polyvinyl alcohol (PVA) hydrogel membrane has been developed for fast on-site detection of Al^{3+} and cysteine due to the excellent chemical stability, low toxicity and good biocompatibility of PVA.[47,48] The picture of PVA-**L2H** hydrogel formation has been given in Figure 10D. Initially, PVA powder (4%, *w/v*) was dissolved in distilled water, and stirred at 100 °C until a completely transparent solution (~2 h) was obtained. After it was ultrasonicated for 20 min (to remove air bubbles), DMSO solution of **L2H** (3 mL, 0.1 mM) was added. IR (ATR mode) and powder XRD analysis were used to evaluate hydrogel formation. IR spectrum of PVA-**L2H** matched well with blank PVA hydrogel (Figure A39I) and no new peaks were present in PVA-**L2H**, indicating the structural backbone remained intact.[49,50] The XRD patterns for both PVA and hydrogels confirmed the semi-crystalline nature of PVA membrane[51-53] (Figure A39II) and characteristic peaks at 2θ = 19.53° and 44.70° for PVA were observed at 19.55° and 44.75° in PVA-**L2H**. Emission spectra were recorded by transferring hydrogels to a cuvette and PVA-**L2H** showed an emission maximum at 402 nm upon excitation at 354 nm. Interaction with Al^{3+} and Cys increased the emission intensity respectively by six- and three-fold with λ_{em} shifted to 478 and 479 nm (Figure A40). With both Al^{3+} and Cys, a change from colorless to greenish yellow (under visible light) and cyan blue (under UV light) was observed (Figure A41).

The PVA-**L2H** hydrogel was transferred to a Petri dish and dried in desiccators. The resultant film was cut into required dimension (1 cm × 1 cm), 15 μL of Al^{3+} and cysteine solution were drop cast to the film and dried again. It was observed from Figure 10E that the fabricated hydrogel sensor could be efficiently utilized for the rapid fluorogenic response of Al^{3+} and cysteine. Moreover, the FESEM analysis was carried out to examine the change in surface morphology of blank PVA hydrogels and PVA-**L2H** hydrogels after the addition of Al^{3+} and Cys. It was inferred from Figure 10F that smooth surface of blank hydrogel got dispersed all over the membrane after incorporation of **L2H**. For PVA-**L2H** + Al^{3+} hydrogels, matrix

exhibited a rough three-dimensional uneven, porous surface while with cysteine a cross-linked fibrous pattern having large porous voids formed. Hence, by utilizing the PVA-**L2H** film, we can detect presence of Al^{3+} and Cys, both at micromolar level concentrations.

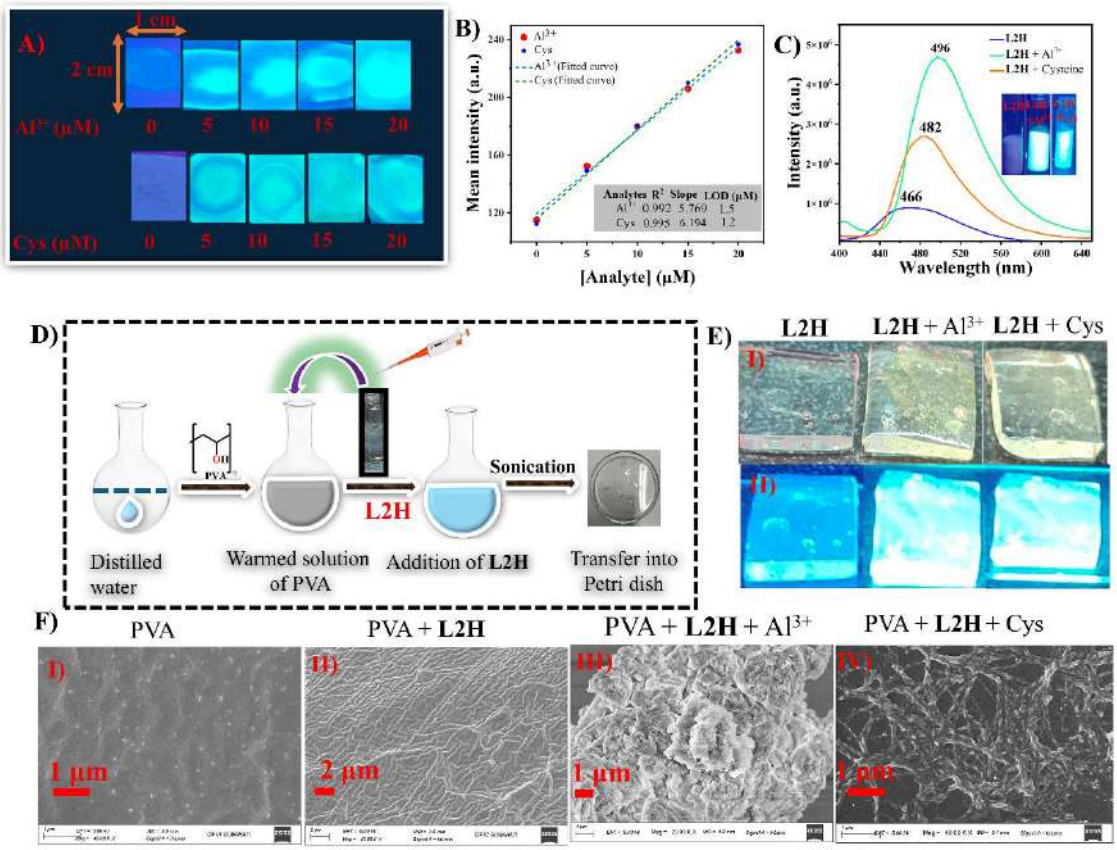

Figure 10. (A) Solid-state sensing of Al^{3+} and cysteine complex by using filter paper strips loaded with **L2H**, (B) mean intensity plots *versus* **L2H** coated paper strips with Al^{3+} and Cys, (C) emission spectra of **L2H** with its *in situ* generated Al^{3+} and cysteine complex (inset: images of silica gel of Al^{3+} and cysteine complex under long UV-lamp), (D) schematic representation of hydrogel formation, (E) visual sensing test of **L2H**-hydrogels before and after the treatment of Al^{3+} and cysteine respectively observed under I) visible light and II) long UV light, and (F) FESEM images of I) blank PVA hydrogel, II) PVA-**L2H** film, PVA-**L2H** hydrogel film in presence of III) Al^{3+} and IV) cysteine.

4.3.8.2 Al^{3+} and Cysteine Detection in Natural Water and Food Samples

Environmental water samples collected from drinking facilities, river and tap were filtered twice through a 0.22 μm membrane filter paper, pH was adjusted to 7.4 prior to analysis and used for preparing solutions. In the blank experiment, **L2H** (4 μM) was titrated with Al^{3+} (0–6 μM) and Cys (0–5 μM), and emission maximum intensities were recorded at λ_{em} = 468 and 478

nm, respectively (Figure A42) and samples were found be negative for these two analytes. Known concentrations of Al^{3+} and Cys were spiked into the water samples, and recovery percentages (Table A7) ranged from 97–99% (for Al^{3+}) and 89–98% (for Cys). These results confirmed the practical applicability of **L2H** for detection of both analytes in real water specimens. To evaluate Al^{3+} content in vegetable samples, familiar aluminium-accumulating vegetables such as carrots, cucumbers, and cabbages were selected. The extraction procedure for vegetable samples was illustrated schematically in Figure A43. At first, all the vegetable samples were chopped into pieces, digested in 5 mL of aqua regia solution and heated until a colorless solution formed. Then the digested mixture was centrifuged at 3000 rpm for 30 min, and the pH of the supernatant liquid was adjusted to 7.4 using 1 M NaOH solution. After filtration through a 0.45 µm membrane syringe filter, the extract was diluted to an appropriate concentration with distilled water. The resulting solution was spiked with different volumes of 3 µM Al^{3+} solution, mixed well and used for fluorescence spectral analysis. A distinct turn-on fluorescence response was observed (Figure A44), and intensity at λ_{em} = 468 nm showed a linear correlation against Al^{3+} concentration (Figure A45). The recovery test of vegetable samples analysis data listed in Table A8.

The control experiments performed with blank vegetable samples sprayed with **L2H** (Set I), and samples with **L2H** + Al^{3+} (Set II) were observed under UV illumination. Samples in Set I were non-fluorescent and those in Set II exhibited a distinct green fluorescence (Figure A46), confirming a selective and visual response of **L2H** probe toward Al^{3+} ions in the treated vegetable samples. Furthermore, **L2H** is also used for the detection of Cys in milk samples after the pretreatment process. To remove the protein, the milk sample was sonicated for 30 min with 1% (*v/v*) of trichloroacetic acid and then centrifuged at 12000 rpm for 8 min. The supernatant liquid was collected, filtered through a 0.22 µm membrane filter paper and pH adjusted to 7.4. A 3 mL of the prepared solution was spiked with 200 µL aliquots of cysteine (1 mM) solution and used for fluorometric analysis. A linear calibration curve at λ_{em} = 478 nm was obtained with a correlation coefficient (R^2) > 0.97 (Figure A47), demonstrating good analytical performance. Upon spiking the milk samples with varying concentrations of Cys (2–6 µM), a high recovery rate of approximately 99% was achieved, as summarized in Table A9.

4.3.8.3 Three- to- Two Logic Gate Operation

The reversible outcomes of **L2H** upon sequential addition of $Al(NO_3)_3$ and Na_3PO_4 solutions also helped to construct a three-to-two decoder logic gate circuit. The spectroscopic findings of **L2H** with other sensing analytes like Al^{3+}, PO_4^{3-} were presented in Figure 11A. Fluorescence spectral analysis revealed that the addition of PO_4^{3-} to the [Al(**L2'**)$(NO_3)_3$] complex resulted in the quenching of the intense emission peak at 477 nm, accompanied by the reappearance of a weak emission peak at 464 nm due to **L2H**. Subsequent addition of Al^{3+} regenerated the peak at 477 nm. This switching process was repeated over six cycles (Figure 11B). The logic gate inputs were defined as In1: **L2H**, In2: Al^{3+}, and In3: Na_3PO_4, while the output signals were monitored at 464 nm (Out1) and 477 nm (Out2). Based on the derived truth table, a combined NOT-AND-OR logic gate circuit was constructed (Figure 11C). Furthermore, in the presence of Na_3PO_4, the emission maximum at 464 nm of **L2H** remained unaltered. The analytical performance of **L2H** was also compared with other previously reported fluorometric sensors, as summarized in Table A10.

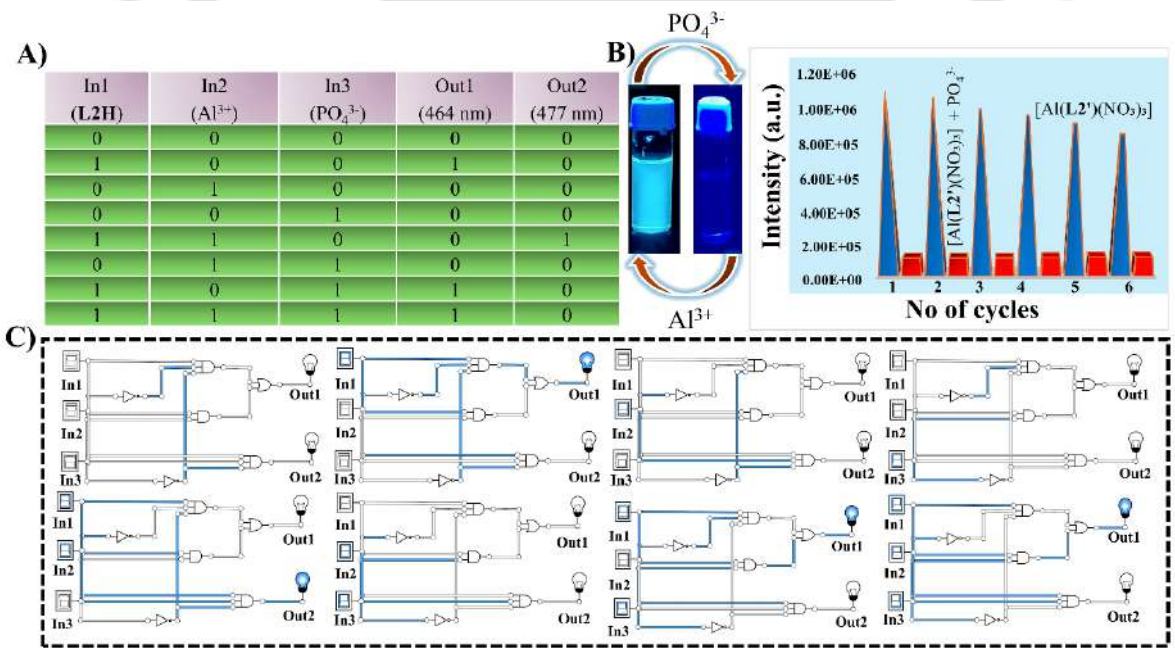

In1 (L2H)	In2 (Al^{3+})	In3 (PO_4^{3-})	Out1 (464 nm)	Out2 (477 nm)
0	0	0	0	0
1	0	0	1	0
0	1	0	0	0
0	0	1	0	0
1	1	0	0	1
0	1	1	0	0
1	0	1	1	0
1	1	1	1	0

Figure 11. (A) Truth table for **L2H** with Al^{3+} and PO_4^{3-}, (B) fluorometric response of **L2H** with alternative addition of Al^{3+} and PO_4^{3-}, and **(**C) fabrication of logic gate circuits with outputs (Out1 and OUT2) by altering inputs of NOT-AND-OR logic gate function for **L2H** with Al^{3+} and PO_4^{3-}.

4.4 Conclusion:

The sensor **L2H** having benzimidazole and quinoline moieties has been synthesized and characterized thoroughly using various spectroscopic techniques which exhibited AIE behaviour. This weakly fluorescent probe was found to be highly specific fluorescence turn-on sensor for Al^{3+} ion and cysteine, having superior selectivity and sensitivity in aqueous surfactant (CTAB) medium. Probe **L2H** can remarkably detect up to 2.75 nM of Al^{3+} and 2.65 nM of cysteine in presence of cationic surfactant CTAB, which is far below than the clinical detection range. Response time was ultrafast ~ 20 s towards Al^{3+} ion and ~ 90 s for Cys. Upon binding with Al^{3+} ion, the bidentate cyclic structure of **L2H** converted to a tridentate **L2'** structure and formed a fluorescent [Al(**L2'**)$(NO_3)_3$] complex and in presence of cysteine, **L2H** underwent oxidative dimerization to form **L2–L2**. Theoretical calculations, including DFT studies performed on **L2H**, [Al(**L2'**)$(NO_3)_3$] and **L2–L2**, showed a decrease in HOMO-LUMO energy gap, while TDDFT results aligned with the experimentally observed red shift in the absorption band. Furthermore, cost-effective portable solid-state tool such as filter paper-based test kit and a PVA-based hydrogel membrane, were fabricated for rapid on-field detection of Al^{3+} and cysteine. The turn-on sensing strategy was also applied in various contaminated water and food samples. The reversibility of **L2H** in the presence of Na_3PO_4 and Al^{3+} enables its application in constructing combined (NOT-AND-OR) logic gate circuit.

References:

1 M. Shyamal, S. Maity, P. Mazumdar, G. P. Sahoo, R. Maity and A. Misra, *J. Photochem. Photobiol. A Chem.,* 2017, **342**, 1-14.

2 D. Y. Patil, A. A. Patil, N. B. Khadke and A. V Borhade, *Inorg. Chim. Acta,* 2019, **492**, 167-176.

3 S. Mahata, G. Janani, B. B. Mandal and V. Manivannan, *J. Photochem. Photobiol. A Chem.,* 2021, **417**, 113340.

4 N. Behera and V. Manivannan, *J. Photochem. Photobiol. A Chem.,* 2018, **353**, 77-85.

5 N. Behera and V. Manivannan, *ChemistrySelect*, 2017, **2**, 11048-11054.

6 G. Yang, P. Li, Y. Han, L. Tang, Y. Liu, H. Xin, K. N. Wang, S. Zhao, Z. Liu and D. Cao, *Mater. Chem. Phys.,* 2023, **295**, 127145.

7 H. Rao, W. Liu, K. He, S. Zhao, Z. Lu, S. Zhang, M. Sun, P. Zou, X. Wang, Q. Zhao, Y. Wang and T. Liu, *ACS Sustain. Chem. Eng.,* 2020, **8**, 8857-8867.

8 Y. P. Li, X. H. Zhu, S. N. Li, Y. C. Jiang, M. C. Hu and Q. G. Zhai, *ACS Appl. Mater. Interfaces,* 2019, **11**, 11338-11348.

9 L. L. Man, S. Z. Li, J. Zhang, Y. Zhang and W. K. Dong, *J. Photochem. Photobiol. A Chem.,* 2023, **437**, 114433.

10 D. Aydin, S. Dinckan, S. N. K. Elmas, T. Savran, F. N. Arslan and I. Yilmaz, *Food Chem.,* 2021, **337**, 127659.

11 D. P. Perl, D. C. Gajdusek, R. M. Garruto, R. T. Yanagihara and C. J. Gibbs, *Science,* 1982, **217**, 1053-1055.

12 B. K. Kundu, P. Mandal, B. G. Mukhopadhyay, R. Tiwari, D. Nayak, R. Ganguly and S. Mukhopadhyay, *Sensors Actuators B Chem.,* 2019, **282**, 347-358.

13 C. Nandhini, P. S. Kumar, R. Shanmugapriya, K. Satheeshkumar, K. N. Vennila, A. G. Al-Sehemi, M. Pannipara and K. P. Elango, *J. Mol. Struct.*, 2022, **1268**, 133685.

14 S. Li, Q. Zhang, Y. Lu, D. Zhang, J. Liu, L. Zhu, C. Li, L. Hu, J. Li and Q. Liu, *ChemistrySelect*, 2018, **3**, 10002-10009.

15 G. I. Giles, K. M. Tasker and C. Jacob, *Free Radic. Biol. Med.,* 2001, **31**, 1279-1283.

16 R. S. Fernandes, N. Dey, *Mater. Today Chem*., 2024, **36**, 101850.

17 S. A. Lipton, Y. B. Choi, H. Takahashi, D. Zhang, W. Li, A. Godzik and L. A. Bankston, *Trends Neurosci.,* 2002, **25**, 474-480.

18 L. O. Ofori, N. P. Withana, T. R. Prestwood, M. Verdoes, J. J. Brady, M. M. Winslow, J. Sorger and M. Bogyo, *ACS Chem. Biol.,* 2015, **10**, 1977-1988.

19 A. Mondal and V. Manivannan, *Spectrochim. Acta - Part A Mol. Biomol. Spectrosc.,* 2024, **322**, 124734.

20 A. Pal and N. Dey, *Colloids Surfaces A Physicochem. Eng. Asp.,* 2024, **687**, 133397.

21 A. Pal and N. Dey, *Soft Matter*, 2024, **20**, 3044-3052.

22 V. Mahendran, K. Pasumpon, S. Thimmarayaperumal, P. Thilagar and S. Shanmugam,

J. Org. Chem., 2016, **81**, 3597-3602.

23 J. Luo, Z. Xie, Z. Xie, J. W. Y. Lam, L. Cheng, H. Chen, C. Qiu, H. S. Kwok, X. Zhan, Y. Liu, D. Zhu and B. Z. Tang, *Chem. Commun.,* 2001, **18**, 1740-1741.

24 S. Hanif, H. Muhammad Junaid, F. Munir, M. Tahir Waseem, S. Majeed and S. A. Shahzad, *Microchem. J.,* 2022, **175**, 107227.

25 S. Jiang, J. Qiu, Y. Chen, H. Guo and F. Yang, *Dye. Pigment.*, 2018, **159**, 533-541.

26 W. W. H. Lee, Z. Zhao, Y. Cai, Z. Xu, Y. Yu, Y. Xiong, R. T. K. Kwok, Y. Chen, N. L. C. Leung, D. Ma, J. W. Y. Lam, A. Qin and B. Z. Tang, *Chem. Sci.*, 2018, **9**, 6118-6125.

27 S. Jiang, J. Qiu, L. Lin, H. Guo and F. Yang, *Dye. Pigment.*, 2019, **163**, 363-370.

28 Y. Liu, C. Deng, L. Tang, A. Qin, R. Hu, J. Z. Sun and B. Z. Tang, *J. Am. Chem. Soc.,* 2011, **133**, 660-663.

29 V. A. Mamedov, *RSC Adv.*, 2016, **6**, 42132-42172.

30 K. Velmurugan, A. Raman, D. Don, L. Tang, S. Easwaramoorthi and R. Nandhakumar, *RSC Adv.*, 2015, **5**, 44463-44469.

31 K. Jiang, S. H. Luo, C. M. Pang, B. W. Wang, H. Q. Wu and Z. Y. Wang, *Dye. Pigment.,* 2019, **162**, 367-376.

32 P. Saluja, N. Kaur, N. Singh, D. O. Jang, *Tetrahedron*, 2012, **68**, 8551-8556.

33 V. P. Jejurkar, G. Yashwantrao, B. P. K. Reddy, A. P. Ware, S. S. Pingale, R. Srivastava and S. Saha, *ChemPhotoChem*, 2020, **4**, 691-703.

34 A. Mondal and V. Manivannan, *Spectrochim. Acta - Part A Mol. Biomol. Spectrosc.,* 2025, **333**, 125865.

35 M. Yang, D. Xu, W. Xi, L. Wang, J. Zheng, J. Huang, J. Zhang, H. Zhou, J. Wu and Y. Tian, *J. Org. Chem.,* 2013, **78**, 10344-10359.

36 A. A. Bhosle, M. Banerjee, V. Gupta, S. Ghosh, A. C. Bhasikuttan and A. Chatterjee, *New J. Chem.,* 2022, **46**, 18961-18972.

37 M. Chakraborty, P. K. Samanta and M. Chakravarty, *ChemPhotoChem*, 2024, **9**, e00238.

38 Z. Y. Yin, J. H. Hu, K. Gui, Q. Q. Fu, Y. Yao, F. L. Zhou, L. L. Ma and Z. P. Zhang, *J. Photochem. Photobiol. A Chem,* 2020, **396**, 112542.

39 A. Kumar, A. Kumar, M. Dubey, A. Biswas and D. S. Pandey, *RSC Adv.*, 2015, **5**, 88612-88624.

40 Y. P. Delgado, J. Z. Barroso, L. A. Garofalo and C. E. Manzanares, *J. Phys. Chem. A*, 2012, **116**, 2071-2079.

41 P. C. Pandey, S. Shukla and Y. Pandey, *J. Mater. Res.*, 2017, **32**, 3574-3584.

42 S. R. Ankireddy and J. Kim, *Int. J. Nanomedicine*, 2015, **10**, 113-119.

43 A. E. Bosnidou, T. Duhamel and K. Muniz, *Eur. J. Org. Chem.,* 2020, **2020**, 6361-6365.

44 S. L. Petrova, A. Jager, E. Pavlova, M. Vragovic, E. Jager, M. Steinhart and D. Klepac, *Eur. Polym. J,* 2024, **220**, 113473.

45 C. R. Frink and M. Peech, *Inorg. Chem.,* 1963, **2**, 473-478.

46 D. A. Thai and N. Y. Lee, *Anal. Methods*, 2021, **13**, 1332-1339.

47 S. Bej, S. Mandal, A. Mondal, T. K. Pal and P. Banerjee, *ACS Appl. Mater. Interfaces,* 2021, **13**, 25153-25163.

48 R. Das, S. Bej, D. Ghosh, N. C. Murmu, H. Hirani and P. Banerjee, *Sensors Actuators, B Chem.*, 2021, **341**, 129925.

49 N. T. Nguyen and J. H. Liu, *Eur. Polym. J.,* 2013, **49**, 4201-4211.

50 H. S. Mansur, C. M. Sadahira, A. N. Souza and A. A. P. Mansur, *Mater. Sci. Eng. C,* 2008, **28**, 539-548.

51 S. Gupta, A. K. Pramanik, A. Kailath, T. Mishra, A. Guha, S. Nayar and A. Sinha, *Colloids Surf. B: Biointerfaces*, 2009, **74**, 186-190.

52 A. B. Bon, A. M. Costero, S. Gil, M. Parra, J. Soto, R. M. Manez and F. Sancenon, *Chem. Commun.*, 2012, **48**, 3000.

53 E. Bozkurt, M. Arık and Y. Onganer, *Sensors and Actuators B: Chemical,* 2015, **221**, 136-147.

54 A. Das and G. Das, *New J. Chem.*, 2022, **46**, 19002-19008.

55 J. Wang, K. Hu, H. Wang, W. Sun, L. Han, L. Li and Y. Wei, *J. Mol Strut.*, 2023, **1271**, 134085.

56 Y. Y. Huang, F. X. Wang, S. Y. Mu, X. Sun, Q. Z. Li, C. Z. Xie and H. B. Liu, *Spectrochim. Acta Part A Mol. Biomol. Spectrosc.*, 2020, **243**, 118754.

57 C. I. David, H. Jayaraj, G. Prabakaran, K. Velmurugan, D. P. Devi, R. Kayalvizhi, A. Abiram, V. R. Kannan and R. Nandhakumar, *Food Chem.,* 2022, **371**, 131130.

58 L. A. Fredin, J. Wallenstein, E. Sundin, M. Jarenmark, D. F. B. de Mattos, P. Persson and M. Abrahamsson, *Inorg. Chem.,*2019, **58**, 16354-16363.

59 H. Chen, B. Zhou, R. Ye, J. Zhu and X. Bao, *Sensors Actuators B Chem.*, 2017, **251**, 481-489.

60 M. Yang, J. Fan, W. Sun, J. Du, S. Long and X. Peng, *Dye. Pigment.,* 2019, **168**, 189-196.

61 W. Niu, L. Guo, Y. Li, S. Shuang, C. Dong and M. S. Wong, *Anal. Chem.,* 2016, **88**, 1908-1914.

62 G. S. Yeom, I. ho Song, S. J. Park, A. Kuwar and S. B. Nimse, *J. Photochem. Photobiol. A Chem.,* 2022, **431**, 114074.

63 M. Qian, J. Xia, L. Zhang, Q. Chen, J. Guo, H. Cui, Y. S. Kafuti, J. Wang and X. Peng, *Sensors Actuators, B Chem.,* 2020, **321**, 128441.

64 Y. Yang, L. Zhang, X. Zhang, S. Liu, Y. Wang, L. Zhang, Z. Ma, H. You and L. Chen, *Chem. Commun.,* 2021, **57**, 5810-5813.

Appendix

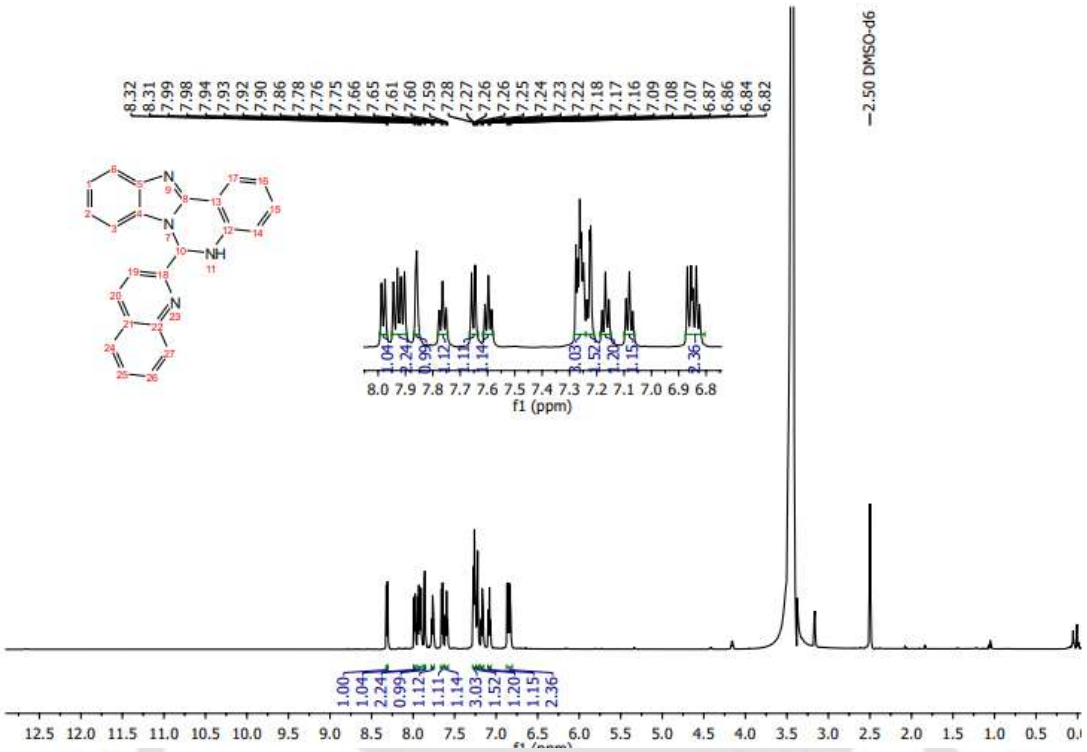

Figure A1. ^{1}H NMR (600 MHz) of **L2H** in DMSO-d_6.

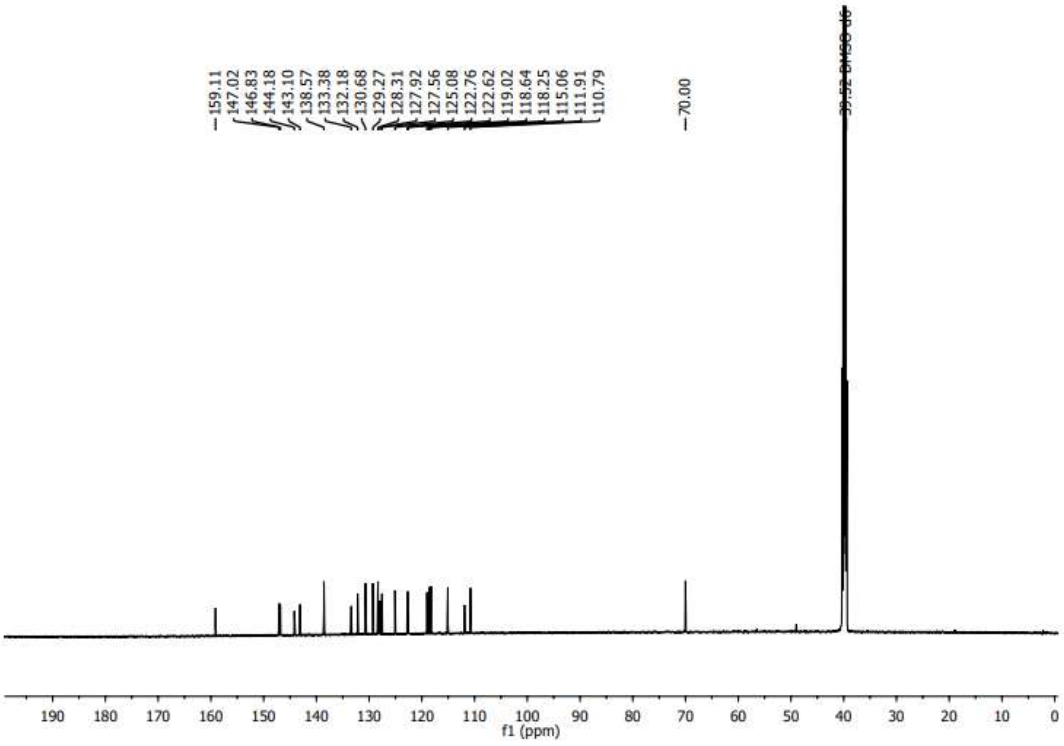

Figure A2. ^{13}C NMR (600 MHz) of **L2H** in DMSO-d_6.

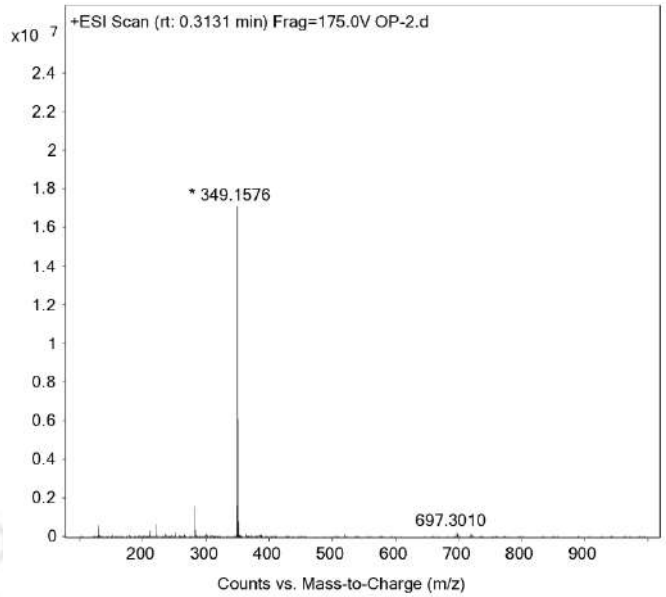

Figure A3. ESI Mass spectrum of **L2H** in acetonitrile.

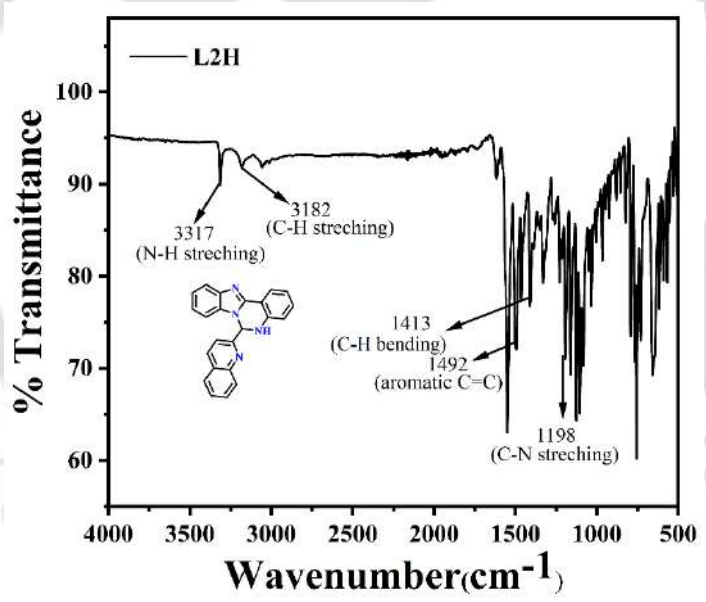

Figure A4. IR spectrum of **L2H**.

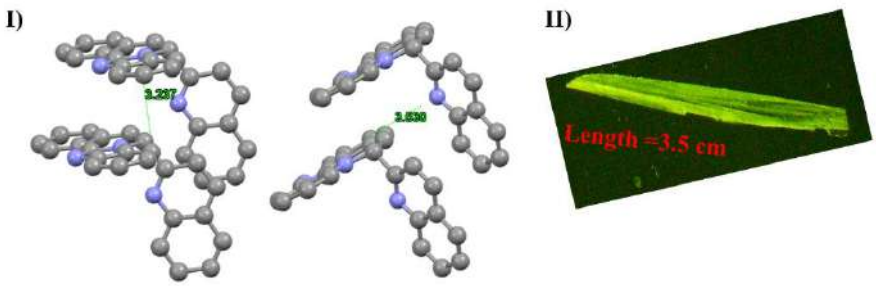

Figure A5. (I) Packing pattern of **L2H** view along *b*-axes, (II) Crystal photograph of **L2H** under long UV lamp.

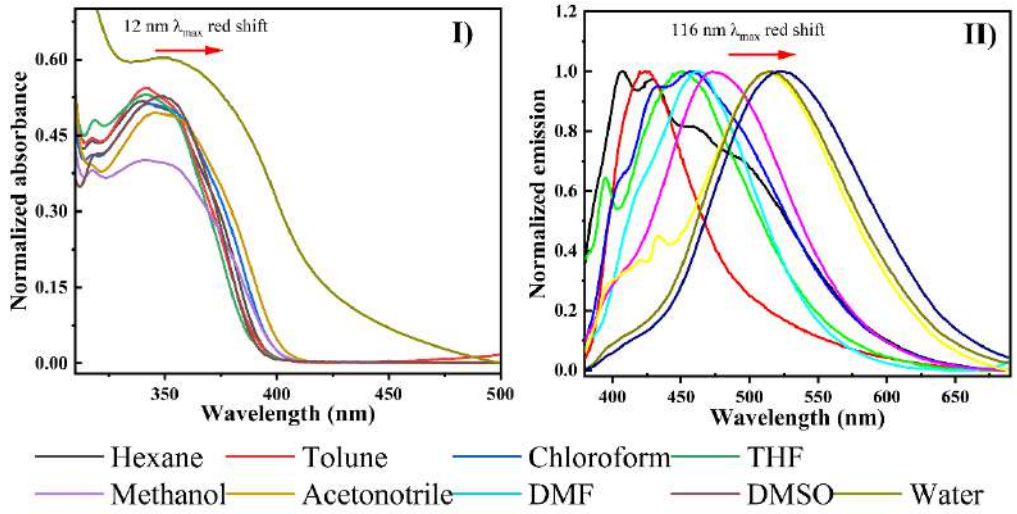

Figure A6. Solvatochromic effect of **L2H** (4 µM) in various polar to nonpolar solvents (I) normalized absorbance and (II) emission plots (λ_{ex} = 354 nm).

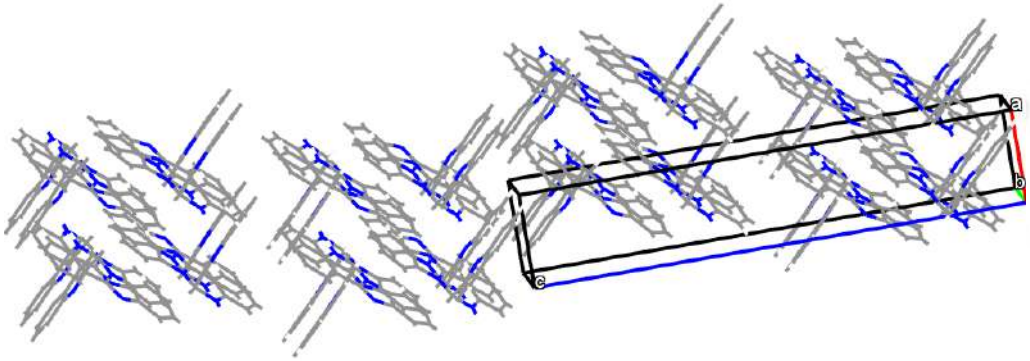

Figure A7. Face to face packing arrangement of the single crystal structure of **L2H** view along *b*-axes.

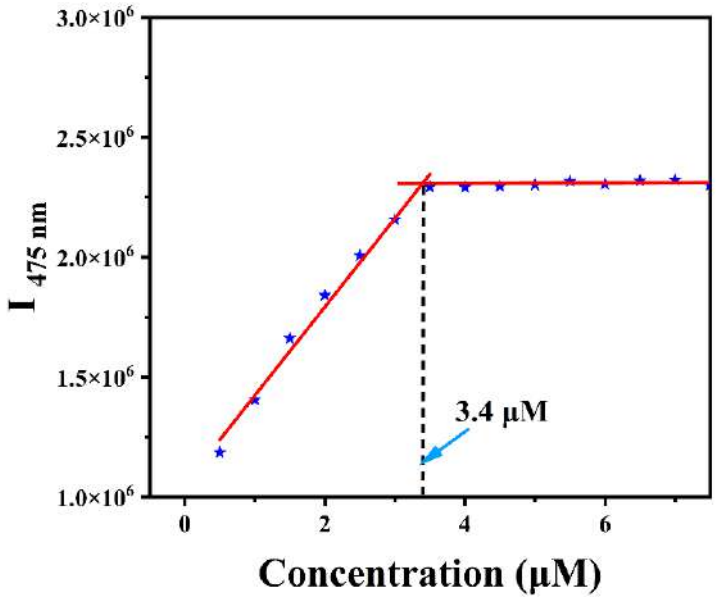

Figure A8. Calculation of critical aggregation constant for **L2H**.

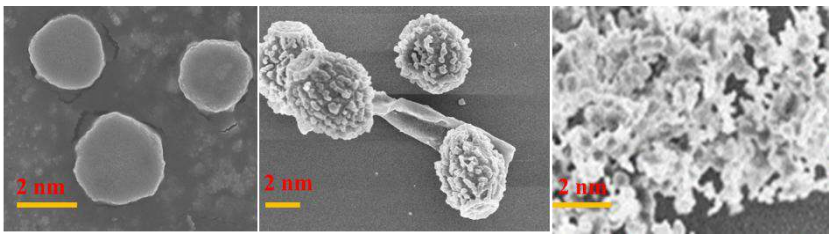

Figure A9. High resolution FESEM images in (0, 40, 90%) water/MeOH mixture.

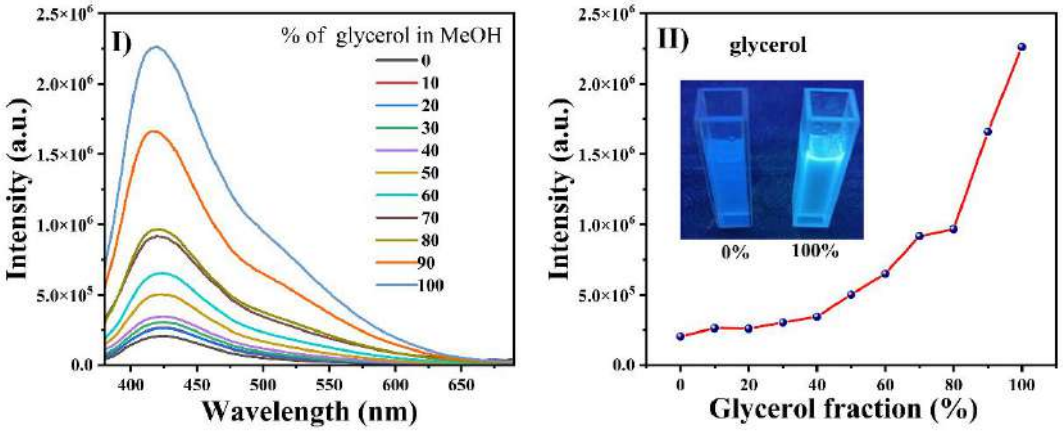

Figure A10. (I) Emission spectra of **L2H** in glycerol at different MeOH fractions, and (II) effect of glycerol fraction on emission intensity.

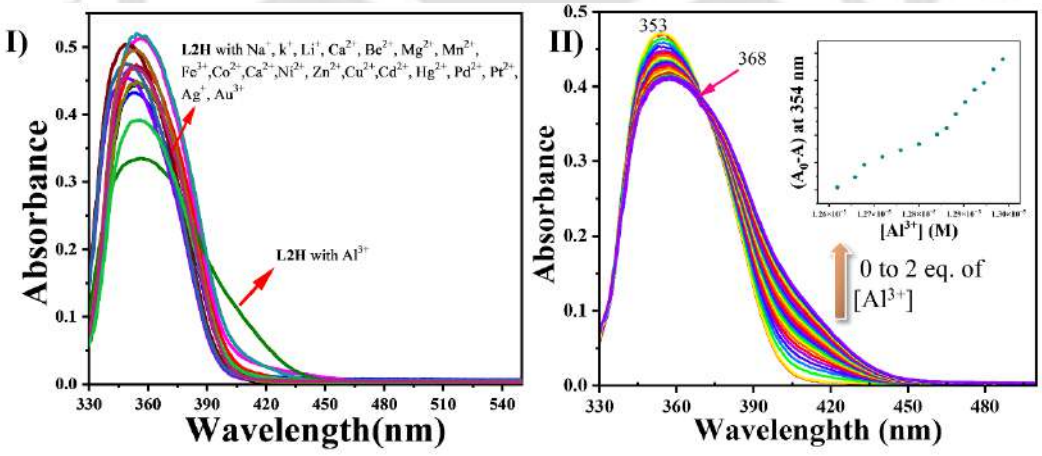

Figure A11. Changes in UV-Vis spectra of **L2H** (4 μM) with the addition of (I) various metal ions and (II) increasing concentration of Al^{3+} ion.

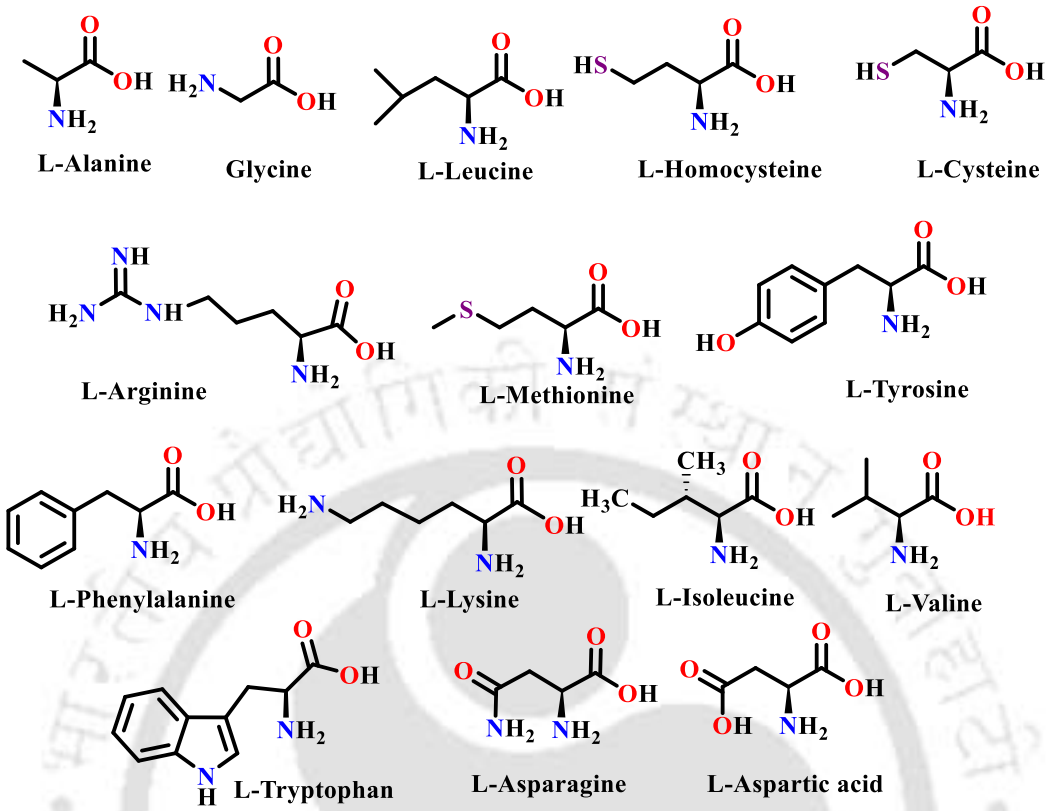

Figure A12. Chemical structure of different amino acids used in our present study.

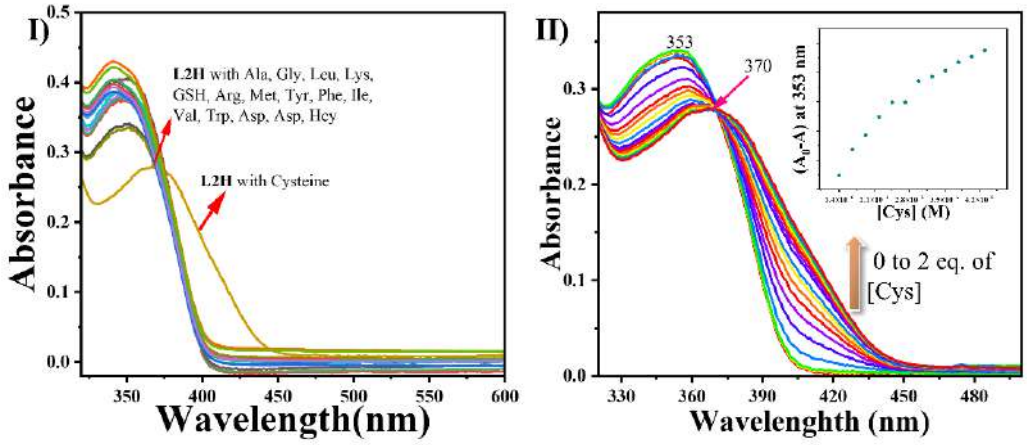

Figure A13. Changes in UV-Vis spectra of **L2H** (4 μM) with the addition of (I) various amino acids and (II) increasing concentration of cysteine solution.

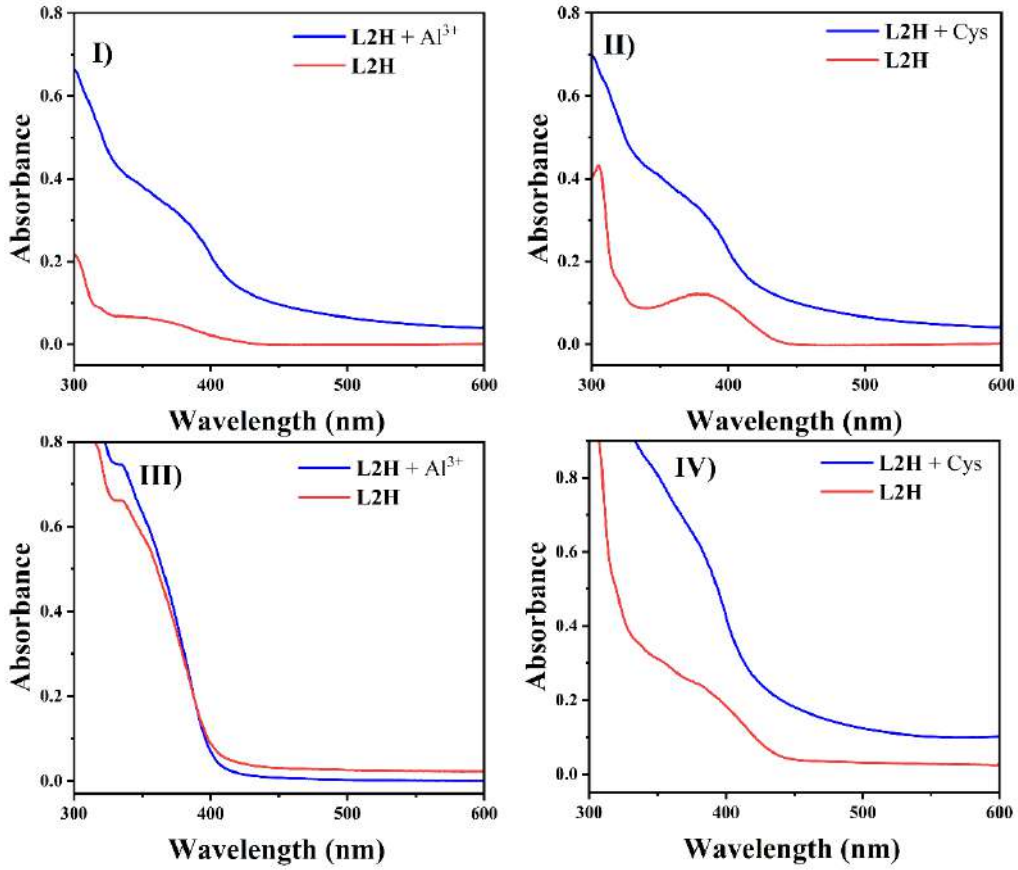

Figure A14. UV-Vis spectra of **L2H** with (I, III) Al^{3+} and (II, IV) cysteine in water and in aqueous CTAB medium (3 mM).

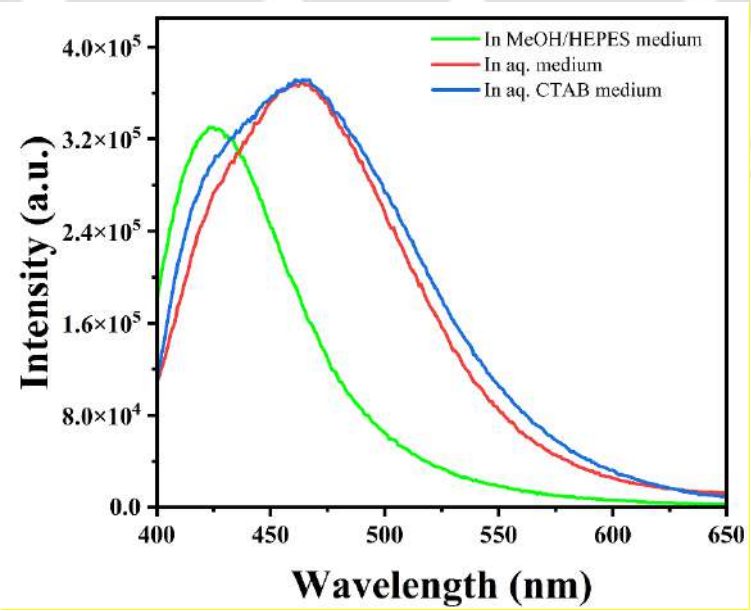

Figure A15. Emission spectra of **L2H** in water, MeOH/HEPES buffer (8:2, *v/v*) and aqueous CTAB medium.

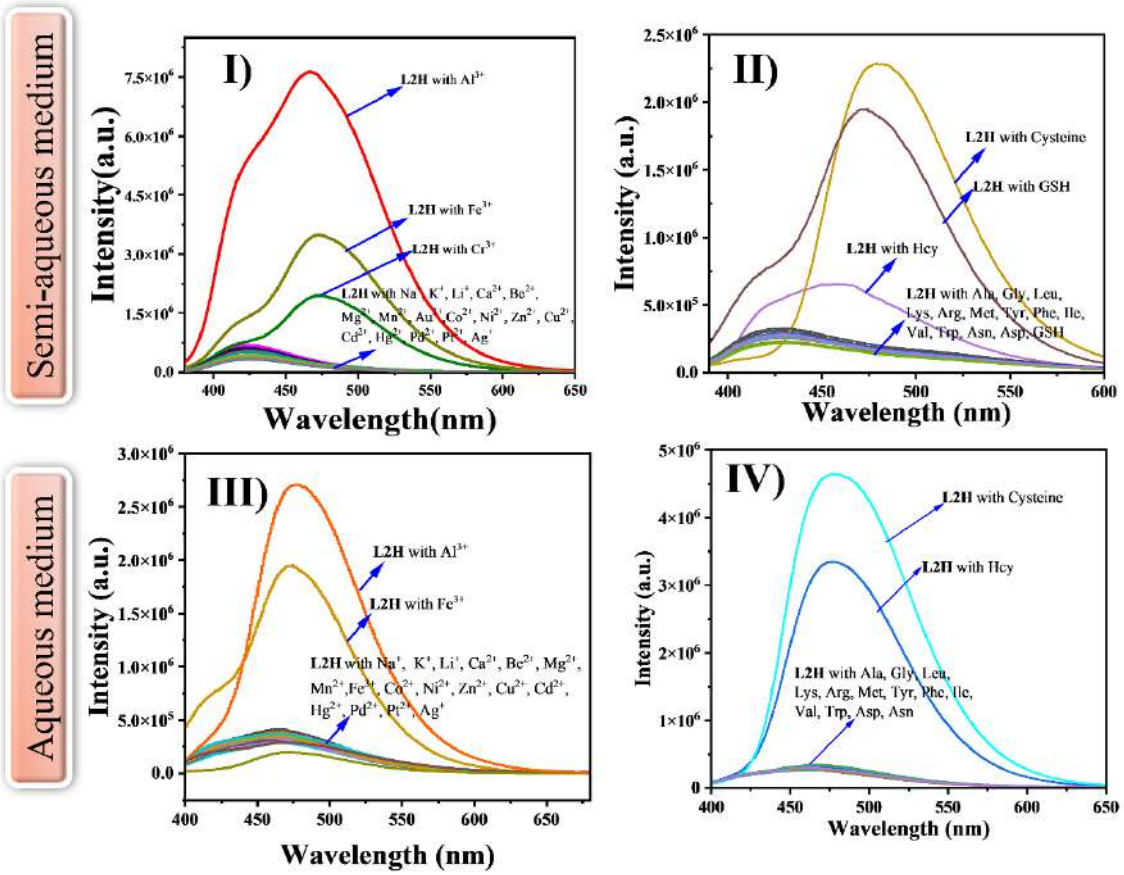

Figure A16. Emission spectra of **L2H** in presence of various metal ion (I, III) and (II, IV) amino acids in MeOH-HEPES (8:2, *v/v*) and pure aqueous medium.

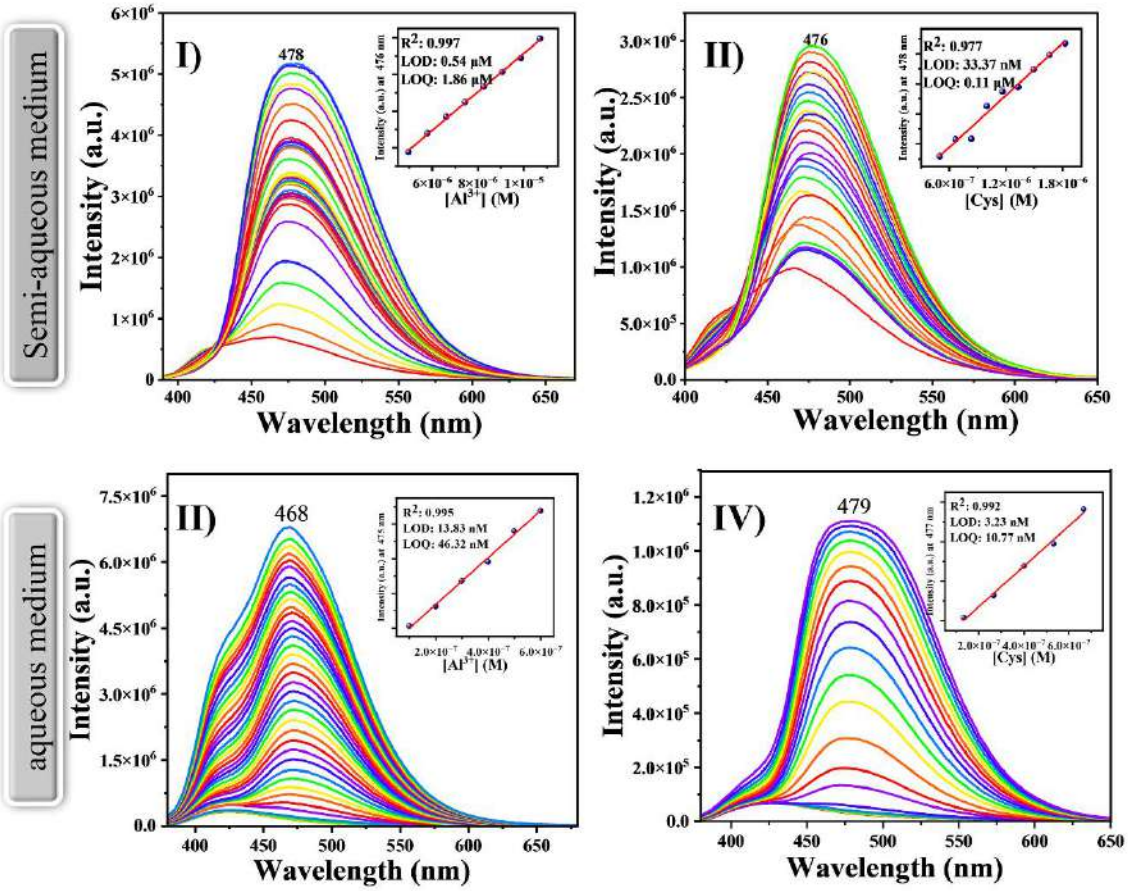

Figure A17. Fluorescence titration profile of **L2H** (4 μM) with Al^{3+} (12 μM) and cysteine (12 μM) in (I, III) MeOH-HEPES (8:2, *v/v*) and (II, IV) aqueous medium, λ_{ex} = 354 nm (inset: shown the LOD values obtained from the titration data plots).

Figure A18. Pictorial representation of **L2H** in presence of various (I) metal ions and (II) amino acids captured under visible light (top) and long UV light (bottom).

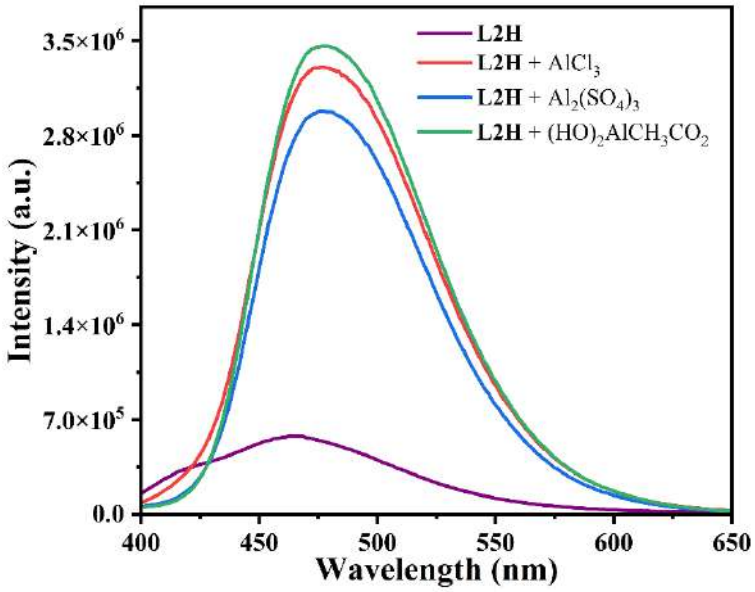

Figure A19. Fluorogenic responses of **L2H** over other common anions of Al^{3+}.

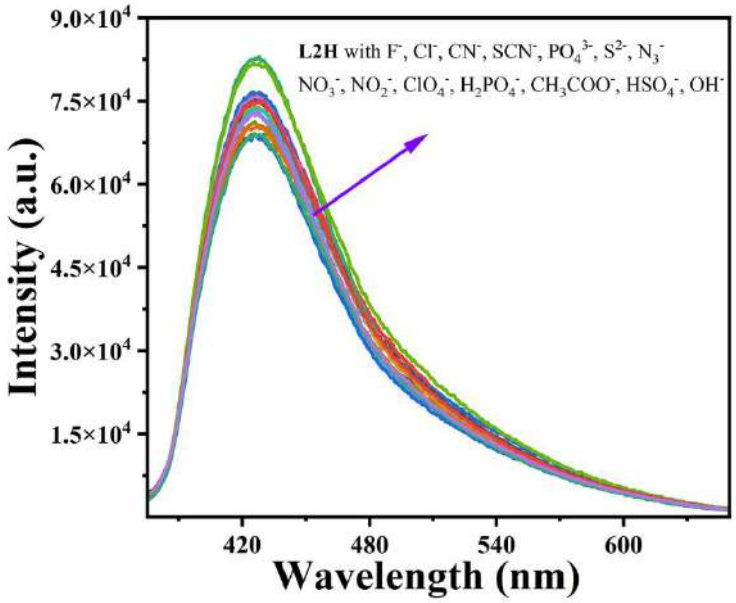

Figure A20. Fluorescence emission spectra of **L2H** with various anions.

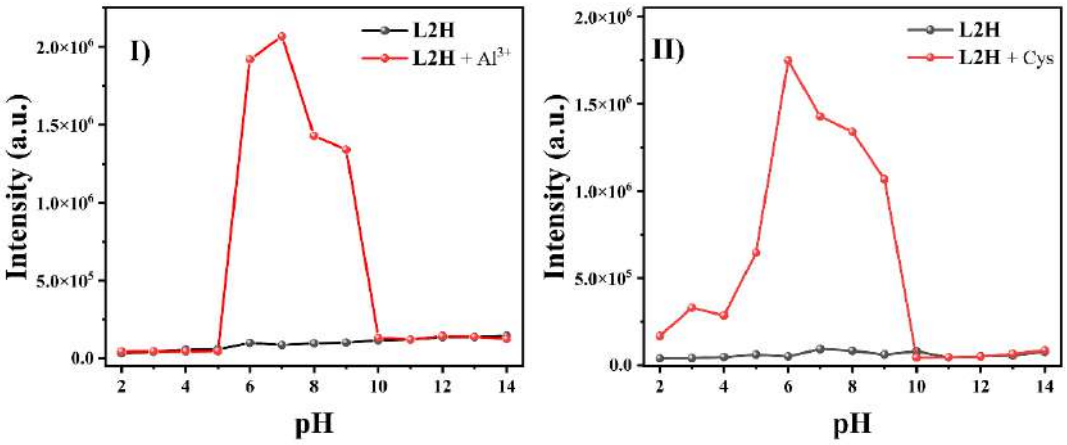

Figure A21. Change of fluorescence intensity of **L2H** (4 μM) before and after the addition of (I) Al^{3+} ion and (II) cysteine solution at diverse pH range (2–14) in CTAB medium.

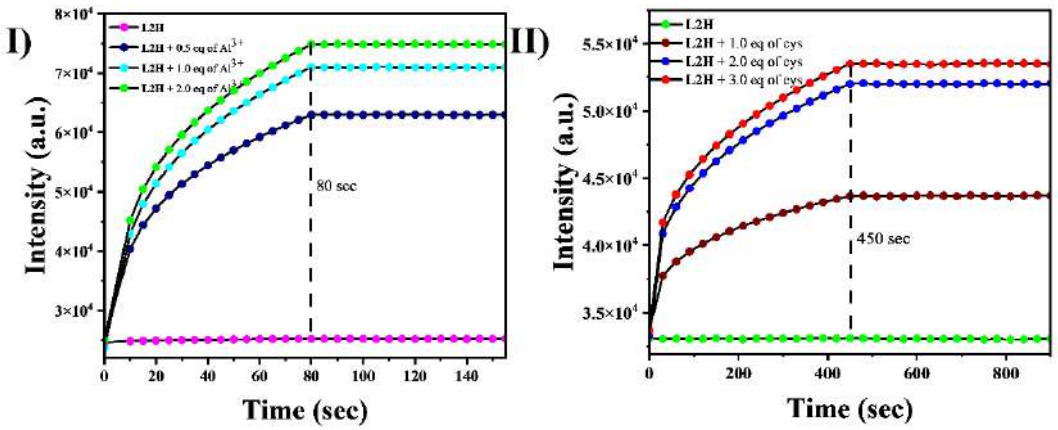

Figure A22. Fluorescence intensity enhancement profile for response time measurement of **L2H** (4 μM) with the addition of (I) Al^{3+} and (II) cysteine in pure aqueous medium from 0 to 15 min.

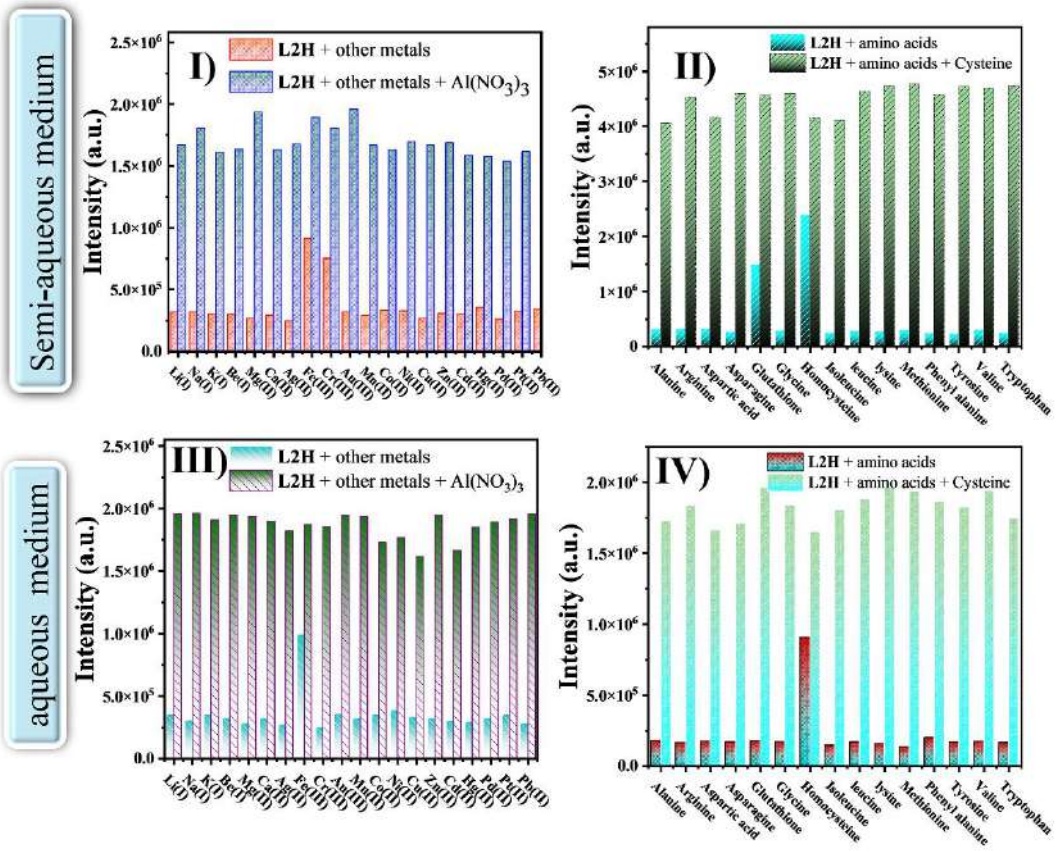

Figure A23. Interference study of **L2H** in presence of various competitive (I, III) metal ions and (II, IV) amino acids in semi-aqueous and aqueous medium.

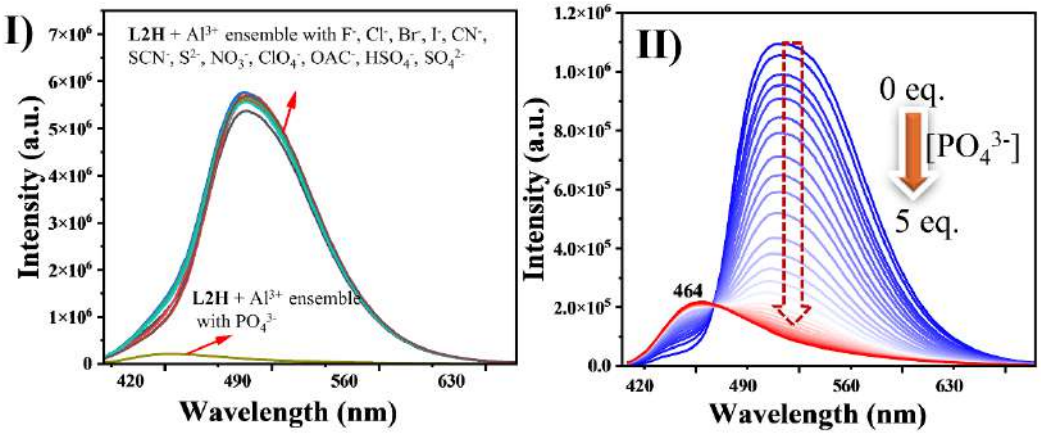

Figure A24. (I) Fluorescence spectra of **L2H** + Al^{3+} complex in presence of different anions, (II) fluorescence titration profile upon gradual addition of PO_4^{3-} with **L2H** + Al^{3+} complex.

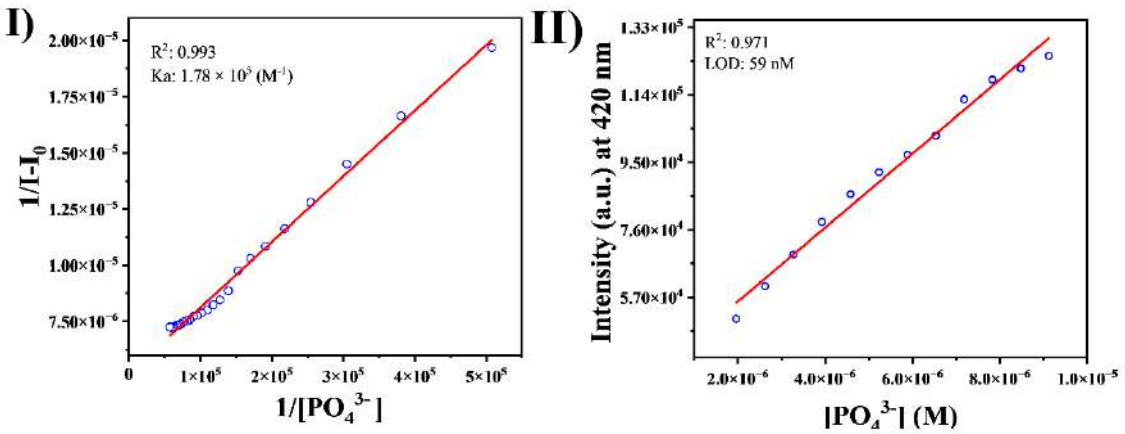

Figure A25. Determination of (I) binding constant and (II) LOD for *in situ* **L2H** + Al^{3+} complex for PO_4^{3-} ion.

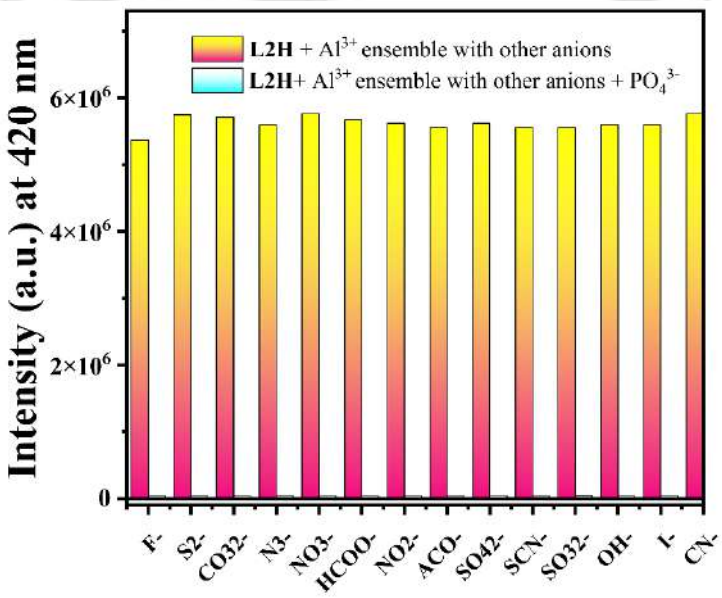

Figure A26. Bar diagram plot for anion competitive study.

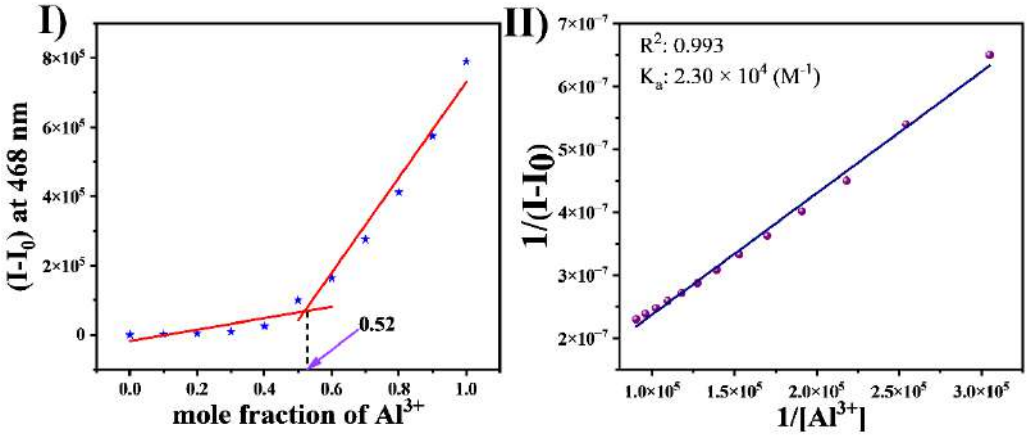

Figure A27. Determination of (I) binding stoichiometry and (II) binding constant of **L2H** with Al^{3+} ion.

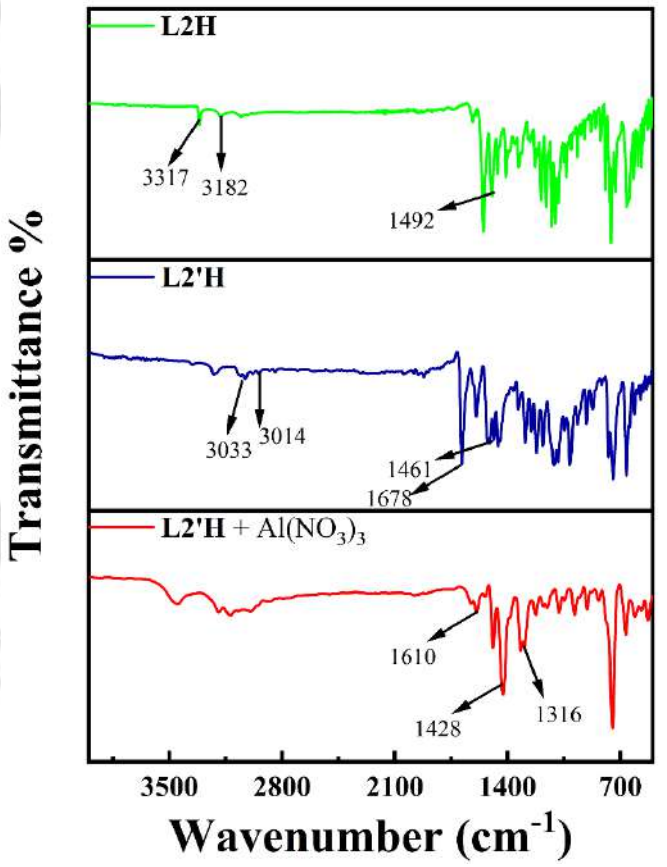

Figure A28 Combined IR spectra of **L2H** with $Al(NO_3)_3$.

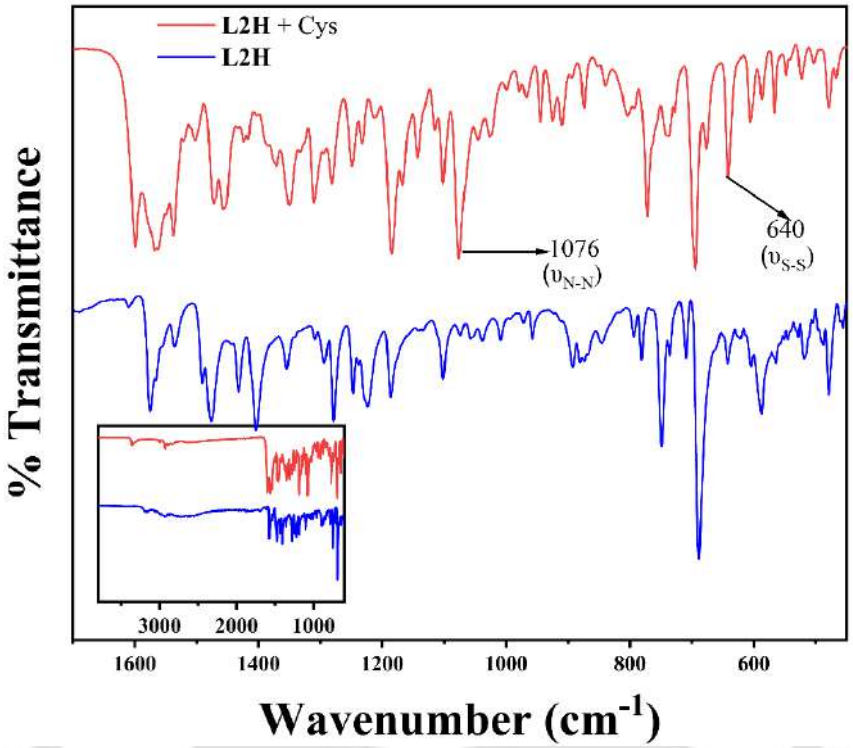

Figure A29 Combined IR spectra of **L2H** with cysteine (inset: full 4000-400 spectrum range).

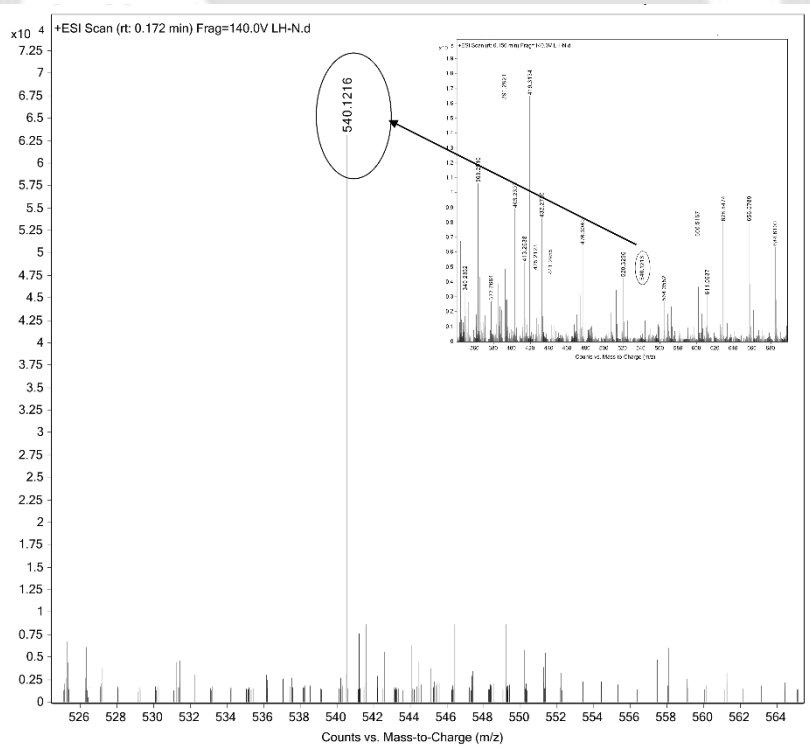

Figure A30. Mass spectrum of $[Al(\mathbf{L2H})(NO_3)_2(CH_3CN)]^+$ complex ion (inset: full range).

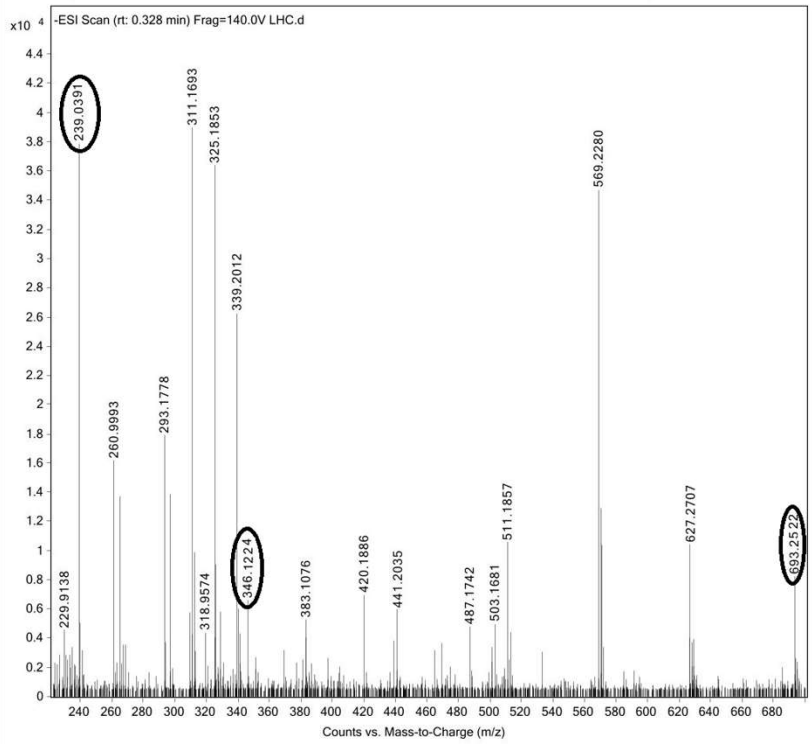

Figure. **A31** Mass spectrum of **L2H** with cysteine.

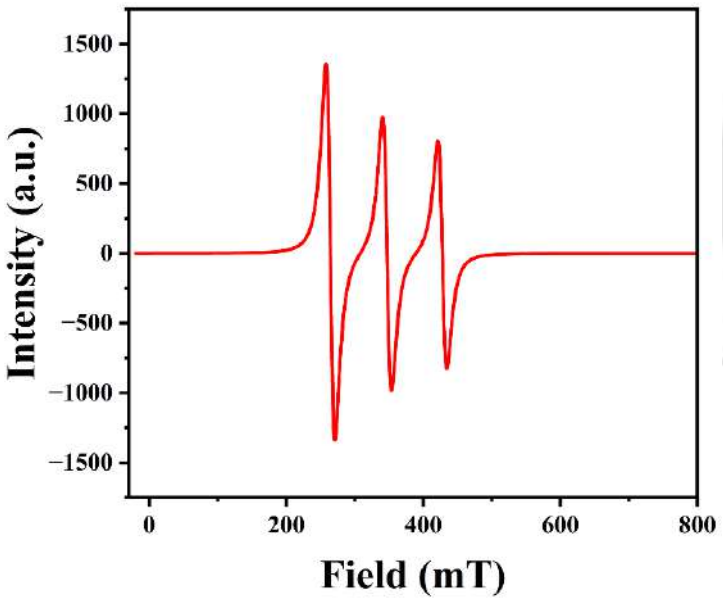

Figure A32. X-band EPR spectrum of **L2H** with cysteine in acetonitrile at 77 K.

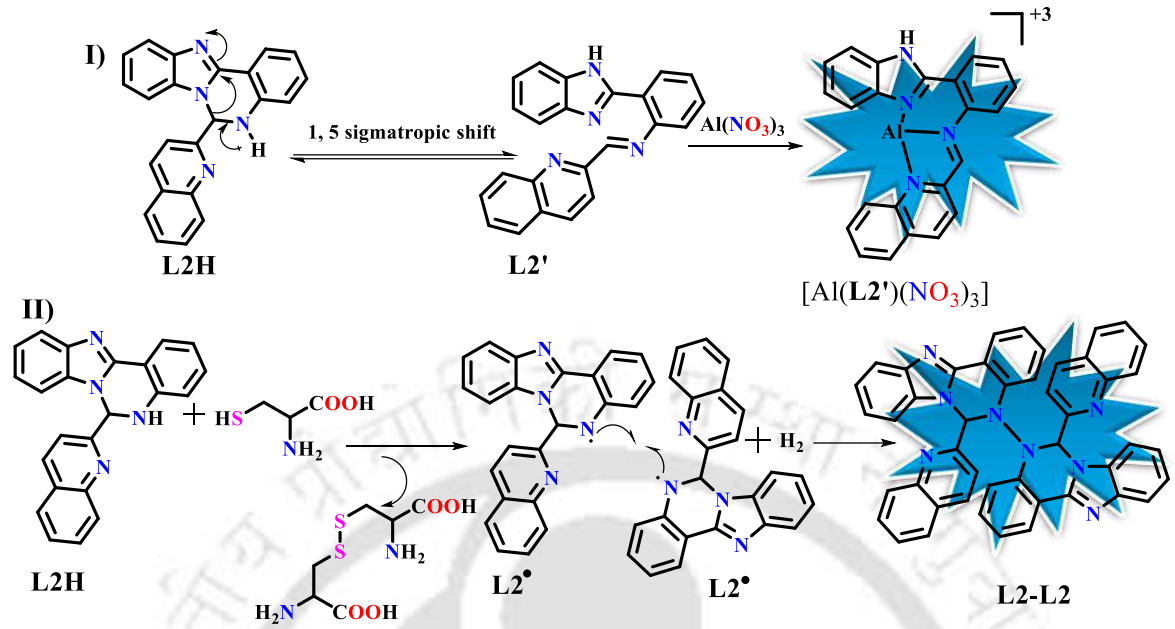

Scheme A. Favourable recognition pathway of **L2H** towards (I) Al^{3+} ion and (II) cysteine.

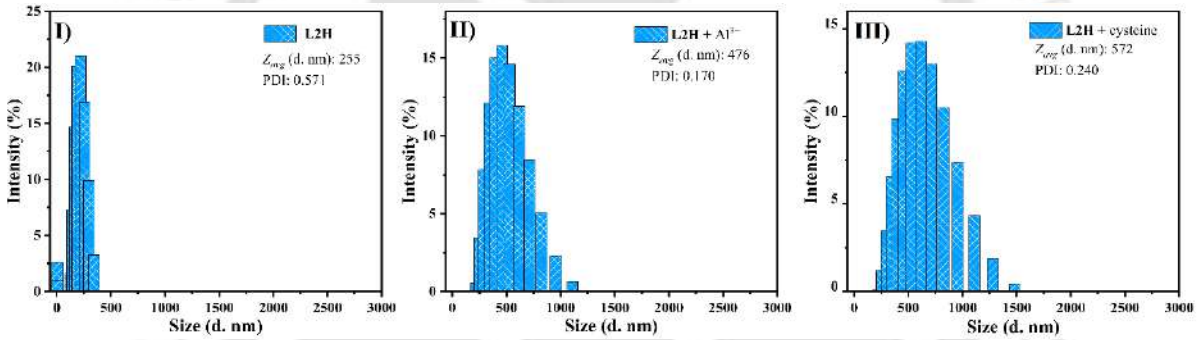

Figure A33. DLS data for (I) **L2H** before and after addition of (II) Al^{3+} and (III) cysteine in surfactant medium.

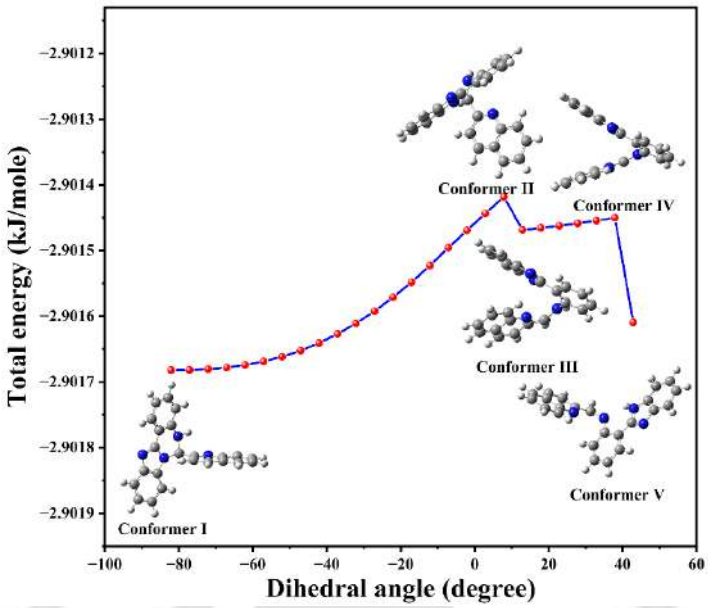

Figure A34. Conversion of cyclic form of **L2H** to acyclic form predicted by plotting DFT calculated energy *versus* dihedral angle (N2–C1–C2–N3) from -100° to +60° by involving the theoretical model in B3LYP/6-311G basic set.

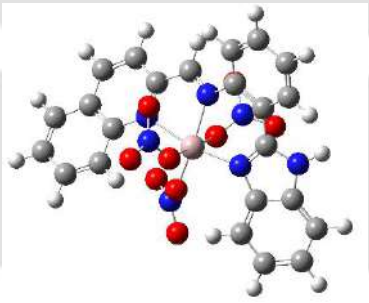

Figure A35. Optimized structure of [Al(**L2'**)$(NO_3)_3$] complex.

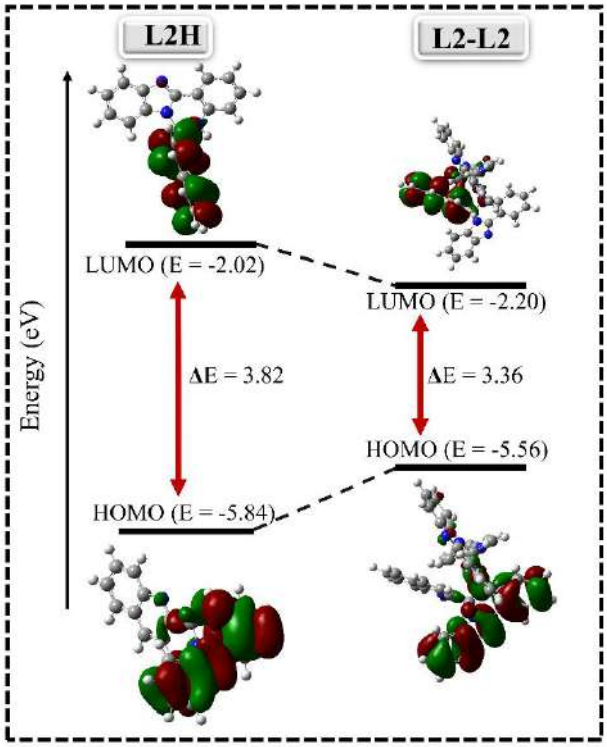

Figure A36. HOMO-LUMO energy gap of **L2H** and **L2–L2** dimer.

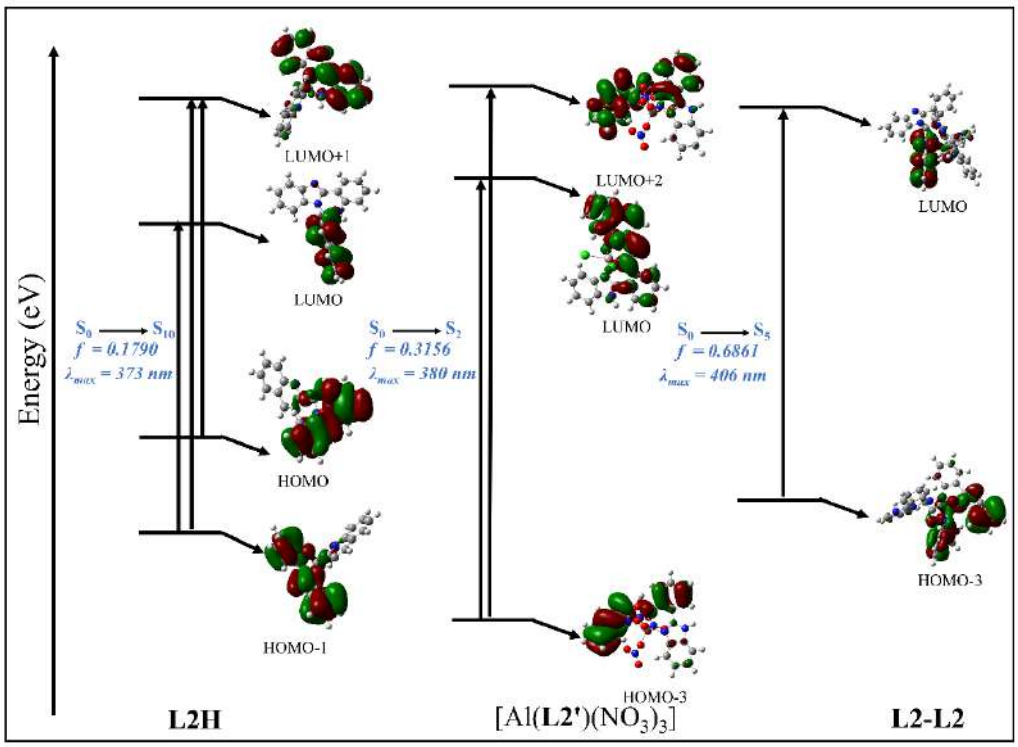

Figure A37. Energy levels profile of major absorption bands associated with free **L2H**, [Al(**L2'**)$(NO_3)_3$] complex and **L2–L2** in gaseous phase.

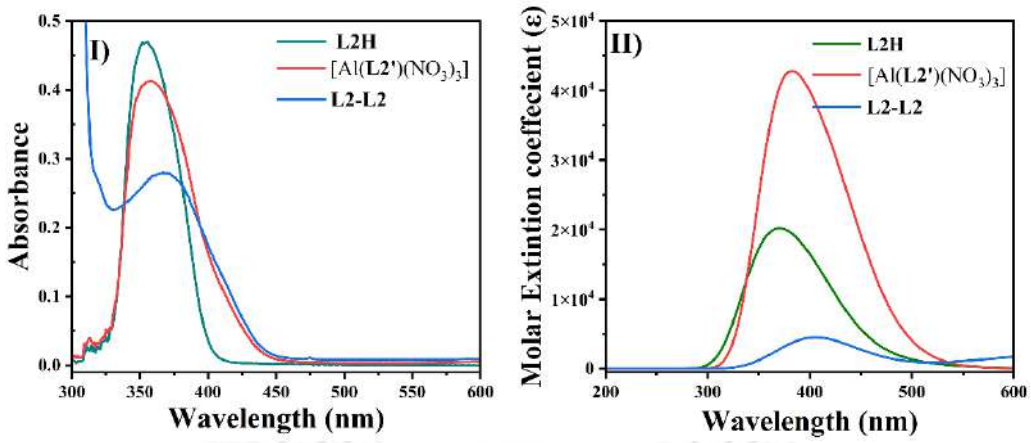

Figure A38. Combine (I) experimental and (II) theoretical absorption spectra of **L2H**, [Al(**L2'**)$(NO_3)_3$] and **L2–L2**.

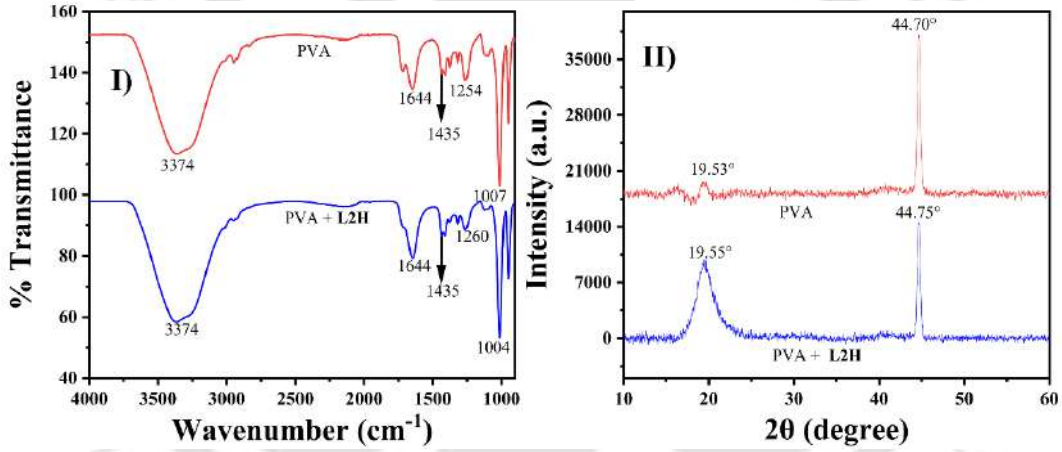

Figure A39. (I) IR and (II) XRD of blank PVA Hydrogels, **L2H** incorporated hydrogels.

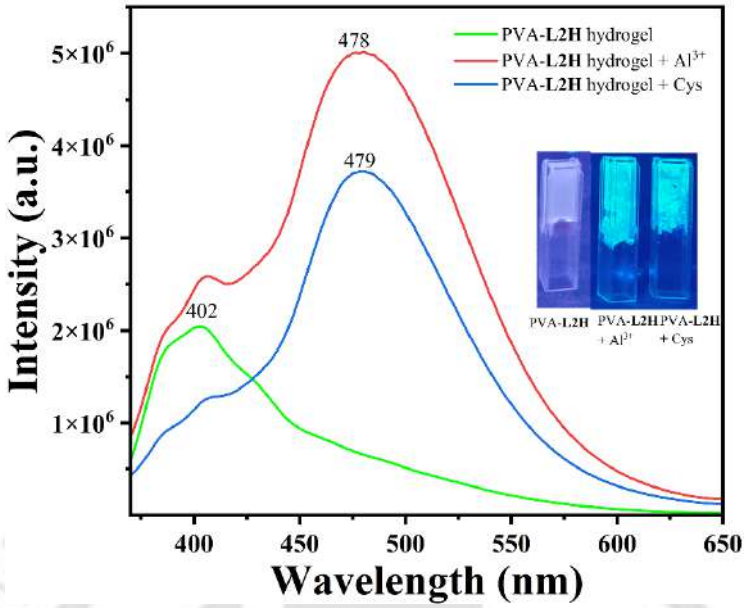

Figure A40. Fluorescence spectra of PVA-**L2H** hydrogel and PVA-**L2H** hydrogel with Al^{3+} (inset: visual colour change of PVA-**L2H** hydrogel in presence of $Al^{3+}$and Cys).

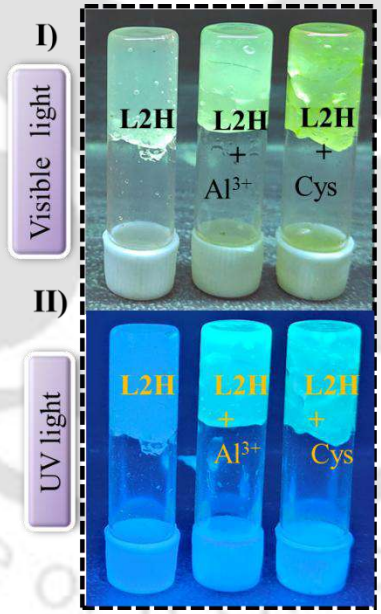

Figure A41. PVA-**L2H** hydrogel in presence of $Al^{3+}$and Cys in (I) visible light and (II) UV light.

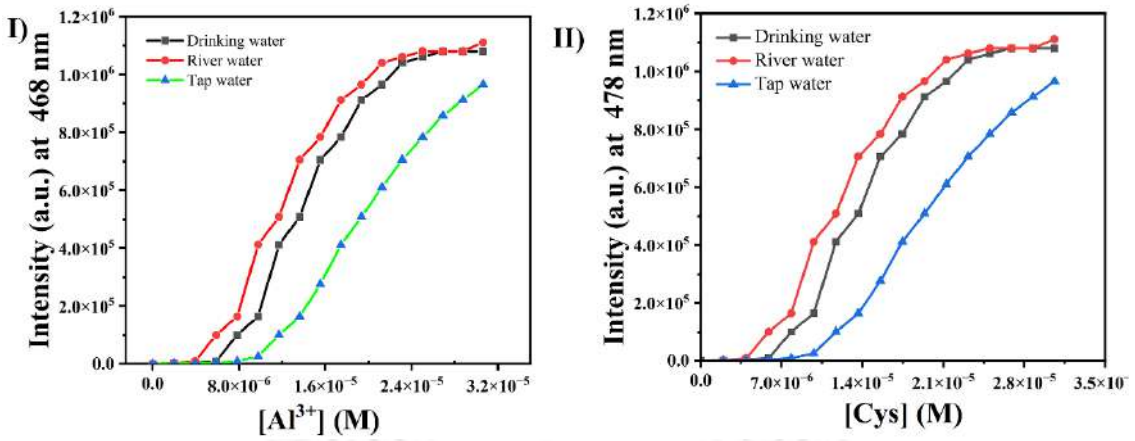

Figure A42. Variation of emission intensity of **L2H** of (I) Al^{3+} ion (3 equiv.) at 468 nm and (II) cysteine (3 equiv.) at 478 nm in all real water samples.

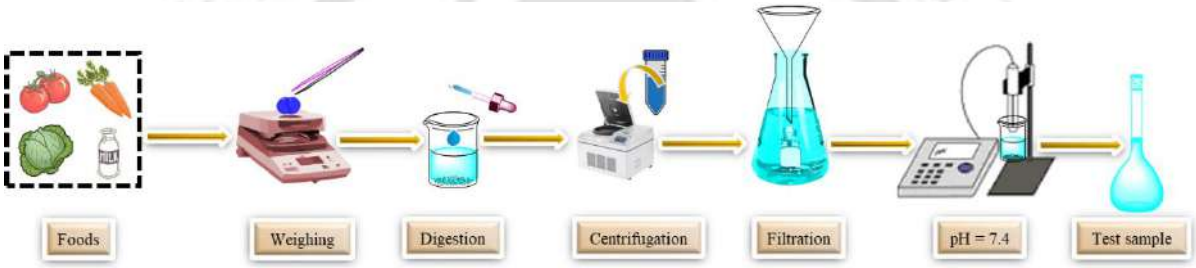

Figure A43. Pictorial representation for pretreatment process of all food samples.

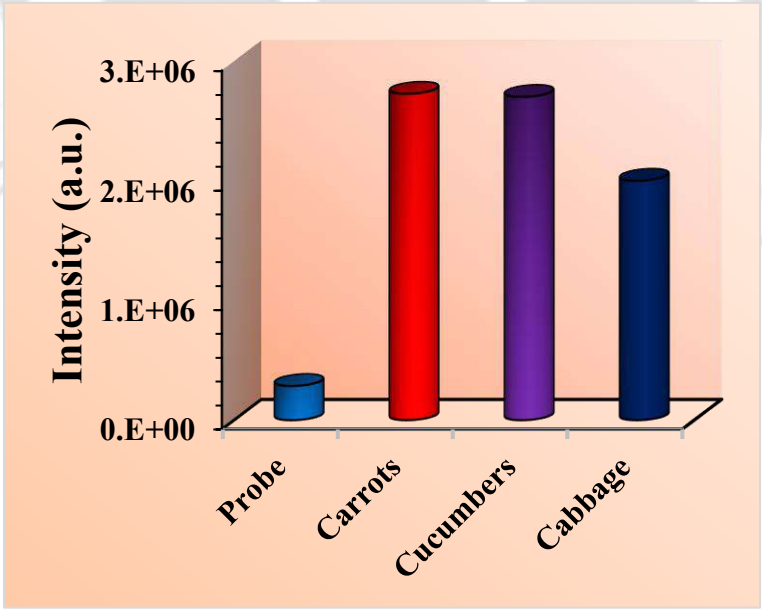

Figure A44. Bar diagram depicting variation of emission intensity change for **L2H** with Al^{3+} solution in different vegetable samples.

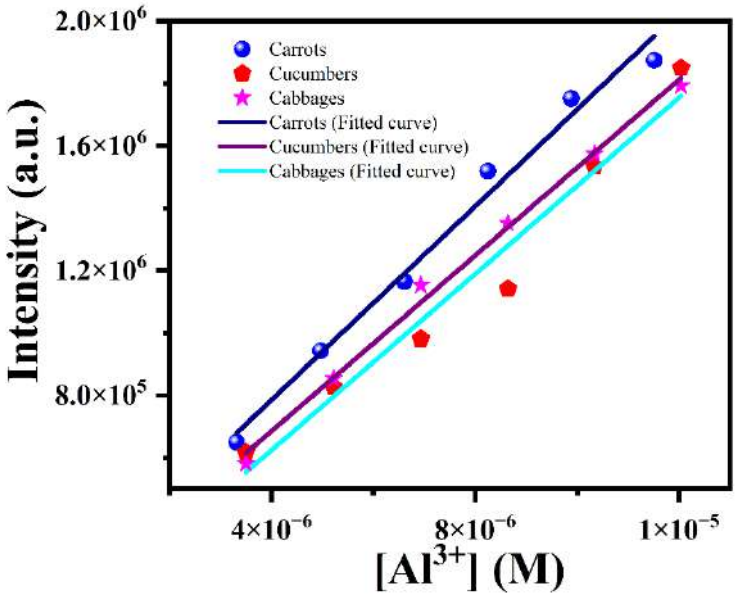

Figure A45. Linear correlation plots between the fluorescence intensity of **L2H** and Al^{3+} concentration in vegetable samples.

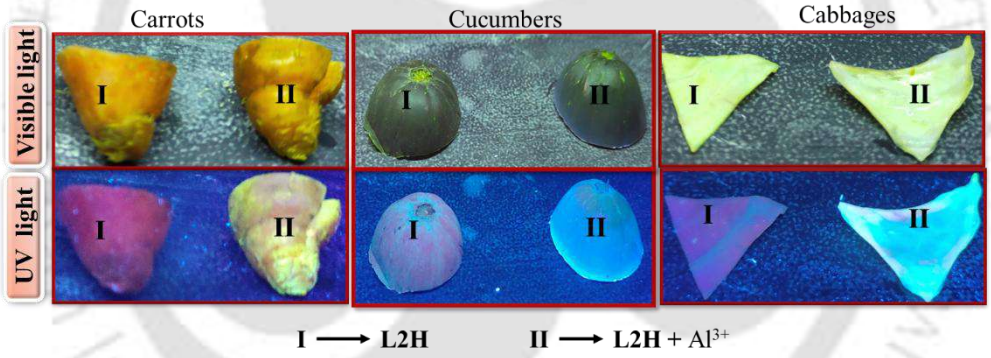

Figure A46. Photographs of **L2H** in vegetable samples in (I) absence and (II) presence of Al^{3+} ion.

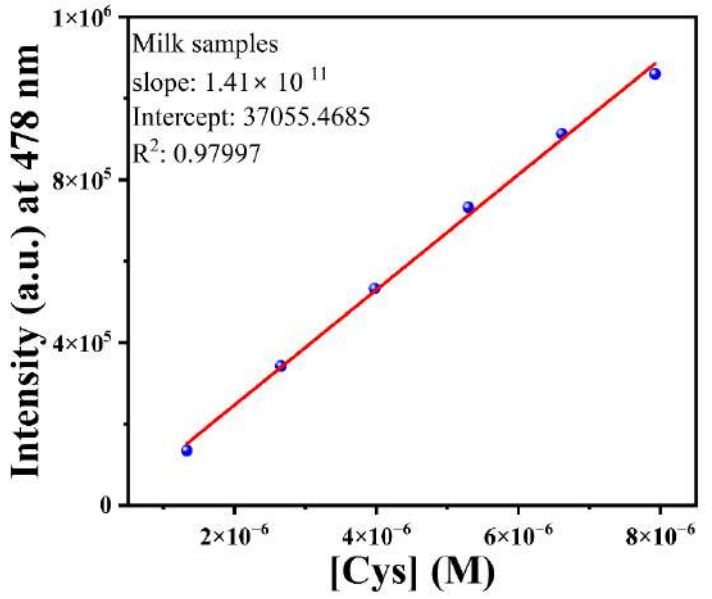

Figure A47. Linear correlation plot between fluorescence intensity of **L2H** and Al^{3+} concentration in milk samples.

Table A1. Crystallographic data and refinement parameters of **L2H**.

Formula	$C_{23}H_{16}N_4$
CCDC No	2440559
Mol. wt.	348.40
T, K	298
Cryst. syst.	Monoclinic
Space group	$P2_1/n$
a, Å	5.0582(10)
b, Å	12.119(2)
c, Å	26.758(5)
α, deg	90
β, deg	90.334(6)
γ, deg	90
V, Å^3	1640.2(5)
Z	4
*D*calcd, g cm^{-3}	1.411
μ, mm^{-1}	0.086
GOF[a] on F^2	1.085
F(000)	728.0
Reflection collected	31173

Unique reflections	2724
R_1[b], wR_2[c] ($I \geq 2\sigma(I)$)	0.1000, 0.1711
R_1[b], wR_2[c] (all data)	0.1924, 0.1987

[a]GOF (Goodness-of-fit) = $[\sum[w(F_0^2 - F_c^2)^2] / M - N]^{1/2}$ (M = number of reflections, N = number of parameters refined). [b]$R_1 = \sum \| F_0 | - | Fc \| / \sum | F_0 |$. [c]$wR_2 = [\sum[w(F_0^2 - F_c^2)^2] / \sum[w(F_0^2)^2]]$.

Table A2. Photophysical properties of **L2H** in different solvents.

Solvents	***λabs(nm)***	***λemi(nm)***	***Band width***	***Stokes shift (nm)***	***Polarity index***	***Dipole moment (D)***
Hexane	339	407	52	68	0	0
Toluene	340	425	66	85	2.4	0.3
Chloroform	341	450	70	109	2.7	1.0
THF	342	457	56	115	4.0	1.6
Methanol	345	422	62	18	5.1	1.6
Acetonitrile	347	472	50	125	5.8	3.5
DMF	348	512	60	164	6.4	3.8
DMSO	349	514	68	165	7.2	3.9
Water	351	523	94	172	10.2	1.85

Table A3. Fluorescence decay parameters of **L2H** in various Water-MeOH fractions (90–60 %).

Entry	***τ_1(ns)***	***τ_2(ns)***	***α_1(%)***	***α_2(%)***	***τ(ns)***	***χ^2***
90%	0.08	9.30	2.57	2.97	5.02	0.95
80%	0.31	4.87	5.75	2.00	1.48	0.97
70%	0.24	3.35	9.24	1.54	0.68	0.97
60%	0.08	9.90	1266.82	1.34	0.08	0.89

Table A4. Fluorescence decay parameters of **L2H**, and **L2H** with Al^{3+} and Cys solution.

Entry	***τ_1(ns)***	***τ_2(ns)***	***α_1(%)***	***α_2(%)***	***τ(ns)***	***χ^2***	***φ_f***	***kr***	***knr***
L2H	0.53	4.96	558.73	2.37	0.55	0.98	0.08	0.14	1.67
L2H + Al^{3+}	3.54	10.47	1.73	12.3	9.61	0.99	0.57	0.05	0.05
L2H + Cys	1.24	8.49	14.46	11.06	4.65	0.99	0.36	0.07	0.14

Table A5. Determination of quantum yield (φ, in %) of **L2H** and **L2H** with Al^{3+} and cysteine ensemble in three different solvent media.

Solvent system	***L2H***	***L2H** with Al^{3+}*	***L2H** with cysteine*
Aqueous medium	2.05 %	43.00 %	20.69 %
Semi-aqueous medium	1.12 %	31.86 %	6.70 %
CTAB medium	8.82 %	57.91 %	26.13 %

Table A6. Main electronic transition calculated by TDDFT method for **L2H**, [Al(**L2'**)$(NO_3)_3$] complex and **L2–L2** in gaseous phase.

Analytes	*Energy (eV)*	λ_{theo} *(nm)*	*Oscillator strength*	*Major Transition*	*Electronic transition*	λ_{exp} *(nm)*
L2H	3.013	461.41	0.0164	(70%) HOMO→LUMO	$S_0 \rightarrow S_3$	351
	3.714	373.27	0.1790	(57%) HOMO→LUMO+1 (17%) HOMO-1→LUMO (12%) HOMO-1→LUMO+1	$S_0 \rightarrow S_{10}$	
	3.785	377.51	0.0769	(62%) HOMO-2 → LUMO (30%) HOMO → LUMO+1	$S_0 \rightarrow S_{12}$	
	3.993	360.44	0.0459	(10%) HOMO+1→ LUMO +1 (68%) HOMO → LUMO +2	$S_0 \rightarrow S_{15}$	
	4.296	338.57	0.0569	(68%) HOMO-4→ LUMO +2 (62%) HOMO-3→ LUMO (23%) HOMO-1 → LUMO +1	$S_0 \rightarrow S_{16}$	
	4.315	337.30	0.1548	(60%) HOMO-1→ LUMO+1	$S_0 \rightarrow S_{17}$	
	4.380	333.05	0.0741	(60%) HOMO-2→ LUMO +1	$S_0 \rightarrow S_{18}$	
	4.414	330.83	0.0276	(48%) HOMO-7→ LUMO (21%) HOMO-6 → LUMO (35%) HOMO-4 → LUMO	$S_0 \rightarrow S_{19}$	
	4.453	328.42	0.0474	(10%) HOMO-2→ LUMO +1 (40%) HOMO-7 → LUMO (17%) HOMO -6 → LUMO (28%) HOMO-3→ LUMO+2	$S_0 \rightarrow S_{20}$	
[Al(**L2'**)$(NO_3)_3$]	4.241	392.29	0.2154	(44%) HOMO-2→LUMO	$S_0 \rightarrow S_1$	355
	4.537	380.83	0.3156	(44%) HOMO-3→LUMO (14%) HOMO-3→LUMO+2	$S_0 \rightarrow S_2$	
	5.002	347.87	0.2845	(36%) HOMO→LUMO+1	$S_0 \rightarrow S_6$	
	5.475	326.44	0.2789	(34%) HOMO-4→LUMO	$S_0 \rightarrow S_7$	
L2–L2	3.624	406.43	0.6861	(68%) HOMO-3→LUMO	$S_0 \rightarrow S_5$	381
	3.578	346.50	0.0202	69%) HOMO-1 →LUMO+1	$S_0 \rightarrow S_6$	
	3.632	341.30	0.1051	(10%) HOMO-4 →LUMO+2 (63%) HOMO →LUMO+2	$S_0 \rightarrow S_7$	
	3.731	332.28	0.0445	(52%) HOMO-4→ LUMO (36%) HOMO-1 → LUMO+2	$S_0 \rightarrow S_8$	
	3.772	328.63	0.1480	(12%) HOMO-5 →LUMO (11%) HOMO-3 →LUMO+2 (53%) HOMO-1 →LUMO+2	$S_0 \rightarrow S_{10}$	

Table A7. Determination of Al^{3+} and cysteine in various real water samples using **L2H** (4 μM).

Analytes	*Water Sample*	*Spiked (μM)*	*Detected (μM)*	*Recovery (%)*	*RSD (%) n = 3*
Al^{3+}	Drinking	4	4.03	99	3.42
	River	4	4.05	98	1.74
	Tap	4	4.11	97	1.02
cysteine	Drinking	4	4.13	96	4.75
	River	4	4.48	89	4.34
	Tap	4	4.07	98	1.03

Table A8. Determination of Al^{3+} in various food samples using **L2H** (4 μM).

Water Sample	*Spiked (μM)*	*Detected (μM)*	*Recovery (%)*	*RSD (%) n = 3*
Carrots	3	3.30	90	4.76
Cucumber	3	3.05	98	1.58
Cabbage	3	3.23	92	9.45

Table A9. Determination of Cys in milk samples using **L2H** (4 μM).

Spiked (μM)	*Detected (μM)*	*Recovery (%)*	*RSD (%) n = 3*
2	2.03	98	7.46
3	3.09	97	2.60
6	6.06	99	1.54

[#]All the experiments were repeated three times.

Table A10. Comparative literature survey of **L2H** with other reported sensors.

Analytes detection	*Probe structure*	*LOD*	*Solvent medium*	*Four major applications*				*Ref*
				Paper strips	*Logic gate and device fabrication*	*pH sensor*	*Solid-state sensing*	
Al^{3+} F^-	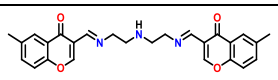	Al^{3+}: 6.9 μM F^-: 68 nM	Aqueous medium	yes	no	no	no	54
Al^{3+}	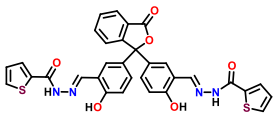	Al^{3+}: 0.56 μM	DMSO	yes	no	no	no	55
Al^{3+}	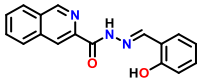	Al^{3+}: 1.11 nM	EtOH	no	no	no	yes	56

Al^{3+} HSO_3^-	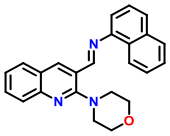	Al^{3+}: 2.14 nM HSO_3^- : 2.31 nM	THF/H_2O (1:1, *v/v*, 50 mM of HEPES, pH = 7.4)	no	yes	no	yes	57
Al^{3+}	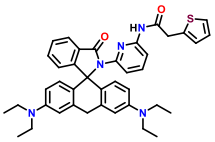	Al^{3+}: 0.177 µM	EtOH/H_2O (1:1, *v/v*)	no	no	no	yes	58
Cysteine	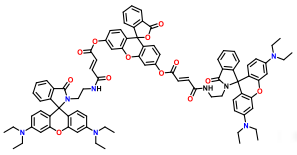	Not mentioned	ACN/H_2O (2:8, *v/v*), (10 mM of HEPES ~7.4 pH)	no	no	no	yes	59
Cysteine Hcy GSH	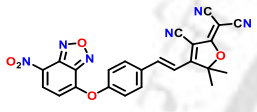	Cys: 0.015 µM Hcy: 0.034 µM GSH: 0.030 µM	PBS-buffer/ DMF (9:1, *v/v*)	no	no	no	yes	60
Cysteine	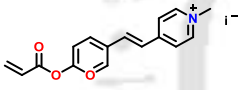	Not mentioned	PBS-buffer/ DMSO (1:1, *v/v*)	no	no	no	yes	61
Cysteine	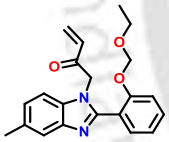	Cys: 39.8 µM	1 mM phosphate buffer	no	no	no	no	62
Cysteine	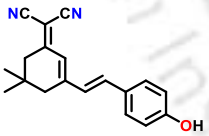	Cys: 0.17 µM	ACN/H_2O	no	no	no	yes	63
Cysteine	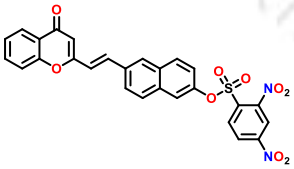	Cys: 2.89 nM	HEPES-EtOH buffer (3/2, *v/v*, pH = 7.40)	no	no	no	no	64
Al^{3+} Cysteine	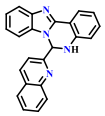	Al^{3+}: 2.75 nM Cys: 2.65 nM	surfactant medium	yes	yes	yes	yes	This work

Chapter 5

Smartphone-based Portable Sensing Device for Fluorometric Detection of As^{3+} ion Using an AIE active Quinazolinone Analogue*

Abstract:

An AIE active molecule **L3H** bearing quinazolinone moiety was synthesized, thoroughly characterized and evaluated as a metal ion sensor. By virtue of having 4-diethylaminophenyl group as fluorophore unit at the periphery, this probe exhibited a selective turn-on response for As^{3+} ion in aqueous HEPES and MeOH-HEPES medium (6:4, *v/v*), with a detection limit of 55 nM and 5.25 μM, respectively. The results of DFT/TDDFT calculations on **L3H** and [As(**L3**)(Br_2)] complex were consistent with the experimental findings. Practical application was demonstrated using portable, cost-effective paper strips, and recovery tests were also conducted on various food and real water samples. Moreover, rapid on-site detection of As^{3+} ion was achieved using a prototype smartphone device. Molecular docking analysis of **L3H** with biomolecules such as BSA and HSA revealed binding affinities of -4.64, -7.12 kcal/mol, indicating their potential for albumin interaction and therapeutic use.

* This work has been submitted for publication:

A. Mondal, S. Sinha, V. Manivannan (*Submitted*).

5.1 Introduction:

Arsenic is a naturally occurring element in the earth's crust, known for its high toxicity and serious health risks.[1,2] The chronic toxicity of arsenic has created various impacts on human health, excessive accumulation leads to diabetes, cardiovascular disorder, neurotoxicity, skin cancer, and hyperpigmentation.[3–5] Arsenic contamination primarily occurs through drinking water, as well as the consumption of crops irrigated with contaminated water.[6,7] WHO recommended a safe limit of arsenic detection in drinking water as 10 ppb,[8] so proper continuous monitoring of arsenic concentration in groundwater and drinking water is crucial for the public health. Traditional methods such as atomic absorption spectroscopy (AAS), inductively coupled plasma-mass spectrometry (ICP-MS), atomic fluorescence spectrometry (AFS), are utilized for accurate measurement of As^{3+} ion, however the methods are often expensive, time consuming, and require specialized equipment and skilled operators.[9] So, various attempts were made to replace these traditional methods for the detection of toxic As^{3+} ion. Hence, there is a growing demand for simple, cost-effective, and portable detection methods that can be directly used at the contamination sites without using expensive equipment.[10–12] Additionally, modern approaches have integrated these chemosensors into portable devices for more user-friendly applications. For instance, smartphone-based platforms have been developed to monitor arsenic concentrations in water. These devices use a simple Bluetooth connection to detect colour changes in the sensor and process the data, enable real-time, contactless monitoring.[13–15] This not only enhances the practicality of arsenic detection but also helps to prevent the risks associated with direct handling of contaminated waste samples. Moreover other innovative methods such as, use of metal nanoparticles have been explored to improve arsenic detection.[16,17] While these nanoparticles can offer enhanced sensitivity, their application is sometimes hindered by issues such as higher costs, complex synthesis, and stability concerns.[18,19] Therefore, ongoing research focuses on developing simple yet efficient organic chemosensors that can operate effectively in various environmental conditions, with lower detection limits and broader usability.

Quinazolinone based heterocyclic compounds have been found to exhibit good luminescence properties.[20–22] The tunable electronic properties, electron-rich nature, and rigid planar structure, it is often used to design such fluorescent probes for the detection of hazardous metal ions.[23,24] Recently, quinazolinone derivatives that are active through aggregation-induced emission (AIE) and twisted intramolecular charge transfer (TICT) properties have been

reported as fluorescent sensors.[25,26] Due to their high selectivity and sensitivity towards metal ions, many researchers were interested in using quinazolinone linked AIE active analogue as a chemosensor.[27,28] In this Chapter, the ability of **L3H** bearing 4-(diethylamino)-2-(hydroxybenzylidene)amino moiety as an AIE active fluorescence probe towards As^{3+} ion in aqueous HEPES medium has been described.

5.2 Experimental Section:

Compound **L'H** was synthesized using the previous literature procedure.[29]

5.2.1 Synthesis

(E)-3-((4-(diethylamino)-2-hydroxybenzylidene)amino)-2-(pyridine-2-yl)-2,3-dihydroquinazolin-4(1H)-one) (**L3H**)

A mixture of **L'H** (0.240 g, 1 mmol) and 4-(diethylamino)-2-hydroxybenzaldehyde (0.193 g, 1 mmol) dissolved in methanol (20 mL) was heated at reflux for 17 h. The pale-yellow precipitate obtained after cooling was collected through filtration and washed with ice-cold ethanol. Yield: 0.360 g (86%). M.P.: 232 °C. 600 MHz ^{1}H NMR (δ (J, Hz), $CDCl_3$): 10.85 (s, 1H, OH), 8.85 (s, 1H, CH=N), 8.59 (d, 1H, J = 4.3 Hz), 7.95 (d, 1H, J = 7.6 Hz), 7.63 (t, 1H, J = 7.5 Hz), 7.37 (d, 1H, J = 1.4 Hz), 7.25 (s, 1H), 7.21 (m, 1H), 7.05 (dd, 1H, J = 5.1 Hz), 6.85 (t, 1H, J = 7.4 Hz), 6.65 (d, 1H, J = 8.0 Hz), 6.22 (dd, 1H, J = 2.2 Hz), 6.12 (dd, 2H, J = 2.1, 3.9 Hz), 5.49 (s, 1H), 3.36 (q, 4H, J = 7.1 Hz), 1.17 (t, 6H, J = 7.1 Hz). 600 MHz ^{13}C NMR (δ, $CDCl_3$): 161.58, 161.19, 160.35, 157.95, 151.40, 150.03, 145.09, 137.26, 134.04, 133.72, 128.85, 123.72, 121.26, 119.93, 116.24, 115.31, 106.39, 103.97, 98.12, 44.67, 12.78; HRMS (*m/z*): calculated for $C_{24}H_{25}N_4O_2$ $[M+H]^+$: 416.2082; found: 416.2065; Selected IR peaks (ATR mode, cm^{-1}): 3403 (ν_{N-H}), 3045 (ν_{C-H}), 1648 ($\nu_{C=O}$), 1617 ($\nu_{C=N}$) (Figure A1-A4).

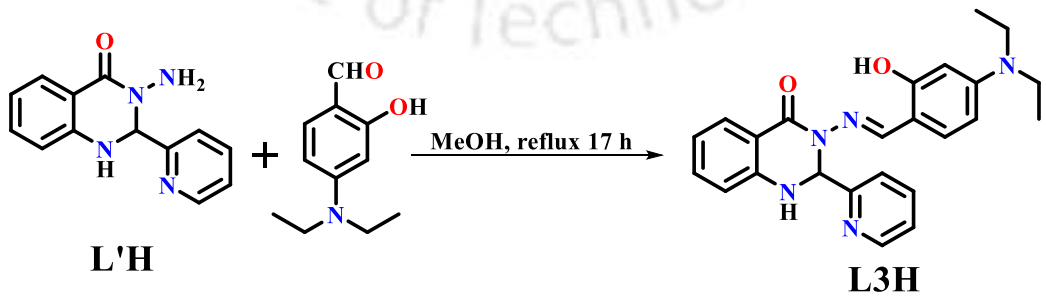

Scheme 1. Synthesis of **L3H**.

5.3 Results and Discussion:

5.3.1 Probe

A quinazolinone-based hydrazides were synthesized (Scheme 1) in order to examine their AIE behaviour. Key considerations in their design included: (i) incorporation of two different fluorophores 4-diethylaminophenyl group anchored to 2-(pyridin-2-yl)-2,3-dihydroquinazolin-4(1H)-one moiety to achieve strong fluorescence (ii) enhancement of intramolecular charge transfer (ICT) pathway *via* imine linked donor-acceptor sites (iii) appropriate peripheral fluorophore arrangement allowing bond rotation in organic solvents and (iv) presence of hydroxyl and azine groups that are known to facilitate photo-induced electron transfer (PET) and excited-state intramolecular proton transfer (ESIPT) processes which render the probe weakly emissive in non-polar solvents. The optimized structures (Figure 1A) showed a slight angular deviation between the fluorophore planes and the quinazolinone unit due to the imine linkage, resulting in a twisted conformation. Electrostatic potential maps (Figure 1B) revealed electron-rich red regions with negative potential localized around hydroxyl groups and blue regions of high positive potential. The highest electron density was observed at N–N and O–H bonds, highlighting their electron donating nature.

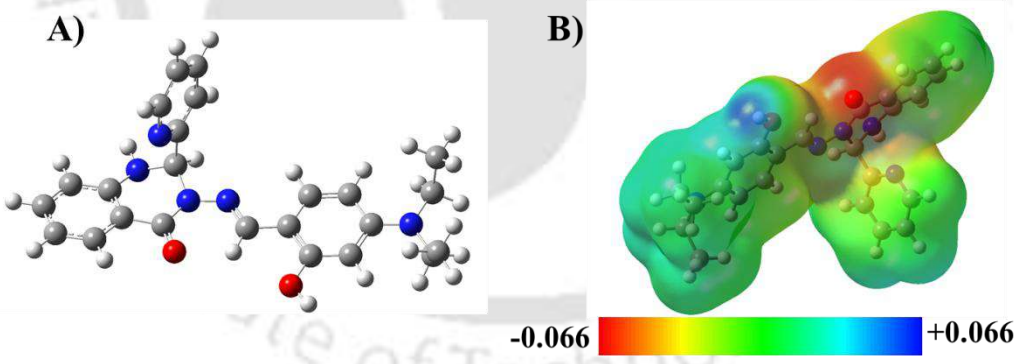

Figure 1. (A) Optimized structure using B3LYP/LANL2DZ level of theory, and (B) electrostatic potential map of **L3H**.

3.5.2 Spectra and AIE Property

UV-Vis and fluorescence spectra of **L3H** were recorded in ten different solvents of varying polarity and spectral values were listed in Table A1. Both absorption and fluorescence spectra of the probe were normalized to unity. By changing from non-polar to polar solvents, **L3H** exhibited a shift of (i) 15 nm in absorbance maximum (Figure A5I) and (ii) 55 nm in emission

peak with λ_{ex} = 372 nm (Figure A5II), which is due to moderate intraligand charge transfer in origin.

The aggregation behaviour of **L3H** in a binary solvent system was investigated using their photophysical properties. THF was found to be good aprotic solvent while water was poor solvent, both UV-Vis and fluorescence spectra were recorded in THF-water mixture. In 10% THF, **L3H** exhibited a sharp absorption band at λ_{max} = 375 nm. No significant change in the absorbance maximum for **L3H** was observed (1:10) only the peak intensity decreased by ~1.5 times (Figure A6). This initial observation suggested aggregate formation in water.[30,31] The probe was weakly emissive in THF, exhibited a weak fluorescence with a maximum at λ_{em} = 536 nm (λ_{ex} = 372 nm) and having the quantum yield (φ) 0.63% for **L3H.** Upon gradually increasing water content (0-100%) in increments of 10%, the λ_{em} shifted to 503 nm (blue shift of ~32 nm). This was accompanied by an increase in fluorescence intensity (Figure 2A, 2B) to an extent of ~5 times (φ = 8.09%), which indicated the formation of H-type aggregates.[31] So, the probe was confirmed to exhibit AIE behaviour in 100% water. In 100% water, upon gradually increasing the concentration of **L3H** from 2 to 10 μM, the intensity at respective λ_{em} exhibited a systematic rise which abruptly levelled off (Figure A7), having a critical aggregation concentration (CAC) of 7.3 μM. The enhanced emission intensity of **L3H** with increasing water fraction was also studied by time-resolved fluorescence lifetime profile (Figure 2C). The average fluorescence lifetime (τ) observed at various water fractions were listed in Table A2. It was observed that τ had higher values in 100% water in contrast to pure THF and increased from 0.25 ns (fw = 0%) to 5.55 ns (fw = 100%). The results suggested that in 100% water, there was predominance of the non-radiative pathway due to molecular aggregation.

The aggregation behaviour was investigated through FESEM and DLS experiments. FESEM imaging revealed that **L3H** initially formed block-shaped particles (average particle size 178 nm) then transformed into oval, flower-like structures (250 nm) in 50% water and finally aggregated into agglomerated structure (680 nm) in 100% water (Figure 3A, Figure A8). DLS data revealed that the average particle size (Z_{avg}) increased from 267 nm (in pure THF) which increased to 780 nm (50% water) and finally reached a maximum of 963 nm (100% water) (Figure 3B), indicating formation of larger aggregates in water. So, both morphology and particle size of **L3H** can be easily tuned by solvent switching.

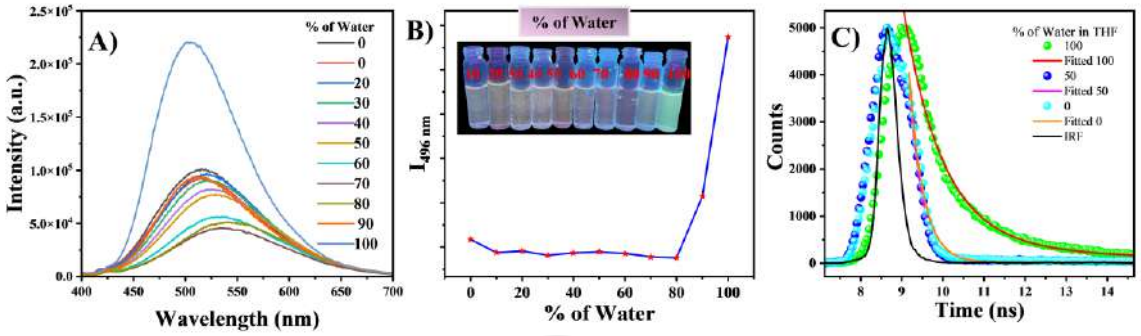

Figure 2 (A) Emission spectra of **L3H** (λ_{ex} = 372 nm) with varying water % in THF solvent, (B) spectral profile diagram showing the maximum intensity with the variation of water (inset: visual illustration of AIE activity under a long UV lamp), (C) time-resolved decay curve (bi-exponential fitting) in mixed THF-water system (*fw* = 0, 50, 100%).

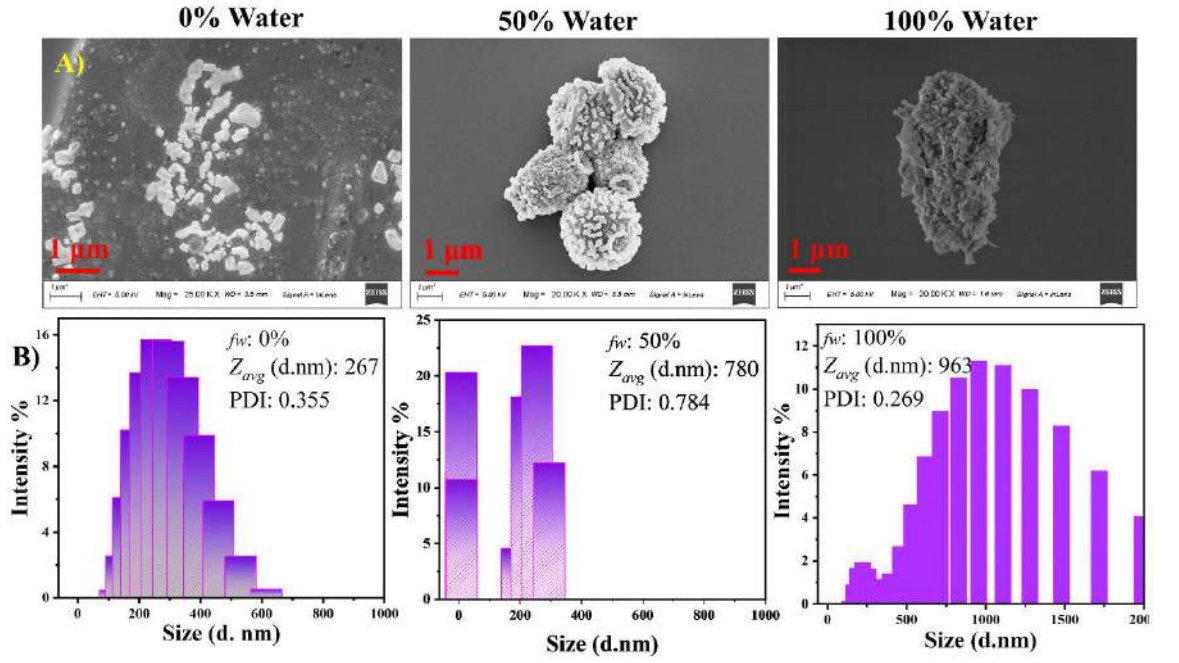

Figure 3. (A) FESEM micrographs images and (B) particle size distribution of **L3H** with varying water percentages in THF (*fw* = 0, 50, 100%).

5.3.3 Detection of As^{3+} Ion

UV-Vis spectrum of **L3H** in aqueous HEPES buffer (pH = 7.4) contained a peak at λ_{max} = 385 nm, which may of $\pi \rightarrow \pi^*$ in origin involving two conjugated ring systems *viz*., quinazolinone and 4-diethylaminophenyl moieties. Upon adding up to 5 equivalents of various metal ions like Al^{3+}, Cr^{3+}, Fe^{3+}, Au^{3+}, Mn^{2+}, Ni^{2+}, Zn^{2+}, Pd^{2+}, Pt^{2+}, Cd^{2+} and Hg^{2+}, the spectral pattern remained mostly unchanged. The intensity of peak at 385 nm got decreased by ~32% for Cu^{2+}, ~36% for

Pb^{2+}, ~50% for Co^{2+} and increased by 10-15% for Li^{+}, Na^{+}, K^{+}, Be^{2+}, Mg^{2+}, Ca^{2+}, Ag^{+} ions (Figure 4A). But upon gradually adding $AsBr_3$ (up to 1.2 equivalents) the bandwidth of 385 nm band (90 nm) got decreased (60 nm), while grew in intensity (1.2 times) and reached saturation (Figure 4B). This band narrowing effect indicated binding of As^{3+} ion with **L3H**, which was also resulted in visible colour change from colorless to pale yellow.

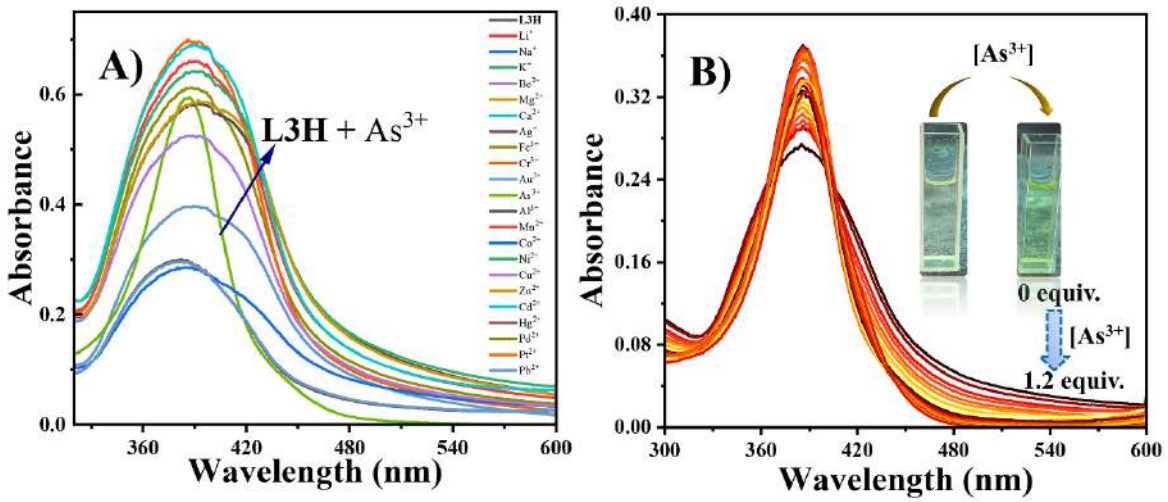

Figure 4. (A) UV-Vis spectral studies of **L3H** with different metal ions, and (B) titration profile of **L3H** (10 μM) with the gradual addition of As^{3+} (0 to 1.2 equivalents) in aqueous buffer.

In aqueous HEPES buffer, **L3H** was weakly fluorescent upon excited at 372 nm and remained weakly fluorescent even after the addition of 5 equivalents of various metal ions *viz*., Li^{+}, K^{+}, Na^{+}, Be^{2+}, Mg^{2+}, Ca^{2+}, Al^{3+}, Cr^{3+}, Fe^{3+}, Au^{3+}, Mn^{2+}, Co^{2+}, Ni^{2+}, Cu^{2+}, Zn^{2+}, Pd^{2+}, Pt^{2+}, Cd^{2+}, Hg^{2+}, Pb^{2+} and Ag^{+} ions. However, it became highly fluorescent upon the addition of 5 equivalents of $AsBr_3$ solution (Figure 5A). From the fluorescence titration profile, it was observed with the gradual addition of $AsBr_3$ solution (up to 1.2 equivalents) the emission peak intensity at 468 nm grew rapidly in intensity (~10 times), resulting in a cyan blue colored solution when held under long UV lamp (inset: Figure 5B) This result indicated that **L3H** was selective towards As^{3+} ion (Figure A9) and a 1:1 binding ratio was determined from job's plot analysis by continuous variation method (Figure A10I). The emission titration curve revealed the binding constant of 4.3×10^4 M^{-1} obtained using Bensi-Hildebrand equation (Figure A10II). The detection limit was calculated to be 55 nM which is much lower than WHO prescribed guideline value (Figure 5C). The ESI MS mass spectrum of 1:1 mixture of **L3H** and $AsBr_3$ contained peak at m/z = 600.0594 fitted well with $C_{25}H_{28}AsBrN_5O_3^{+}$ (m/z = 600.0586), corresponding to the formula $[As(\mathbf{L3})Br(CH_3OH)]^{+}$ ion (Figure A11). To evaluate the interference of other metal ions, competitive experiments were performed by adding equimolar

amount of competing metal salts (5 equivalents) followed by addition of $AsBr_3$ solution (Figure 5D). No specific spectral interference occurred for the detection of As^{3+} in presence of metal ions listed above. The probe **L3H** also produced a strongly emissive yellow colour in MeOH/HEPES (6:4, *v/v*, pH = 7.4) when observed under a long UV lamp in presence of As^{3+} ions, UV-Vis titration was carried out with $AsBr_3$ solution (up to 1.5 equivalents). The 373 nm band of free probe shifted and split into two having their λ_{max} values at 403 and 424 nm (Figure A12). Upon excitation with 372 nm light, **L3H** exhibited a weak emission peak at 510 nm and the fluorescence intensity increased ~16 times with the incremental addition of As^{3+} ion (Figure A13I). Based on the titration studies, the detection limit was evaluated to be 5.25 μM (Figure A13II). The time dependent fluorescence spectral study was performed at room temperature in aqueous HEPES as well as MeOH/HEPES medium by monitoring the intensity, respectively, at 468 and 510 nm at different times from 0 to 20 min (Figure A14). The response time in this two media were ~4.2 (HEPES) and ~7.5 min (MeOH/HEPES), thus detection was more sensitive and faster in the HEPES medium.

The fluorometric response of **L3H** was analyzed by varying the pH (using 1 M HCl and NaOH solutions), both in presence and absence of As^{3+} ion. As shown in Figure A15, no significant binding was observed at low pH (1 to 3) and the emission intensity decreased progressively above pH = 7, indicating that the most effective pH range for As^{3+} detection was 3-7. The reversible behaviour of **L3H** with As^{3+} ion was monitored using NaF by emission titration profile (Figure A16). After adding an equimolar amount of NaF to **L3H** bound As^{3+} complex, the emission intensity at 510 nm was lost. This exercise has been repeated six times through the sequential addition of As^{3+} and F^- and recyclability was established.

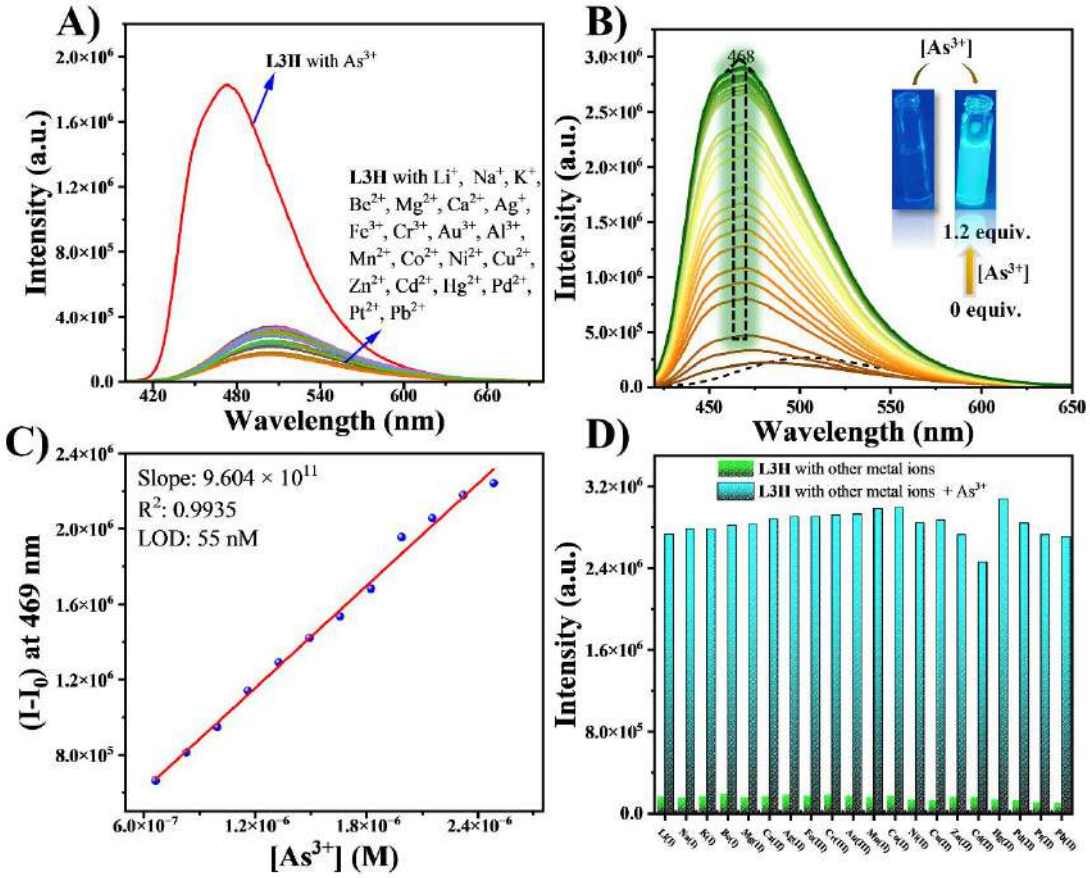

Figure 5. (A) Fluorescence spectral change of **L3H** (10 μM) with the addition of 5 equivalents of different metal ions, (B) spectral emission intensity profile depicting the titration of **L3H** in aqueous HEPES buffer, (C) plot of intensities at 468 nm *versus* concentration of As^{3+} ion, and (D) competitive bar diagram study of **L3H** in presence of various interfering metal ions.

5.3.4 Interaction with As^{3+} Ion

The characteristic IR peaks due to $\nu_{C=N}$ and ν_{O-H} observed respectively at 1616 and 3409 cm^{-1} exhibited significant change upon binding with As^{3+} ion. While peak at 1616 shifted to 1645 cm^{-1}, the 3409 cm^{-1} peak completely disappeared, indicating involvement of imine-N and phenolate-O in binding with As^{3+} ion (Figure A17). The crystalline block-shaped structure observed in FESEM image of **L3H**, changed to rod-shaped structure after addition of $AsBr_3$ (Figure A18I), so the significant change in shape indicated the formation of complex between **L3H** and As^{3+} in condensed state. DLS analysis revealed increased Z_{avg} values from 207 nm (**L3H**, 10 μM) to 544 nm in presence of As^{3+} ion in HEPES medium (Figure A18II).

In ^{1}H NMR titration of **L3H** dissolved in $CDCl_3$, with DMSO-d_6 solution of $AsBr_3$ (up to 1 equivalent) the imine peak originally at 8.88 ppm exhibited a downfield shift to 8.77 ppm and the phenolic-OH peak almost disappeared (Figure A19). Singlet due to -NH proton shifted from 5.49 to 5.77 ppm and other peaks in the aromatic region, 7.97 - 6.67 ppm got downfield shift. These changes indicated involvement of the phenolic-OH and imine-N in binding with As^{3+} ion.

5.3.5 Computational Studies

DFT/TDDFT calculations were performed on **L3H** and [As(**L3**)(Br_2)] and optimized geometry of complex (Figure A20) revealed that **L3**$^-$ was bound to central As^{3+} ion in a bidentate manner through azomethine nitrogen and phenolate oxygen atoms.[6] As depicted in Figure 6, free **L3H** exhibited a HOMO-LUMO energy gap of 3.64 eV, which decreased to 2.72 eV upon complexation with As^{3+}. As a result of complexation, the energy of both HOMO and LUMO got reduced. The HOMO of **L3H** was distributed over the azine bond, 3-(diethylamino)phenol, azomethine, and quinoline rings, while the LUMO was spread across the entire molecule. After binding with As^{3+}, the HOMO became delocalized over the ligand framework along with the metal center, and the LUMO shifted more towards 3-diethylamino and phenolic regions. The electron density overlaps near the metal center, suggested the suppression of PET process due to the involvement of nitrogen lone pair in coordination and as a result, on set of chelation enhanced fluorescence (CHEF) could be the basis for turn-on mechanism (Scheme 2). The UV-Vis spectra calculated using TDDFT results supported the red shift in absorption maximum observed experimentally (Figure A21, Table A3).

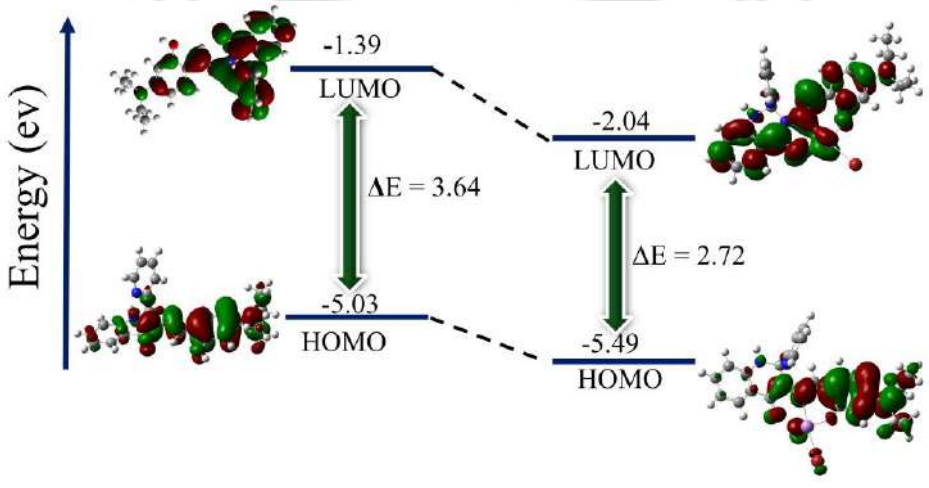

Figure 6. HOMO-LUMO energy level diagram of **L3H** and [As(**L3**)(Br_2)] complex.

Time-resolved Photoluminescence studies (Figure A22, Table A4) revealed that average lifetime of 0.47 ns for free **L3H** got enhanced to 1.38 ns in HEPES medium after adding $AsBr_3$. A similar result was also observed in MeOH/HEPES medium, where the lifetime increased by seven times from 0.14 to 0.97 ns. In HEPES medium, the quantum yield of free **L3H** was found to be 0.17, which increased to 0.47 upon the addition of $AsBr_3$ and in MeOH/HEPES medium, increased from 0.09 to 0.38. So, in case of free **L3H** fluorescence was not observed due to presence of active PET process, after binding with As^{3+} PET process was restricted and turn-on fluorescence signal was observed.

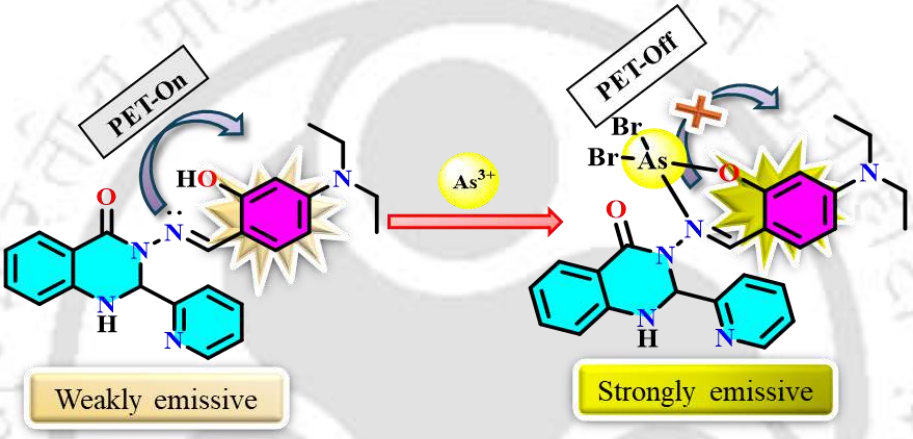

Scheme 2. Plausible sensing mechanism.

5.3.6 Removal of As^{3+} Ion in Contaminated Wastewater

The ability of **L3H** to chelate with As^{3+} ion accompanied by colour change from colorless to pale yellow upon addition of aqueous arsenic(III) solution, motivated us to check its removal from contaminated water. Typically, after keeping the solution containing 1:1 mixture of **L3H** and $AsBr_3$ overnight, greenish yellow colour precipitate and a colorless supernatant solution remained. ICP-MS data confirmed that ~67% reduction in concentration of As^{3+} ions in the supernatant liquid compared to original wastewater (Table A5). Removal efficiency was determined by using the following equation:

% of removal efficiency (R): $\frac{C_0 - C_t}{C_t}$

Where, C_o was the initial concentration and C_t was the concentration of As^{3+} ions remained after the adsorption by the sensor and R was the removal efficiency.

5.3.7 Practical Application

5.3.7.1 Smartphone-Based Portable Device for Fluorometric Detection of As^{3+} Ion

The fluorescence-based As^{3+} detection was further analyzed using a portable device, enabling fast, on-spot detection. The prototype consisted of a dark chamber box, a portable UV lamp, a smartphone, and a smartphone holder. For RGB analysis, **L3H** with varying As^{3+} concentrations (0-2.0 μM) in HEPES and MeOH/HEPES medium was added to a sample vial and placed in the dark box (Figure 7). Fluorescence images were captured using a digital smartphone, and corresponding RGB values were calculated using ImageJ software. Fluorescence intensity changes were estimated from the "G/B" and "R/G" plots. Figure A23 displayed the linear calibration plots, with the linear regression coefficient (R^2) of 0.999, 0.994 (for cyan colour solution) and 0.995, 0.998 (for yellow colour solution), which helped to estimate As^{3+} concentration in an unknown sample for rapid on-location detection.

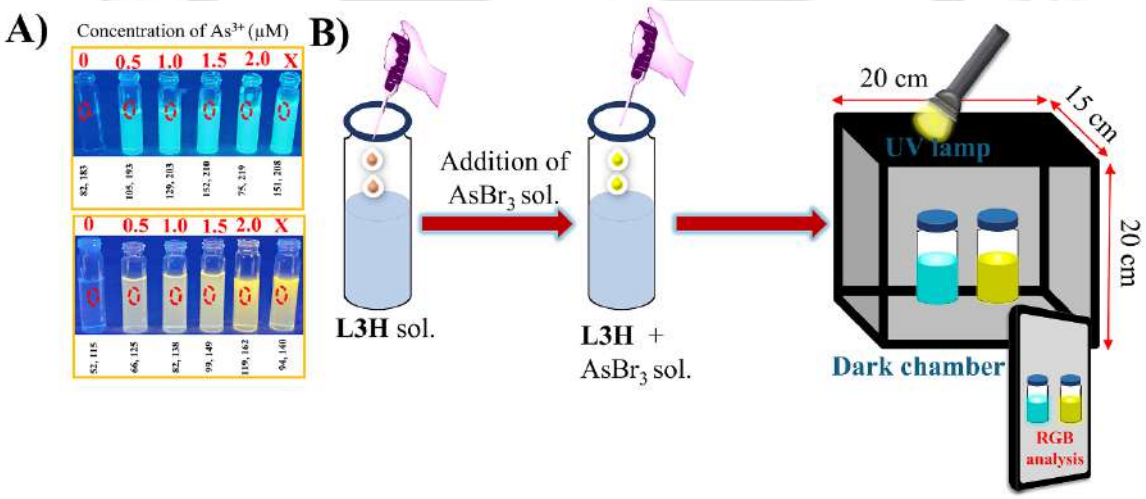

Figure 7. (A) Fluorescence images of probe **L3H** in presence and absence of As^{3+} ion (0-2 μM) in HEPES and MeOH/HEPES medium, and (B) fabrication of a portable device for on-location estimation of As^{3+} ion.

5.3.7.2 Portable-Paper Test Kit

By considering the high cost of sensing platform and the necessity for on-site detection in the remote areas, a portable sensing paper strips kit were developed. Whatman filter paper (Grade 1) was cut into round shaped pieces having a diameter of 1.2 inches and dipped in 0.1 mM aqueous solution of **L3H** and dried in air. These test strips were dipped separately in 2, 4, 6 and 8 μL solutions of 0.10 mM As^{3+} ion and dried. Upon inspection with 365 nm (long UV lamp),

these sample loaded filter papers exhibited distinct and intense yellow fluorescence, as depicted in inset-Figure 8. The intensity of colour on tested paper strips increased with increasing amount of As^{3+} solution and were quantitatively analyzed by using RGB values obtained from ImageJ software (Figure 8). Thus, this technique can be reliable for rapid on-site detection of As^{3+} ion.

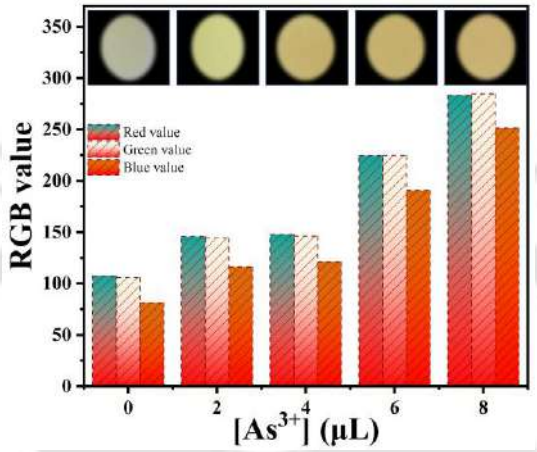

Figure 8. Visual sensing of As^{3+} on paper strips kit (inset: images depicted circular yellow colour test strips after dipping into the various As^{3+} solutions, with their respective RGB values).

5.3.7.3 Logic Gate Construction

As the fluorescence response of **L3H** towards As^{3+} was studied in two different solvents *viz.,* HEPES and MeOH/HEPES, a three-input / two-output based molecular logic gate was formulated. The turn-on emission intensity with high value was denoted as 1 and turn-off with low value denoted as 0. Therefore, by providing combination of three chemical entities as input signals **L3H** (In1), As^{3+} (In2) and F^- (In3) and deciphering the emission intensity as output 468 nm and 510 nm, as mentioned in truth table (Table A6). When both input In1 and In2 were absent, the emission intensity was low, indicated by 0-state. If **L3H** was absent, regardless of any of the analytes As^{3+} and F^- being available, no emission would be observed and hence demonstrated as 0. Out1 exhibited a high signal (1) only when In1 and In2 were present simultaneously and In3 was absent. By adding a NOT gate to In3, all three input signals were combined through AND gate with Out1 to indicate high 1-state. In presence or absence of In2 and In3 signals, when In1 was set to 1, Out2 consistently remained at 1, indicating a direct

circuit connection from In1 to Out2 was feasible. This combination helps to construct an advanced-level molecular logic gate with NOT and AND operations (Figure 9).

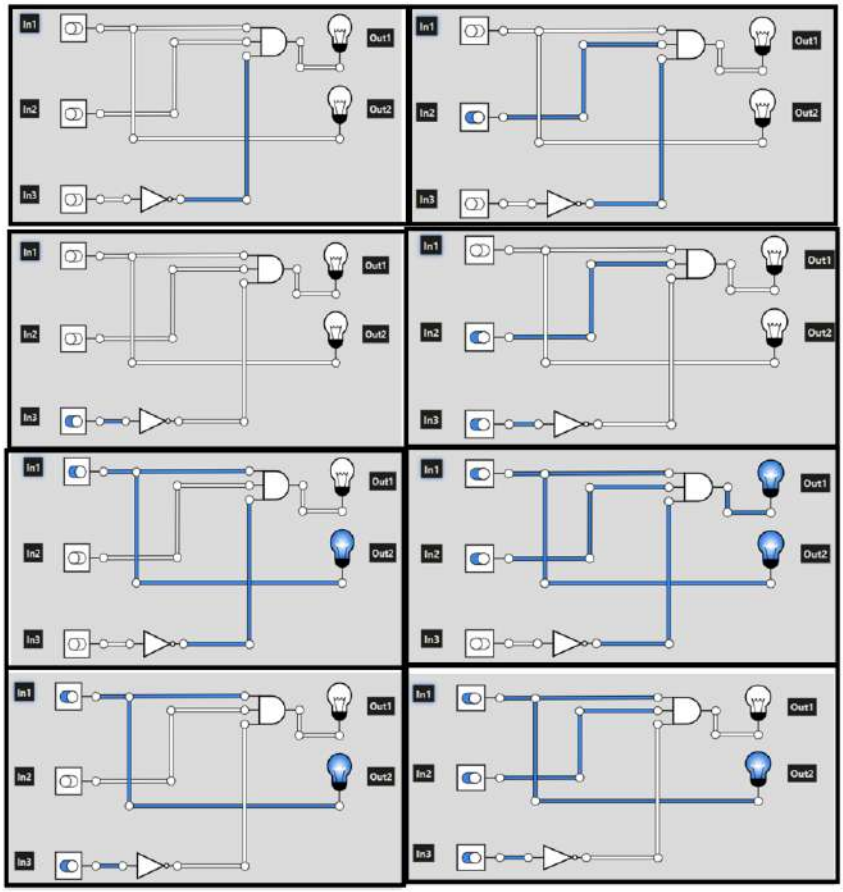

Figure 9. NOT-AND logic functions for the sensor **L3H** with $AsBr_3$ and NaF solution.

5.3.7.4 Real Sample Testing

The sensing ability of **L3H** with As^{3+} ions were applied to honey, milk, and water samples. Honey and milk were collected from the local market in Guwahati. Lipids were removed from the milk using trifluoroacetic acid, followed by filtration to eliminate solid particles. Honey samples were extracted 60% aq. ethanol, filtered using a 0.45 µm syringe filter, and diluted with deionised water. Similarly, river, tap, and lake water samples were collected from the Guwahati area and filtered without pre-treatment. All real samples were spiked with a known concentration of $AsBr_3$ solution and analysed *via* fluorescence spectroscopy to calculate As^{3+} concentrations. Linear calibration plots were constructed between emission intensity *versus* [As^{3+}] (Figure A24). As^{3+} levels in the spiked samples were determined using these plots (Table 1) and results indicated about 99 % recovery with RSD < 5%, demonstrating accurate detection

of As^{3+} ions. Table A7 presented the structure of various fluorometric, colorimetric chemosensors for the detection of As^{3+} ion in terms of analytical performance.

Table 1 Determination of spiked As^{3+} ion into different food and water samples.

Samples	***Spiked (μM)***	***Detected (μM)***	***Recovery (%)***	***RSD (%) n = 3***
Honey	5	5.03	99	3.42
Milk	5	5.05	98	1.74
River	5	5.11	97	1.02
Tap	5	5.13	96	4.75
Lake	5	5.48	89	4.34

5.3.8 Molecular Docking Studies

For understanding the intermolecular interaction and the binding site of **L3H** with BSA and HSA, *in silico* molecular docking studies were performed.[32,33] Figure 10 depicted the conformational model and 3D interaction of complex formed by the biomolecule and ligand. HSA exhibited binding energy of -7.12 kcal/mol, indicating stronger binding affinity toward **L3H** compared to BSA. The detailed list of 10 docked conformers, along with various amino acid residues obtained from docking analysis were mentioned in Table A8, Figure A25. In BSA, interaction of **L3H** includes i) pi-alkyl interaction between aromatic 2-hydroxybenzene group and Pro 498, ii) interaction between N-diethylamino group and Val 497, Ala 500 and iii) H-bond between (N-H) of quinazoline ring and Ala 583. In HSA, possible interaction of **L3H** includes i) H-bond between (N-H) of quinazoline ring and Ala 583, ii) pi-alkyl interaction between aromatic 2-hydroxybenzene group and Pro 498, iii) interaction between N-diethyl amino group and Val 497, Ala 500.

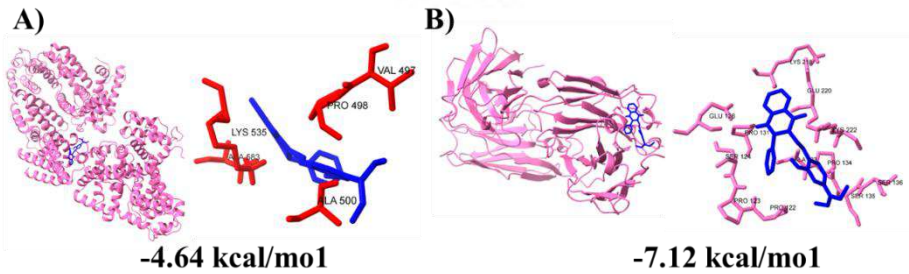

Figure 10. Computational docking analysis of **L3H** between (A) BSA and (B) HSA along its amino acid residues in 3D-image.

5.4 Conclusion:

In summary, a fluorometric AIE based chemosensor **L3H** exhibited selective and sensitive detection of As^{3+} ion among various metal ions. Nanomolar detection of As^{3+} in aqueous buffer makes it a practically usable sensor with a very less response time. The 1:1 binding interaction of **L3H** with As^{3+} was revealed by Job's plot, ESI MS, IR spectral analysis. The reversibility in presence of F^- with As^{3+} ion helped us to construct NOT-AND logic gate circuit. Lifetime decay curve suggested As^{3+} ion blocked the PET process and turn-on fluorescence emission set-on. The DFT/TDDFT calculation indicated a decrease in HOMO-LUMO energy gap in [As(**L3**)(Br_2)], which supported the experimentally observed bathochromic shift in absorption spectra. The real-life practical application of **L3H** also extended to different food and real water samples for As^{3+} detection. The probe can also be utilized by smartphone linked prototype without the help of any sophisticated tools. *In silico* docking analysis have shown that **L3H** exhibited a stronger binding interaction with BSA and HSA biomolecules, with binding energies of -4.64, -7.12 kcal/mol, respectively.

References:

1 R. Purkait, S. Maity and C. Sinha, *New J. Chem.*, 2018, **42**, 6236-6246.

2 P. G. Sutariya, H. Soni, S. A. Gandhi and A. Pandya, *New J. Chem.*, 2019, **43**, 737-747.

3 N. Yadav and A. K. Singh, *RSC Adv.*, 2016, **6**, 100136-100144.

4 K. Chauhan, P. Singh, B. Kumari and R. K. Singhal, *Anal. Methods*, 2017, **9**, 1779-1785.

5 K. Nagaraj, A. N. Shetty and D. R. Trivedi, *Sensors and Diagnostics*, 2023, **3**, 64-78.

6 M. Tripathy, S. Rana, U. Subuddhi and S. Patel, *J. Photochem. Photobiol. A Chem.*, 2023, **435**, 114329.

7 N. K, A. Singh, A. N. Shetty and D. R. Trivedi, *Supramol. Chem.*, 2021, **33**, 534-549.

8 K. Dhanasekaran, R. Tamizhselvi, S. Mohandoss, M. Beena, A. Palaniappan and A. A. Napoleon, *Spectrochim. Acta - Part A Mol. Biomol. Spectrosc.*, 2024, **316**, 124325.

9 V. C. Ezeh and T. C. Harrop, *Inorg. Chem.*, 2013, **52**, 2323-2334.

10 A. Bonyar, P. Nagy, V. Mayer, A. Vitez, A. Gerecs, H. Santha and G. Harsanyi, *Sensors*

Actuators, B Chem., 2017, **251**, 1042-1049.

11 V. D. Awasthi, S. P. Singh, S. Ramachandran and R. Bandyopadhyaya, *J. Environ. Chem. Eng.*, 2023, **11**, 111012.

12 A. Mondal and V. Manivannan, *Spectrochim. Acta - Part A Mol. Biomol. Spectrosc.*, 2025, **333**, 125865.

13 K. Shrivas, S. Patel, D. Sinha, S. S. Thakur, T. K. Patle, T. Kant, K. Dewangan, M. L. Satnami, J. Nirmalkar and S. Kumar, *Microchim. Acta*, 2020, **187**, 173.

14 A. Motalebizadeh, H. Bagheri, S. Asiaei, N. Fekrat and A. Afkhami, *RSC Adv.*, 2018, **8**, 27091-27100.

15 S. Srivastava and V. Sharma, *Appl. Water Sci.*, 2021, **11**, 1-8.

16 M. Yeasin Pabel, S. Yasmin, M. A. A. Shaikh and M. H. Kabir, *Sensors Actuators A Phys.*, 2024, **366**, 115028.

17 J. Wang, M. Sun, L. Wang, X. Xiong, W. Yuan, Y. Liu, S. Liu, Q. Zhang, J. Liu, Y. Wang and D. C. W. Tsang, *Chemosphere*, 2023, **336**, 139089.

18 X. Dai and R. G. Compton, *Analyst*, 2006, **131**, 516-521.

19 W. Yang, L. Ye, Y. Wu, X. Wang, S. Ye, Y. Deng, K. Huang, H. Luo, J. Zhang and C. Zheng, *J. Hazard. Mater.*, 2024, **470**, 134038.

20 D. F. Nugraha, D. Kim, E. Yang, S. W. Lee, D. R. Whang, S. A. Lee, S. H. Park and D. W. Chang, *ACS Appl. Electron. Mater.*, 2023, **5**, 1174-1182.

21 D. M. Kapse, O. S. Singh, M. Ghadiyali, S. Chacko and R. M. Kamble, *RSC Adv.*, 2022, **12**, 6888-6905.

22 S. S. Mahadik, D. R. Garud, R. V. Pinjari and R. M. Kamble, *J. Mol. Struct.*, 2022, **1248**, 131541.

23 A. G. Al-Sehemi, M. Pannipara and A. Kalam, *Spectrochim. Acta - Part A Mol. Biomol. Spectrosc.*, 2017, **171**, 97-103.

24 P. N. Borase, P. B. Thale and G. S. Shankarling, *Dye. Pigment.*, 2016, **134**, 276-284.

25 Y. Li, Q. Peng, S. Li, Y. Cai, B. Zhang, K. Sun, J. Ma, C. Yang, H. Hou, H. Su and K.

Li, *Sensors Actuators, B Chem.*, 2019, **301**, 127139.

26 K. Li, Y. Liu, Y. Li, Q. Feng, H. Hou and B. Z. Tang, *Chem. Sci.*, 2017, **8**, 7258-7267.

27 C. Cao, X. Liu, Q. Qiao, M. Zhao, W. Yin, D. Mao, H. Zhang and Z. Xu, *Chem. Commun.*, 2014, **50**, 15811-15814.

28 M. Lamoria, D. Manna and M. D. Milton, *J. Mol. Struct.*, 2025, **1319**, 139385.

29 Z. Li, Y. Xiang and A. Tong, *Anal. Chim. Acta*, 2008, **619**, 75-80.

30 M. Wu, D. D. Yang, H. W. Zheng, Q. F. Liang, J. B. Li, Y. Kang, S. Li, C. Jiao, X. J. Zheng and L. P. Jin, *Dalt. Trans.*, 2021, **50**, 1507-1513.

31 B. Das, M. Dolai, A. Dhara, A. Ghosh, S. Mabhai, A. Misra, S. Dey and A. Jana, *J. Phys. Chem. A*, 2021, **125**, 1490-1504.

32 A. Mondal and V. Manivannan, *Spectrochim. Acta - Part A Mol. Biomol. Spectrosc.*, 2024, **322**, 124734.

33 S. Gurusamy, M. Sankarganesh, V. Sathish, P. Thanasekaran and A. Mathavan, *J. Photochem. Photobiol. A Chem.*, 2022, **425**, 113674.

34 K. Nagaraj, A. Nityananda Shetty and D. R. Trivedi, *Microchem. J.*, 2024, **206**, 32-39.

35 D. De, P. Ghosh, S. De and P. Sahoo, *Environ. Sci. Adv.*, 2024, **3**, 1578-1585.

36 S. Nag, A. Mondal, H. Hirani and P. Banerjee, *Mater. Adv.*, 2022, **3**, 4649-4658.

37 D. Maity, S. Kumar Mandal, B. Guha and P. Roy, *Inorg. Chim. Acta*, 2021, **519**, 120258.

Appendix

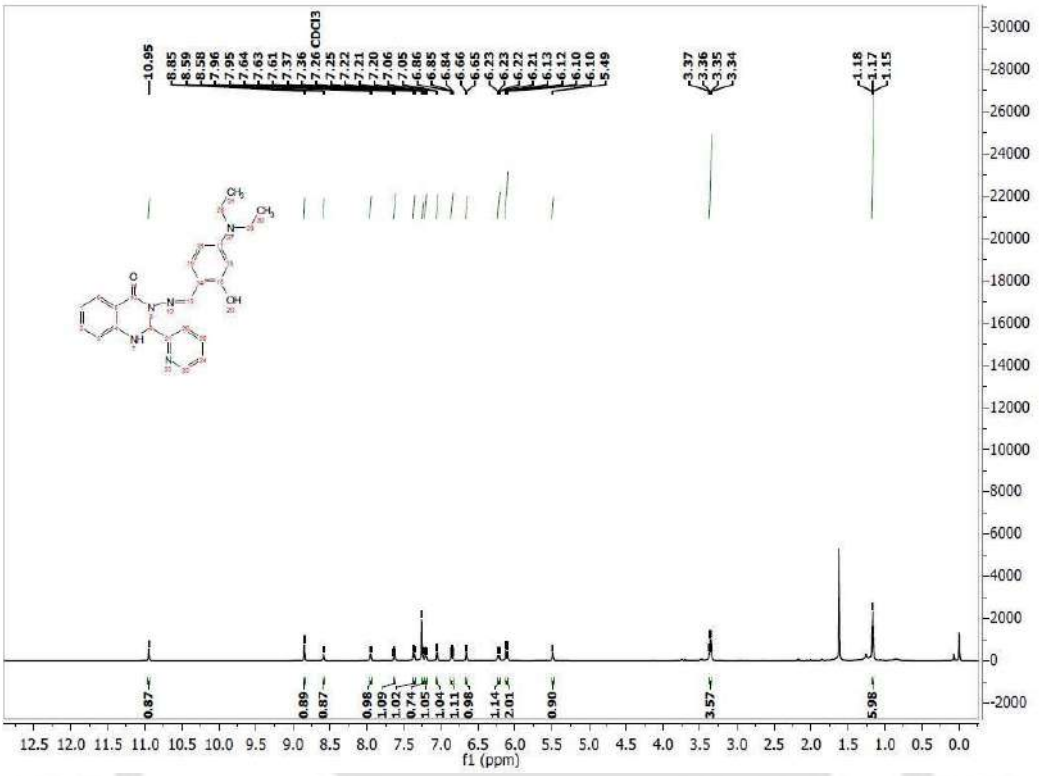

Figure A1. ^{1}H NMR (600 MHz) of **L3H** in $CDCl_3$.

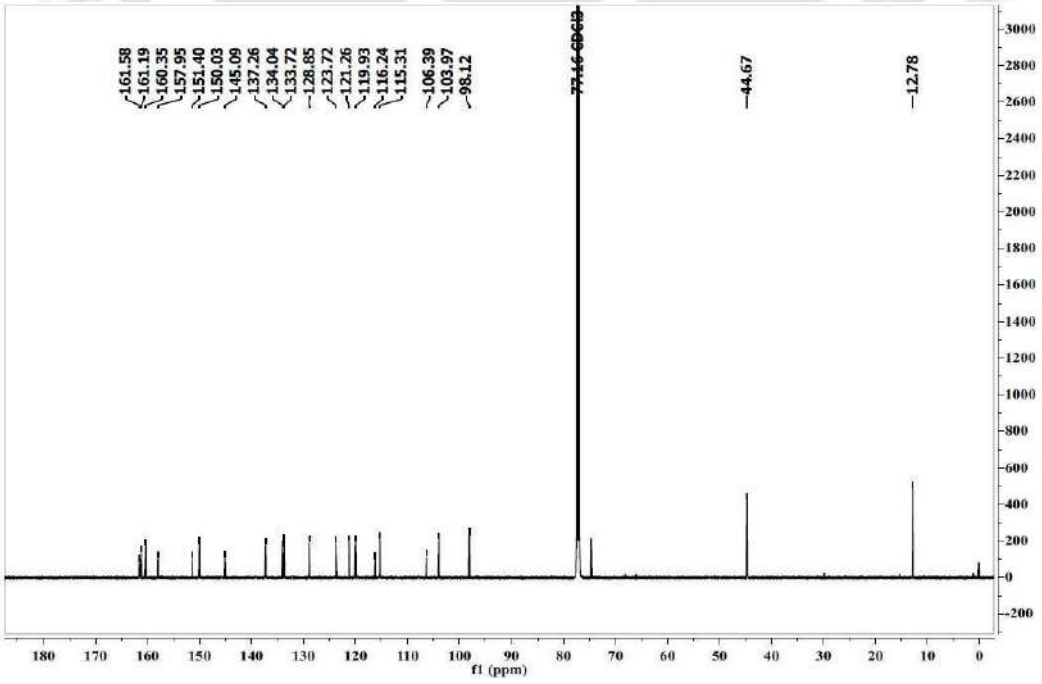

Figure A2. ^{13}C NMR (600 MHz) of **L3H** in $CDCl_3$.

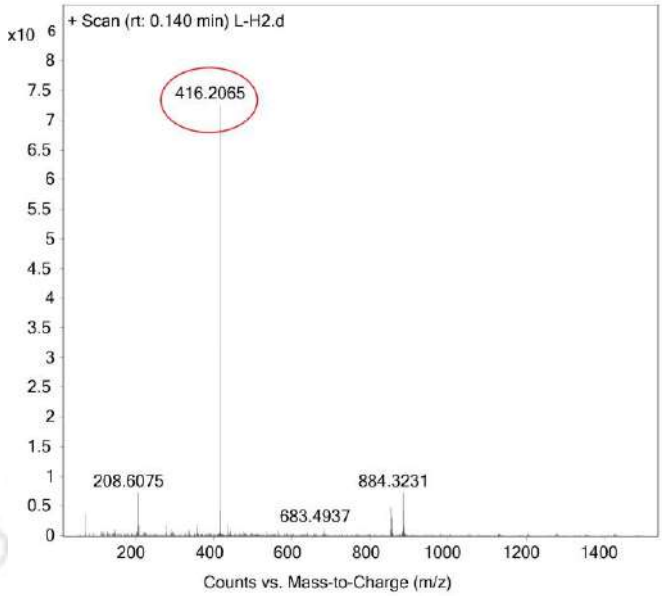

Figure A3. Mass spectrum of **L3H** in acetonitrile.

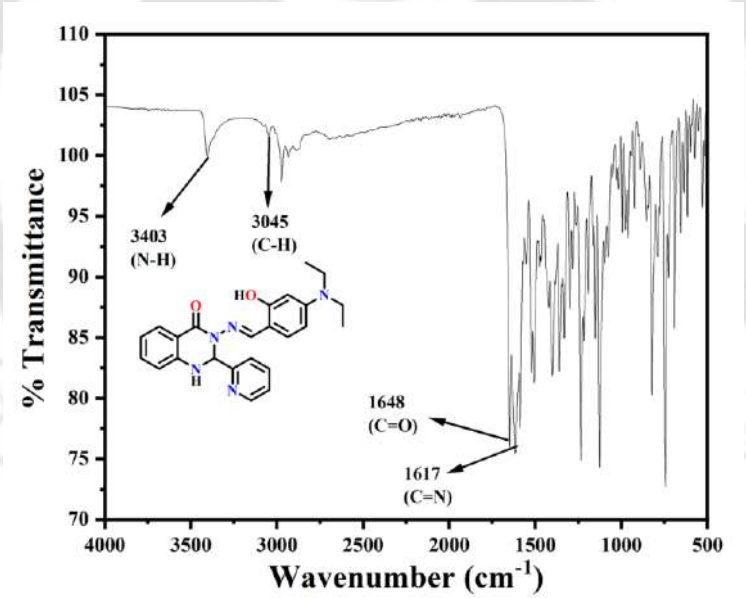

Figure A4 IR spectrum of **L3H**.

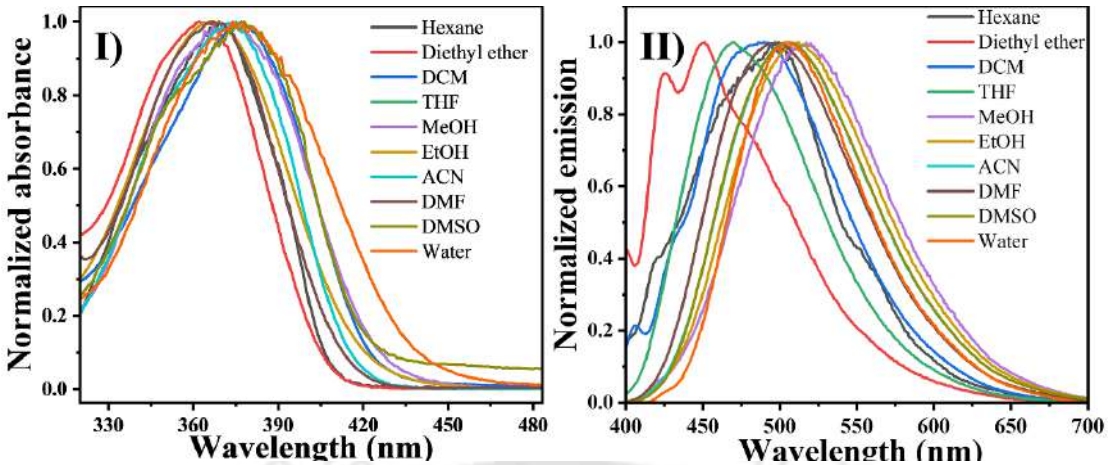

Figure A5. Normalized UV-Vis (I) and emission spectra (II) of **L3H**.

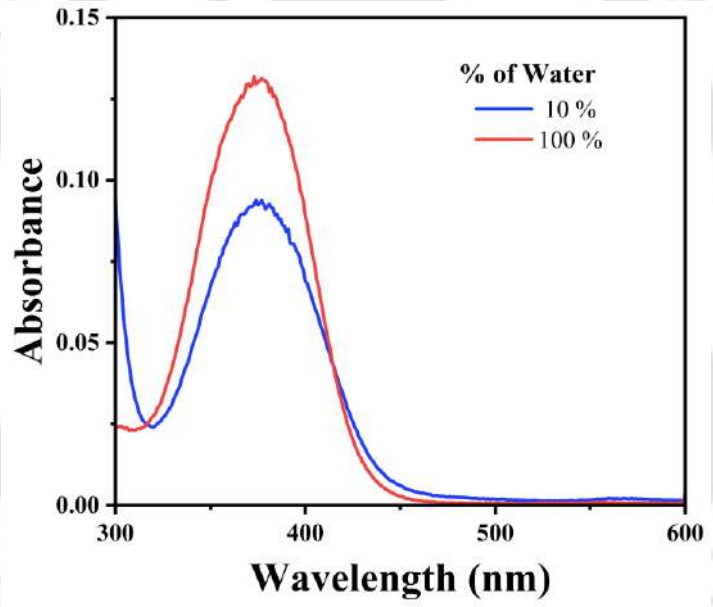

Figure A6. Absorption spectra of **L3H** with varying water percentages in THF (10, 100%).

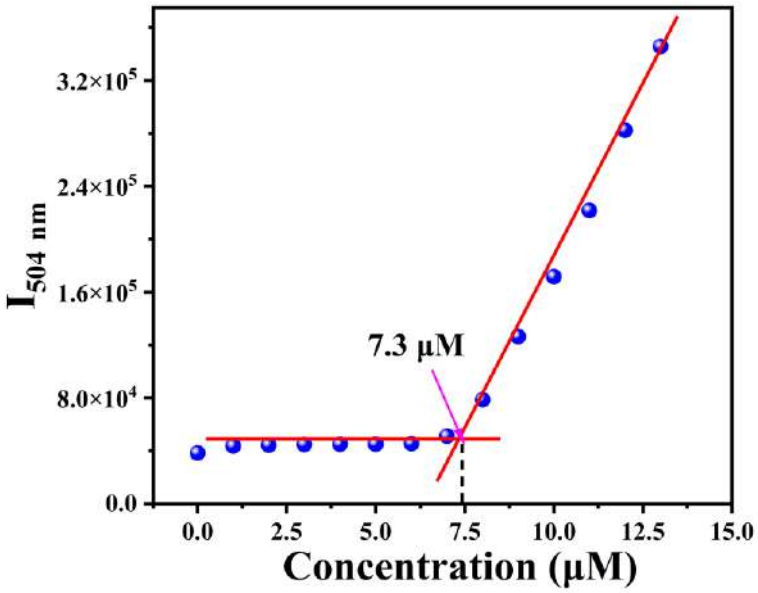

Figure A7. Determination of critical aggregation constant for **L3H**.

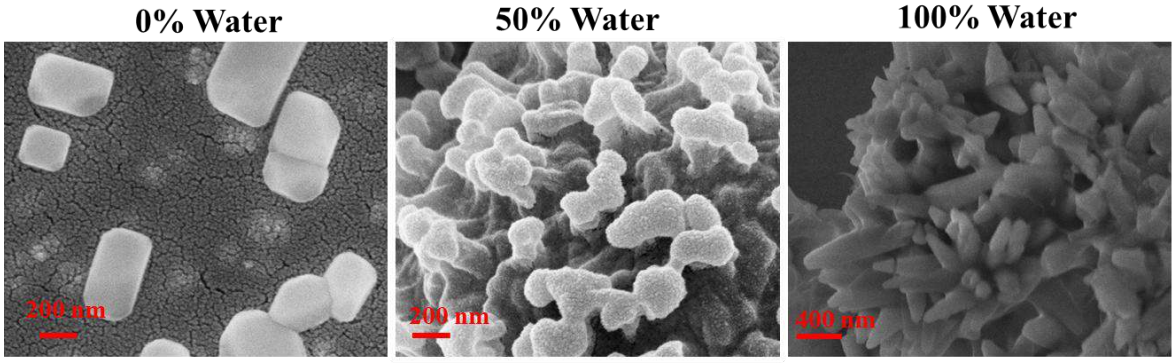

Figure A8. High resolution FESEM images of **L3H** with varying water percentages in THF (0, 50, 100) %.

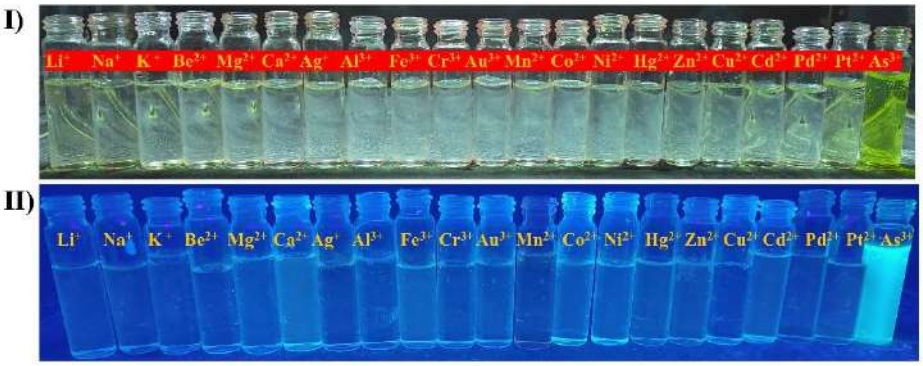

Figure A9. Images of **L3H** solution in presence of several metal ions under (I) visible light, (II) long UV light.

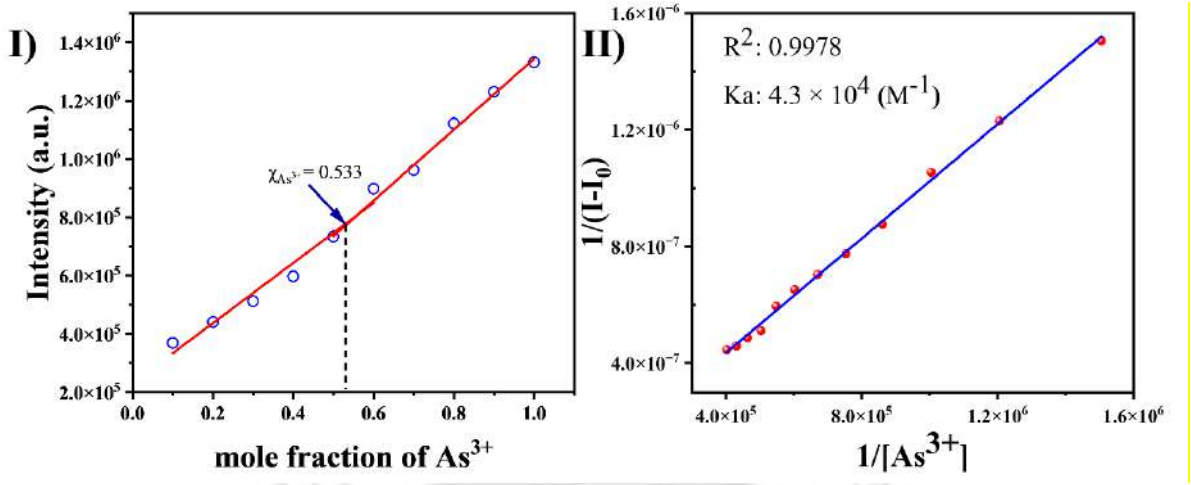

Figure A10. Determination of (I) binding constant and (II) job's plot for **L3H** + As^{3+} complex.

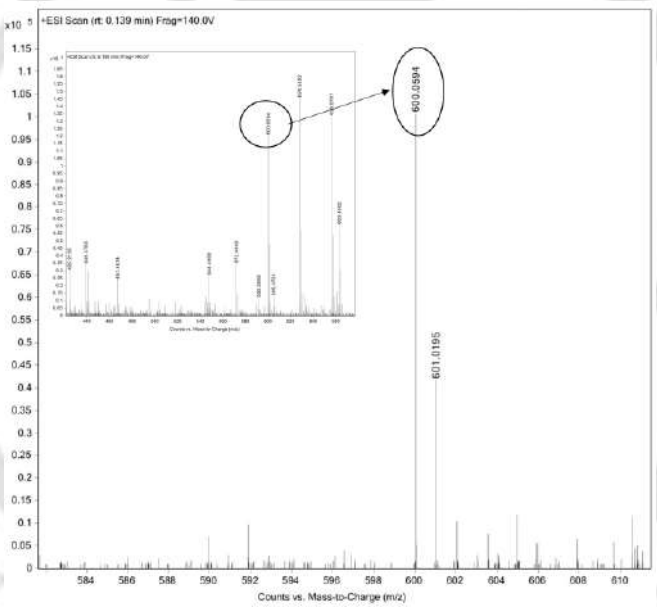

Figure A11. Experimental mass spectrum for [As(**L3**)Br(CH_3OH)]$^+$ complex ion (inset full range).

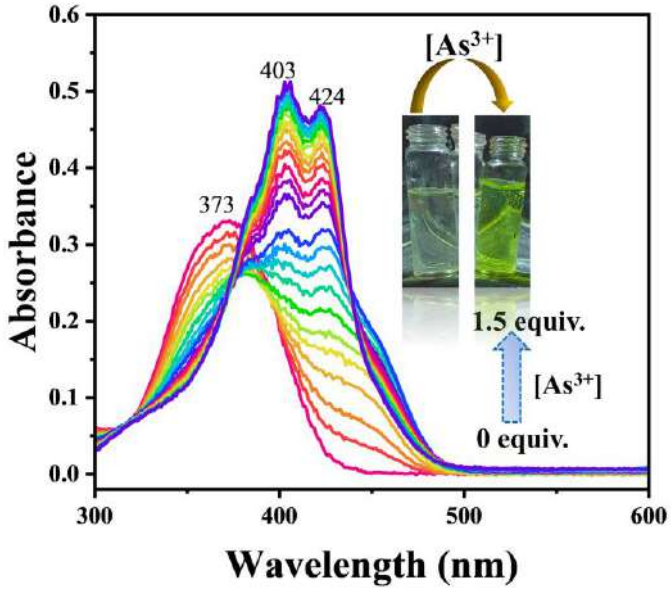

Figure A12. The UV-Vis absorption spectra of **L3H** in (6:4, *v/v*) MeOH/HEPES buffer with the stepwise addition of $AsBr_3$.

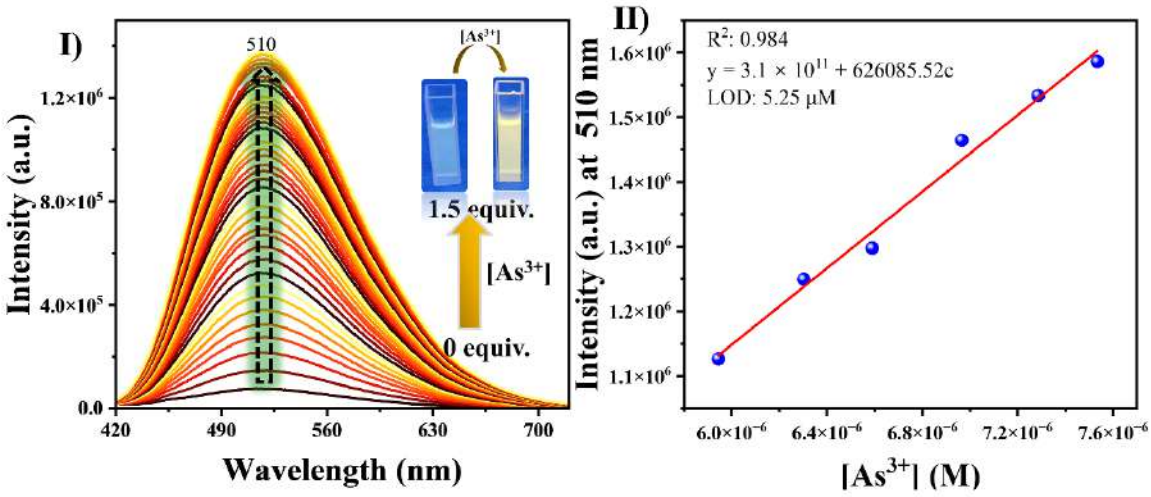

Figure A13. (I) Change in emission spectra of **L3H** (10 µM) in MeOH/HEPES medium upon gradual addition of As^{3+} ion, (II) calibration plot for the calculation of LOD value.

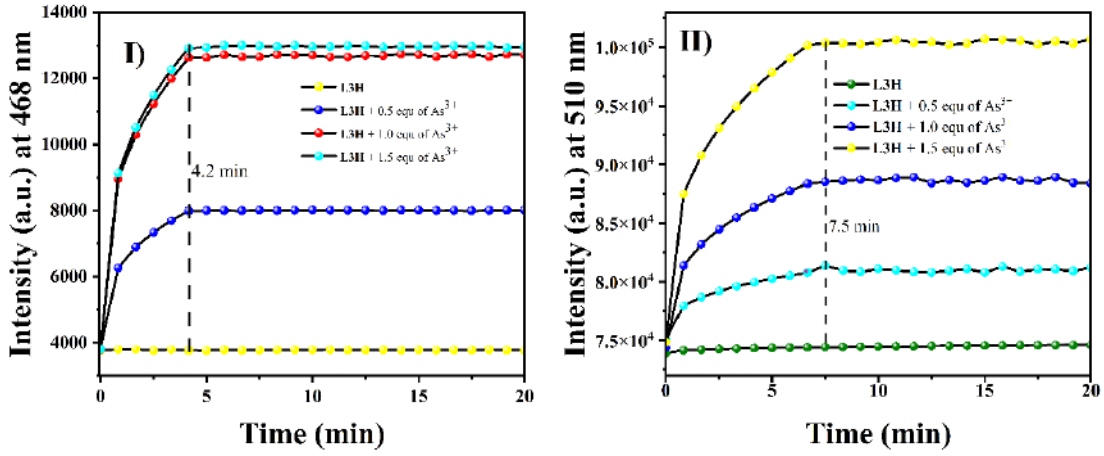

Figure A14. Response time of **L3H** with As^{3+} ion in (I) aqueous HEPES buffer and (II) MeOH/HEPES (6:4, *v/v*) medium.

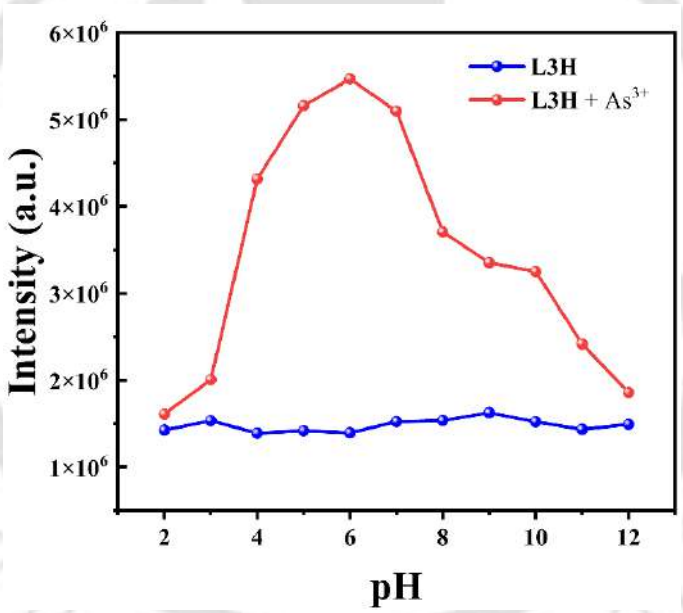

Figure A15. Effect of variable pH for As^{3+} ion detection.

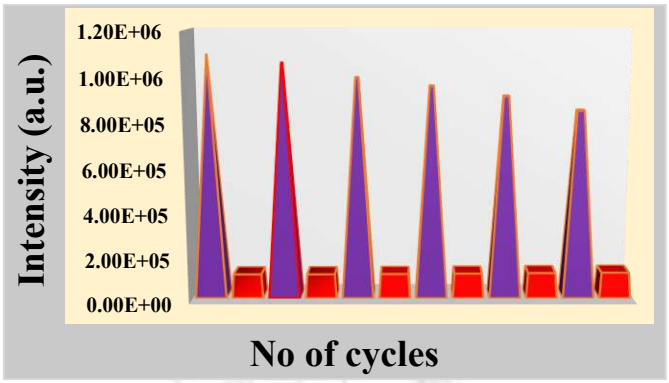

Figure A16. Reversibility of the fluorescence response (up to six cycle) with the alternative addition of As^{3+} and F^- in **L3H** solution.

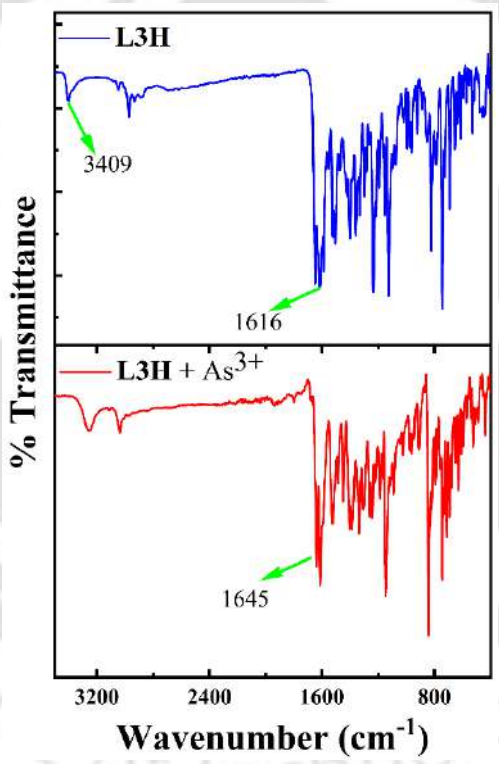

Figure A17. Combined IR spectra of free **L3H** and **L3H** + As^{3+} complex.

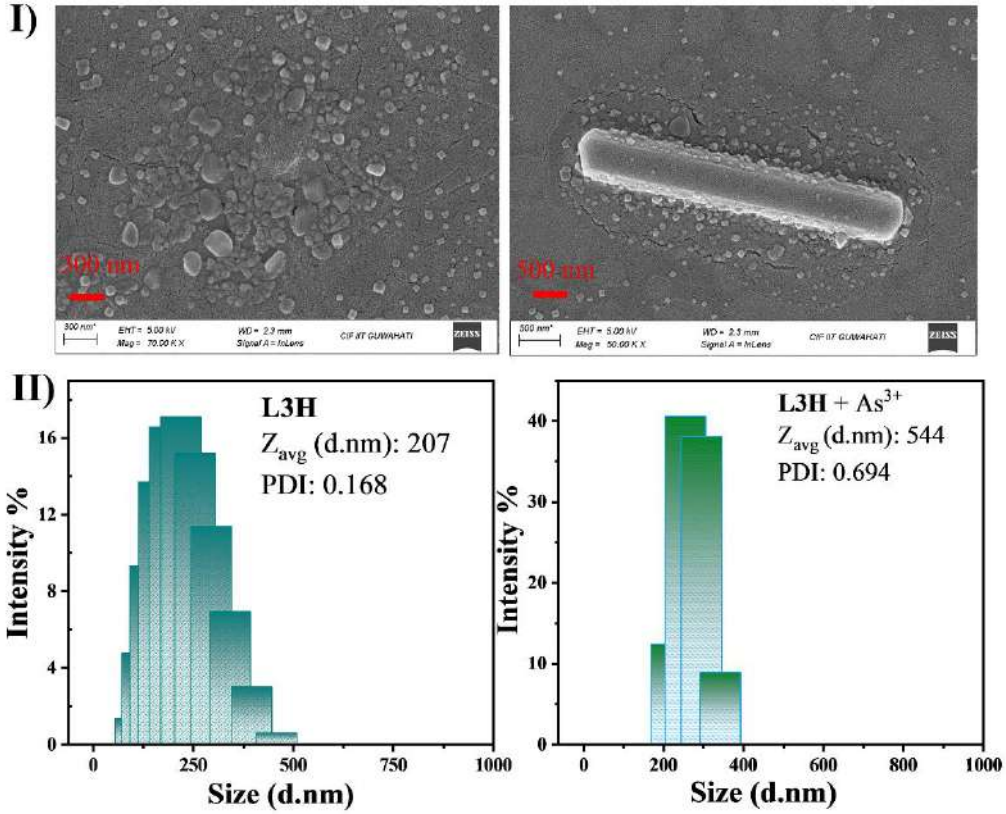

Figure A18. (I) FESEM images and (II) particle size measurement for free **L3H** and *in situ* **L3H** + As^{3+} complex.

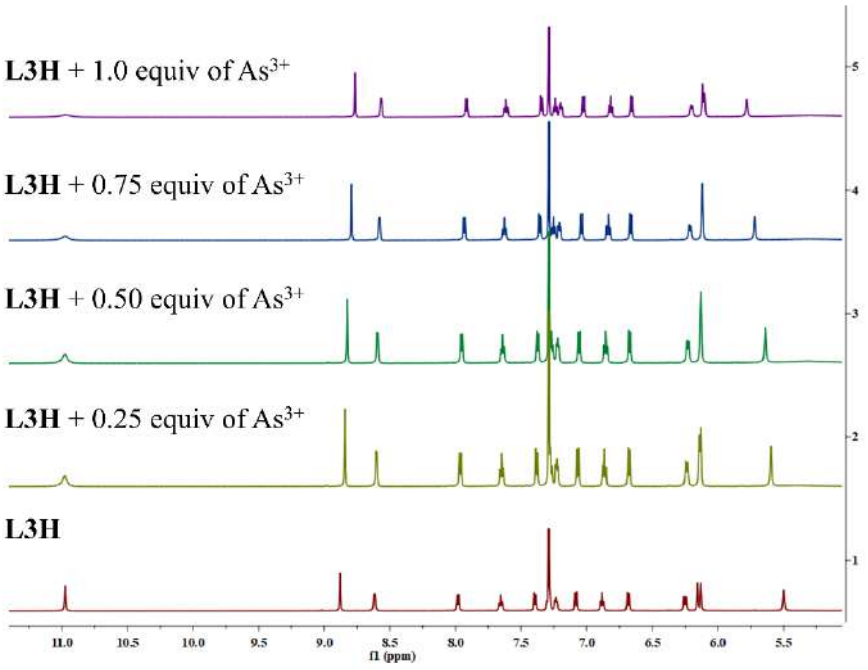

Figure A19. ^{1}H NMR titration spectra of **L3H** with As^{3+} ion in $CDCl_3$.

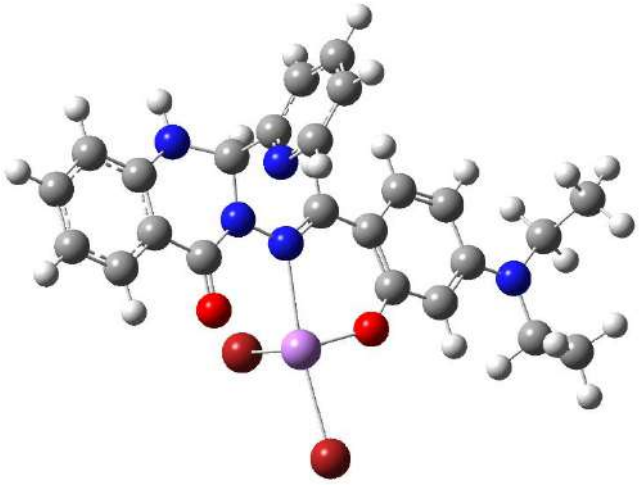

Figure A20. Optimized structure of [As(**L3**)(Br_2)] complex.

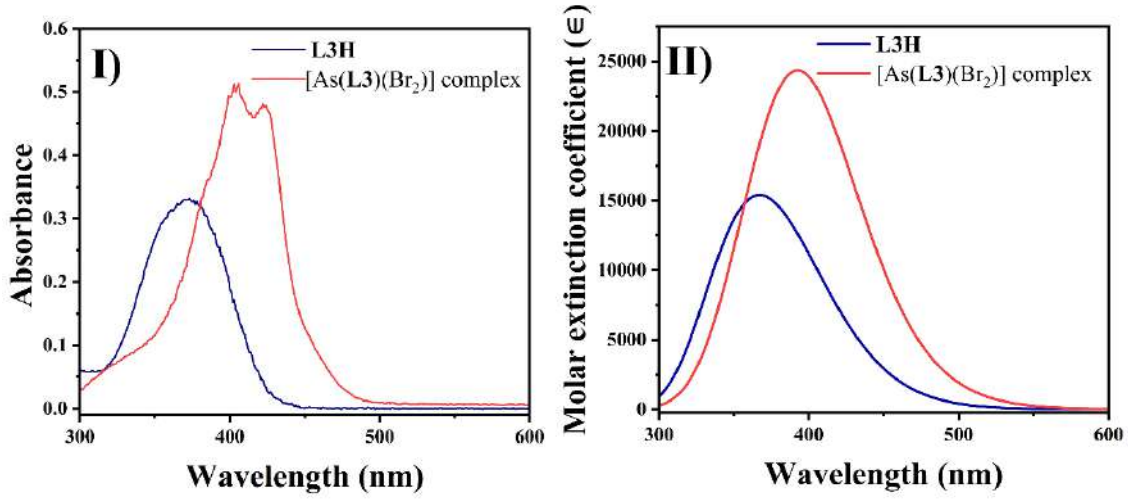

Figure A21. (I) Experimental and (II) theoretical UV-Vis spectra of **L3H** and [As(**L3**)(Br_2)] complex.

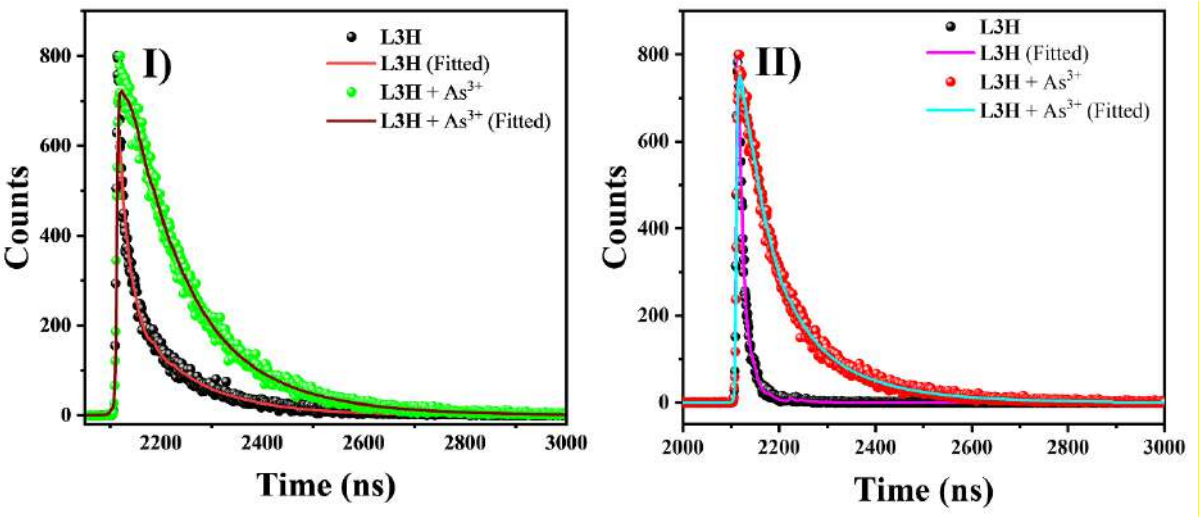

Figure A22. Fluorescence decay parameters of **L3H** and its As^{3+} complex in (I) aqueous HEPES buffer and (II) MeOH/HEPES (6:4, *v/v*) medium.

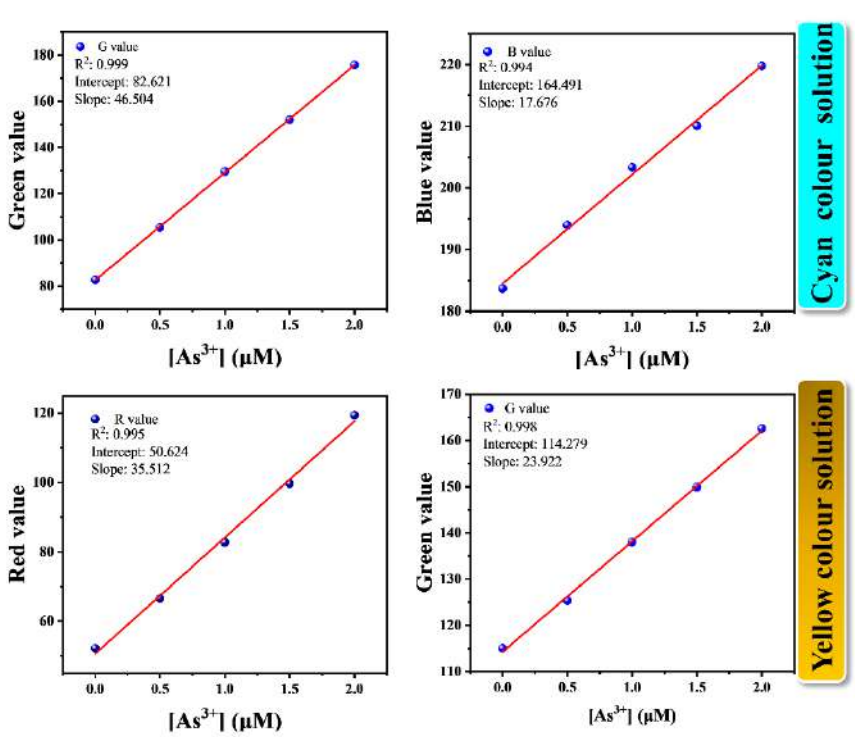

Figure A23. RGB values from the photographic images of cyan and yellow colour solutions.

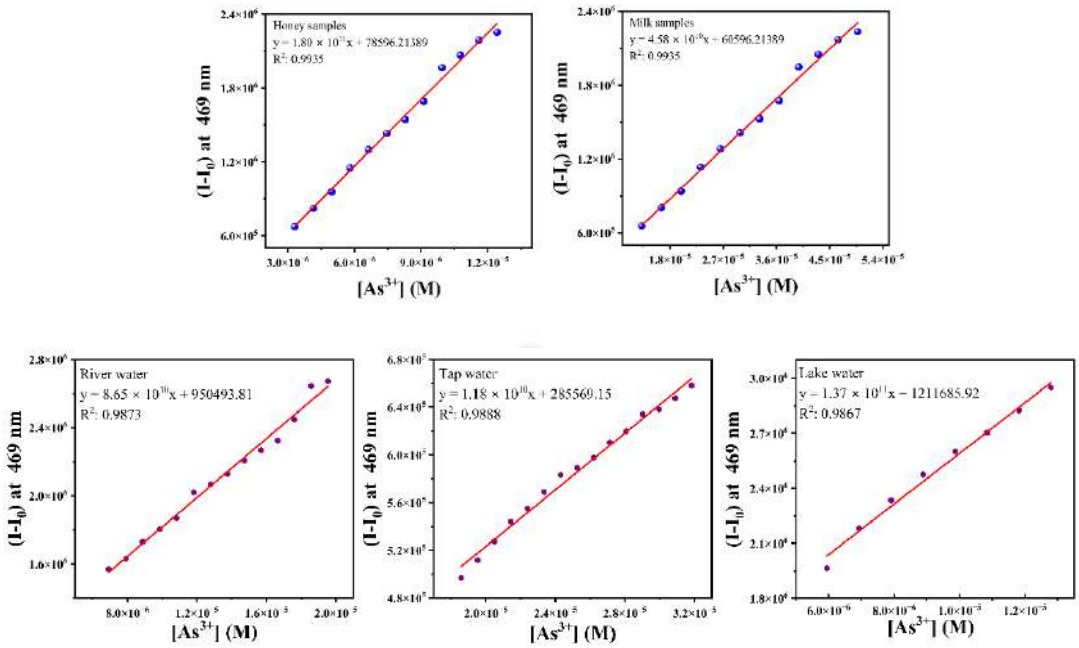

Figure A24. Linear calibration plots of maximum intensity *versus* the amount of As^{3+} ions for the analysis of food and real water samples.

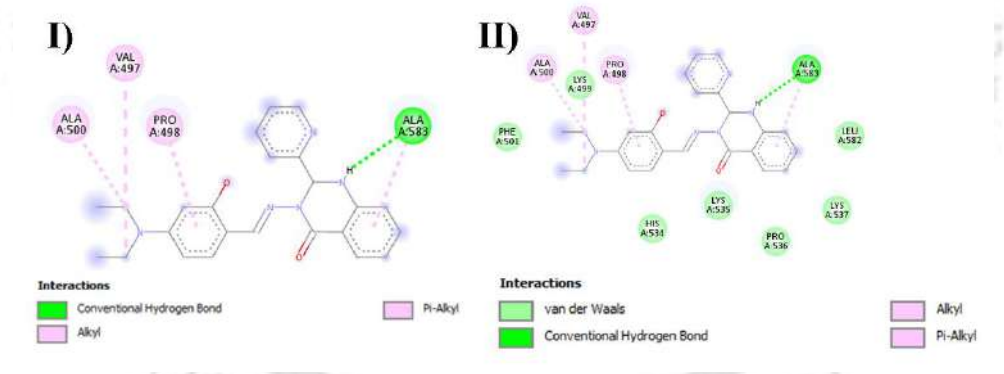

Figure A25. 2D plot for showing the interaction of (I) BSA and (II) HSA with **L3H** depicting amino acid residues.

Table A1. Photophysical data of **L3H** in various solvents.

Solvents	***λ_{max} (nm)***	***λ_{em} (nm)***	***Stokes shift (nm)***
Hexane	368	497	129
Diethyl ether	362	450	88
DCM	368	487	119
THF	372	468	96
MeOH	372	510	138
EtOH	365	505	140
Acetonitrile	373	495	122

DMF	367	493	126
DMSO	378	503	125
Water	395	504	109

Table A2. Fluorescence decay parameters of **L3H** in various Water-THF fraction (100%, 50%, 0%).

Entry	τ_1*(ns)*	τ_2*(ns)*	α_1*(%)*	α_2*(%)*	τ*(ns)*	χ^2
0%	0.191	0.192	-6616	6721.52	0.25	0.98
50%	0.342	0.342	4808.60	177.85	0.34	0.99
100%	0.949	5.240	4671.10	435.50	5.55	0.90

Table A3. Main electronic transition calculated by TDDFT method for **L3H**, [As(**L3**)(Br_2)] complex.

Analytes	*Energy (eV)*	λ_{theo} *(nm)*	*Oscillator strength*	*Major Transition*	*Electronic transition*	λ_{exp} *(nm)*
L3H	2.98	415.64	0.6475	(19%) HOMO-1→LUMO (67%) HOMO→LUMO	$S_0 \rightarrow S_1$	370
	3.37	366.85	0.0623	(57%) HOMO→LUMO+1	$S_0 \rightarrow S_2$	
	3.50	353.36	0.1244	(10%) HOMO-1→LUMO+1 (69%) HOMO→LUMO+1	$S_0 \rightarrow S_3$	
	3.83	323.05	0.2504	(11%) HOMO-1→ LUMO+1 (63%) HOMO→ LUMO+2 (22%) HOMO→ LUMO+3	$S_0 \rightarrow S_4$	
	3.89	318.12	0.0100	(66%) HOMO-1→ LUMO+1	$S_0 \rightarrow S_5$	
	4.00	309.71	0.0569	(20%) HOMO-2→ LUMO (61%) HOMO→ LUMO+3 (13%) HOMO-1→ LUMO+4	$S_0 \rightarrow S_7$	
	4.16	297.71	0.0387	(11%) HOMO-3→ LUMO (56%) HOMO-2→ LUMO (16%) HOMO-1→ LUMO+2 (14%) HOMO→ LUMO+2	$S_0 \rightarrow S_8$	
	4.22	293.23	0.0127	(20%) HOMO→ LUMO+4 (63%) HOMO-1→ LUMO+2 (20%) HOMO-1→ LUMO+3	$S_0 \rightarrow S_9$	
	4.36	284.09	0.0332	(63%) HOMO-1→ LUMO+3	$S_0 \rightarrow S_1$	
[As(**L3**)(Br_2)]	3.046	407.04	0.2508	(11%) HOMO-4→LUMO (33%) HOMO-1→LUMO	$S_0 \rightarrow S_1$	450
	3.155	392.92	0.1188	(24%) HOMO →LUMO (14%) HOMO→LUMO+1	$S_0 \rightarrow S_2$	
	3.232	383.60	0.2105	(51%) HOMO→LUMO+2 (12%) HOMO-3→LUMO	$S_0 \rightarrow S_4$	

			(44%) HOMO-1→LUMO (36%) HOMO→LUMO+1 (10%) HOMO-3→LUMO	
3.365	368.40	0.0114	(23%) HOMO-2→LUMO (52%) HOMO-1→LUMO+2	$S_0 \rightarrow S_6$
3.499	354.26	0.0301	(57%) HOMO→LUMO+4	$S_0 \rightarrow S_8$
3.510	353.15	0.0161	(37%) HOMO-4→LUMO	$S_0 \rightarrow S_9$

Table A4. Fluorescence decay parameters of **L3H** with As^{3+} ion in HEPES buffer and MEOH/HEPES (6:4, *v/v*) system.

Solvents	***Entry***	***τ_1(ns)***	***τ_2(ns)***	***α_1(%)***	***α_2(%)***	***τ(ns)***	***χ^2***
HEPES	**L3H**	0.178	1.53	0.13	0.03	0.47	0.90
	L3H + As^{3+}	0.816	1.85	0.06	0.08	1.38	1.00
MEOH/HEPES	**L3H**	0.091	0.25	0.26	0.04	0.14	1.00
	L3H +As^{3+}	0.558	1.72	0.11	0.06	0.97	0.99

Table A5. Removal of As^{3+} ion from wastewater.

Ion type	***Initial concentration (ppb)***	***Final concentration of As^{3+} ion after pretreatment (ppb)***	***Removal (%)***
As^{3+}	84	28	67

Table A6. Truth table of the three-input molecular logic gate demonstrating NOT, AND operations.

In1 (L3H)	***In2(As^{3+})***	***In3(F^-)***	***Out1 (468 nm)***	***Out2 (510 nm)***
0	0	0	0(low)	0(low)
0	1	0	0(low)	0(low)
0	0	1	0(low)	0(low)
0	1	1	0(low)	0(low)
1	0	0	0(low)	1(high)
1	1	0	1(high)	1(high)
1	0	1	0(low)	1(high)
1	1	1	0(low)	1(high)

Table A7. Comparative study of existing methods and present methods for selective detection of As^{3+} ion.

Sensors	*Detected Analytes*	*Detection method*	*Detection medium*	*Detection limits*	*Application*	*References*
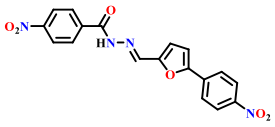	AsO_2^-	Colorimetric	DMSO/ H_2O (6:4, *v/v*)	98.9 nM	A) Paper strips, B) Water and food samples, C) logic gates construction	34
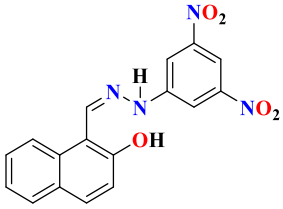	AsO_2^-/ AsO_4^{3-} and S^{2-}	Colorimetric	DMSO/ H_2O (4:1, *v/v*, pH 7.0, 10 mM Tris-HCl buffer)	0.15 µM and 0.17 µM	Portable paper strips for real water sample analysis	35
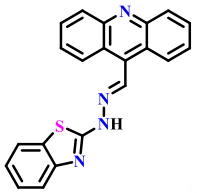	As^{3+}	Colorimetric	Aqueous medium	72.1 nM	A) logic gates circuits B) RGB-based smartphone device	36
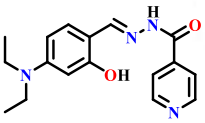	Al^{3+} and AsO_2^-	Colorimetric and Fluorometric	H_2O/ACN (4:1, *v/v*)	1.89 µM and 2.2 µM	A) logic gate circuits, B) cell imaging studies	6
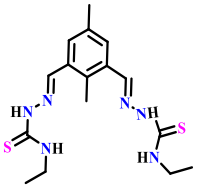	PO_4^{3-} and AsO_3^{3-}	Colorimetric and Fluorometric	ACN/H_2O (9 : 1, *v/v*, pH = 7.2).	34 nM and 15 nM	A) logic gate circuits, B) Real water samples	1
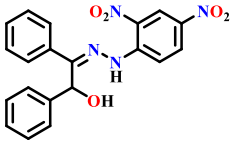	F^-, CH_3COO^-, $H_2PO_4^-$, AsO_2^-	Colorimetric	H_2O/DMSO (1:9, *v/v*)	5.26 µM, 2.90 µM, 2.00 µM, 1.92 µM	Real water samples	7
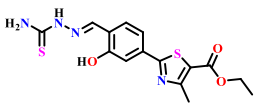	As^{3+}	Colorimetric and Fluorometric	DMSO: H_2O (7:3 *v/v*)	7.19 nM	A) Paper strips analysis, B) Real water samples, C) Cell imaging of cancer cell	8
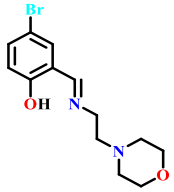	Zn^{2+}, $H_2AsO_4^-$	Fluorometric	H_2O/CH_3OH (9: 1, *v/v*, pH = 7.4)	0.44 µM and 0.32 µM	Bio-imaging studies	37

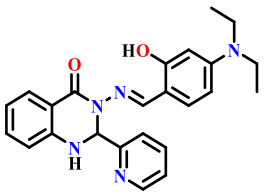	As^{3+}	Fluorometric	Aqueous HEPES buffer, MeOH/HEPES (6:4, *v/v*, pH = 7.4)	55 nM and 5.25 µM	A) Paper strips analysis, B) Real water and food samples analysis, C) logic gate fabrication, D) Smartphone based portable device	This work

Table A8. Docking results for the favorable conformers.

Protein	***Amino acids residue***	***Binding energy (kcal/mol)***
BSA	PRO 498, VAL 497, ALA 500, ALA 538.	-4.64
HSA	ALA 583, PRO 498, LYS 499, VAL 497, ALA 500, PHE 501, HIS 534, LYS 535, PRO 536, LYS 537, LEU 582.	-7.12

Thesis Summary:

This dissertation includes five chapters out of which Chapter 1 contains an introduction about chemosensors and various other sensing mechanisms. Some recent examples of metal ions, biothiols and phosphate ions have been discussed. At the end of this chapter material and methods used for the experiments were mentioned in detail. Chapter 2 deals with the synthesis and characterization of 3-hydroxy-N'-(11H-indeno[1,2-b]quinoxalin-11-ylidene)-2-naphthohydrazide (**LH**) and the probe was utilized in selective naked-eye detection of Cu^{2+} ion in presence of various metal ions. It has been found that *in situ* formed [Cu(**L**)Cl(H_2O)$_2$] (complex **1**) selectively detects cysteine and ATP over other interfering amino acids and anions, respectively. In Chapter 3, a probe N-(naphthalen-1-yl)-2-(pyren-1-ylmethylene) hydrazine-1-carbothioamide (**L$_1$**) has exhibited specific recognition of Pd^{2+} ion in EtOH-aqueous HEPES buffer (pH = 7.4, 3:7, *v/v*). Several practical applications showed that Pd^{2+} can be detected using **L$_1$** in various real water specimens and commercially available drug samples. After that in Chapter 4, a probe (**L2H**) having 2-(2-aminophenyl)-1H-benzimidazole and quinoline rings has been synthesized, and it is found to be a turn-on fluorescent sensor towards Al^{3+} ion and cysteine in aqueous CTAB medium. **L2H** acted as an ultrafast sensor and selectively detects the analytes in nanomolar range. The portable solid-state tool such as filter paper strips and hydrogel membrane test kits has been fabricated for rapid on-spot detection of Al^{3+} and cysteine. This probe is also utilised to detect the analytes in various contaminated water and food samples. In the final Chapter 5, a fluorometric AIE based chemosensor **L3H** exhibited a selective and sensitive turn-on detection of As^{3+} ion in aqueous HEPES medium. It exhibits nanomolar detection towards As^{3+} with a very less response time, which makes it a practically usable sensor. Real-life practical application was also performed for detecting As^{3+} in different food and real samples. The probe can also be utilized by a smartphone linked device for fast on-site As^{3+} ion recognition without using any sophisticated instruments.

Future Perspective:

In Chapter 2, a chemosensor based on a ninhydrin-quinoxaline derivative was utilized for bare-eye detection of Cu^{2+} ion. By modifying binding subunit part of the probe with hydroxy-substituted photoactive moieties such as coumarin, anthracene, rhodamine and fluorescein, which contains N,O and O,O-donor atoms can help in selective recognition several transition metal ions. Various colorimetric chemosensors contain a rigid metal-chelated complex *via*

metal displacement assay used in the detection of several phosphate ions and biothiols. In Chapter 3, we have seen that a pyrene linked chromogenic and fluorogenic probe acted as a turn-off fluorescent sensor for recognition of Pd^{2+} ion. In future, various heterocyclic thiosemicarbazide precursors can be synthesized using isoquinoline, coumarin, pyrimidine, furan and benzothiazole moieties. Such probes containing N,S-donor atoms, hold great potential for selective detection of kinetically soft Pd^{2+} ion along with other toxic metals *viz.,* Cd^{2+}, Pb^{2+} and Hg^{2+} ions. Lastly, in Chapter 4, 5 two AIE active fluorescent chemosensor were utilized in fluorescent turn-on detection of cysteine, Al^{3+} and As^{3+} ions. The design of new AIE-gens through systematic modification of fluorophore unit within the probe skeleton could increase quantum yield in solid state, thereby high sensitivity towards detection of analytes can be achieved.

List of Publications

From Thesis:

1. A. Mondal, V. Manivannan, A naphthyl appended ninhydrin based colorimetric chemosensor for Cu^{2+} ion: detection of cysteine and ATP, *Spectrochim. Acta A Mol. Biomol. Spectrosc.,* **2024**, 322, 124734.
2. A. Mondal, V. Manivannan, Aggregation induced emission active pyrene scaffold for real-time chromogenic and fluorogenic selective detection of Pd^{2+} ion and device fabrication, *Spectrochim. Acta A Mol. Biomol. Spectrosc.,* **2025**, 333, 125865.
3. A. Mondal, V. Manivannan, Solvent-tuned fluorometric detection of Al^{3+} ion and cysteine by a benzimidazole-linked AIE active sensor in solution and solid matrix, *ChemistrySelect*, **2025**, 10, e03977.
4. A. Mondal, S. Sinha, V. Manivannan, Smartphone-based portable sensing device for fluorometric detection of As^{3+} ion using an AIE active quinazolinone analogue, (*Manuscript submitted*).